

Photovoltaic-powered ultrafiltration/reverse osmosis for brackish water desalination: supercapacitor control system

zur Erlangung des akademischen Grades eines
DOKTOR-INGENIEURS
von der KIT-Fakultät für Elektrotechnik und Informationstechnik
des Karlsruher Instituts für Technologie (KIT)

genehmigte
Dissertation
von
M. Sc. Sheying Li

Tag der mündlichen Prüfung: 26. Juli 2022

Erster Gutachter: Prof. Dr. Bryce S. Richards

Zweiter Gutachter: Prof. Dr.-Ing. Andrea I. Schäfer

Contents

Contents	i
Kurzfassung	v
Acknowledgements	vii
Abstract	ix
Publications	xi
1. Introduction	1
1.1. Motivation.....	1
1.2. Membrane technology.....	2
1.3. Photovoltaic energy.....	3
1.4. System control.....	4
1.5. Thesis objectives and research questions	6
2. System components and design considerations	9
2.1. Photovoltaic modules	9
2.1.1. PV module degradation and failure modes	10
2.1.2. Recommendations.....	11
2.2. Power conditioning device.....	11
2.2.1. DC-DC converter	12
2.2.2. Maximum power point tracking.....	12
2.2.3. Drive controller.....	13
2.2.4. DC-AC inverters	14
2.2.5. Recommendations.....	14
2.3. Short-term energy storage	14
2.3.1. Lead-acid batteries.....	15
2.3.2. Lithium-ion batteries.....	16
2.3.3. Supercapacitors	16
2.3.4. Recommendations.....	16
2.4. Motor-pump subsystem.....	17
2.4.1. Pump motors	17
2.4.2. Pump.....	18
2.4.3. Recommendations.....	25
2.5. Pressure-driven membrane processes.....	26

2.5.1. Membrane fouling and control.....	26
2.5.2. Membrane integrity and damage.....	35
2.5.3. Operation and maintenance.....	38
2.5.4. Recommendations.....	42
2.6. Sensors.....	43
2.6.1. Flowmeters.....	43
2.6.2. Pressure sensors.....	44
2.6.3. Water quality sensors.....	44
2.6.4. Temperature sensors.....	45
2.6.5. Recommendations.....	46
2.7. PV-membrane brackish water desalination system.....	46
2.7.1. System performance.....	46
2.7.2. System reliability.....	49
2.7.3. System operation and maintenance.....	49
2.7.4. Recommendations.....	50
2.8. Summary.....	50
3. Materials and methods.....	53
3.1. Photovoltaic powered membrane system overview.....	53
3.1.1. System descriptions.....	54
3.1.2. Helical rotor pump and motor.....	56
3.1.3. Set-point operation strategy.....	57
3.2. Feed water and membrane.....	58
3.2.1. Feed water preparations.....	58
3.2.2. Membrane modules.....	60
3.3. Solar array simulator and solar days.....	61
3.4. Energy storage units.....	63
3.4.1. Supercapacitor energy buffering.....	63
3.4.2. Lithium-ion battery energy storage.....	64
3.5. Charge controller and system resilience.....	65
3.5.1. Flow chart.....	65
3.5.2. Settings for system control.....	67
3.5.3. Parameters of system resilience.....	68
3.6. UF membrane backwashing control and water.....	69
3.6.1. Backwashing system overview.....	69
3.6.2. Bladder tank.....	70
3.6.3. Backwashing pump.....	70
3.6.4. “Simulated fouling” setup.....	71

3.6.5. Energy consumption calculations	72
3.6.6. Backwashing figures-of-merit.....	75
3.7. Experimental design.....	77
3.7.1. Steady-state experiments	77
3.7.2. Ramp rates in PV voltage	78
3.7.3. Real solar days.....	84
3.7.4. Ultrafiltration membrane backwashing.....	84
3.7.5. System performance with Li-ion batteries and SCs.....	86
3.8. Error analysis	86
4. Effect of ramp rates in solar irradiance	89
4.1. Steady-state experiments.....	89
4.2. Square waves of solar irradiance.....	91
4.3. Ramp rates of PV voltage without energy buffering.....	93
4.4. Charge controller performance.....	98
4.5. Voltage threshold variations.....	101
4.6. Summary	104
5. Effect of energy buffering control on reducing system shut-downs and enhancing resilience...105	
5.1. Directly-coupled system resilience with different solar days.....	105
5.2. System resilience with SCs and charge controller	107
5.3. Impact of feed salinity on system resilience with/without SCs buffering control.....	114
5.4. Impact of PV power capacity on system resilience with SCs buffering control	116
5.5. Summary	122
6. Energy consumption analysis of system backwashing	123
6.1. Energy consumption with “simulated fouling”	123
6.2. System performance under real solar days with bentonite	128
6.3. Bladder tank backwashing with high fouling rate.....	138
6.4. Comparisons between “simulated fouling” and real fouling.....	143
6.5. Summary	144
7. Use of lithium-ion batteries for energy storage	147
7.1. Operation performed on the partly cloudy day (with and without fully-charged batteries)	147
7.2. Operation under other solar days (with and without fully-charged batteries)	150
7.3. Operation with different energy storage capacities	152
7.4. System performance comparisons of batteries and SCs.....	160
7.5. Summary	163
8. Conclusions and outlook.....	165

Contents

8.1. Conclusions	165
8.2. Outlook and suggestions for further research.....	167
Bibliography	169

Kurzfassung

Diese Arbeit untersuchte die technische Machbarkeit, die Herausforderungen und die Leistungsfähigkeit eines photovoltaisch betriebenen Membransystems (PV-Membran) zur Aufbereitung von Brackwasser in abgelegenen Gebieten. Im ersten Teil der Arbeit wurde ein umfassender Überblick über die Effizienz, den Betriebsbereich und die Zuverlässigkeit aller Komponenten eines kleinen PV-Membransystems zur Brackwasserentsalzung gegeben. Es wird vorgeschlagen, dass ein kleines PV-Membransystem, das auf einer von einem bürstenlosen Gleichstrommotor angetriebenen und von Silizium-Photovoltaikmodulen gespeisten Spiralrotorpumpe basiert, eine Lebensdauer von 20 Jahren erreichen kann. Um die Verschmutzung und Beschädigung der Membran zu verringern, wird empfohlen, das System mit einem Rückgewinnungsgrad von weniger als 30%, einem Sanftanlauf des Speisedrucks < 0.7 bar/s und einem statischen Permeatdruck < 0.3 bar zu betreiben.

Im zweiten Teil wurde ein neuartiger Laderegler entwickelt, der auf voreingestellten Schwellenwerten für die Spannungsmessung basiert, um die Energie von PV-Paneelen und Superkondensatoren (SCs) zu verteilen. Die Auswirkungen von Rampenraten sowohl der Sonneneinstrahlung (SI) als auch der PV-Ausgangsspannung (V_{PV}) auf das System wurden systematisch mit hoher zeitlicher Auflösung (1 s) untersucht. Es zeigte sich, dass der Laderegler die SCs in die Lage versetzte, die Leistungslücke für 6 min 20 s zu überbrücken, so dass in einem Worst-Case-Szenario mit einer schnellen Rampenrate von $V_{PV} = 2$ V/s zusätzliche 10 L Permeatwasser produziert werden konnten. Der Ladezustand der SCs variierte zwischen 11 und 86%, unabhängig von der Höhe der Rampenrate. Die Spannungsschwellen bei $V_{pump_on} = 160$ V und $V_{pump_off} = 60$ V wurden bestimmt, um eine hohe Permeatproduktion bei niedriger spezifischer Energieverbrauch (SEC) zu erreichen. Im dritten Teil wurde der Laderegler mit SC-Energiepufferung an verschiedenen Tagen mit voller Sonneneinstrahlung (9 – 12 Stunden) eingesetzt, um die Anzahl der Systemabschaltungen zu reduzieren und die Ausfallsicherheit des Systems zu erhöhen. Die Schlüsselparameter - die Anzahl der Abschaltvorgänge ($\#_{SD}$), die Abschaltdauer (t_{SD}) sowie der Resilienzfaktor im Fluss (RF_{flux}) - wurden untersucht, insbesondere an einem teilweise bewölkten Tag, der während 90-minütiger Perioden stark schwankende SI aufwies. An teilweise und stark bewölkten Tagen wurde t_{SD} um 37% bzw. 12% reduziert, und $\#_{SD}$ wurde mit dem Laderegler und den SCs um 2 bis 13 Ereignisse minimiert. Die durchschnittliche SEC wurde an sehr bewölkten und sonnigen Tagen um 22% bzw. 8% verbessert. Während der 90-minütigen Fluktuationen konnte t_{SD} auf 1 – 4.5 min begrenzt werden, und $\#_{SD}$ wurde um 1 – 4 Ereignisse bei Speisewassersalzgehalten von ≤ 7.5 g/L reduziert. Bei einer Erhöhung der PV-Leistung auf 600 – 1000 W wurden keine Systemabschaltungen beobachtet, der RF_{flux} stieg von 0.3 auf 0.8 – all dies deutet auf eine verbesserte Systemstabilität mit den SCs und dem Laderegler hin.

Im vierten Teil dieser Arbeit wurde der Energieverbrauch von zwei Ultrafiltrationsmembran-Rückspülkonfigurationen - einem Blasentank und einer von SCs angetriebenen Rückspülpumpe - unter verschiedenen SI-Bedingungen untersucht. Der Blasentank weist einen BW-SEC von 0.3 Wh/L auf, während die

BW-Pumpe einen SEC von 0.09 Wh/L unter simuliertem Fouling und $SI = 1000 \text{ W/m}^2$ aufweist. Bei variierenden realen Sonnentagen mit dem Blasenspeicher bleibt der Gesamt-SEC bei etwa 4 Wh/L, was auf einen geringen energetischen Nachteil bei der Durchführung eines BW-Zyklus alle 90 Minuten hinweist. Es wurde festgestellt, dass ein BW-Intervall von 60 Minuten einen Gesamt-SEC von 3.7 Wh/L aufweist und ein Gleichgewicht zwischen SEC und der Abschwächung der Membranverschmutzung erreicht. Das vorgeschlagene Konzept der Anwendung eines Ventils zur Simulation des Foulings kann Studien zum Fouling von UF-Membranen unterstützen, ohne dass die Gefahr eines irreversiblen Foulings an der Membran besteht. Trotz des höheren BW SEC wurde der Blasentank als robusterer Aufbau für die Realisierung der BW-Funktionalität für PV-Membransysteme empfohlen. Im letzten Teil der Arbeit wurde das Potenzial von Lithium-Ionen-Batterien (Li-Ion) und SCs zur Überwindung langfristiger (1 d) und kurzfristiger (einige Minuten) SI-Schwankungen an Sonnentagen untersucht. Es wurde ein Vergleich zwischen voll aufgeladenen Batterien und SCs durchgeführt, um die Systemleistung an einem teilweise bewölkten Tag zu bestimmen. Mit voll aufgeladenen Li-Ionen-Batterien wurde sauberes Trinkwasser mit einem durchschnittlichen SEC von etwa 4 Wh/L produziert. Die tägliche Wasserproduktion verbesserte sich von 663 L auf 767 L (16% Steigerung) bei einem Rückgang der durchschnittlichen elektrischen Leitfähigkeit von 310 $\mu\text{S/cm}$ auf 274 $\mu\text{S/cm}$ (12% Verbesserung) im Vergleich zum direkt gekoppelten System. Die erhöhte Wasserproduktion trat bei einer anfänglichen Batteriekapazität von mehr als 50 Ah auf. An sonnigen und stark bewölkten Tagen mit voll geladenen Batterien stieg die tägliche Wasserproduktion um 15% bzw. 80%, während sich die Wasserqualität um 18% bzw. 21% verbesserte. Im Vergleich zur Leistung des direkt gekoppelten Systems an dem teilweise bewölkten Tag ermöglichten die SCs eine Steigerung der Wasserproduktion um 9% und eine Verbesserung der SEC um 13%.

Acknowledgements

This Ph.D. has been an adventure and a defining experience for me, and has led me to learn immensely and work with a diverse group of wonderful and generous people. I am deeply grateful to my supervisors, Prof. Bryce Richards and Prof. Andrea Schäfer, for making this Ph.D. possible and for guiding the whole path of this research. Your deep insights, knowledge, vision, guidance, and experience have been precious to me, and you have taught me to become a better scientific researcher for my future career.

I would also like to thank the Chinese Scholarship Council (CSC) for funding this Ph.D. fellowship. I express gratitude to the Institute Microstructure of Technology (IMT) workshop for their invaluable technical support throughout this project, especially when I was pregnant and not able to carry the heavy metal tubes and pull all of the pieces together. A special thanks is given to Herr Benz Jürgen. Thank you for your help. I have such clear memories of changing the membrane module, lifting the pump, moving the Bosch profile, and cleaning the membrane! I am also grateful to Herr Achim Voigt. Thank you for your patient discussions and consultations throughout this research. I have learned so many electrical engineering skills from you. I would also like to thank the MSc students who have contributed substantially to this research: Matej Nikola Raic, Vanessa Celia Molinares, Michele Milia, and Ana Carvalho.

My heartfelt gratitude goes to Hu Ping, who has been a true friend. I remember when I was desperate, and not able to finish my work; you have helped me so many times by being my driver, my dear sister, and talked me through frustrations and troubles; we have laughed and cried together. I have been so lucky to have you as my best friend in Germany. I wish you and your family all of the very best for your futures. A special thank you also goes to Natalia Kiseleva, Reetu Joseph, Michael Adams, Nicolo Baroni and Yang-Hui Cai, who have been excellent colleagues and even better friends. Thank you for your precious friendship.

Finally, my particular gratitude is expressed to my parents, my sister, my brother, and my family. I thank my sister so much for coming to Germany to take care of my small baby twice. To my family, thank you for all of your continual love and support. Thank you to my husband, Jiuce, for your unconditional love and support. Most importantly, I am eternally grateful to my lovely daughters, Chenchen and Hanhan. Thank you for the joy and happiness that you have brought to me. You make my life amazing and delightful.

Abstract

This thesis investigated the technical feasibility, challenges, and performance issues of a photovoltaic powered membrane system (PV-membrane) for treating brackish water in remote areas. The first part of the thesis presented a comprehensive review of the efficiency, operating range, and reliability of all components of a small-scale PV-membrane system for brackish water desalination. It is suggested that a small-scale PV-membrane system, based on a helical rotor pump driven by a direct-current brushless motor and powered by silicon photovoltaic modules, is capable of achieving a lifetime of 20 y. To mitigate membrane fouling and damage, the system is recommended to operate with the recovery of less than 30%, the soft start of feed pressure < 0.7 bar/s, and static permeate pressure < 0.3 bar.

In the second part, a novel charge controller based on pre-set voltage sensing thresholds was developed to distribute energy from PV panels and supercapacitors (SCs). The effects of ramp rates in both solar irradiance (SI) and PV output voltage (V_{PV}) on the system were systematically examined with high-temporal-resolution (1 s). It was found that the charge controller enabled the SCs to bridge the power gap for 6 min 20 s, thus permitting an additional 10 L of permeate water produced under a worst-case scenario with a rapid ramp rate of $V_{PV} = 2$ V/s. The state-of-charge of the SCs varied from 11 to 86%, independent of the magnitude of the ramp rate. The voltage thresholds at $V_{pump_on} = 160$ V and $V_{pump_off} = 60$ V were determined to achieve a high permeate production at a low specific energy consumption (SEC). In the third part, the charge controller with SCs energy buffering was applied under varied full-length solar days (9 – 12 h) to reduce system shut-down events and enhance system resilience. The key parameters – number of shut-down events ($\#_{SD}$), shut-down duration (t_{SD}), as well as resilience factor in flux (RF_{flux}) – were examined, in particular on the partly cloudy day that exhibited highly fluctuating SI during 90-min periods. On partly and very cloudy days, t_{SD} was reduced by 37% and 12%, respectively, and $\#_{SD}$ was minimized by 2 – 13 events with the charge controller and SCs. Average SEC was improved by 22% and 8% under the very cloudy and sunny day, respectively. During the 90-min fluctuations, t_{SD} was found to be restrained to 1 – 4.5 min, and $\#_{SD}$ was reduced by 1 – 4 events at feedwater salinities of ≤ 7.5 g/L. Increasing the PV capacity to 600 – 1000 W – zero system shut-down events were observed, RF_{flux} increased from 0.3 to 0.8 – all of which suggested enhanced system resilience with the SCs and charge controller.

The fourth part of this thesis investigated the energy consumption of two ultrafiltration (UF) membrane backwashing configurations – a bladder tank and a backwash (BW) pump powered by SCs – under varied SI conditions. The bladder tank exhibits a BW SEC of 0.3 Wh/L, while the BW pump exhibits an SEC of 0.09 Wh/L under simulated fouling and $SI = 1000$ W/m². Under varied real solar days with the bladder tank, the total SEC remains at approximately 4 Wh/L, which indicates a small energetic penalty for implementing one BW cycle every 90 min. It was found that a BW interval of 60 min exhibited a total SEC of 3.7 Wh/L, and reached a balance between SEC and the mitigation of membrane fouling. The proposed

concept of applying a valve to simulate fouling can assist UF membrane fouling studies without the risk of inducing irreversible fouling to the membrane. Despite its higher BW SEC, the bladder tank was recommended to be a more robust setup for realizing BW functionality to the PV-membrane systems. The final part of the thesis examined the potential for lithium-ion (Li-ion) batteries and SCs to overcome long-term (1 d) and short-term (a few minutes) SI fluctuations under solar days. A comparison was performed between fully-charged batteries and SCs to determine system performance on the partly cloudy day. Clean drinking water was produced at an average SEC of approximately 4 Wh/L with fully charged Li-ion batteries. The daily water production improved from 663 L to 767 L (16% increase) with a decline of average electrical conductivity from 310 $\mu\text{S}/\text{cm}$ to 274 $\mu\text{S}/\text{cm}$ (12% improvement), compared to the directly-coupled system. Enhanced water production occurred at an initial battery capacity higher than 50 Ah. On the sunny and very cloudy days with fully charged batteries, daily water production increased by 15% and 80%, while water quality improved by 18% and 21%, respectively. When compared to the directly-coupled system performance on the partly cloudy day, the SCs enabled a 9% increase and 13% improvement in water production and SEC, respectively.

Publications

Journals

Sheying Li, Achim Voigt, Y.H. Cai, Andrea I. Schäfer, Bryce S. Richards, Renewable energy powered membrane technology: Energy buffering control to reduce the shut-down events and enhance system resilience under different solar days, *Renewable Energy* (under review)

Sheying Li, Michele Milia, Andrea I. Schäfer, Bryce S. Richards, Renewable energy powered membrane technology: Energy consumption analysis of ultrafiltration backwash configurations, *Separation and Purification Technology* (2022) 287, 120388.

Sheying Li, Ana P.S.G.de Carvalho, Andrea I. Schäfer, Bryce S. Richards, Renewable energy powered membrane technology: Evaluation of lithium-ion battery storage for a photovoltaic-powered brackish water desalination system, *Applied Sciences* (2021) 11, 856.

Sheying Li, Achim Voigt, A.I. Schäfer, B.S. Richards, Renewable energy powered membrane technology: An energy buffering control system for improved resilience to periodic fluctuations of solar irradiance, *Renewable Energy* (2020) 149, 877-889.

Sheying Li, Y.H. Cai, A.I. Schäfer, B.S. Richards, Renewable energy powered membrane technology: A review of the reliability of photovoltaic-powered membrane system components for brackish water desalination. *Applied Energy* (2019) 253, 113524.

Conference

Sheying Li, Achim Voigt, Andrea I. Schäfer, Bryce S. Richards, A supercapacitor-based charge controller for a photovoltaic-powered desalination system. *Desalination for the Environment Clean Water and Energy*, 3-6 September 2018, Divani Caravel Hotel, Athens, Greece.

Author statements

Parts of this thesis have already been published in scientific journals, and the contributions of other co-authors were included in this thesis. The contributions of the co-authors are specified as follows:

Achim Voigt: design of the charge controller used in Chapters 4 and 5, and helped to solve maximum power point tracker issues in Chapter 5;

Michele Milia: assisted with the backwashing setup used in Chapter 6, and performed experiments in Section 6.1;

Ana P.S.G.de Carvalho: assisted with battery setup, and performed battery experiments in Chapter 7;

Y.H. Cai: helped review membrane aspects in Chapter 2, and assisted with risk assessment review and system cleaning in Chapter 5;

Prof. Schäfer: helped supervise the research, conceived the original idea, assisted with analysis and interpretation of results, and provided critical feedback;

Prof. Richards: helped supervise the research, conceived the original idea, assisted with the design of experiments, analysis and interpretation of results, and provided critical feedback and helped shape the research.

1. Introduction

1.1. Motivation

The shortage of potable water has become one of the most serious problems globally due to the rapid growth of population, industrialization, and climate change. Up to 2020, 771 million people still lacked access to safely managed drinking water, and 50% of inhabitants still lack even basic drinking water lived in sub-Saharan Africa [1]. It is estimated that by 2030, approximately 660 million more people will not have access to electricity – approximately 35 million more people than projections from the year from the World Energy Outlook – 2019 due to the pandemic [2]. A direct correlation exists between the availability of electricity and drinking water, with the impacts of energy poverty suggesting that populations living with electricity are also prone to have access to an improved water source (and vice versa) [3]. This highlights opportunities for decentralized technologies for applications where little water and energy infrastructure exist and the population density is sparse.

The provision of potable water through brackish water desalination is an attractive way to cope with water scarcity in many regions worldwide. Nanofiltration/reverse osmosis (NF/RO) membrane technology has been considered as an efficient solution to desalinate brackish water to supply clean drinking water due to its low specific energy consumption (SEC, units: Wh/L), which represents the energy input required to treat 1 m³ of water [4, 5]. When renewable energy powered membrane (RE-membrane) systems are applied in remote areas that lack an electricity grid, such decentralized technologies can provide an ideal solution. In particular, as a consequence of steady price declines over the last decade [6], photovoltaic (PV) energy has become an affordable source of clean electricity, and is currently (2020 data) one of the cheapest sources of electricity [7]. Such photovoltaic powered membrane filtration (PV-membrane) systems are attractive as a result of several synergies between the two technologies [8]. Firstly, both PV panels and NF/RO membrane elements are modular and can be scaled to meet the desired clean water demand. Secondly, the demand for drinking water is higher in arid regions of the world, and these same regions typically also constitute an excellent solar resource [9]. Thirdly, the prices for PV modules have been decreasing dramatically and steadily, and reached US\$ 0.2 per Watt-peak (W_p) in 2021 [10], while the RO module market is predicted to thrive at a compound annual growth rate (CAGR) of 7.6% over the forecast years 2020 – 2030 [11], making the technology increasingly cost-effective over time. Indeed, a study concluded that the cost of clean drinking water from small-scale decentralized membrane systems can be less than what locals are already paying for *untreated* water in several locations in sub-Saharan Africa [8]. While this research does not focus on cost analysis, it should be noted that certain geographic locations that have an abundance of sunshine represent obvious potential markets for PV-membrane technology.

1.2. Membrane technology

Membrane technologies have played critical roles in drinking water production, wastewater treatment and reclamation, and industrial process water treatment, with proven efficiency from a technical, economical, and ecological point of view [12]. Pressure-driven membrane filtration processes, such as microfiltration (MF), ultrafiltration (UF), NF, and RO membranes – listed in order of decreasing membrane pore size – frequently appear as standard components in RE-membrane systems. The driving force for water permeation is transmembrane pressure (TMP), which is provided by a pump. Contaminants are removed by various mechanisms, depending on membrane pore size [13]. Overall, as the pore size becomes smaller, the filtration processes require more energy, while smaller contaminants can be retained.

MF and UF are low-pressure processes that typically require a TMP < 3 bar. MF (pore size 0.1 – 1.0 μm) is capable of removing most fine suspended solids or particles and bacteria, while UF (pore size 2-50 nm) can remove viruses, colloids, and organic macromolecules down to a size of around 20 nm [14]. The permeation mechanism of MF and UF is primarily dependent on a pore flow model, whereby permeants are separated by pressure-driven convective flow through tiny pores [15, 16].

The pore size of NF is normally on the order of 1 nm, corresponding to a molecular weight cut-off (MWCO, defined as the molecular weight of a solute corresponding to a 90% rejection coefficient for a given membrane) ranging from 100 – 5000 g/mol [17, 18]. NF exhibits high retention to multivalent inorganic salts, such as calcium (Ca^{2+}) and magnesium (Mg^{2+}) – that contribute to water hardness – and small organic molecules at modest applied pressures (commonly with a TMP of 5 – 15 bar) [19]. RO membranes are dense membranes without predefined pores and require high pressures up to 100 bar, depending on the osmotic pressure of feed water [20, 21]. Ultimately, RO membranes can retain most dissolved solids, including monovalent ions, such as sodium and chloride, which makes them a suitable process for desalinating seawater. The commonly used spiral wound NF/RO membrane module is shown in Figure 1-1. It is mainly thin film composite (TFC) polyamide membranes consisting of three layers: a polyester web acting as structural support; a microporous interlayer; and an ultra-thin barrier layer on the upper surface. The feed channel spacers are added to keep the membrane layers apart and improve mass transfer on the membrane surface. The well-established solution-diffusion models are used for NF/RO to explain and describe the permeation process, whereby permeants dissolve into the membrane and subsequently diffuse through the membrane following a concentration gradient [16]. Separation is realized between different permeants due to the difference in solubilities and mobilities of permeants in the membrane [15, 16]. Typically, the MF/UF is employed as a pre-treatment to protect the NF/RO against fouling [22].

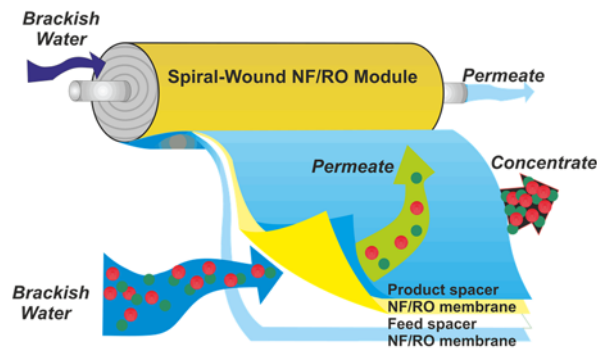


Figure 1-1: Schematic of a spiral wound NF/RO membrane module illustrating the flow of feed, permeate, and concentrate streams.

A key limitation for application in water filtration systems is membrane fouling, as it reduces membrane lifetime and increases the energy consumption, thus incurring high operation and maintenance (O&M) costs [23-26]. Further discussions regarding membrane fouling are provided in Section 2.3. From a practical and environmental perspective, the main operating challenge in desalination systems is brine disposal, which comprises up to 33% (worst case) of the total cost of seawater desalination processes [27]. In large-scale seawater desalination plants, brine is mostly discharged to the sea, which could be deleterious to the marine environment as a result of its high salinity or presence of pollutants if the brine is from multiple plants operating in the same area for a long period of time. The cost of this disposal method ranges from US\$ 0.05/m³ to US\$ 0.3/m³ [28, 29]. In small-scale brackish water desalination plants, brine can be disposed to sewer systems if available, and the cost of this disposal method varies from US\$ 0.3/m³ to US\$ 0.7/m³ [28, 29]. For inland plants, deep-well injection and evaporation ponds are appropriate brine disposal choices with approximate costs of US\$ 0.5-2.7/m³ and US\$ 3.3-10/m³ [28, 29], respectively. Land application is mainly used for low brackish water brine volumes, and depends on the availability of suitable land and groundwater conditions, which costs approximately US\$ 0.7-2/m³ [28, 29]. In small-scale brackish water desalination systems, the relatively low recovery of low-pressure RO membrane assures low concentrate concentration and possibilities for using the disinfected waste stream for washing and livestock watering (zero concentrate generation depending on feed quality).

1.3. Photovoltaic energy

Solar cells are made from semiconductor materials that create direct-current (DC) electricity by electromagnetic means when exposed to sunlight. Within a PV module, several individual solar cells are connected in series and parallel to build the output voltage and current. The solar cells are encapsulated between layers of glass or transparent polymers to protect the electrical circuit from the environment. More PV modules are then connected and mounted on the supporting structure to form a PV array. PV technology converts sunlight into electricity directly without interference. PV modules are rugged in design, and require

very little maintenance. Generally, PV modules have a warranty for 25 to 30 years in the field by manufacturers [30, 31]. PV construction as stand-alone systems give outputs from microwatts to megawatts, and consequently are commonly used as power sources for water pumping, RO and power plants. In particular, in remote areas where electricity is lacking, the use of PV power has been increasingly deployed as a promising technology for fulfilling energy requirements. Moreover, due to its steady price decline over the last decade, PV has become an affordable source of clean electricity.

The main challenge associated with PV power is the intermittent and fluctuating nature of the solar, which occurs due to passing clouds and weather disturbances caused by weather systems [32-34]. In a PV-membrane system, variations in SI are directly translated into varied output power from PV modules, which then induce fluctuations in pump pressure and flowrate. Here, it is necessary to distinguish fluctuation from intermittency. The former results in both reduced voltage and current of the PV module, which ultimately leads to lower power output. Consequently, it might cause large variations in pressure and flux [35] that are not necessarily enough to cease operation of the pump. In the latter case, intermittency – defined as the change of variability of SI during short time intervals – leads to a system shut-down during periods of insufficient power availability [36, 37].

Fluctuations can significantly affect the SEC of the system during variable operation [38]. In a PV-membrane system, it was reported that the SEC under fluctuating conditions (simulated square waves of SI) was ~17% higher than when operated under steady-state conditions [39]. When the same system was operated with a period of 60 minutes on a solar day, the peak values of SEC during the fluctuating (cloudy) periods were 2–5 times higher than those during steady-state operation (cloudless periods) [40]. Intermittent operation might cause system shut-downs, which could potentially increase the amount of wear-and-tear on the pump and motor [41, 42], deteriorate membrane system performance, and reduce membrane lifetime [42-44]. In addition, manufacturers recommend that RO membranes be operated at a constant permeate flowrate in order to extend lifetime [45]. Traditionally, energy storage devices (detailed in Section 2.3) are commonly applied in PV-membrane systems to overcome fluctuations and intermittencies. Meanwhile, advanced system control strategies are required to be incorporated to manage and operate desalination systems.

1.4. System control

For an RE-membrane system that is directly-coupled or equipped with energy storage devices, it is necessary to decide when to activate or deactivate operation of the system in terms of different control algorithms [46]. The challenge is to optimize energy management between the load and RE resources to achieve a low SEC [47] and minimize the number of system shut-down events, which increases the robustness and reliability of such systems overall [48]. The hysteresis control method is commonly utilized to maintain the load (which, in the present case, is the pump) in a certain state, thus avoiding the pump or energy storage devices from being activated/deactivated too frequently [46, 47, 49].

Several control strategies have been used in RE-membrane systems [50-54]. For the directly-coupled system, Khiari *et al.* [55, 56] presented a power control strategy that stabilized direct current (DC) bus voltage, which enabled maximum power extraction with power converters from the RE source on a directly-coupled wind/PV hybrid membrane system. Kim *et al.* developed a dynamic model and supervisory control strategy for the hybrid RO desalination system. The control strategy was implemented to meet the power consumption required by the system supervisor via adjusting the pump shaft rotational speed and maintaining the set-point operation pressure [57]. In a PV-membrane desalination plant, Bilton [58] *et al.* designed a control algorithm using a block diagram of the system model in MATLAB/Simulink based on physics and empirical equations. A buck converter was used to match the output voltage of the pump, while a microcontroller was used to drive the motor of the solar tracker to obtain maximum power from the PV. The results indicated a daily production of 300 L on a sunny summer's day, with the SEC from 2.5 – 4 Wh/L at a water salinity of 32.664 mg/L. Moreover, a design tool incorporated a simulated membrane fouling model during intermittent operation, and a genetic algorithm was proposed to assure more reliable PV membrane systems [59].

For systems that incorporated energy storage devices, an energy management system was commonly designed to distribute energy between the RE resources and load. Karavas *et al.* developed an energy management system for a PV-membrane seawater desalination system, which incorporated hybrid capacitors (380 F, 48 V) and hydraulic pressure vessels (11 bar, 180 L) [50]. The system was capable of producing water continuously on a cloudy day with rapid SI fluctuations (maximum SI variations of 400W/m²). The hybrid capacitors provided energy for 10 min prior to shut-down of the pump, and then the pressure vessels supplied the system with pressurized feed seawater for an addition 20 min. Liu *et al.* [51] applied a feedback control to adjust the feed pressure and flowrate in a wind-powered membrane system for brackish water desalination (3000 mg/L total dissolved solids, TDS). The control was based on pre-set pressure to discharge the water in a hydraulic accumulator (300 L) by using data acquisition and a series of solenoid valves. This allowed the system to be operated under low wind speeds of approximately 4 m/s with an average salt retention of 97%, resulting in a permeate salt concentration of 90 mg/L and a system efficiency of 35%. Furthermore, in a hybrid PV and wind-membrane system, a control method based on hourly predictions of water demand and weather variables was proposed to schedule the use of either batteries or a diesel generator [53, 54]. Soric *et al.* designed a regulator that used a buffering SC (250 F) to smooth the voltage output of the PV panels to the pump. The control was based on voltage measurements and relays to activate or deactivate the cut-off of the PV or pump power [60]. It indicated a permeate flux of 70 L/m²h (RO membrane: DuPont SW30-2540) at retention > 95% with water production of 1 m³/d within the feed concentration in the range of 8 to 22 g/L. However, the performance was not studied under high temporal resolution [60]. In a PV power system with fuel cells, batteries, and SCs, to maximize the SOC of the SCs and minimize the consumption of hydrogen, an energy management system that combined fuzzy logic, frequency decoupling, and state machine control strategies in terms of preset values was proposed [61]. The simulated results showed a 5.4% increase in SOC and a 19.6% reduction in hydrogen consumption [61].

It was observed that the SCs were used in parallel with batteries to extend battery lifetime by buffering the peak current pulses and reducing the charge/discharge cycles in the battery. Glavin *et al.* [62] developed a hybrid SC-battery energy storage system for a PV system, in which the SCs provided the high peak power, while the battery supplied the low power, based on operating conditions. The results indicated that the SCs increased the battery SOC by 12% under peak load, consequently reducing the size of the battery and avoiding deep discharge of the batteries. Bludszuweit *et al.* [63] implemented the batteries and SCs to smooth fluctuations on a large-scale grid-connected wind turbine system. The SCs buffered the transient energy for 1 – 10 s to prevent the current peaks to reach the LA batteries, which smoothed the power output for 10 min. These applications highlight the feasibility of coupling SCs in combination with batteries to the RE systems to improve the performance and reduce the size of the batteries. For an on-grid system equipped with a Li-ion battery (capacity of 0.55 kWh), a bidirectional converter by using a current control scheme that is based on the SOC of the batteries for load levelling and peak shaving was developed to transfer power in both directions [64]. The simulated results demonstrated that the batteries absorbed 35 W power from the grid, while 200 W of power was injected into the grid within 25 ms (corresponding to the energy capacity of 10^{-3} Wh). The energy transfer of the bidirectional AC/DC converter was confirmed.

1.5. Thesis objectives and research questions

A systematic approach was conducted to study the characteristics and energy buffering control of the PV-membrane system, and thus the following research questions were developed to evaluate system performance, reduce system shut-downs, and enhance system resilience to periodic fluctuations and intermittency of SI under real weather conditions.

i) What kind of combinations of the PV-membrane system components lead to the greatest efficiency, widest operating range, and exhibit the highest robustness and reliability? This study was useful for identifying the optimal combination of components, system operation, and possible reliability improvements, allowing both the weakest links to be avoided and optimization of future systems (Chapter 2). The review presented in this chapter has contributed to a publication: **Li, S.**, Cai, Y.H., Schäfer, A.I. and Richards, B.S., *Renewable energy powered membrane technology: A review of the reliability of photovoltaic-powered membrane system components for brackish water desalination. Applied Energy, 2019, 253,113524.*

ii) What are the impacts of ramp rates of PV voltage on the PV-membrane system over a range of variations? This was needed to elucidate the dynamic characteristics of the system and determine the energy buffering control to enhance system resilience to periodic fluctuations of SI (Chapter 4). The experimental results presented in this chapter have contributed to a publication: **Li, S.**, Voigt, A. Schäfer, A.I. and Richards, B.S., *Renewable energy powered membrane technology: Energy buffering control system for improved resilience to periodic fluctuations of solar irradiance. Renewable Energy, 2020, 149, 877-889.*

iii) How can the supercapacitors (SCs) and charge controller reduce system shut-down events and enhance system resilience on varied full-length solar days under different feed salinity and PV power capacity, in particular reducing the number of system shut-down events (number of shut-downs and duration) and SEC? This information was used to establish the effect of energy buffering, system control, and varying solar days on brackish water filtration performance (Chapter 5). The experimental results presented in this chapter have contributed to a publication: **Li, S.**, Voigt, A., Cai, Y.H., Schäfer, A.I. and Richards, B.S., *Renewable energy powered membrane technology: Energy buffering control to reduce the shut-down events and enhance system resilience under different solar days. Renewable Energy, (submitted).*

iv) What is the most energy-efficient option for ultrafiltration backwashing – bladder tank or SCs powered pump? By understanding the impacts of backwashing parameters (transmembrane pressure, interval, and frequency) on reducing UF membrane fouling and SEC, two backwashing configurations were determined (Chapter 6). The experimental results presented in this chapter have contributed to a publication: **Li, S.**, Milia, M., Schäfer, A.I. and Richards, B.S., *Renewable energy powered membrane technology: Energy consumption analysis of different ultrafiltration backwashing configurations for brackish water desalination. Separation and Purification Technology, 2022, 287, 120388.*

v) What are the impacts of different energy storage options on the PV-membrane system when compared with Li-ion batteries and SCs? This was used to understand the potential of incorporating Li-ion batteries and SCs for energy storage on the PV-membrane system during different solar days from less cloudy to cloudier (Chapter 7). The experimental results presented in this chapter have contributed to a publication: **Li, S.**, Carvalho, A., Schäfer, A.I. and Richards, B.S., *Renewable energy powered membrane technology: Electrical energy storage options for a photovoltaic-powered brackish water desalination system. MDPI: Applied Sciences, 2021, 11, 856.*

The availability of RO membrane modules for brackish water allowed the system to be operated over a wide pressure range. The synergies of PV and membrane technology further improve the feasibility of PV-membrane system applications, in particular in off-grid and remote areas. A comprehensive review of the efficiency, operating range, and reliability of the PV-membrane system components for brackish water desalination is presented in Chapter 2, the aim of which is to ensure reliable and robust design over the lifetime of the system.

The main challenge for the directly-coupled PV-membrane system is the fluctuations and intermitten-
cies of SI. SCs are capable of providing energy buffering in several minutes and reduce the system shut-down events. The motivation for using them is provided in Section 1.4. To optimize energy management within the system, a charge controller was developed to manage the energy distribution between the SCs and PV. The working principles are described in Section 3.5, while the experimental results of using energy buffering control to deal with varied ramp rates in PV voltage and enhance system resilience by reducing shut-downs under real solar days are provided in Chapters 4 and 5, respectively. By reducing UF membrane fouling, and extending system robustness and reliability, backwashing control was established within the PV-membrane system (detailed in Section 3.6). Two different backwashing configurations (bladder tank

and BW pump powered by SCs) were implemented to compare energy consumption. The experimental results are provided in Chapter 6. In the final chapter, the impacts of incorporating Li-ion batteries in the PV-membrane system were investigated under different solar days and compared with the SCs energy buffering. The effects of varied levels of fluctuations (from very cloudy, less cloudy, to sunny) and energy storage capacities were studied. The experimental results are provided in Chapter 7.

The following chapters will describe the performance of the PV-membrane system with and without system control when it is subjected to both fluctuations and intermittency from SI. It is worth mentioning that the steady-state performance of the PV-membrane system is described in detail to provide a baseline for further comparisons under fluctuating conditions (Section 4.1).

2. System components and design considerations

Several of the results in this chapter have been published as a review paper in Applied Energy 253, 113524 (2019) [65]. The co-author Yang-Hui Cai helped with the summary of the membrane section. The co-authors Andrea I. Schäfer and Bryce S. Richards were involved with the review and edit of the original manuscript.

While small-scale PV-membrane systems have received significant attention in recent years and a considerable number of demonstration systems have been established [8], the total number of systems deployed globally remains relatively low [8], and there are many different system design configurations. This makes it difficult to obtain reliable data regarding long-term performance, as well as information concerning the efficiency, robustness, and reliability of such systems. Many PV-membrane systems are being targeted for deployment in remote areas of developing countries, where the technical skills required for O&M are initially not present, and a supply chain for spare parts is not established [8, 66]. Therefore, the robustness and reliability of PV-membrane systems are paramount in order to ensure that long-term operation is achieved, and that poor system design does not diminish the ability of a relatively “high-tech” water treatment solution in a developing country. In addition, when engineering such systems, one needs to consider maximizing the efficiency of all components, and achieving water production over the widest possible power range, to realize the lowest cost of water. This chapter provides an extensive assessment of what kind of combinations of the PV-membrane system components lead to operation with the highest efficiency, over the broadest possible power input range, and with the highest reliability. Recommendations are given at the end of each subsection.

2.1. Photovoltaic modules

The efficiency of a PV cell is one of the key parameters for determining the performance of a PV system, and this is influenced by temperature [67], SI , tilt angle of the PV module [68], dust [69], humidity [70-72], and convective cooling via wind [31]. The range of semiconductors used to fabricate PV devices exhibits different performance responses to increased operating temperatures. Typical efficiencies of commercially available PV modules produced currently are given in Table 2-1. It is worth noting that these are determined under standard test conditions (STC) of 1000 W/m² of air-mass 1.5 global (AM1.5G) irradiation at a temperature of 25°C. In addition, the temperature coefficient (TCE) values are listed, indicating the relative reduction in efficiency per increase in degree Celsius of the operating temperature of the PV module. The TCE values have also been confirmed by several independent outdoor evaluations [73]. Wafer-

based silicon technologies comprise 94% of the world’s PV module shipments [6]. Of these, standard screen-printed devices based on either crystalline silicon (c-Si) or multi-crystalline silicon (mc-Si) wafers show the largest negative TCE, while the situation improves somewhat for high-efficiency c-Si and amorphous silicon (a-Si)/c-Si heterojunction technologies [73]. Among the thin-film PV technologies, copper indium gallium selenide (CIGS) has a similar TCE to c-Si; however, a-Si and cadmium telluride (CdTe) both exhibit the best (least negative) TCE values [73]. This is critical since, although the performance of PV modules is rated under STC, in reality, the nominal operating cell temperature is more typically 45–50°C [73]. Therefore, a PV module with a less negative TCE can have a higher output power and energy yield under realistic operating conditions, with this difference being exacerbated in warmer climates [73].

Table 2-1: Energy conversion efficiency (η) of various PV module technologies measured at STC along with the temperature coefficient (TCE) of power loss [6, 73]. Note that 1J, 2J, and 3J refer to single, double, and triple junction stacks, respectively.

PV technology	Wafer-based silicon PV technologies			Thin-film PV technologies		
	Screen-printed c-Si or mc-Si	c-Si/a-Si heterojunction	High-efficiency c-Si	a-Si (1J, 2J, 3J)	CIGS	CdTe
η (%)	15.8 – 17.8	18.5 – 21.4	19 – 21.3	7 – 10	~13.8	~16
TCE (%/°C)	-(0.45 – 0.50)	-0.30	-0.36	-(0.2 – 0.25)	-(0.35 – 0.45)	-0.25

2.1.1. PV module degradation and failure modes

PV modules possess no moving parts, which are considered to be the major source of reliability issues in other electrical generating systems. Alternatively, the operating lifetime is mainly dominated by the stability and corrosion resistance of the fabricating materials. For wafer-based silicon PV modules, 30 years of warranty have been provided by the manufacturer, while CdTe and CIGS are being covered by 25 years [68, 74]. Extensive factory testing of PV modules ensures their robustness to endure temperatures from -40 – +85°C, relative humidity up to 85%, and that they can withstand 25 mm diameter hailstones impinging at 23 m/s [75]. Despite these advantages, several failure modes and degradation mechanisms are still encountered that may reduce power output or cause failures of modules. Five main modes of degradation that result in performance loss and failure are proposed based on field-aged modules [76]: i) degradation of the polymeric encapsulation; ii) adhesion loss within the PV module laminate; iii) degradation caused by moisture intrusion; iv) degradation of cell/module interconnects; and v) degradation of the semiconductor. An extensive review of nearly 2000 degradation rates measured on individual PV modules during field testing over the last 40 years has been published [77], as plotted in Figure 2-1. For some thin film PV technologies, notably CdTe, significant advancements have been made to decrease degradation rates when comparing installations from “pre” and “post” year 2000. CIGS, which is susceptible to water vapor, has also made

substantial progress to achieve more stable devices. The average degradation rates of c-Si and thin-film PV technologies were reported to be 0.7 and 1.5%/year, respectively [77]. Nevertheless, CdTe is proper for on-grid systems, as it cannot properly operate for a longer time in an open-circuit. Degradations on an array of eight CdTe modules operated outdoors in open-circuit conditions were observed [78]. Specifically, it was found that power, V_{oc} and fill factor (FF) degraded 12%, 6% and 7% respectively after exposure at $SI = 650 \text{ kWh/m}^2$ (under STC) over seven months. The degradations occurred because of the decreased doping concentration close to the junction and increased series resistance in the transparent conducting oxide (TCO). As a result, the current flow was interrupted due to damage of the TCO layer [79]. In contrast, no degradations were found on similar arrays of grid-connected CdTe PV modules operated at maximum power point (MPP) over the same period of time.

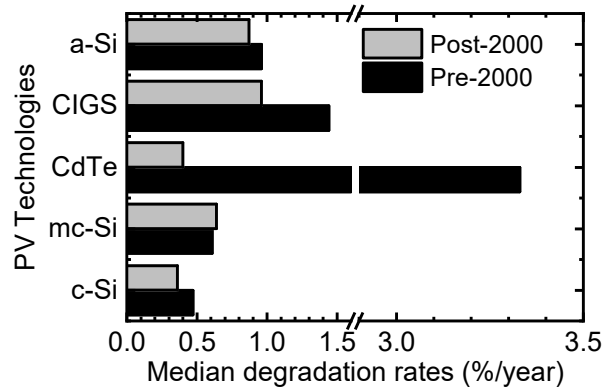


Figure 2-1: Summary of the median degradation rates of different PV technologies. “Pre” and “Post” refer to installations prior to and since the year 2000, respectively. Adapted from [65], CC BY-NC-ND 4.0 License.

2.1.2. Recommendations

The following recommendations for selecting PV panels in RE-membrane systems are given:

- Silicon-based PV panels (either mc-Si or c-Si) are preferable, due to overall technical maturity, readily availability, the lowest risk option and supported by 25-year warranties;
- With regard to other PV technologies: a-Si is not appropriate due to low efficiency, CIGS (if available) is better used in hot climate areas, and CdTe is typically employed only in on-grid systems;

2.2. Power conditioning device

An electric motor to power a pump is the key load in any RE-membrane system. Electric motors operate most effectively within a certain voltage and current range. Naturally, however, the power output of a PV panel varies throughout the day with the availability of sunshine (solar irradiance, SI). Therefore, to optimize power coupling between the PV panels and the pump motor, it is strongly recommended to use

power conditioning devices that serve to deliver the desired voltage to an electrical load. Energy conversion always comes at an energetic cost and power losses will be incurred, although this is typically 5% or less [80]. Perhaps more significant is that the increased number of additional components in the system will cause additional failure modes. As a result, it is critical to determine that the losses incurred are compensated for by having an overall net benefit to both the performance and reliability of the RE-membrane system. Power conditioning can take several different forms, including DC-to-DC converters, maximum power point tracking (MPPT), inverters that enable alternating current (AC) loads to be supplied, and drive controllers for motors. Each of these is discussed in detail below.

2.2.1. DC-DC converter

A single c-Si solar cell exhibits a maximum voltage of approximately 0.6 V, which is too low to power any load. Therefore, typically dozens of cells are connected in series to build voltage. For example, a c-Si PV module will be most efficient when operating at its maximum power point (MPP), in which it commonly ranges from $V_{mp} \sim 18 V_{DC}$ (often used for charging 12 V_{DC} batteries) up to $V_{mp} \sim 60 V_{DC}$ (larger modules). A DC-DC converter is frequently required to match the output of the PV panel to the required voltage for the pump motor, normally in the range $V_{pump} = 30 - 300$ V. A DC-DC converter can either achieve an up or down in the output voltage via “boost” or “buck” operation, respectively. Both of these circuits necessitate the combination of a switch and an inductor, along with capacitors to smooth and reduce the ripple of the output [81]. The power conversion efficiency of a DC-DC converter is in the range of 75 – 98%, with a typical conversion efficiency being 85% at full load [82-84]. According to one manufacturer, DC-DC converters are typically designed and built for an expected lifetime of 20 – 30 y in harsh environments [85], matching that of the PV module. Failures with DC-DC converters mainly result from: i) electrical overstress causing the failure of key components, such as the metal-oxide-semiconductor field-effect transistors (MOSFETs) that are utilized for power conversion; ii) resistor failures caused by sulfur corrosion of silver electrodes due to environmental stress at high temperature and humidity; and iii) poor wetting of the solder to the printed circuit board (PCB). Several measures can be carried out to prevent or decrease the failure rates, e.g., high quality components, professional assembly processes (achieving good soldering process control), good environmental controls [86, 87], and electronics mounted within dust- and water-proof housing (e.g., IP65).

2.2.2. Maximum power point tracking

The power delivered by a PV system relies on irradiance and temperature, while the current being drawn from the cells affects the operating voltage. An MPPT must be included in order to ensure the operation of the PV module at its most efficient point, thus extracting the highest power from the system [88]. The efficiency of an MPPT itself can reach as high as 99% [89, 90], but more typically, the power consumption of MPPT lies in the range of 4 – 7% of the PV array output [80]. Power conditioning systems can improve performance in a well-matched PV system by 10 – 15% [91], thus justifying their inclusion in a

system. For instance, a typical MPPT (nominal voltage output: $48 V_{DC}$) efficiency curve over a wide range of power outputs and at different PV panel voltages is shown in Figure 2-2. It can be observed that, firstly, higher efficiencies are achieved when the output voltage of the PV panel at the maximum power point, V_{mpp} , is closer to the desired $48V_{DC}$ output from the MPPT, because the controller needs to keep the module operating at V_{mp} in order to ensure the rated output power of the PV module. Secondly, it can be seen that high efficiency is achieved from approximately 10 – 100% of the rated power of the MPPT, and only at very low power operation does efficiency decrease significantly. Since an MPPT is primarily based on a DC-DC converter, it is assumed to have the same lifetime as the DC-DC converter discussed in the previous section.

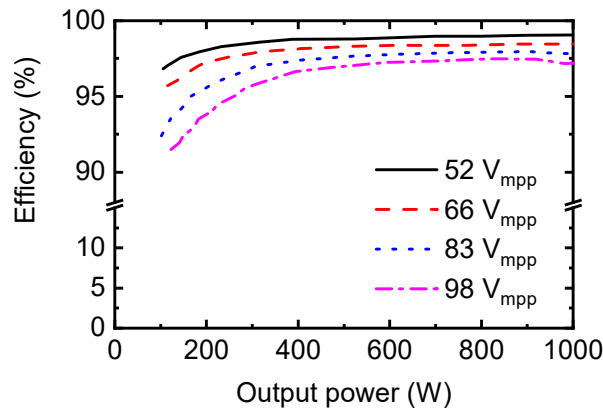


Figure 2-2: MPPTs can exhibit high-efficiency operation over a very wide range of output power. Higher efficiency operation is achieved when the PV array output voltage V_{mpp} is closest to the output voltage of the MPPT, in this case, $48 V_{dc}$ (data obtained from [92]).

2.2.3. Drive controller

A drive controller is required to fulfil the particular current requirements of the pump motor, especially for positive displacement pumps. The motors coupled with such pumps need a high start-up current – approximately 6-10 times higher than the normal operating current of the motor for seconds [62] – followed by a constant current to provide a given torque that is proportional to the pumping pressure [93]. The drive controller can conduct this conversion with approximately 95% efficiency, while the transistors in the controller are used for commutation of the brushless DC motor to avoid further efficiency losses. Additional features can be established to improve reliability, such as robust sensorless control for safety-critical applications, ruggedized packaging suitable for high vibration employment, small footprint suitable for cold-wall or heat-sink mounting, and highly qualified PCB screening [94]. The elimination of Hall (current) sensors and feedback units that are typically inside of the motor housing has greatly augmented the reliability of the controller, which in turn reduces motor size and cost [94].

2.2.4. DC-AC inverters

An inverter is necessary to convert the DC output from a PV module to AC, for example, if an AC motor is present in the PV-membrane system. The main functions of an inverter include: i) inverting the DC voltage of a PV array output into AC output; ii) wave shaping the AC voltage output; and iii) regulating the effective value of the voltage output. Often, MPPT circuitry is integrated within the inverter. Manufacturers report that today's inverters are developed with a peak efficiency higher than 94% and have an mean time between failure (MTBF) of greater than 10 y.

However, several reliability problems have arisen with inverters. Firstly, inverter failures occurred due to electro-mechanical wear on capacitors. It is worth noting that the capacitors are commonly used to smooth the power output at varying levels of current; however, electrolytic capacitors have a limited lifetime and age faster than dry components. Secondly, over-current and over-voltage can damage the inverter bridge, attributable to excess heat generated by current or voltage spikes. Finally, the mechanical stress resultant from ultrasonic vibrations, which arise from the cores of inductive components, can cause friction that further adds to excess heat and consequent damage to components in the inverter. To keep the inverters reliable, consistent maintenance schedules and occasional replacement of capacitors are needed to prevent most failures caused by wear and tear. The failure rates of inverters investigated as part of RE pumping systems will be discussed in Section 2.7.

2.2.5. Recommendations

Power conditioning devices play a critical role in optimizing power coupling between the PV panels and pump motor, and thus the following recommendations are given:

- i) Include a DC-DC converter to match the required voltage output for the pump motor with a design lifetime of 20 y;
- ii) Include MPPT to assure that the PV modules operate at MPP, thus extracting the highest power from the systems of the day;
- iii) Include a drive controller to provide the necessary current to the pump motor, especially when positive displacement pumps are present, with a reported lifetime of 15 y;
- iv) Exclude a DC-AC inverter, as it increases the additional risk of failure, especially considering the good availability and high performance of DC-powered pumps.

2.3. Short-term energy storage

PV resources are inherently both fluctuating and intermittent. The amount of power generated by PV panels can fluctuate as a consequence of passing clouds, while there are periods of intermittency – for example, at night – where the power output is zero. The power variations generated by the PV sources have been regarded as detrimental to membrane systems that were expected to operate under circumstances of

constant flow and pressure [45, 95]. A lack of power can produce reduced permeate quality and daily permeate production, and thus the water demand cannot be met. Moreover, the constant on/off cycles lead to performance deterioration of the system, increasing the potential wear and tear on the pump and motor [96]. Consequently, it is typical to rely on an energy storage device – most commonly lead-acid batteries – to balance demands from the electrical load with the power available from the PV system. To reduce the cost and maintenance requirements associated with batteries, several RE-membrane systems store the permeate water in the tank to overcome the challenge of longer-term fluctuations and intermittency [42, 97]. Although it is easier and less expensive to store water than electricity, major issues remain, including reduced water quality and frequent system shut-downs [98], and potential damage to the pump motor and RO membrane (e.g., delamination) [42, 99, 100], which are caused by the short-term variability of the RE resource.

Different energy storage technologies, such as chemical or electrochemical, mechanical, electromagnetic, or thermal stages, can be used in small-scale PV-membrane systems [101]. However, some essential criteria, including efficiency, charging/discharging cycles, self-discharging rate, cost, and lifetime, must be considered to allow efficient and reliable system operation, particularly during periods of fluctuation and intermittence [101, 102]. It is worth noting that the number of cycles represents how many times the energy storage technology can undergo the process of complete charging and discharging. Although other novel battery technologies, such as nickel-cadmium (Ni-Cd) batteries, metal-air batteries, and advanced sodium-sulphur (Na-S) batteries, are being developed, their performances prevent applications in RE systems. For example, Ni-Cd batteries show the drawbacks of memory effect, the negative environmental impact of cadmium, and high initial cost [101]. Metal-air batteries present low efficiencies (<65%) and a limited number of charge/discharge cycles (approximately 300 to last 10 y) [103, 104]. Na-S batteries require a high operating temperature (350°C), thus making sulphur batteries difficult to use for residential applications [105]. The following sub-sections will emphasize the relative merits of the most promising technologies to enable an appropriate choice to be made for small-scale RE systems.

2.3.1. Lead-acid batteries

In off-grid RE-membrane systems, lead-acid (LA) batteries are the most commonly used storage technology due to low cost, relatively low level of maintenance, and readily availability [62, 106]. The self-discharge rates for LA batteries are low, i.e., approximately 0.1 – 0.3% per day, and this low leakage loss makes them suitable for longer-term storage applications [107]. However, the main disadvantages are the limited number of charging/discharging cycles, as well as the reduced lifetime attributable to deep discharging or operation at high temperature (with the upper limit of 45 °C) [5, 62, 108, 109]. When LA batteries are employed in a PV system to supply a daily load, incomplete battery charge/discharge can result in battery degradation, such as electrolyte stratification, gas bubble entrapment, excessive sulfation, and degradation of the positive electrode. As a result, battery life is shortened [110, 111]. As a consequence, it is paramount to keep an average state-of-charge (SOC) higher than 50% to achieve expected battery performance and lifetime in small-scale PV systems [62]. Normally, LA batteries achieve a lifetime of 3 – 5 y in

RE systems [62], although it is sometimes as low as 2 y under extreme conditions [112, 113]. For a small-scale PV-membrane system equipped with a 300-500 W motor, 1 kWh of battery storage could allow an additional 2-3 h of full operation.

2.3.2. Lithium-ion batteries

Lithium-ion (Li-ion) batteries present the highest energy density (90 – 200 Wh/kg) and highest power density (500 – 2000 W/kg) among all battery technologies. These parameters are the key drivers for their implementation in transportation applications. Compared to LA batteries, Li-ion batteries exhibit high efficiency (> 90%), long charging/discharging cycles (4000 cycles), 10 y lifetime [114], and are relatively maintenance-free [115]. Furthermore, with the reduced cost per kWh, they are considered to be promising energy storage units for RE systems, and are widely expected to emerge as a highly competitive technology for medium- and long-term PV applications [116].

2.3.3. Supercapacitors

Supercapacitors (SCs) store energy through building-up positive and negative charges within an electrolytic solution, and have been used for short-term energy buffering in RE systems [102, 117]. SCs exhibit a lifetime of 8 – 10 y [118, 119], efficiency of 84 – 98%, and their greatest advantage over batteries is high charging/discharging cycles (> 500,000 times) [120]. In addition, SCs can be charged substantially faster than conventional batteries, which makes them superior candidates for applications that need to be charged/discharged in 1 – 2 min [121]. The main disadvantages of SCs are, firstly, the high self-discharging rate (1.5% per day) [122]. This is significantly higher than that encountered with either LA or Li-ion batteries, which achieve 5% per month and 1-2% per month, respectively [123]. Secondly, the amount of stored energy in SCs is much more limited than that in batteries, normally only providing energy buffering for minutes [35]. The degradation in SCs is also accelerated at high thermal cycles between 40 °C and 60 °C due to the increase of internal reaction, which leads to an increase of the degradation rate and a decrease of capacitance [124]. They are also estimated to be five times more expensive than LA batteries with similar capacity [125]. Notably, SCs could be a potentially cost-effective solution if the benefits of energy buffering, i.e., minutes as opposed to hours of storage, are significant.

2.3.4. Recommendations

From the above discussions, the following suggestions for energy storage components for PV-membrane systems are given:

- Energy storage can improve system performance by reducing the number of system shut-down events – offering energy buffering between the RE source and power requirements – as well as allowing autonomous system operation;

-
- Li-ion batteries are appropriate to offer energy storage for long-term fluctuations – a lifetime up to 15 years, more charging cycles, low self-discharge, and minimal maintenance – while their price is decreasing steadily, such that they should be further employed in PV-membrane systems;
 - SCs are good candidates for buffering short-term fluctuations due to high efficiency, 8 – 10 years lifetime, and a large number of charge/discharge cycles.

2.4. Motor-pump subsystem

2.4.1. Pump motors

Three types of motors are commonly used for RE-powered water pumping applications: i) brushed permanent magnet (PM) DC motors; ii) brushless permanent magnet DC motors, and iii) AC motors. Normally, the selection of a motor for an RE-powered system depends on the size and availability of electronics that go with it. DC motors are attractive and efficient for low power demand (< 5 kW) [91]. In terms of simplicity, DC motors have proven to be an excellent match for simple RE-powered water pumping applications, because the PV modules produce DC electricity that can be directly utilized by the motor (with or without power conditioning devices). For higher power demand applications (>10 kW), AC motors may be used in conjunction with an inverter, with the range of AC motors available being much greater and the prices being generally 20% lower than DC motors with a similar power rating [91]. The use of inverters for controlling AC motor speeds results in high efficiency over broad speed and load ranges, but presents the associated disadvantage of increased failure risks via the inclusion of an additional system component.

PM DC motors are generally of the type used for RE applications. The brushed commutator leads to rotation of the PM brushed motor without inducing the surrounding magnetic field electrically. No power is consumed in the field windings, which leads to efficiency in the range of 64 – 80% [126]. For a submersible DC water pump, it is necessary to remove the pump from deep wells when the brushes are maintained or replaced periodically (every 2000 – 4000 h or 2 y), which leads to an increase of both system downtime and O&M costs [127-129]. Typically, brushed DC motors have an expected lifetime of 4 to 8 y, while the exact requirements for maintenance depend on the type of coupling (direct, drive, gear) [128]. Concerning the brushless DC motor, the PM is the central rotor, and the field windings are electronically switched via a rotor position sensor. They are commonly used for small-scale RE applications, as they are highly efficient (up to 90%), require very little maintenance apart from preventing ingress of water and dust, and provide a service lifetime of 10 – 20 y [128, 129]. The typical operating power range, efficiency, as well as advantages and disadvantages of different motor technologies, are summarized in Table 2-2.

Table 2-2: Comparison of motors suitable for powering pumps in RE systems. Adapted from [65], CC BY-NC-ND 4.0 License.

Pump motors	Power	Efficiency	Advantages	Disadvantages
AC induction motor	>10 kW	90 – 95%	Larger range available Diversity of control strategies Maintenance-free ~20% cheaper than DC motor 15 – 20 y lifetime	Needs an inverter, incurring the increased risk of failure (~10 y MTBF)
DC brushed PM motor	<5 kW	64 – 80%	Simple for small loads No complex control circuits needed	Maintain and replace brushes every 2000- 4000 h or 2 y Shorter service time 4-8 y
DC brushless PM motor	<5 kW	80 – 90%	10 – 20 y lifetime Little maintenance	Extra electronic circuit for the rotor position sensor results in twice the price of the motor

2.4.2. Pump

The pump is one of the key components of the PV-membrane system, as it creates the required feed flowrate and pressure for the membranes to function, and also defines the power requirements from the PV panels. For NF/RO membrane brackish water desalination systems on the scale of 1.0 – 1.5 kW, the typical operating pressure and flowrate required for the pump range from 3 to 14 bar at up to 600 – 4800 L/h (assuming that 25% of the feedwater is recovered as permeate) [130-132], while ideally being powered by a DC motor. It is worth mentioning that while the discussion here focuses on high-pressure pumps for driving the membrane filtration system, it is also suitable for scenarios in which feed water is pumped from a borehole to the surface. The main difference is that the pump within the membrane system requires a higher pressure at a lower flowrate than for pumping application. Considering different pump applications suitability for different kinds of liquids is normally specified in pump catalogues, and especially the particles of inorganic and organic solid matter can be suspended in liquids either as contaminants or for transportation [133]. To avoid liquid-solid mixtures that can damage the pump, the use of MF/UF membranes is preferable.

In general, pumps are categorized into dynamic pumps and positive displacement pumps. These two types of pumps have inherently dissimilar characteristics and are suited to different operating conditions.

The diagrams of each pump are provided in Figure 2-3. To distinguish it from motor efficiency, pump efficiency, η_{pump} , is defined in Eq. 2-1:

$$\eta_{pump} = \frac{P_{hydraulic}}{P_{shaft}}, \quad \text{Eq. 2-1}$$

where $P_{hydraulic}$ is the hydraulic power possessed by the fluid; and P_{shaft} is the mechanical shaft power provided by the pump motor to the pump.

i) Dynamic pump

A dynamic pump depends on fluid velocity and the resulting momentum to produce pumping power and move fluid through the system and create the required pressure. The main type of pump in this category is the centrifugal pump, which has long been the most commonly used pump worldwide due to its robustness, simplicity, and cost-effective design [129]. The operating principle is that water is sucked by the centrifugal force generated by the impeller, and then the water is pumped towards the outlet when the impeller rotates at high speed. A single-stage pump refers to a single impeller (Figure 2-3A). However, most borehole pumps are multi-stage - where the discharge from one impeller feeds into the next inlet - with each one adding a further pressure difference (Figure 2-3B). Centrifugal pumps exhibit an optimum efficiency at a certain design head and design rotation speed, with the efficiency decreasing as the pump head and flowrate deviate from this design point. They indicate a relatively high hydraulic efficiency (30 – 60%), with larger capacity pumps reaching higher efficiencies. However, efficiency decreases rapidly when the operating pressure departs from the design specifications, which leads to a limited operating range. Centrifugal pumps are most economically used with large flowrates (25-100 m³/d) and low-to-medium pressure (1 – 3 bar) requirements compared with positive displacement pumps [91]. Therefore, centrifugal pumps have largely been replaced by positive displacement pumps to achieve efficient pumping in small-scale RE-membrane and water pumping systems [134].

2. System components and design considerations

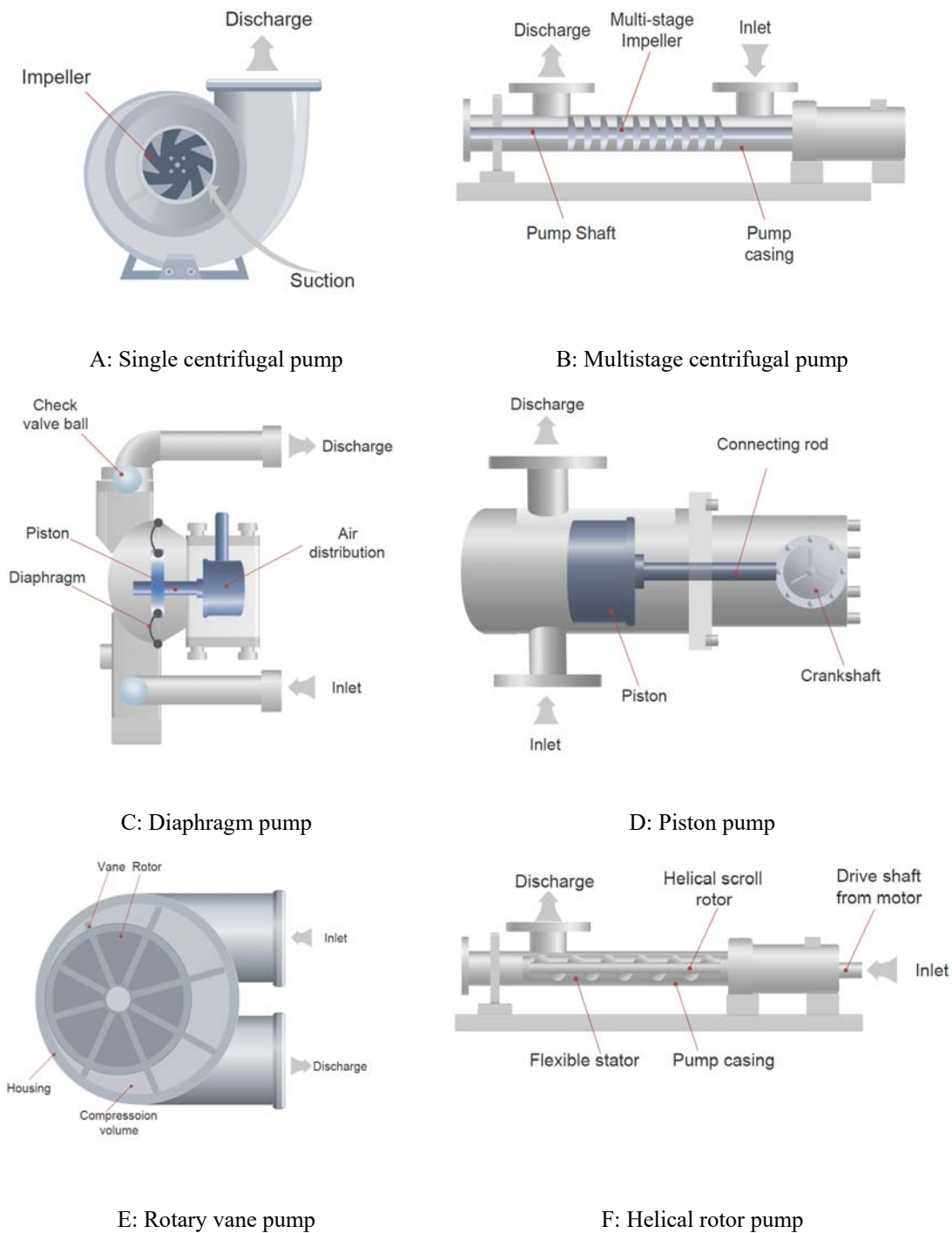


Figure 2-3: Diagrams of the most common pumps used in water treatment systems, showing the passage of water from the inlet to discharge sides of the pump and the main components.

ii) Positive displacement pump

The positive displacement pump operates with a force of a fixed amount of water from the inlet to the discharge side of the pump within each revolution or stroke [129]. Due to the fixed volume of water displaced during each pump stroke, the flowrate is directly proportional to the speed of oscillation or rotation, and is independent of pressure fluctuations on either the suction or discharge side of the pump. Positive displacement pumps are capable of providing higher operating pressures at the expense of lower flowrates when compared to centrifugal pumps of the same power rating. In addition, they can operate with higher efficiency over wider speed and pressure ranges, which is particularly useful for coupling with RE sources that generate various power supplies. Positive displacement pumps can be divided into two categories in terms of their operation: i) reciprocating pumps; and ii) rotary pumps. Reciprocating pumps use a crankshaft to transfer the rotational drive power to a plunger, piston, or diaphragm oscillating within a cylinder; whereas, rotary pumps use rotating screws, lobes, gears, or rollers that are directly connected to the drive shaft from the motor. In particular, helical rotor pumps (Figure 2-3F) have been widely employed in PV-powered water pumping applications over the last few decades [135]. An eccentric single-helix-shaped metal rod as a rotor sealed within a thick rubber stator is utilized in these pumps, in which the small gap between these forms a progressive cavity, and thus causes the water to be expelled. The pressure created by the pump is in proportion to the length of the rotor and stator.

iii) Pump performance comparison

Protogeropoulos and Pearce conducted a detailed investigation that compared the performance of several different types of pumps designed for PV-powered water pumping systems [134]. The present review extends this original work to highlight the efficiency improvement of positive displacement pumps and broadens the analysis to include a larger range of pumps, i.e., piston, diaphragm, helical rotor, and rotary vane pumps, and single- and multi-stage centrifugal pumps. The pumps reviewed here represent a power rating of lower than 1.5 kW, and were tested over their full range of operation in terms of pressure and flowrate given by manufacturers. Figure 2-4 illustrates the key results of water flowrate, efficiency, and pumping SEC as a function of the head for the eight different pumps. It is worth noting that the pumping SEC in this case represents how much energy would be consumed by pumping (not treating) 1m³ of water as a function of absolute head.

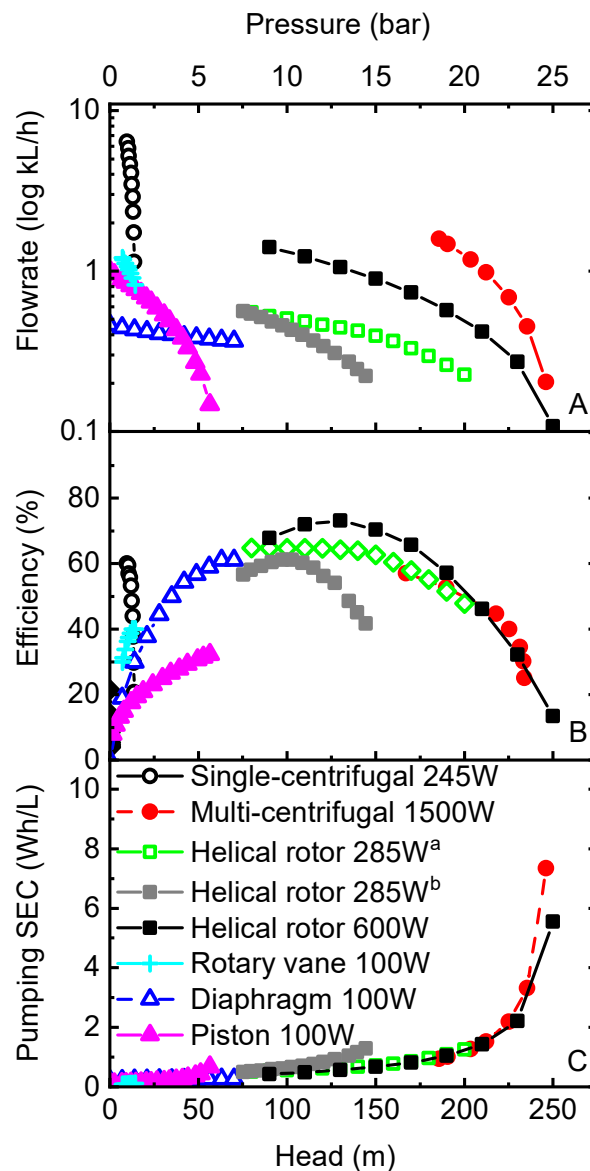


Figure 2-4: Flowrate, efficiency, and pumping SEC as a function of the head (pressure) for a range of powered pumps. The pumps were arranged in the sequence of dynamic (single-centrifugal 245 W, multi-centrifugal 1500 W), rotary (helical rotor 285 W^a, helical rotor 285 W^b, helical rotor 600 W, and rotary vane 100 W), and reciprocating pumps (diaphragm 100 W, piston 100 W). The numbers in the legends represent the motor power. It should be noted that the multistage centrifugal pump has an AC motor, while all of the rest are DC powered pumps. Adapted from [65]. CC BY-NC-ND 4.0 License.

The specified pumps above show the general pump performance, as they represent a range of different pump manufacturers and pump types. As shown in Figure 2-4, the single-stage centrifugal pump has a larger capacity but a very low operating pressure, which results in a low pumping SEC (Figure 2-4C). The multi-stage centrifugal pump, however, achieves a much higher pressure (18 – 25 bar) via applying stacked impellers once coupled to a higher power motor (1.5 kW). It is then capable of achieving a maximum efficiency of 56% (Figure 2-4B), but this efficiency deviates quickly (25-56%) when moving away from the

design pressure, and the pumping SEC reaches 7.5 Wh/L at a maximum pressure of 25 bar (Figure 2-4C). Comparatively, the positive displacement pumps present higher operating pressure, but lower flowrates (Figure 2-4). It can be seen from Figure 2-4 that the reciprocating pumps (diaphragm and piston pumps) show a lower efficiency and pressure range than the rotary pumps (helical rotor and rotary vane pumps). From Figure 2-4C, it can be seen that the SEC of the reciprocating pump is relatively low (<1 Wh/L), because it was calculated by the ratio of power rating to flowrate, which is caused by the low operating pressure (up to 7 bar) and power rating (100 W). The 600 W helical rotor pump was the most efficient pump out of these pumps in this study ($\eta_{\text{pump}} = 75\%$). It can be operated over a head of 100 – 150 m (10 – 15 bar) with a minimum pumping SEC of 0.5 Wh/L, while it increased up to 5.5 Wh/L at a pressure of 25 bar. The SEC increased rapidly at a pressure higher than 20 bar, as very little water was pumped with the motor power. Although the 600 W pump is the most efficient pump among the others, the PV-membrane systems reported in the literature have normally applied 4 – 12 bar [9, 98, 136, 137] to treat brackish water with TDS in the range of 1000 – 10,000 mg/L. Therefore, the smaller helical rotor pump (285 W) appears to be the optimal choice, with a reasonable SEC (1.5 Wh/L) at high pressure (20 bar), as well as a wide operating power range. For a small-scale PV-membrane system, the pumping SEC contributes to 70-80% (assuming 20-30% recovery) of the total SEC.

iv) Pump reliability

In addition to pump performance, reliability is an important criterion to select the proper pump. Lifetime testing of the diaphragm and helical rotor pumps has been conducted [138], with the pumps being tested until failure at their maximum rated pumping head. Here, these tests need to be distinguished from the normal tests, as the highly accelerated life test is used to estimate the lifetime and determine the safety margins of the design beyond specification levels, thus evaluating the reliability and failure analysis. The diaphragm pumps were powered with a 160 W PV array and had a lifetime of 0.75 – 2.4 y at a maximum design pressure of 7 bar. All of the diaphragm pumps failed due to the worn diaphragm seals. The diaphragm pumps with a significant amount of metal achieved a longer lifetime (2.4 y) than the ones made from plastics (0.75 and 1.33 y, respectively), the possible reason for which was that the greater weight reduced pump movement during commissioning [138]. Overall, it was found that the operating lifetime can be extended to over 6 y if the maximum operating pressure was limited to 3 bar [139]. Nevertheless, such low pressures are not relevant for desalinating brackish water. Regular servicing of diaphragm pumps needs to be carried out, such as replacing the diaphragms (2 – 3 y) and seals (3 – 5 y), as well as regular maintenance being performed every 1 – 2 y, to ensure long life expectancy [128, 135, 138]. In contrast, helical rotor pumps powered with 320, 480, and 640 W PV arrays and operated with a pressure ranging from 5 – 10 bar demonstrated no measurable degradation in performance over 3 y. Moreover, one pump was tested for over 1 y at a maximum design pressure of 15 bar, but it showed no measurable signs of degradation, as well. The above analyses further demonstrated the superior capacity of helical rotor pumps compared to diaphragm pumps in terms of longer operational lifetime and higher operating pressures.

Clearly, the materials of the pumps play a crucial role in robustness. The majority of materials currently used in pumps are divided into metals with iron, significant proportions of chrome and nickel, copper or aluminium, and other metallic and non-metallic materials [133]. Cast iron, aluminium bronze, and steel are appropriate for pumping fresh water (less than 1% sodium chloride, NaCl) [133]. However, in brackish water, these materials will cause corrosion cracking, and thus they are not recommended by manufacturers for brackish or seawater applications. Non-metallic materials are also essential in pump construction, with nearly all pumps containing gaskets, seals, and O-rings made of thermoplastics, thermosetting plastics, or elastomers, which tend to absorb liquids during contact, as well as age very rapidly with increased temperature [133].

In particular, the wetted parts of the pumps – mainly including the rotor, stator, and torsion shaft – have a major impact on the lifetime of pumps. Generally, the wetted parts are made from thermoplastics, thermosetting plastics, elastomers, stainless steel (SS), ceramics, and other materials [133]. For PV-membrane applications, it is critical to consider the chemical resistance of the wetted parts in saline-containing corrosive waters, and the ability to cope with higher operating pressure. As a consequence, the majority of metallic materials for the wetted parts used now are SS, such as ASTM304, ASTM316, duplex 2205, and super duplex. The corrosion resistance of the three types of SS (ASTM 304, ASTM 316, and 2205 duplex) as a function of NaCl concentration and temperature is illustrated in Figure 2-5 [140]. Here, pitting is referred to as a form of localized corrosion caused by aggressive water, such as salty water that produces attacks in the form of spots or pits. It is worth noting that SS is mainly discussed here, as they are the mainly used materials in salty water. As indicated in Figure 2-5, if the feed water temperature remains below 20°C, then no pitting problems are observed with either ASTM 304 or ASTM 316. However, at a temperature of 30°C, corrosion problems can occur with ASTM 304 at an NaCl concentration of > 2,000 mg/L. On the other hand, with ASTM 316, such pitting problems are commonly only expected at temperature > 40°C and NaCl concentration > 5,000 mg/L. More information can be obtained by examining the situation with seawater desalination systems, in which pitting problems occur with ASTM 304 and 316 at temperature >20 °C and NaCl concentration > 10,000 mg/L. In this case, 2205 duplex or 2207 superduplex can be employed to markedly improve the reliability of the pumps. It can be seen that 2205 duplex achieves significantly better performance at higher temperatures, chloride (Cl⁻), and NaCl concentrations than either ASTM 304 or ASTM 316 without pitting. It was reported that the typical groundwater temperature in regions with a tropical climate at a depth of 50 m was maintained at 25 °C [141]. Therefore, ASTM 316 SS is anticipated to fulfil the requirements for the vast majority of brackish water RE-membrane applications. However, duplex or super duplex SS are more properly employed at higher ambient temperatures (> 40 °C) and concentrations (seawater) applications to avoid corrosion.

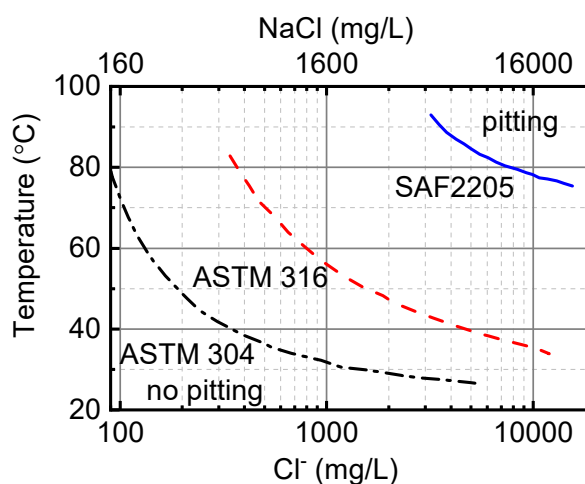


Figure 2-5: Critical pitting temperatures for ASTM 304, ASTM 316, and 2205 duplex stainless steel, at varying concentrations of sodium chloride with a pH of 6. Pitting occurs above the curve areas. Adapted from [65]. CC BY-NC-ND 4.0 License.

The pitting corrosions can also be increased by other factors, e.g., increased temperature, low pH, and the addition of oxidative chemicals. Schäfer *et al.* [142] identified several physico-chemical water quality problems during an extensive sampling trial in Ghana, the results of which indicated that the naturally existing water samples of pH values were in the range of 3.7 to 8.9. Moreover, the corrosion rate increased when the pH decreased (increasing acidity) [85]. This occurs as the low pH solutions accelerate corrosion by providing hydrogen ions, causing attack and damage on the surface of the steel, as well as increasing the weight loss.

2.4.3. Recommendations

For small-scale RE membrane system applications, the following recommendations are given:

- i) Brushless DC motors are preferred due to higher efficiency, 15 – 20 y lifetime, and less maintenance compared to brushed motors;
- ii) Helical rotor pumps appear to be the most appropriate pumps, as they combine the characteristics of high efficiency and pressure with low flowrate over a broad operating range, which are challenging to obtain with other pumps;
- iii) The combination of helical rotor pumps with brushless DC motors achieve the most reliable and efficient pumping performance that fulfils: 1) the pressure and flowrate requirements with low maintenance, and 2) the target system lifetime of 20 y;
- iv) The wetted parts of pumps made of ASTM 316 stainless steel are suitable for the majority of applications for brackish water PV-membrane systems.

2.5. Pressure-driven membrane processes

2.5.1. Membrane fouling and control

The main challenge with an effective pressure-driven membrane is fouling [143]. Fouling occurs by a decrease of flux if the system is operated at constant pressure, or an increase in the TMP required to maintain a specific flux. Consequently, the performance of the membrane (i.e., permeability and retention) is deteriorated due to the deposition of suspended or dissolved substances (foulants) on the external surfaces of the membrane, at the pore openings, or within the pores [18, 144]. Membrane fouling can cause reduced life expectancy and severely decrease the performance of a membrane system, such as the decline of permeate flux and diminished permeate water quality. The increased feed pressure needed to keep the permeate flow constant leads to an increase of SEC. More frequent cleaning is necessary to reduce membrane fouling, and as a result, the corresponding maintenance cost would be increased.

Typically, membrane fouling is categorized into biofouling, inorganic fouling, and organic fouling. Biofouling is caused by microbial attachment to the membrane surface followed thereafter by its growth, and multiplication when a sufficient supply of organic nutrients in the pre-treated feed water or organic nutrients is deposited on the membrane [22, 145]. Inorganic fouling – including scaling and colloidal fouling – occurs due to deposition of insoluble salts and/or colloidal solids or particles on the membrane surface [145]. Organic fouling, on the other hand, takes place as a result of low and high molecular weight organic molecules and/or dissolved organic matter on the membrane surface, such as natural organic matter (NOM), synthetic organic compounds, disinfection by-products, and soluble microbial products [146, 147]. Here, it is necessary to distinguish the fouling mechanisms for MF/UF and NF/RO. The main fouling mechanisms for MF/UF are pore-clogging/blocking and adsorption, and cake formation on the membrane surface, which all lead to an increase in hydraulic resistance to permeate flux [148].

In addition to the increase of hydraulic resistance, the salt concentration polarization (CP) layer at the surface of NF/RO membranes will be enhanced due to colloidal/particulate fouling and biofouling layers, ultimately resulting in increased osmotic pressure and significantly decreased flux [149, 150]. Membrane fouling is determined by the coupled influence of physical and chemical interactions between foulants and membrane. These interactions are dominated by the characteristics of foulants (molecular weight, polarity), the solubility of salts, feed water solution chemistry (pH, ionic strength, divalent cation concentration), membrane properties (surface morphology, hydrophobicity, charge, MWCO), water temperature, operation mode (constant permeate flux or constant feed pressure), and hydrodynamic conditions (initial permeate flux and crossflow velocity) [151]. A mixed fouling layer will be formulated by different types of foulants in the case of complicated water sources. Moreover, for direct-coupled PV-membrane systems in remote areas, the TMP and permeate flux are various due to the fluctuations and intermittency of solar energy supply, which influence the physical and chemical conditions on the membrane surface. Consequently, the

fouling behaviours/mechanisms may be different from stable and constant operational conditions. Therefore, further research that involves fouling behaviours/mechanisms in RE-membrane systems is required to enhance system robustness and reliability.

The various approaches to mitigate the effects of membrane fouling are determined by its complexity [148]. These approaches are classified into four main topics: i) pre-treatment of feed water; ii) membrane selection; iii) optimization of operating parameters; and iv) regular and periodic cleaning. The first three methods are focused on the prevention or mitigation of membrane fouling; whereas, the fourth approach is concentrated on coping with the consequences of membrane fouling [22, 148, 151-154]. These will be discussed in the following sections.

i) Pre-treatment of feed water

It is crucial to have adequate pre-treatment prior to the membrane system to minimize membrane fouling, and increase the efficiency and life expectancy of the membrane elements. This is because pre-treatment can largely reduce the potential of different foulants attached to the membrane surface [155]. Numerous indices of feed water fouling potential have been applied to determine the fouling potential of feed water for the NF/RO system. Such colloidal fouling potential indices include the silt density index (SDI), the modified fouling index (MFI), and turbidity of permeate from pre-treatment [156]. It can be considered sufficiently low to control colloidal and particulate fouling if an MFI value is less than 1 (corresponding to an SDI value of < 3) [35]. The commonly used organic fouling potential indices are dissolved organic carbon (DOC) and total organic carbon (TOC), assimilable organic carbon (AOC) and adenosine triphosphate (ATP) constitute biofouling potential indices [157], and the supersaturation index and the scaling potential index indicate scaling potential. Scaling can occur when the supersaturation index is higher than 1 [156]. Usually, multiple different pre-treatment options are combined to allow optimal membrane system performance as a consequence of the complexity of feed water potential foulants, feed water quality, and treatment purposes [158].

The potential pre-treatment options for the MF/UF membrane include conventional processes (e.g., coagulation, flocculation, and media filtration), adsorption, pre-oxidation, and biological treatment, and other pre-treatments, such as magnetic ion exchange (MIEX). These techniques have proven to be effective to minimize colloidal fouling, organic fouling, and biofouling. Malgorzata investigated the impacts of pre-coagulation (aluminium-based coagulant) on the removal of NOM for the UF membrane. The results showed that the highest NOM substances' separation was achieved at a water pH of 6 when the alum was used, and pre-coagulation was able to reduce organic fouling [159]. The efficiency of pre-treatment in decreasing fouling potential is strongly dependent on the type of agents, dosage, mixing methods, contact time, temperature, and feed water chemistry [153].

In addition, MF, UF, and NF are increasingly applied as a pre-treatment for RO systems due to the advantages and potential benefits compared to conventional pretreatment processes [22, 160]. Firstly, it allows consistent and excellent RO feed water quality (typically $SDI < 2.5$). This permits the enhancement

of NF/RO performance and increased lifetime by 20-30%, as well as increased recovery and permeate flux (approximately 22% higher permeate flux than conventional processes), independent of fluctuations in raw water quality [161, 162]. Secondly, it can greatly reduce the land footprint (40-70% reduction) due to the modular designs, which in turn makes it easier to couple into RE-membrane systems where space is limited [34]. Thirdly, it is convenient to transport and install MF/UF modules, which can be operated with low pressure and simple maintenance to save O&M costs [158, 163]. Moreover, based on a study of cost comparison between UF and conventional pre-treatment for a 90,000 m³/d RO desalination plant, the total water cost using UF is reported to be 0.52 \$/m³, which is only slightly higher than the water cost of conventional pre-treatment of 0.51 \$/m³ [164]. For this reason, it is recommended to apply a membrane-based process as a pre-treatment for RE-membrane systems. Among these membranes, Schäfer *et al.* [165] concluded that open UF was superior to MF, and NF was superior to tight UF, based on the estimation of membrane costs as a function of water quality parameter – defined based on the colloid, organics, and cation retention when NOM was included in feed water. It was concluded that the cost of additional energy required to operate NF was cheaper than the chemicals needed to achieve the same level of organic removal with MF. Therefore, for small-scale RE-membrane systems in remote areas, higher economic potential can be attained by applying the NF membrane instead of UF or MF.

Chlorination has been employed to reduce biofouling potential, as it can inactivate most pathogenic microorganisms with a reaction time of 20 – 30 min [45, 166]. It is worth noting, however, that a free residual chlorine concentration of 0.5 – 1.0 mg/L should be maintained through the whole pre-treatment line [45]. Consequently, a dechlorination process upstream is required to protect the polyamide (PA)-based NF/RO membranes against oxidation damage. The addition of a scaling inhibitor, such as sodium hexametaphosphate (SHMP), organophosphates and polyacrylates, or antiscalant and acidification, are commonly used to reduce scaling potential attributable to the rising solubility of scales, e.g., calcium carbonate, magnesium sulphate, and calcium fluoride [146]. It is recommended to use a scale inhibitor at system recovery >20% to prevent membrane scaling because the high operating recovery will result in an enhanced CP on the membrane surface, thus increasing the scaling potential for the membrane [167].

ii) Membrane selection

The appropriate membrane can not only effectively remove contaminants and ensure good product water quality, but also reduce fouling potential and cleaning frequency. Eventually, it increases system efficiency, extends membrane lifetime, and conserves O&M costs [168]. The ideal membrane should be selected and considered based on the following aspects: feed water quality; target water production; target water quality; membrane characteristics; and membrane cost.

To achieve appropriate membrane selection, it naturally requires analysis of the physical-chemical-biological characteristics of the feed water. Membrane system design and simulation software available by membrane suppliers is a useful and essential tool for selecting membranes. The permeate quality and SEC of different potential membranes (NF or RO) in the simulation results indicate whether the local drinking water guidelines or World Health Organization (WHO) guidelines can be fulfilled, such as a TDS <

600 mg/L is required to pass the palatability test for good drinking water. It must also be kept in mind that the seasonal variation of feed water quality and quantity must be considered. NF is recommended to be used if it can achieve the target water quality due to its lower energy consumption, reduced fouling tendency, and higher water production compared with RO. As an example, Katie and Korak [169] identified the membranes used in the PV-membrane system with simulations in reverse osmosis system analysis (ROSA) software. The results demonstrated that NF90 required lower feed pressure, but still fulfilled the target water quality, in comparison with the BW30 membrane and other NF/RO membranes. Nevertheless, design and simulation tools are not able to substitute pilot-scale testing with specific water. In particular, when arsenic, iron, or heavy metals are contaminated with water, the potential membranes to remove these contaminants should be tested at least at the laboratory scale via exploring methodologies that can attain comparable results to real applications [170].

Other membrane properties, such as permeability, fouling resistance, and robustness, that can be obtained from the membrane manufacturer should be considered in order to ensure long-term applications. For example, the membrane has been proven successfully operated (> 3 y) for a river water RO plant in Infra-Zeitz (Germany). No biofouling was detected due to a well-selected fouling-resistant membrane (BW30-365FR) along with a weekly low dose of biocide.

Certainly, the issue of cost cannot be avoided during membrane selection. The total cost, including capital costs (membrane cost) and O&M costs, is important, yet often difficult to establish in advance. Ang *et al.* [171] provided a comprehensive evaluation by combining cost modelling, membrane performance, fouling propensity, and energy consumption to identify the potential of NF (NF270, NF90, and TS80) and low-pressure RO (XLE) membranes to replace the typical brackish water RO membrane (BW30). The authors concluded that NF90 and XLE membranes could be used as an alternative to BW30 for very low TDS (400 mg/L) brackish water, as both membranes encountered reduced fouling issues, consumed less energy, and offered cost savings. For medium TDS (4000 mg/L) brackish water, however, the NF90 membrane appeared to be the preferred candidate compared to XLE due to its robust performance, such as 21% and 17% cost savings for total costs and operation costs, respectively, per cubic meter treated water compared to the XLE membrane. For small-scale RE-membrane systems in remote areas, design and simulation tools are suggested to be used for initial membrane selection, after which pilot testing is needed to evaluate the long-term performance of the system.

iii) Optimization of operating parameters

To minimize the rate of fouling and eliminate the potential for mechanical damage to the system, the membrane is normally operated according to the specifications of the manufacturers [45]. Operating parameters include numerous factors, e.g., temperature, cross-flow velocity, recovery, TMP, and initial permeate flux. Those parameters are varied in terms of energy supply in a direct-coupled PV-membrane system, thus causing the complexity of optimization of those parameters.

For the MF/UF membrane, Grozes *et al.* [172] studied the effects of several operating parameters on NOM fouling, including permeate flux, concentrate velocity, backwash frequency, and TMP. It was concluded that NOM fouling can be minimized by reduced flux, increased concentrate velocity, and backwash frequency. By doing so, the shear on the membrane surface increased and these operating parameters, especially concentrate velocity, should be adapted to keep the increase of TMP below a certain threshold (in their case, it is 1 bar). In 1995, Field *et al.* [173] proposed the “critical flux” concept to control membrane fouling. Critical flux here refers to the point at which flux ceases to increase linearly with TMP. It is dependent on the hydraulic conditions of the membrane process. Operation at critical flux can markedly reduce membrane fouling, especially colloidal fouling, for the long-term MF/UF membrane process.

Generally, the groundwater NR/RO desalination operation can mitigate membrane fouling attributable to the reduction of membrane affinity at low groundwater temperature, but it will decrease permeate flux [174]. The cross-flow velocity increases along with the increasing of feed flow rate, and ultimately it can improve shear stress and weaken CP/fouling. Minor variations of recovery can significantly affect the overall cost (capital and O&M costs) of the membrane system, and the extent of typical limiting factors, such as fouling propensity and mineral scaling potential [175]. In small-scale PV-membrane systems, it is suggested to operate the system with a recovery of 10 – 25% to reduce maintenance and the requirement for using antiscalants according to the membrane system design guidelines from manufacturers [45, 176]. Typically, membrane systems with lower than 50% overall recovery will use single-stage configuration; whereas, two-stage configuration (the feed water for the second stage is the concentrate from the first stage) is recommended when overall recovery is between 50% and 75%.

The TMP is a critical indicator to monitor fouling of the membrane system when keeping the flux constant. Moreover, TMP mainly determines water flux and energy consumption. With the increase of TMP, the hydrodynamic driving force toward the membrane surface and the permeate flux will increase, causing enhanced CP, which may increase fouling potential. High pressure/permeate flux makes the membrane surface more favourable to adsorption and deposition of foulants. For the NF/RO membrane, a better understanding of critical flux needs to be achieved, as its fouling compositions are more complex than those of MF/UF, and osmotic pressure cannot be ignored [174]. In addition to optimized operation parameters, fouling control is also influenced by start-up strategies. Chen *et al.* [177] reported that the gradual pressure start-up from low to high values every 30 min led to a smaller fouling rate than the direct start-up to high values. Furthermore, the membrane operating conditions are also constrained by different membrane properties, including maximum membrane recovery, maximum operating pressure, maximum permeate flow, maximum feed water flow rate, and minimum concentrate flow rate, which can be obtained from the membrane manufacturer [45]. Therefore, these limitations of parameters should be considered when optimizing operation parameters.

The SEC of the PV-membrane system is greatly affected under different operational conditions. As shown in Figure 2-6, the SEC of commercial NF/RO membranes under different operation conditions (provided in Table 2-3) were plotted as a function of permeability. Generally, the results reveal that lower

permeability membranes exhibit significantly higher SEC. Although NF270 seems to be the most energy-efficient membrane, the salinity removal may not fulfill the guidelines [178]. Regarding the BW30 membrane operating under conditions (a) and (b), the higher SEC primarily resulted from the higher feed flow rates caused by additional energy consumption by the pump. For NF90 at condition (c), the higher SEC occurred as a consequence of the low TMP (4.8 bar) and high feed concentration, as very little permeate could be produced; whereas, at condition (a), the low SEC was resultant from very little energy needed at low pressures with very low feed concentration and high recovery. Ultimately, despite the low SEC of TFC-S and NF270 membranes, they were not able to meet the recommended drinking water guidelines as a result of lower salt retention. Many studies indicated that RO membranes with high permeability lead to lower energy consumption in desalination [179, 180], which is proportional to applied hydraulic pressure to drive water across the membrane [181]. One process modelling of commercial thin-film composite (TFC) RO membranes in seawater desalination concluded that 3.7% energy consumption was reduced by increasing water permeability from 2 L/m²h bar to 10 L/m²h bar [182]. Similar conclusions were reached when modelling RO brackish water desalination [182]. This effect was constrained by two aspects. Firstly, hydraulic pressures are small when applying TFC membranes, and thus the potential for further efficiency gains is limited. Secondly, CP limits further flux increase at higher water permeability. Therefore, it is more important to increase water-solute selectivity, rather than increasing membrane permeability, to improve membrane performance and water quality [181, 182].

Table 2-3: Examples of operational conditions in terms of TMP, feed flowrate, recovery, and feed TDS concentration for different NF and RO membranes. Note that (a), (b), and (c) represent different operational conditions. Adapted from [65], CC BY-NC-ND 4.0 License.

Membrane	TMP (bar)	Feed flowrate (L/h)	Recovery (%)	Feed TDS (mg/L)
Duraslick	13	—	50	3500
TFC-S	10	300	55	5300
ESPA4	10	300	58	5300
ESPA3	9.5	—	70	4000
TW30	14	728	70	2000
BW30 ^(a)	4.5	600	17.3	282
BW30 ^(b)	11	400	40	5300
BW30 ^(c)	5	550	13.4	3632
NF90 ^(a)	4.3	600	45	282
NF90 ^(b)	9	300	40	5300
NF90 ^(c)	4.8	567	27.8	3632
NF270 ^(a)	4.3	600	45	282
NF270 ^(c)	4.8	567	39.7	3632

Note: “—” denotes information not provided.

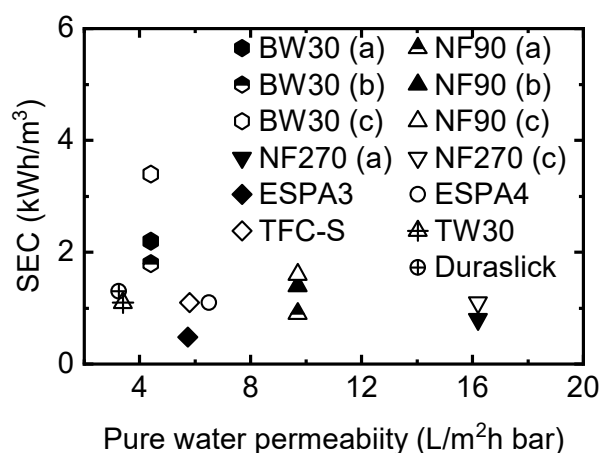


Figure 2-6: SEC as a function of water permeability for different membranes applied under different operational conditions as described in Table 2-3. Adapted from [65]. CC BY-NC-ND 4.0 License.

iv) Membrane cleaning

Membrane cleaning remains an essential step in maintaining the performance of the membrane process [152] to minimize the fouling rate. RO membrane cleaning typically starts when the normalized permeate flow drops by 10%, or the normalized salt retention decreases by 5-10%, and/or the normalized pressure drop (the differential between feed and concentrate pressure) increases by 10-15% [183]. The typical cleaning frequencies for full-scale NF systems are from once per 3 months to once per 2 y, with an average of 6 months. However, for treating surface water, the cleaning frequencies may differ from once per week to once per 3 months [152]. The ideal cleaning processes should be effective against several foulants, and gentle to the membranes to maintain and restore their characteristics [152]. Many cleaning methods exist, including both physical- and chemical-based methods, and resistance removal and flux recovery are used to evaluate their cleaning efficiency [22].

The commonly used physical cleaning methods for pressure-driven membranes are summarized in Figure 2-7. The physical cleaning method of MF/UF includes hydraulic methods, pneumatic methods, and sonication. The hydraulic cleaning method applies strongly changing hydrodynamics of membrane systems to force foulants to leave the membrane surface, and includes forward flushing, backwashing, and backpulsing. The differences among them are wash direction and wash time. Generally, backwash is performed for 30-60 s every 5-15 min of filtration, while backpulsing time is much shorter (<1 s) at a higher frequency [174]. Moreover, pneumatic methods, such as water/air flushing, constitute effective and promising methods to clean membranes, which can produce turbulence and flow on the membrane surface and unstable bubbles, thus sweeping away foulants. Mechanical cleaning, such as sponge ball wiping, can also be utilized to clean large diameter tubular membranes [184]; however, it increases both energy consumption and cost. In comparison, osmotic backwash (OB) processes are promising methods to clean NF/RO membranes due to low maintenance costs and lower chemical consumption [185]. In 1997, Rolf and Eckehard patented it as a “suck back effect” with the potential to exploit OB for self-cleaning of membranes at the second stage of NF/RO membrane system operation [186, 187]. In RE-membrane systems without energy storage, the

OB process occurs if operating pressure drops below the osmotic pressure. Consequently, the foulants deposited on the membrane are removed. This indicates that the RE-membrane system could potentially benefit from operation under fluctuations [39, 188], but no detailed investigations have yet been conducted. Chen *et al.* [189] identified the key factors affecting both physical and chemical cleaning of UF and RO membranes, including the production interval between cleaning, duration of backwash, and pressure during forward flush. The UF physical cleaning protocol was designed as being 1 min backwash followed by 1 min forward flush at 1.7 bar using RO permeate once every 30 min of operation. In this case, the cleaning efficiency (the flux recovery: clean water flux ratio between after cleaning and initial flux) decreased with the increase of the production interval between cleaning, pressure during forward flush, as well as the duration of backwash. Meanwhile, the RO physical cleaning protocol was developed, i.e., 5 min backwash followed by 1 min forward flush at 6.2 bar using RO permeate once every 6 h of operation. The higher flux recovery was obtained by increasing the production interval between cleaning. It is worth noting that these protocols can be varied with different feed water and membranes. Although these physical cleaning methods appear to be environmentally-friendly and more effective, implementations of these methods may result in more complex control and design of the system [152, 190].

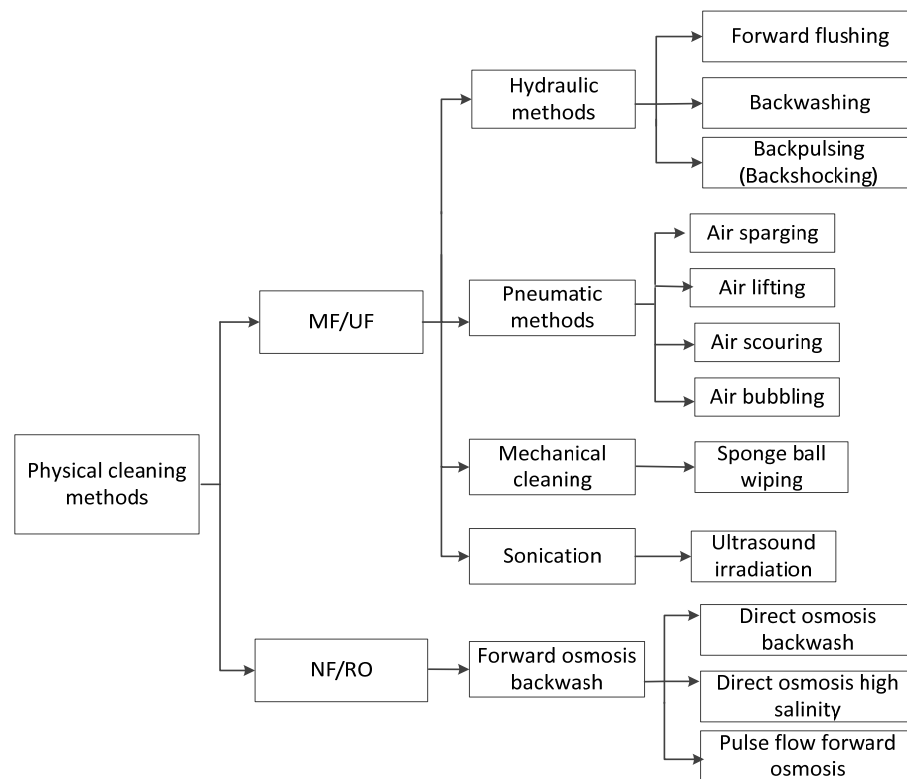


Figure 2-7: Overview of physical cleaning methods for pressure-driven membranes. Adapted from [65]. CC BY-NC-ND 4.0 License.

For chemical cleaning, the proper chemical agents can be determined by distinguishing fouling types and foulants components, as well as chemical properties and economic factors [22]. The optimal (the least membrane damage and maximum cleaning efficiency) selection of cleaning agent depends on foulants

[152]. A large number of chemical cleaning agents are commercially available, and commonly used ones fall into six categories: acids; alkalis; metal chelating agents; surfactants; oxidants; and enzymes [151]. For pressure-driven membranes, the common chemical cleaning agents and fouling removal targets are presented in Table 2-4. Alkaline solutions, such as sodium hydroxide, are more effective in removing organic fouling and biofouling; whereas, acids, e.g., hydrochloric acid, nitric acid, and sulphuric acid, are suited for removing membrane scaling [152]. The commonly used cleaning agent is ethylene diamine tetraacetic acid (EDTA), which can effectively remove scaling and organic foulants associated with calcium ions [152]. Sodium dodecyl sulphate (SDS) is a typical surfactant in cleaning, which can be used for effectively removing colloidal fouling and organic fouling under proper cleaning conditions [191]. It is recommended to use alkaline cleaning as the first cleaning step. In contrast, acid cleaning should only be applied as the first cleaning step if the presence of only calcium carbonate or iron oxide/hydroxide on the membrane elements is known, as acid cleaners normally react with silica, organics (for instance humic acids), and biofilm present on the membrane surface, which may cause a further decrease of membrane performance.

When the NF/RO system suffers from colloidal, organic fouling, or biofouling in combination with calcium carbonate, then a two-step cleaning program will be needed: alkaline cleaning followed by an acid cleaning [183]. Typically, the following six steps exist in the cleaning membrane module *in situ*: i) prepare the cleaning solution; ii) low-flow pumping; iii) recycle; iv) soaking; v) high-flow pumping; and vi) flush out the cleaning solution [37]. Usually, a combination of physical and chemical cleaning methods is applied to enhance cleaning effectiveness [152]. In addition, according to a study about cost analysis of a large-scale RO membrane desalination system (100,000 d/m³, sand filtration as pretreatment), the chemicals' cost for cleaning was approximately 35% of the total operation cost [192].

The effectiveness of chemical cleaning is influenced by the type of cleaning agent and its concentration and operation conditions, including cleaning time, crossflow velocity, feed pressure, and temperature [151]. Madaenl *et al.* [193] investigated the effect of agent concentration, cleaning time, crossflow velocity, and temperature on chemical cleaning of the RO membrane. They found that higher crossflow and temperature can improve cleaning effectiveness, and higher concentration can improve the cleaning process, but the effect is limited at high concentrations.

Table 2-4: Overview of common chemical cleaning agents for the pressure-driven process. Adapted from [65]. CC BY-NC-ND 4.0 License.

Category	Examples	Fouling removal targets
Acids	HCl, HNO ₃ , H ₃ PO ₄ , citric acid, oxalic	Inorganic fouling (scaling)
Alkalis	NaOH, KOH, Na ₂ CO ₃	Organic fouling
Chelants	EDTA	Scaling
Oxidants	H ₂ O ₂ , NaClO, KMnO ₄	Biofouling, organic fouling
Surfactants	SDS, CTAB, Tween 20, alkyl sulphate	Colloidal fouling
Enzymes	Lipases, proteases	Organic fouling (e.g., proteins, lipids), biofouling

2.5.2. Membrane integrity and damage

i) Membrane integrity and monitoring

The removal of some chemical and biological species via the membrane system can be variable, depending on specific solutes in the feed solution, membrane characteristics, and operational parameters, such as temperature and flux [20]. This can be further deteriorated by performance issues, such as membrane fouling and membrane integrity loss [20]. For instance, MF/UF membranes are capable of effectively removing pathogens, which may still pass through the membrane if the integrity is compromised, such as broken fibre, fibre degradation, or O-ring failure [55]. The failures of membrane fibres or sheets are mainly caused by: i) chemical corrosion, such as oxidation; ii) faulty installation and maintenance; iii) membrane stress and strain under operating conditions, such as backwash or excessive movement attributable to bubbling; and iv) damage by sharp residuals from pre-treatment [55, 58, 59]. Zondervan *et al.* [60] conducted a systematic study of factors that affect UF membrane lifetime – including the fouling status of the membrane, cleaning agent concentration, the magnitude of the back pulse, and the number of applied back pulses – and the integrity of the membrane was determined utilizing permeability testing, pressure decay test, and bubble tests. The results indicated that the membrane fouling status associated with the number of applied pressure pulses were significant aging factors, and ultimately contributed to membrane failures [60]. Since NF/RO are not absolute barriers against microorganisms [61], some passage of particulate compounds (turbidity) may occur despite the absence of pores in the membranes due to manufacturing imperfections. This indicates that the integrity of the NF/RO membranes might be compromised during commissioning and operation of the system, such as the inter-connector, or end connector O-rings, and membrane element glue lines [57].

For the above-mentioned reasons, it is crucial to perform accurate and efficient integrity tests and monitoring, as well as reachable flux, salt retention, and membrane recovery of the membrane system in order to ensure the quality of filtered water [194]. In most cases, the purposes of membrane integrity tests

include verification of high filtered water quality, demonstration of regulatory compliance, and detection of equipment/filtration problems [194]. Membrane integrity tests are specific for a certain membrane type, and depend on the membrane manufacturer and membrane system supplier. Generally, membrane integrity monitoring techniques are classified into two main groups: direct methods; and indirect methods. Direct methods refer to tests that are directly applied to the membrane element. It is worth mentioning that these tests can only be applied prior to loading elements into the system or after disassembling the elements from the system for spiral wound NF/RO membranes. Indirect methods, on the other hand, are tests applied to water quality parameters in the permeate solution, such as particles (turbidity), salinity (conductivity), organic matter – total organic carbon (TOC) and dissolved organic carbon (DOC) – and microorganisms, which allow continuous operation of a membrane system. The pressure decay test (PDT) and diffusive airflow (DAF) test appear to be the most commonly used *in situ* direct methods for MF/UF due to simplicity, low maintenance, reliability, and high sensitivity to detect membrane breaches [194]. It takes about 30-60 min to conduct such tests to reduce system downtime [195]. Moreover, indirect methods, such as particle counting, turbidity monitoring, and routine microbial analysis, are the most frequently used for MF/UF. The common direct methods for NF/RO membrane integrity monitoring are vacuum tests and pressure tests; whereas, the common indirect methods include in-line conductivity monitoring for the permeate, conductivity probing for each membrane element, in-line TOC/DOC monitoring, and microbial seeding of the permeate solution [196, 197]. Importantly, it might be necessary to apply more than one monitoring method in order to ensure reliable operation of the NF/RO system [196]. These available integrity monitoring methods are employed at different levels and stages during the O&M of the NF/RO system in terms of integrity testing goals [169].

Currently, TOC/DOC monitoring is used in large-scale water treatment plants, such as wastewater reclamation plants in Singapore [198]. However, considering applications in small-scale PV-membrane systems in remote areas, they are both expensive and complicated. Schäfer *et al.* [199] reported that conductivity was a good surrogate parameter for the RE-membrane system. Therefore, in-line conductivity monitoring as an indirect method is suggested to be utilized during system operation, due to its simplicity, low maintenance, and sensitivity. In contrast, direct methods, such as PDT and vacuum tests, are recommended to be used during RO element delivery, system assembly, and troubleshooting stages by a qualified operator. For instance, Alghoul *et al.* [200] implemented in-line conductivity monitoring of permeate salinity (lower than 50 mg/L TDS) to monitor integrity for their small-scale PV-membrane brackish water desalination units (5.1 m³ freshwater per day with SEC 1.1 Wh/L).

ii) Membrane damage

Abrupt pressure or flow variations on membrane elements can cause membrane damage during start-up, shut-down, cleaning, or other sequences [45]. In general, damage of pressure-driven membranes is classified into physical and chemical damage. This damage can produce membrane failure or membrane integrity loss, ultimately resulting in an increase of permeate flux and a decrease in salt retention.

Physical damage (e.g., abrasion) is mainly resultant from sharp precipitates, large particles, spacer rubbing/moving protrusion or spacer material, and membrane element telescoping (longitudinal unravelling of the spiral wound membrane elements). It occurs due to loss of function in the pre-treatment, to the membrane cleaning process, or to operational problems [201]. Physical damage could take place when some particulate matter enters or is generated in the membrane module, and then physically abrades or penetrates the membrane layer and compromises the product water quality [202]. Even particles in the size range of 10 to 50 μm can cause damage to a membrane surface. Therefore, it is critical to maintain pre-treatment in good conditions to ensure that no bypassing occurs. In addition, the appropriate operation of the membrane system can prevent physical damage. According to one membrane manufacturer [45], telescoping is likely to occur when excessive pressure drops from feed to concentrate if the system is operating beyond the recommended maximum feed flow rates or the feed pressure builds up too rapidly during the start-up stage. As a consequence, the membrane module can be mechanically damaged. Therefore, a soft start-up to increase the feed pressure and feed flow rate is suggested [45], and the rate of feed pressure increase should be lower than 0.7 bar/s to realize a soft start [45]. Furthermore, the high TMP or major loss of TMP can produce a pressure differential which could severely damage the membrane. Moreover, if the permeate line is pressurized during operation and the system shuts down, the membrane might become exposed to a static permeate backpressure. To avoid membrane damage from backpressure, the static permeate back pressure must not exceed 0.3 bar at any time [45]. One manufacturer also reported that excessive permeate back pressure was one of the most common causes of mechanical damage to NF/RO during operation [203]. When a permeate valve is closed during operation or cleaning, permeate side pressure can build up until it equals the feed pressure. In addition, the tail of the membrane element has a lower pressure on the feed side as a consequence of pressure drop. Consequently, the permeate pressure could exceed the feed pressure, thus pouching the membrane leaf and causing delamination of the thin film PA layer from its support layer [203]. The membranes are anticipated to undergo plastic creep at constant pressure and temperature; thus, in the RE-membrane system, the fluctuating pressure and flowrate with cycling on/off may result in material fatigue [204]. Richards *et al.* [205] analyzed the rate of change of TMP (ΔTMP) in a small-scale wind-powered membrane system from 24 h of realistic wind data. It was determined that the maximum rate of pressure change was within the region of soft start even under extreme wind speed fluctuations, and thus it was not a concern during long-term operation.

Chemical damage primarily occurs due to the presence of chlorine (e.g., hypochlorite, hypochlorous acid, or chlorate) or some oxidants in the feed water, which could oxidize the active PA layer of the NF/RO membrane, resulting in higher salt passage and higher water permeability. The damage is both irreversible and continuous as long as the membrane is in contact with these chemicals [202]. Kang *et al.* [206] showed that a reversible N-chlorination and an irreversible ring-chlorination occurred with the hypochlorite degradation reaction of an aromatic PA membrane. They suggested that the PA membranes must not be used in acidic environments with residual active chlorine, and short-time treatment with alkaline hypochlorite solution could improve membrane performance slightly. Additionally, the oxidants are broadly used for dis-

infection of feed water prior to the NF/RO system to reduce biofouling potential, leaving the system exposed to a greater risk of chemical damage [207]. Therefore, it is suggested to choose chlorine-resistant PA-based NF/RO membranes, as well as assuring that there are no oxidants in the feed water prior to the NF/RO system by using physical adsorption (activated carbon adsorption) or chemical neutralization (bisulphites neutralization) to reduce the chemical damage risks of the PA-NF/RO membrane. Tin *et al.* [208] compared the chlorine resistance and separation performance of a prototype chlorine-resistant NF membrane with a commercial NF membrane. It was concluded that the prototype NF membrane exhibited stable performance with the exposure of a 1000 g/L NaOCl solution up to the cumulative chlorine exposure of 50,000 g/h. For a RE-membrane system, it is important to choose a robust membrane that can cope with operator errors and harsh conditions. New membrane materials are also being developed, which will increase the number of available options.

Overall, to avoid physical damage of membranes, the transportation, installation, and O&M process of membrane elements should be handled carefully [209]. In addition, specific chemicals, such as chlorine, should be prevented from contacting PA-based NF/RO membranes during operation to avoid chemical damage of membranes.

2.5.3. Operation and maintenance

i) System operation with fluctuations and intermittency

As discussed in Section 2.5.1, MF/UF membranes are always implemented as a pre-treatment for RE-membrane systems to protect NF/RO against fouling [210]. Fluctuations and intermittency will cause variations of pressure and feed flow rate, such that the membrane can withstand the changes of pressure and flow, and the size exclusion of contaminants would not be affected. The NF/RO membranes that experience pressure and flow variations may cause osmotic backwash and variation of contaminant retention. Membranes are typically expected to operate at constant operating conditions without abrupt pressure or cross-flow variations to reduce the potential of excessive mechanical stress on the membrane module [45].

Due to the transient nature of RE resources, any system that is directly-coupled to membranes is required to operate over a broad power range. Richards *et al.* observed that system shut-downs attributable to the lack of energy during periods of severe energy fluctuations (ranging from 20 to 800 Wh/m² for 2 h) can cause the retention of the NF/RO membrane to drop significantly to unacceptable levels [211]. Furthermore, the variable operation caused by the fluctuating solar resource could result in mechanical fatigue of the NF/RO membrane, and thus reduce both performance and lifetime [43].

To prevent deterioration of membrane system performance and operating time, Rahal and Infield [204] suggested that an upper limit should be set to the cycling on/off frequency during periods of low wind speeds of the membrane system. Park *et al.* [98, 212] conducted a systematic study on both the effect of wind speed fluctuations and intermittency on the performance of a wind-membrane system for brackish water desalination (2.75g/L and 5.5 g/L, BW30 membrane). The fluctuations at low average wind speeds

resulted in high turbulence intensity and long periods of oscillation, producing the worst system performance. This is largely attributable to insufficient power being available to restart the system. When the intermittency of wind power was less than 1 min duration, it was found to be the most deleterious to water quality and quantity.

Shen *et al.* [178] compared the performance of three membranes (BW30, NF90, and NF270) under fluctuating solar energy. The results from short-term fluctuations (up to 10 min, resulting from passing heavy clouds) demonstrated that the tight BW30 and NF90 membranes exhibited high abilities to produce good quality drinking water, but the loose NF270 showed decreased performance. Richards *et al.* [211] compared the performance of a PV-membrane system at six remote field locations to assess the impacts of fluctuating energy on inorganic contaminant removal via one BW30 membrane. The results indicated that the retention of ions (e.g., Ca^{2+} and Mg^{2+}) was above 95% with each groundwater during continuous operation. The retention dropped to between 40-50% for one sample under severe fluctuations (thunderstorms), while at another location the retention dropped to unacceptable levels ($< 30\%$) due to system shut-downs when significant cloud cover resulted in insufficient solar power to operate the system. Lai *et al.* [43] reviewed the effects of wind intermittency and fluctuation on the RO membrane system and summarized solution strategies into three categories: i) choose and size the energy storage unit optimally to maintain a constant energy supply for RO unit operation; ii) build a hybrid energy system combined with other forms of energy; and iii) adjust the effective capacity of the RO unit to cope with fluctuations of available wind energy. Furthermore, membrane system recovery is critical for successful operation in RE-membrane systems. Freire-Gormaly and Bilton [36] conducted experimental investigations on the impacts of intermittent operation of membrane performance. The results revealed that the average normalized permeability (ratio of membrane permeability and an average of the first 5 min of collected data) decreased to $87 \pm 9\%$ for intermittent operation with antiscalant and rinsing over 6 d, while the continuous operation with antiscalant decreased to $30 \pm 4\%$. These quantification results would subsequently be used to develop robust design algorithms for RE desalination systems. Richards *et al.* [39] applied SI step response testing to determine the effects of SI fluctuations on the performance of PV-membrane systems. It was concluded that the operating conditions during the first couple of minutes following a system shut-down event were crucial with: i) shorter off-periods leading to good performance being achieved more rapidly; and ii) short-term power availability significantly improving system performance. García Latorre *et al.* [213] studied the relation of energy consumption as a consequence of a wind power RO seawater plant working under variable load conditions. It was observed that no membrane deterioration occurred over the 1 y of the test period with variable pressure (35-80 bar) and flow (8-10 m^3/h) operations. There were also no membrane fouling or system breakdowns when operating in a discontinuous mode with a wide range of power (2.5 – 30 kW). It was concluded that a power input approximately 20% lower than the design specifications led to optimum plant performance.

Further research on the issue of robustness of membranes operating under fluctuating energy conditions in small-scale RE-membrane systems – particularly long-term studies – is required to evaluate the performance and improve the reliability of these systems in remote locations.

ii) Safe operating window (SOW)

The concept of a safe operating window (SOW) was proposed to elucidate the factors that resolve the optimal operating strategy for variable operation of RE-membrane systems [214]. SOW is employed to determine the safe operation (both physically and performance) with main constraints to allow maximum water production at minimal cost, as well as minimizing the risk of performance degradation caused by high recovery operation [215]. Directly-coupled RE-membrane systems are needed to operate over a markedly wide power range – for example, from as low as 10% to the maximum power rating – due to the transient nature of the RE resource and the absence of energy storage components. Hydraulic inputs, such as feed pressure and flowrate, have to be controlled to optimize system performance according to the available power range.

The concept of SOW for the transient operation of wind-powered RO membrane systems was first proposed by Feron in 1985 [214], who observed that the operation is anticipated to encounter both intermittency and fluctuations in terms of instantaneous wind speed or solar radiation. Feron determined that irregular operation would not cause any major problems with controlled cycling on/off of the plant, such as that the changing of pressure rate and cycling frequency did not cause any damage to the membranes [214]. The SOW originally proposed was a curved-sided quadrilateral derived from the constraints based on the membrane characteristics defined by maximum feed water pressure, maximum concentrate flowrate (or crossflow velocity), minimum concentrate flowrate, and maximum permeate concentration [214]. Miranda and Infield [42] modelled wind-membrane seawater desalination systems to enable independent control of feed flowrate and pressure at any point within the SOW in terms of wind speed. Moreno and Pinilla [216] used ROSA software [45] to identify the operating limits of a wind-powered RE-membrane plant. The minimum operating pressure and feed flowrate to produce adequate permeate quality was determined based on the analysis. Pohl *et al.* [217] used ROSA to perform detailed modelling, and investigate the use of four different operating strategies for transient operation within a SOW.

Richards *et al.* [215] performed experimental investigations of an operating strategy for transient operation of an RE-membrane system within a SOW. The SOW was defined by several constraints, including: i) the maximum pressure and flowrate produced by the pump; ii) the maximum recovery rate to prevent scaling and fouling; iii) the minimum set-point pressure of the regulating valve on the concentrate water; iv) the minimum recovery required to produce permeate flux; and v) the maximum set-point pressure of the regulating valve on the concentrate water. Moreover, different operating strategies were evaluated. Constant recovery operation was found to constitute the optimum operating strategy, as it led to the lowest SEC while maintaining good retention. However, it is practically challenging to implement this approach; thus, a constant set-point operation was recommended as the operating strategy for such systems to provide a more robust and effective solution in remote areas with a minor reduction in performance [215]. Richards

et al. [205] tested wind-membrane system performance by using an RO module (BW30) and brackish (5.5 g/L NaCl) feed water with 24 h of real wind speed data (average wind speed 6.1 m/s; interval of 1 s) of realistic fluctuation levels. The authors performed the SOW work by overlaying the operating point of the wind-membrane system throughout the day, plotted in terms of pump motor power and TMP (as illustrated in Figure 2-8). It was found that the time spent within the SOW per day increased from 16 h 47 min with a 10 bar set point under the operating conditions up to 19 h 56 min with the larger SC energy buffers.

Therefore, the developed SOW method can be used to evaluate the performance of a broad range of small-scale RE-membrane water filtration systems, assist with system design, and determine the necessity of including energy buffering components.

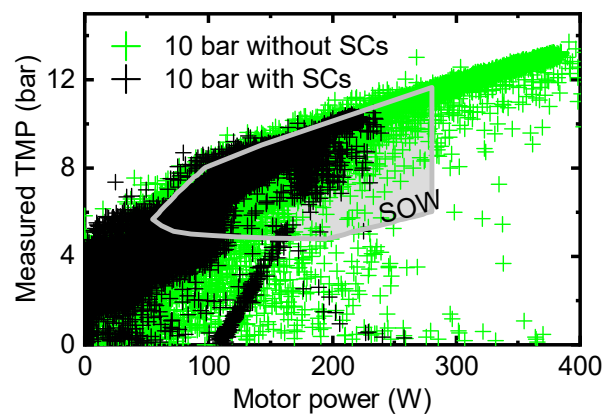


Figure 2-8: Performance comparisons of the RE-membrane system with/without SCs at each second of the 24 h period plotted on top of the SOW. Adapted from [65]. CC BY-NC-ND 4.0 License.

iii) Operational experience

To investigate the effects of membrane lifetime in terms of different operational experiences, authors reviewed the methods for removing natural organic matter (NOM), which is the main pollutant in surface water treatment based on Scotland and Norwegian operational experiences [184, 218, 219]. In both of these locations, small NF systems were implemented early. In Scotland, tubular cellulose acetate (CA) membranes [184] were applied to replace the initial Magnum 8231LP cellulose triacetate membranes [218] to overcome the need for regular operator attendance, frequent intervals for chemical cleaning to prevent the spiral wound NF membrane modules from plugging, and the CA membranes were mechanically cleaned by using foam balls which can be passed automatically up the tube to clean the membrane surface [184]. Consequently, the site visit frequency of the operator was reduced from daily to once per week, and the membrane lifetime was extended from an initial 1 y to 3 y due to the change of membrane modules. The operational experiences in Norway showed the recommended system design with a moderate flux ($< 20 \text{ L/m}^2\text{h}$) and recovery ($< 70\%$), and operated with daily cleaning to control fouling with predominantly CA NF membranes at high NOM content/color and low turbidity. Practical experiences showed the best spiral wound NF membranes could be operated for weeks with an almost constant flux up to $20 \text{ L/m}^2\text{h}$ [220], and demonstrated a typical membrane lifetime of 6-10 y [221]. For the removal of high color (> 50

mg Pt/L) contaminants in Norway, it is recommended to apply the MF and UF membranes in the system with a flux of 130-160 L/m²h and 50-70 L/m²h, respectively. The operational experiences from these two cases showed that a good membrane lifetime can be achieved for a small system and extended by proper chemical dosing, regular chemical cleaning, and efficient pre-treatment.

iv) Membrane maintenance

Small-scale powered RE-membrane systems applied in remote areas must be well operated and maintained by non-experts. General maintenance guidelines provided by manufacturers are not ideal for a specific system and site conditions. In a large-scale conventional RO system, condition-based maintenance (CBM) was used to monitor operational parameters, e.g., permeate flow rate or pressure drop (from feed to concentrate side), and maintenance actions are performed when the measurements reach a pre-set threshold. It was suggested for experienced operators to perform maintenance when the normalized product water flow rate decreases by 10% or the normalized pressure drop increases by 15% in large-scale grid powered RO systems [183]. However, in a small-scale NF/RO system, CBM was too complex and involved extensive trial and error practices, which are not possible for local operators without requisite expertise. Kelly *et al.* proposed model-based maintenance schedules under determined conditions, which can assist inexperienced operators to conduct maintenance at proper times in small-scale PV-membrane systems [222]. The results demonstrated the potential to implement model-based methods to allow non-experts to operate an RE-membrane system under uncertain, changing conditions, while still meeting community water demand [222]. Researches on the development of predictive tools and remote sensing technologies for small-scale RE-membrane systems are required to improve system O&M. Initially, qualified operators must operate such systems, ideally under service contracts. This will assure reliable operation when such technologies are established, and actual O&M needs are determined.

As small-scale RE-membrane systems are operated with minimal maintenance or chemicals, the operational lifetimes of NF/RO membranes were reported in the range of 1 – 3 y [136, 223, 224], with one membrane manufacturer quoting an operational lifetime of 1 – 2 y for membranes operated at low recovery in the range of 25% with preventative cleaning [45]. Comparatively, membranes in large-scale brackish water RO plants normally exhibit an operational lifetime in the range of 5 – 10 y, with a longer life expectancy in systems with lower feedwater concentrations attributable to less fouling, lower pressure operation, proper chemical dosing, and effective pre-treatment [210, 221]. The MF/UF membranes used as pre-treatment in RO seawater applications are commonly replaced every 5-10 y [225]. Yet, it is anticipated to have a longer membrane lifetime in brackish water desalination. Additional research focusing on understanding membrane lifetime and O&M methods suitable for remote regions for small-scale RE-membrane systems should be performed. Indeed, this constitutes the greatest remaining challenge for such technologies.

2.5.4. Recommendations

The following recommendations for small-scale PV-membrane systems in remote areas are given:

-
- UF as a pre-treatment process to reduce NF/RO membrane fouling is a good precaution and provides a dual barrier to pathogenic water contaminants;
 - Apply lower retention NF membranes to meet drinking water guidelines, and thus conserve energy;
 - To reduce membrane fouling: i) optimize the TMP and initial permeate flux (critical flux) to obtain low recovery; and ii) use simple and low-cost daily physical cleaning methods for membrane maintenance;
 - To target 20 years of system life expectancy: i) select proper NF/RO membranes to aim for 6-10 years of membrane lifetime; then, ii) replace the NF/RO membranes 1-2 times throughout the system's lifetime;
 - Apply in-line conductivity measurement of the permeate to monitor membrane integrity;
 - Employ a constant set-point system operation strategy, while assuring that the system operates within SOW;
 - Perform post-treatment by chlorination, such as chlorine for disinfection.

2.6. Sensors

For research and development purposes, the number of sensors is high, but for systems that are implemented commercially, the number of sensors can be markedly reduced, and the most important selection criteria are to be established individually. Based on previously published reports [9, 35, 98, 226, 227], the selection criteria of sensors, e.g., operating range, accuracy, response time, and chemical resistance, are determined according to the application purposes. The failure modes and effects analysis of components are discussed in detail below.

2.6.1. Flowmeters

In a PV-membrane system, flow meters are used to measure flowrates of the water in the feed, permeate, and concentrate streams. They are the most prone to failure compared to other sensors, as they frequently contain moving parts. Several types of flow meters are currently available. Positive-displacement flow meters measure flow by accumulating a fixed volume of fluid, and then calculating the number of times that the volume is filled. Other flow meters can indirectly calculate flow in terms of forces created by the flowing stream when it overcomes a known constriction. For instance, a differential pressure flow meter calculates the flow by measuring the pressure drop across an obstruction inserted in the flow. The turbine flow meter calculates the flow by measuring the rate of spin of the turbine. An electromagnetic flowmeter calculates the flow by measuring the voltage, which is induced when the water moves through a magnetic field created by energized coils.

In the previous PV-membrane system, the flow meters utilized a pelton wheel-like rotor whose motion is converted by a pickup coil into the output of frequency that is proportional to flow. This flow sensor was

chosen due to its wide operating range, and the ability to measure very low flowrates (down to 16.5 L/h). The greatest challenges with flow meters were encountered during three field trials – in the Australian outback in 2002 and 2005, and northern Tanzania in 2013 – 2014. As the sensors were designed for the application of clean water [228], they are susceptible to failure that is attributable to corrosive brackish water. In particular, the ball bearings inside of the sensor were severely corroded, as the corrosion resistance of SS 440C is similar to that of 304 in many environments [229]. Later, this was replaced with a hybrid bearing consisting of an SS bearing race together with ceramic balls (e.g., silicon nitride), which was more effective in brackish water [230]. The flow sensor is reported to achieve a lifetime of 15 y [231].

2.6.2. Pressure sensors

Pressure sensors are employed for measuring the pressure of water in both the feed and concentrate streams in the PV-membrane system. It has a sensing element of a certain area and reacts to the force applied by water pressure. To notify the operators or initiate automatic safety actions during transient states, the pressure sensors must respond rapidly enough to abrupt pressure changes. Mostly, the response time degrades due to voids and blockages in the sensing lines [232]. The most common failures that occurred are ascribed to mechanical damage, electrical overload, overpressure, pressure spikes, or ingress of moisture/chemicals into the product [233]. To indicate the pressure during the process in commercial RE-membrane systems, analogue pressure gauges are commonly installed at or near the pump's pressure port [234], and as a result, the gauges can fail as a consequence of pipe vibration, overpressure, pressure spikes, corrosive media, clogging, and water condensation [235, 236]. In particular, excessive vibration is the primary source of pressure gauge failures, in which the gauges are not able to accurately read a pointer on a dial during vibration. Ultimately, incremental damage to the pointer mechanism moves the pointer off zero, thus causing inaccurate indications. A surge of media that flows through the pipe affects the pressure gauge when power cycling of pumps or switching on/off of valves occur, thus producing pressure spikes that lead to the damage of gauges. Indeed, the gauge pointer can be bent and eventually ruptured as a result of frequent pegging against the stop pin. The sensing material in gauges can be: i) damaged by corrosive liquids (e.g., salty water) if improper construction materials are used; ii) clogged by suspended particles in the not properly pretreated water, thus making readings unreliable; and iii) damaged with the intrusion of humid ambient air, such that the water accumulates and condenses in the internal parts [235]. High reliability of commercial gauges is attributed to reduced wearing parts, protected internals against corrosive atmospheres, and ultrasonically cleaned and lubricated processes to decrease the influences of harsh environments. Pressure sensors achieve a lifetime of 5-15 y [233].

2.6.3. Water quality sensors

Common sensors that are applied to determine water quality are categorized into electrical conductivity (EC), pH sensors, TOC analyzers, ion-selective electrodes (ISE), and turbidity meters. EC sensors measure electrical conductivity, which is determined by using the distance between the electrodes with a known

surface area. TDS is normally used to calculate the concentration of water as an indicator of water purity. Failures of electrical wiring can occur, such as open circuits, short circuits, and plugging that reduces ion contact with the electrodes [237]. They can also fail to conduct ions across plates (voltage collectors) due to collector plate fouling or scale build-up, which are caused by material degradation, such as corrosion, abrasion, or cracking [237]. EC sensors are reported to have a lifetime of 10 y [238].

A pH sensor measures the hydrogen ion concentration in a liquid, and a differentiated potential is formed between the electrode and solution, which is directly proportional to the pH value. The possible failure modes of pH sensors are probe cracks or breaks caused by brittle glass, and electrode breakage (open circuit) due to material flaws or insulation flaws (short circuits). The expected lifetime of the pH sensor is reported to be 1-3 y [239]. TOC analyzer detects CO₂ produced by organic matter oxidation at high temperature through a catalytic oxidation combustion technique. It is used for measuring organic matter, primarily contributed by NOM, such as humic substances and partially degraded animal matter [240]. It is also one of the indirect methods to monitor membrane integrity. In addition, the TOC analyzer may report false-negative TOC results when too much dissolved oxygen is removed [114]. In most cases, TOC has an expected lifetime of 10 y with regular replacement of ultraviolet lamps every 2 y [241]. An ISE is used for measuring the concentration of a specific ion in water, such as fluoride or silver ion (Ag⁺), which responds selectively towards one or several specific ions [242]. Measurement errors can occur, as ISE could be far more sensitive to the interfering ions than to the primary ions, and therefore it is necessary to first remove the interfering ions to guarantee accuracy [242]. The typical lifetime of ISE is 2-5 y [116]. A turbidity meter is employed for determining true turbidity and suspended solids in water with a nephelometer or absorptiometer to measure the scattered light or absorption of light intensity [243]. The LED is expected to have a typical lifetime of 10 y [244].

2.6.4. Temperature sensors

Resistance temperature detectors (RTD) and thermocouples are the two most common temperature sensors employed in commercial RE-membrane systems. They are used to monitor the temperature of the feed water because the membrane flux changes with temperature with a rate of up to 3%/°C [245]. Open circuits and short circuits are the typical failure modes of RTD due to their structure [237]. A short circuit to the ground can occur when a metallic or conductive sheath is used. In addition, calibration shifts can appear due to oxidation, metal ion migration from the sheath to the sensing element at a higher temperature than 500 °C, and electrical insulation resistance changes attributable to moisture [246]. Other failures exist, such as drift, which is more of a problem for thermocouples than RTDs. The drift is resultant from a change in the metal chemistry, excessive heat, work hardening of the wire (by vibration or bending), contamination (from chemicals or moisture), or ionizing radiation. Chemical or moisture contaminations can produce a corrosive attack on the wires and then pass through the sheath by osmosis, thus penetrating cracks in the sheath, or by cross-contamination between the individual wires and the sheath.

In RE-membrane applications, rapid temperature changes are not expected to be encountered, and the temperature sensors can have a lifetime of 10 to 20 y [232].

2.6.5. Recommendations

To determine the transient nature of the PV-membrane system accurately when directly subjected to fluctuating power, the following suggestions are provided:

- i) Take care of the selection criteria of the sensors – in the sequence of operating range, accuracy, response time, chemical resistance, and cost – in order to ensure system performance at any point in time;
- ii) Flow, pressure, and EC sensors are paramount to assure reliable system operation;
- iii) A magnetic inductive flow sensor is recommended, as it contains fewer moving parts, low maintenance requirements, 15 y lifetime, and high reliability. However, it requires slightly higher costs.

2.7. PV-membrane brackish water desalination system

2.7.1. System performance

To allow comparisons, small-scale systems are generally defined as the motor power rating < 1.5 kW with permeate capacity < 3 m³/d. The combination of NF/RO membranes and PV modules for brackish water desalination has been implemented most frequently in RE-membrane systems [247]. Details of small-scale PV-membrane brackish desalination systems (1000-10,000 mg/L) are summarized in Table 2-5.

Table 2-5: Overview of some existing outdoor small-scale (motor power rating < 1.5 kW, permeate capacity < 3 m³/d) PV-membrane brackish desalination systems for drinking water, illustrating the different configurations, operating conditions, and system performance. Adapted from [65], CC BY-NC-ND 4.0 License.

Location	Feed TDS (mg/L)	Production (m ³ /d)	PV size (kW _p)	Pump type	Motor power (kW)	TMP (bar)	SEC (Wh/L)	Retention (%)	Recovery (%)	Ref.
White Cliffs, Australia	3500	0.5	0.34	Rotary vane	0.15	5 – 10	2 – 8	93 – 95	20 – 22	[9]
Perth, Australia	5000	0.4	0.12	Piston	–	2 – 12	–	84	16 or 25	[248]
Pine Hill, Australia	5300	1.1	0.3	Helical rotor	0.3	4 – 12	2.3	98	28	[226]
Perth, Australia	2000 – 4000	0.5 – 1.0	1.20	Positive displacement	0.25	–	4.0 – 5.8	83 – 88	17 – 20	[249]
Lisbon, Portugal	1200 – 3200	0.02	0.1 – 0.15	Diaphragm	–	3.3 – 4.2	25.6	94	< 2.4*	[250]
Bangi, Malaysia	2000	5.1	2	Rotary vane	0.6	15	1.1	97*	–	[200]
La Mancalona, Mexico	2100	1	400	High pressure	75	6	0.2 – 2	99	33	[251]
Amman, Jordan	400	0.1	0.07	High pressure	0.025	–	–	96	–	[252]
Hammam Lif, Tunisia	2800	0.05	0.59	–	–	–	22.8	–	–	[253]
Marseille, Mexico	8000 – 22000	~ 1	1.03	High pressure	–	–	4.3*	95	–	[60]
Jordan	1700	0.28	433	Diaphragm Centrifugal	–	6	16	94	54	[254]
Coite-Pedreiras, Brazil	1200	6	1.10	High pressure	1.5	8.3	3.0	85 – 99	27	[255]
Cairo, Egypt	2000	1.0	1.07	Booster	0.375	–	4 – 5.2	–	50	[256]
Saudi Arabia	400 – 500	0.4 – 0.7	0.25	High pressure	–	–	–	75*	–	[257]
Tanzania	3000 μS/cm	2.4	2.25	Helical rotor Centrifugal	0.75	6	4.4	83	12	[258]
Jordan	7000	2 – 7	1.1	High pressure	–	–	2	–	–	[259]
St. Dorcas, Tanzania	3632	1.3 – 1.6	0.3	Helical rotor	0.3	4.8	1.6 – 1.9	> 97	23 – 28	[260]

Note: (*) calculated by current authors; (–) not specified results.

In RE-membrane systems, power from the RE resource is required to drive a pump to raise the feed-water pressure to pass through the membrane system. The required pressure is highly relevant to the design of the RE-membrane system, as well as the characteristics of the feed water. SEC is one of the most important criteria to determine the feasibility of these systems, which indicates the required power to achieve permeate water flux through the membrane surface. The SEC needs to be as low as possible to provide maximum water production with minimum energy requirements; therefore, it is also one of the key factors for compared overall system performance.

As shown in Table 2-5, the SEC exhibits a very wide range, which highlights the importance of the overall system design and operating conditions of the PV-membrane system. For instance, Joyce et al. [250] used a 12" long spiral-wound RO membrane (MP-TA50-J4) coupled to a 12 Vdc diaphragm pump connected with a 100 –150 Wp PV array. The system was capable of producing 20 L/d of permeate, but at a very high SEC at 25.6 Wh/L. The high SEC resulted from the small size of the PV-membrane system, which was designed to operate at relatively low pressure (3.3 – 4.2 bar) and flowrate (140 – 200 L/h), resulting in a very low recovery of < 2.4%. As a consequence, 97% of the energy presented to the membrane got lost in the concentrate stream and needle valve. Moreover, the high SEC associated with small-scale membrane systems was caused by energy losses of components throughout the systems. The present authors have also observed a significant reduction in the SEC simply due to scaling-up the size of the system components, going from a system based on ¼" diameter tubing [9] to ½" diameter stainless steel pipe [199, 226]. In addition, the power requirements depend on recovery, pressure, and thus salt concentration. The minimum SEC varies from 2.3 Wh/L at a feed concentration of 1000 mg/L to 26 Wh/L at a feed concentration of 7500 mg/L [9].

Another important step in the design process is to determine the most appropriate membrane in terms of feed water quality. This fact was already highlighted by a performance comparison of four 4" diameter NF/RO membranes (BW30, ESPA4, NF90, TFC-S) on a brackish (5300 mg/L) bore in a PV-membrane system [199]. It was concluded that for this specific test site with 5300 mg/L feed water, the ESPA4 membrane was the optimal choice. Other membranes were able to produce better quality water, but with a higher SEC (BW30, NF90); whereas, the TFC-S membrane was not able to fulfil the recommended drinking water guidelines.

Operating pressure has a significant impact on energy consumption, as well. The higher operating pressure requires a larger pump and RE supply, indicating that the design criteria of the RE-membrane system operating in remote areas is different from conventional membrane plants. The most important factors are energy requirements and robust long-term operation, other than designing to achieve maximum water flux in terms of pressure, recovery, and retention.

Table 2-5 shows that diverse system combinations result in markedly different system performance, in particular the SEC exhibits the most important criteria to determine system performance, thus highlighting the significance of investigating different system configurations.

2.7.2. System reliability

As new technological developments have occurred in the past few years, including the improvement of pump performance and efficiency, the use of brushless DC motors, and power electronics components, such as MPPTs, controllers, and inverters, the reliability and robustness of PV-membrane systems have been largely improved [80]. Although statistics on reliability and failure modes are rarely reported, some information can be obtained from PV-powered water pumping programs that have been implemented worldwide. In an early PV water pumping program in Mali [80] from 1983 to 1989, 66 systems were monitored, and 37 failures were recorded. This corresponded to a mean of one failure in 139 pumping months (an MTBF of over 30,000 h). In another pumping program in Thailand, PV-powered water pumping systems were installed in 1,000 rural villages in 1999, and 45% of the systems (489 units totally) were either damaged or inoperable after 5 y of installation [261]. A 3-y survey suggested that over half of the failures were due to inverter failures (19%) and motor-pump failures (32%) [261].

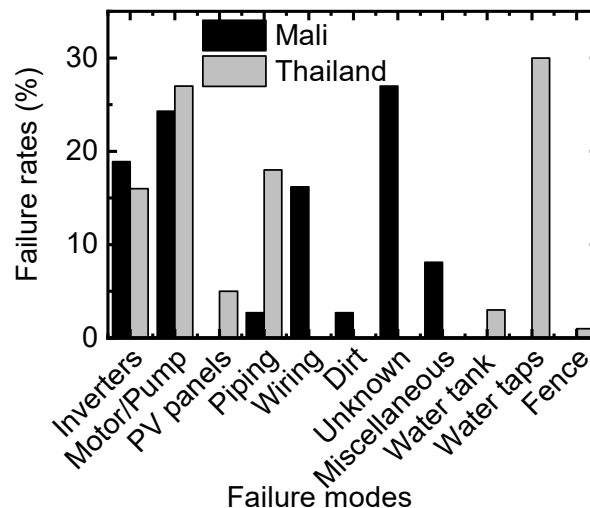


Figure 2-9: Failure rates and mechanisms of PV water pumping programs in Mali (1983 – 1989) and Thailand (1999). Adapted from [65]. CC BY-NC-ND 4.0 License.

The broad range of possible failures is indicated in Figure 2-9. Apart from inverter failures and pump motors breaking down, the remaining failure modes typically constituted structural or infrastructure problems, including leakages (water tanks and taps) and drying-up of seasonal water sources. The cause of a relatively high amount of failures (27%) in Mali is still unknown, thus highlighting the significance of accurate monitoring and data collection.

2.7.3. System operation and maintenance

Maintenance of RE-membrane water pumping systems ranges from preventive maintenance, predictive maintenance, to corrective maintenance [128]. Preventive maintenance, based on the manufacturer's recommendations, is critical for efficient and trouble-free operation, as it aims to prevent unanticipated

component failure. A proper protocol of preventive and routine maintenance will decrease component failures, extend system lifetime, and reduce overall operating costs.

Predictive maintenance is conducted in terms of data analysis collected during the monitoring of system performance, noise, vibrations, and temperature of motors. For instance, water leakage may indicate that the mechanical parts might need a replacement; bad bearings and shafts may be in a state of non-alignment; vibration may indicate the beginning of a failure; and overheating of motors may indicate mechanical overload, bad bearings, or insulation failure of the motor windings.

Corrective maintenance can be markedly reduced if preventive and predictive maintenance is well implemented. Whereas, some routine corrective protocols can be scheduled, such as: correction of small leakages at pipes or connections, in particular where high pressure or screw connections exist; replacement of membranes as a result of fouling; and replacement of damaged power conditioning devices or rusted metallic components.

2.7.4. Recommendations

It is important to select reliable components and optimize their combination to achieve a robust system design that adapts to local applications, and thus the following recommendations are given:

- i) Couple the pumps directly to the RE energy supply without AC to DC converting or inverting to obtain higher efficiency and reliability;
- ii) To avoid potential problems encountered in a directly-coupled system ascribed to frequent system shut-downs, apply SCs to buffer short-term fluctuations to reduce system re-starts and Li-ion batteries to provide energy for hours of operations;
- iii) Employ UF pre-treatment to extend the lifetime of the NF/RO membrane, and perform regular maintenance to improve overall system robustness and reliability.

2.8. Summary

For a well-designed small-scale PV-membrane system with a targeted 20 y lifetime, reliable components are selected with the following recommendations:

- i) Silicon-based PV panels – 25 y of warranty supported;
- ii) Brushless DC motor - a lifetime of 20 y can be realized with limited O&M;
- iii) Helical rotor pump - a target 20 y lifetime can be achieved with O&M.

Less reliable components should be avoided or replaced periodically:

- i) DC-AC inverters should be avoided in order to reach 10 y lifetime via consistent O&M and occasionally replacement of components (e.g., capacitors, transistors);

ii) NF/RO membrane should be replaced in order to target a lifetime of 6–10 y via system operation with recovery less than 30%, and realize soft starts with the increase of feed pressure less than 0.7 bar/s;

iii) Sensors should be replaced to achieve 5–15 y lifetime with O&M, such as cleaning of the electrode or wet parts.

3. Materials and methods

3.1. Photovoltaic powered membrane system overview

A new bench-marked PV-membrane system for brackish water desalination was designed by the author and used for laboratory-scale experiments. Based on the requirements of permeate water production (approximately 1 m³/d) and SEC (1 – 4 Wh/L), the system is designed with 1/2" diameter SS316 pipes at a low recovery of less than 30%. In particular, the wetted parts in the system are selected to be SS316 to improve the system's reliability and robustness. The system controls, including charge controller and backwash control, were implemented to make the best use of available power, as well as extend the lifetime of the system. The details are described in the following sections.

The system was mounted on the Bosch profile, as shown in Figure 3-1. The main components of the membrane system, including the SS tank, helical rotor pump, membrane housing, sensors, and backwashing setup, are illustrated in Table 3-1.

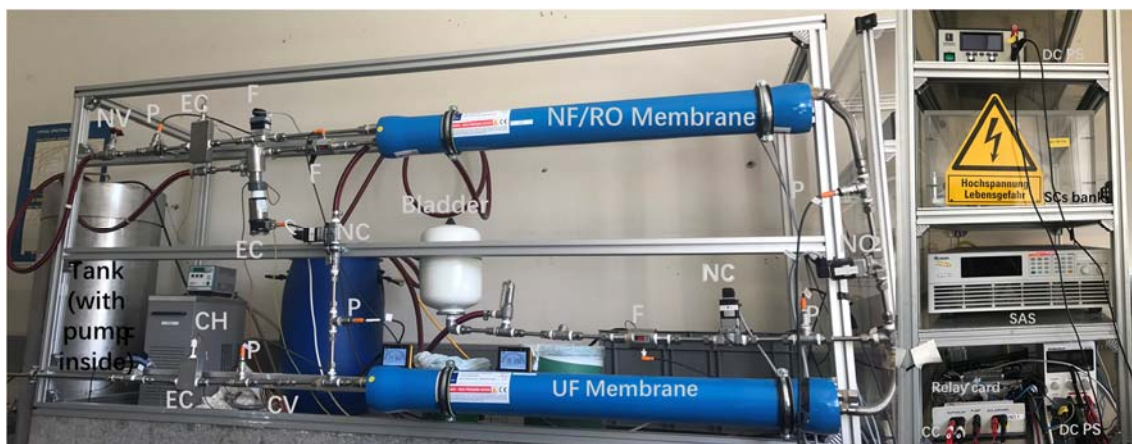


Figure 3-1: Photograph of the bench-mounted PV-membrane system in the laboratory at KIT. Note that the abbreviations of the main components can be found in Table 3-1.

Table 3-1: Abbreviations of the main components included in the PV-membrane system.

UF	Ultrafiltration	EC	Electrical conductivity	NV	Needle valve
NF/RO	Nanofiltration / Reverse osmosis	F	Flow sensor	NO	Normally open
SAS	Solar array simulator	P	Pressure sensor	NC	Normally close
CC	Charge controller	CH	Chiller	CV	Check valve
RC	Relay card	PS	Power supply for sensors and valves		

3.1.1. System descriptions

A diagram of the PV-membrane system illustrating the main components, and the location of the sensors and valves, is shown in Figure 3-2. The filtration system is based on a helical rotor pump (Grundfos SQFlex 0.6-2 N) driven by a DC motor, which draws water through the UF membrane before pumping it through the RO membranes at up to 15 bar. The motor is able to operate over a wide range of 30 to 300 V_{dc}, with a maximum current of 8.4 A, and input power of 1.4 kW. It is worth noting that this pump/motor combination includes a built-in MPPT, which can always extract the maximum power from the energy resources (PV and energy storage units). The backwashing functionality is achieved by either the bladder tank (comfort MAG-W) or the second BW pump via a series of controlled solenoid valves (detailed in Section 3.6). An eight-channel relay card (Conrad 8-channels) was implemented to control the switching of the valves and the filtration pump. The UF permeate water is flushed back to the UF membrane to reduce membrane fouling. In addition, the electrical configurations of the Li-ion batteries and SCs are further extended for comparison of the energy storage options in the PV-membrane system. Note that the charge controller (labelled as 1) was designed in-house as discussed in Section 3.5, while the other charge controller (labelled as 2) was used for the battery setup as detailed in Section 3.4.2.

In this research, a 4" multibore UF membrane (DuPont dizzer P4040-6.0, membrane area: 6 m² [262]) for pretreatment and one 4" spiral wound RO membrane (DuPont Filmtec BW30-4040, membrane area: 7.2 m² [45]) for desalination were used. The UF membrane was used to remove viruses, colloids, and organic macromolecules as a pretreatment so that it can protect the RO membrane from fouling. The RO membrane was chosen to remove monovalent ions (Cl⁻) in the feed water, so that the permeate water complies with a target value of 1000 mg/L NaCl taken from the WHO, where it is noted that drinking water becomes unpalatable at higher values [263].

A solar array simulator (SAS, Chroma 62000H) was used to simulate the PV power output to allow for the system operation (additional details in Section 3.3). All membrane performance parameters – transmembrane pressure (TMP), flux (J), recovery (Y), retention (R), and SEC – were calculated using well-defined relationships for the previous system [264, 265]. The details are discussed in Section 3.2.

The following sensors – flow, pressure, and EC sensors – are implemented in the system to measure the transient operations under fluctuations and intermittencies. All of the outputs from the sensors were recorded through a data acquisition card (National Instruments, DAQ 6299), and a LabVIEW interface was developed to monitor the instantaneous system performance and output the data. The types and locations of the sensors are provided in Table 3-2. A chiller (Julabo, FC600) was connected with a double-wall stainless steel tank (SS316, volume of 250 L) to maintain the feedwater temperature at 20 ± 0.5 °C. The permeate and concentrate streams were recycled back to the feed tank to keep the salinity of the feed water constant throughout all of the experiments.

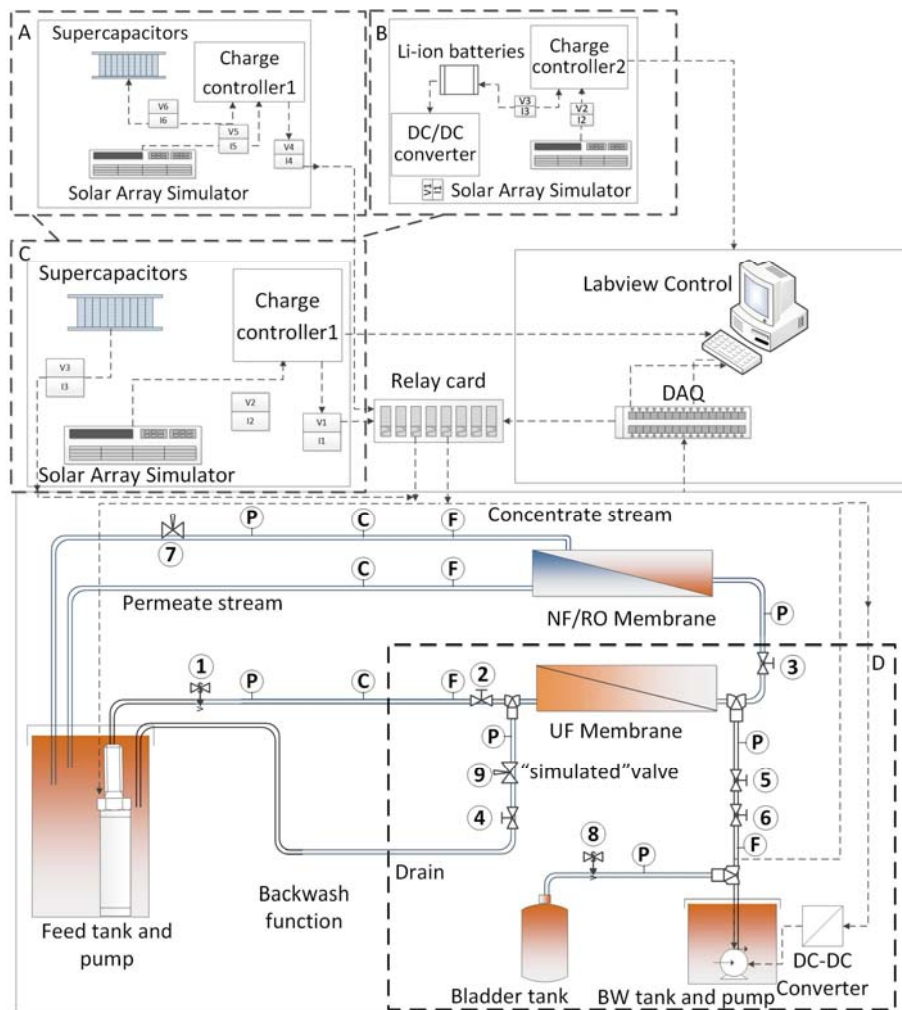


Figure 3-2: Schematic of the PV-membrane system equipped with two electrical energy storage options (A, B), as well as two backwashing configurations (C, D), illustrating: A) supercapacitors; B) Li-ion batteries; C) a BW pump powered by SCs immersed in the BW tank; and D) a bladder tank. The light dashed lines indicate electrical connections, while the bold dashed lines highlight the UF membrane and the components needed for realising the BW function. P, C and F represent the pressure, conductivity and flow sensors. Note that the directly-coupled system is configured by connecting the SAS to the pump, and the change among the different configurations is manually switched. The key valves in the system are labelled as ①, ⑧: safety valves; ②: check valve; ③: normally-open valve; ④, ⑤, ⑥: normally-closed valves; and ⑦, ⑨: needle valves. Adapted from [266], CC BY-NC-ND 4.0 License.

Table 3-2: Specifications of the sensors employed in the PV-membrane system, illustrating the types, locations, and performance parameters. The specific location of the sensors can be found in Figure 3-2.

Parameters	Location	Manufacturer (Type)	Model	Operating range	Uncertainty	Ref.
Flowrate	Feed Concentrate	Bürkert paddle-wheel	8030	50 – 2000 L/h	0.5	[267]
	Permeate Backwash	IFM magnetic- inductive	SM6000	5 – 1500 L/h	0.5	[268]
Pressure	Feed Before NF/RO After NF/RO UF concentrate UF permeate	Bürkert	8316	0 – 16 bar	0.25	[269]
EC	Feed Concentrate	Georg Fischer	Signet 3-2822	100 μ S/cm – 200 mS/cm	± 2	[270]
	Permeate	Bürkert	8222	0.05 μ S/cm – 10 mS/cm	± 3	[271]
Current	After SCs, pump and batteries	Omega	DRF-IDC	0 – 5 A	0.3	[272]
Voltage	After SCs, pump and batteries	Omega	DRF-VDC	0.06 – 650 V	0.3	[273]

The main control strategies in the PV-membrane system include: i) the power input of the filtration pump via SAS; ii) the back-pressure needle valve on the concentrate stream to create the back pressure; iii) the charge controller to manage the power distribution between the PV and SCs; iv) a series of solenoid valves to control the backwash of the bladder tank and pump powered by SCs; and v) the relay card to control the solenoid valves, shut-down of the feed, and backwash pump.

3.1.2. Helical rotor pump and motor

The helical rotor pump was used in the PV-membrane system, as it was designed for continuous, as well as intermittent, operation based on renewable energy (RE) sources [274]. This pump used an eccentric single-helix-shaped metal rod as a rotor sealed within a thick rubber stator, and the small gap between these forms the progressive cavity, resulting in water being expelled [133]. The pressure created by the pump is in proportion to the length of the rotor and stator [133]. To avoid dry running, a water level electrode was placed on the motor cable 0.3 – 0.6 m above the pump, which measured the contact resistance to the motor sleeve through the water. The pump will be cut out either when the water level falls below the water sensor,

or when the tank is filled with water with a conductivity of $< 70 \mu\text{S}/\text{cm}$. The pump will automatically cut in again after 5 min if the water level is above the water level electrode.

The motor (MSF 3N with material SS316) has been developed for this SQFlex pump based on the PM principle along with a built-in microprocessor-based MPPT. It is worth noting that the built-in MPPT allows the pump duty point to be continuously optimized regarding the input power available. The motor has a maximum power input of 1.4 kW, with a speed range of $500 - 3600 \text{ min}^{-1}$, over a broad voltage range from $30 - 300 \text{ V}_{\text{dc}}$ and a maximum current up to 8.4 A [274]. This motor can be powered with alternate current voltage (single phase, $90 - 240 \text{ V}$, $50/60 \text{ Hz}$), as well. In this case, the pump is supposed to be operated with slow variations, and thus the rapid change of voltage (e.g., rectangle waves) could potentially damage the built-in electronics due to the pulsed current peak. To prevent burnout of the motor, the motor will automatically compensate by reducing speed. The motor will cut out for 10 s if the speed falls below 500 min^{-1} , prior to attempting to restart the pump.

3.1.3. Set-point operation strategy

The set-point operation strategy was established in previous work to obtain high flux and low SEC within the SOW [264]. In this work, this method was used to conduct the experiments throughout, which was achieved by regulating the needle valve (valve ⑦ in Figure 3-2) on the concentrate stream at 10 bar. The descriptions of the system operation on real solar days, at varied feed salinity and PV power capacity are detailed below.

i) Set-point operation strategy on real solar days at a feed salinity of 5 g/L and a rated PV of 500 W

- Prepare the feed water solutions (e.g., 5 g/L NaCl);
- Set the voltage and current values from SAS (steady-state values), $V = 180 \text{ V}$, $I = 2.8 \text{ A}$, press the “on” button;
- Start the LabVIEW program;
- Regulate the needle valve to obtain a 10 bar set-point at a feed flowrate of 420 L/h;
- Stop SAS and LabVIEW;
- Feed the solar irradiance curves together with temperature in SAS;
- Select the Excel sheet number, column / row of SI, and column / row of temperature;
- Press “load” and return to the main interface;
- Set the SAS values to $V_{\text{mp}} = 500 \text{ W}$, $I_{\text{mp}} = 188 \text{ V}$, $\text{FF} = 0.75$, $\beta = -0.41\%/^{\circ}\text{C}$;
- Choose the “Sandia model”, and set the initial time to 30 s and time interval to 1 s;
- Start the experiment.

ii) Set-point operation for different feed water salinity by using the rated PV of 500 W

- Prepare the feed water solutions;
- Set the $V = 180 \text{ V}$, $I = 2.8 \text{ A}$ values from SAS;

- Regulate the needle valve to 10 bar while observing the pressure value in LabVIEW to reach a stable state;
- Stop SAS and LabVIEW;
- Start the experiment.

iii) Set-point operation for varied PV power capacity by using the same feed water salinity

- Set the $V = 180$ V, $I = 2.8$ A values from SAS;
- Regulate the needle valve to 10 bar while observing the pressure value in LabVIEW to reach a stable state;
- Stop SAS and LabVIEW;
- Start the experiment.

3.2. Feed water and membrane

3.2.1. Feed water preparations

In this research, the synthetic feed water applied was prepared via deionized (DI) water (BWT Moro 350, Germany, $EC = 15 \mu\text{S}/\text{cm}$) and 5 g/L NaCl (> 99%, Sigma-Aldrich, general-purpose grade) to facilitate the comparison with previous results. The NaCl concentration (g/L) was calculated from EC ($\mu\text{S}/\text{cm}$) with a conversion factor $k = 0.59$ that was measured in deionized water at 20 °C. In addition, different feed water quality was varied for different purposes. For the experiments conducted in Section 5, other feed salinities (1, 2.5, 7.5, and 10 g/L NaCl in Section 5.3) were prepared to determine the impacts of varied salinity on the ability of the charge controller to reduce system shut-downs and enhance resilience.

For the experiments conducted with UF backwashing (see Chapter 6), bentonite (Clariant Tixoton, median particle size of 500 nm, particle to pore size ratio of 25, see Figure 3-3) was added to the 5 g/L NaCl feed water as a cake foulant at concentrations of 100 (36 NTU) and 300 mg/L (100 NTU), respectively. It is worth noting that while real brackish water is typically not turbid, synthetic water with bentonite was used to study the implementation of UF membrane backwashing, and evaluate the energy consumption of both RO desalination and UF backwash (BW) processes.

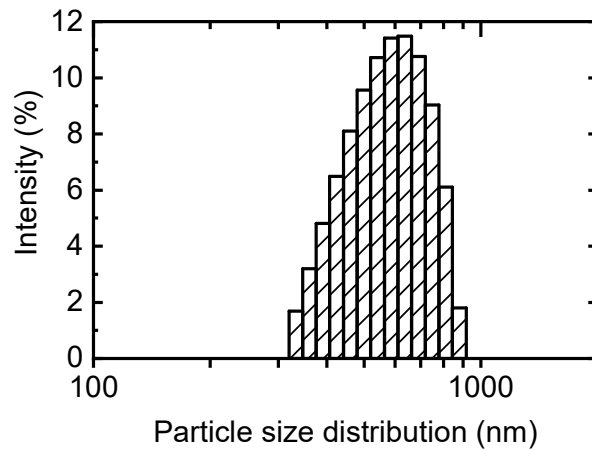


Figure 3-3: The dynamic light scattering measurement of bentonite powder dispersed in saline water solution (NaCl 5 g/L), illustrating the size distribution of the particles. The intensity is the relative frequency intensity weighted, representing how often the particle size distributes in the region. Adapted from [266], CC BY-NC-ND 4.0 License.

In order to calculate the observed bentonite mass (starting NTU = 100, 60 g), the turbidity of the samples (three taken at each cycle) was measured by a turbidity meter (calibration curve provided in Figure 3-4). Three samples were taken from the same positions of the feed tank (200 L) at the end of filtration cycles 1, 2, and 3, assuming homogenous mixing of the bentonite suspensions.

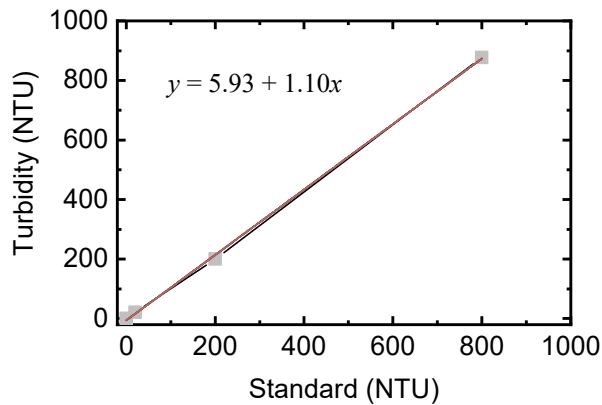


Figure 3-4: Calibration curve of the turbidity meter using standard solutions. Adapted from [266], CC BY-NC-ND 4.0 License.

A recirculating pump (Pentair Jung pump U3KS/2) and an air bubbler (Nitto LA-120, airflow of 120 L/min) were both used to mix the water in the feed tank. The mixing was started prior to adding bentonite to the feed tank, and remained running continuously throughout all of the experiments. In order to ensure the same feed water concentration, a new batch of 200 L feedwater (5 g/L NaCl) was freshly prepared prior to each experiment, avoiding issues of the bentonite settling at the bottom of the feed tank. An

overall system cleaning protocol was implemented at the end of each BW experiment as follows: i) reconnect the filtration pump to the outlet of the UF membrane module; and ii) back flush the UF membrane and feed stream using the filtration pump and DI water (flowrate of approximately 500 L/h) for 1 h to remove the remaining foulant, thus ensuring the same conditions for all of the experiments. The back flush (for system cleaning purposes) was ended when the water turbidity passing into the drain reached the same value as the feed tank water (normally achieved around 20-30 min, depending on the fouling rate of UF membrane). To avoid dry running of the filtration pump, the DI water was continuously filled to the feed tank, and the wastewater was discarded to the sink. Note that energy consumption during system flushing is not included.

3.2.2. Membrane modules

As discussed in Section 3.1.1, the PV-membrane system is equipped with a UF pretreatment membrane and a RO membrane. The choice of the RO membrane module is determined by the characteristics of the feedwater and the contaminants that are required to be removed. In this case, the contaminants referred to are monovalent ions (Na^+ , Cl^-). The RO membrane (BW30) was used through the experimental work to permit comparisons of system performance, as done in previous study [98, 275]. The membrane performance parameters (flux, TMP, retention, recovery, and SEC) were defined in the following well-known relationships [199, 226], as shown in Eq. 3-1 to Eq. 3-5:

$$J = \frac{Q_p}{A}, \quad \text{Eq. 3-1}$$

where J is the flux; A is the membrane active area (m^2); and Q_p is the permeate flowrate (L/h).

$$TMP = \frac{(P_{inter-vessel} + P_C)}{2} - P_{permeate}, \quad \text{Eq. 3-2}$$

where TMP is the transmembrane pressure of the RO membrane (bar); $P_{inter-vessel}$ is the pressure after UF membrane (bar); P_C is the pressure in the concentrate stream (bar); and $P_{permeate}$ is the relative pressure of permeate side (0 bar).

$$R = \left(1 - \frac{EC_P}{EC_F}\right) \cdot 100, \quad \text{Eq. 3-3}$$

where R is the recovery (%); EC_P is the electrical conductivity of permeate ($\mu\text{S}/\text{cm}$); and EC_F is the electrical conductivity of feed ($\mu\text{S}/\text{cm}$).

$$Y = \left(\frac{Q_P}{Q_F}\right) \cdot 100, \quad \text{Eq. 3-4}$$

where Y is the retention (%); Q_P is the flowrate of permeate stream (L/h); and Q_F is the flowrate of the feed stream (L/h).

$$SEC = \frac{P_{pump}}{Q_p}, \quad \text{Eq. 3-5}$$

where SEC is the specific energy consumption (Wh/L); and P_{pump} is the electrical power of the pump motor (W).

3.3. Solar array simulator and solar days

An SAS was used to simulate the output from silicon PV panels, which enabled repeatable experiments in a laboratory environment, and such that different system configurations can be compared. The specifications of PV modules – V_{mp} (maximum power voltage), P_{mp} (maximum power), fill factor (FF), and temperature coefficient (β) – along with the SI were employed as inputs to the SAS. The SI data were converted to a current-voltage curve via the built-in Sandia formula, and the available PV power is calculated accordingly by using Eq. 3-6 [276]:

$$P = P_{REF} \cdot \frac{SI_{rr}}{SI_{rrREF}} \cdot \left[1 + \frac{\beta}{100} \cdot (T - T_{REF}) \right], \quad \text{Eq. 3-6}$$

where P represents the PV power (W); SI_{rr} expresses the solar irradiance (W/m^2); β represents the temperature coefficient of a silicon PV module ($-0.41\%/^{\circ}C$); T is the cell temperature ($^{\circ}C$); T_{REF} is the reference array temperature at $50^{\circ}C$; and SI_{rrREF} is the reference irradiance of $1000 W/m^2$.

Three different settings of PV modules based on the power requirements were applied in this research: i) to study the impacts of ramp rates in PV voltage on the PV-membrane system, 350 W simulated output ($P_{mpp} = 350 W_p$, $V_{mp} = 188 V$, $I_{mp} = 1.9 A$) was sized to match the system, such that sufficient power was guaranteed to start and run the pump efficiently while charging the SCs under high SI ($1000 W/m^2$); ii) to evaluate system performance with SCs and electrical control, as well as backwashing functionality, under real solar days, five 100 W PV modules (Sunmodule SW100 Poly) were connected in series to have a rated power capacity of 500 W ($P_{mpp} = 500 W_p$, $V_{mp} = 188 V$, $I_{mp} = 2.7 A$) [277]. A high system voltage at maximum power point ($V_{mp} = 188 V_{dc}$) was realized via these PV configurations, as well as charging the SCs; iii) to assess the impacts of the PV power capacity in improving system resilience, and reduce system shut-downs with SCs and charge controller, the PV power capacity (300, 400, 600, 800, and 1000 W) was varied via maintaining the same PV voltage ($V_{mpp} = 188 V$) and adjusting the photocurrent (I_{PV} varied from relatively 23% lower to 100% higher compared with the results above); and iv) to investigate system performance when equipped with Li-ion batteries, the same rated PV capacity at different voltages is set in the SAS for further comparisons, i.e., $P_{mpp} = 500 W_p$, $V_{mp} = 75.2 V$, and $I_{mp} = 6.6 A$. The FF (0.75) and β (-0.41%) remain the same values for all three settings. It is worth noting that the PV settings for batteries were based on those used for previous SC experiments; however, here the PV was scaled up by 25%, so that the higher current can be achieved, and the voltage was maintained. Therefore, four PV panels were connected in series to achieve 500 W output power. The SAS combines all of these parameters to define the PV output power throughout real solar days.

Real SI data in different days were used to determine the performance of the PV-membrane system both with and without SCs and charge controller in a real solar environment over 7 – 12 h. The SI data with high-temporal-resolution (1 s) were obtained from the KIT Solar Park in Karlsruhe (Germany, latitude: 49°00'33.73" N, longitude: 8°24'15.98" E), representing different levels of fluctuations in real weather conditions, i.e., sunny (05 May 2016), partly cloudy (26 May 2016), and very cloudy days (13 Oct. 2016), as described in Figure 3-5.

The module temperature data and actual available power from the PV panels are presented for further comparisons. It is important to note that the measurements can be slightly different from the real weather conditions, as dust or shadows on the PV panels might occur. On the partly cloudy day, eight sharp drops in SI occurred in the periods around 11:00-12:30 (labelled ① – ⑧ in Figure 3-5B). The fluctuations in SI in this 90-min window were typically from seconds to minutes. The SI on the very cloudy day exhibited periods of large fluctuations, as heavy clouds were passing from 7:30 to 14:30, and subsequently the low SI dropped steadily from 14:30 to 15:30. The sunny day exhibited an overall shining day, and showed a typical SI ranging from 100 to 900 W/m². It can be seen that the SI does not reach 1000 W/m² due to the season in this latitude and the temperature exceeding 25 °C (see Figure 3-5D).

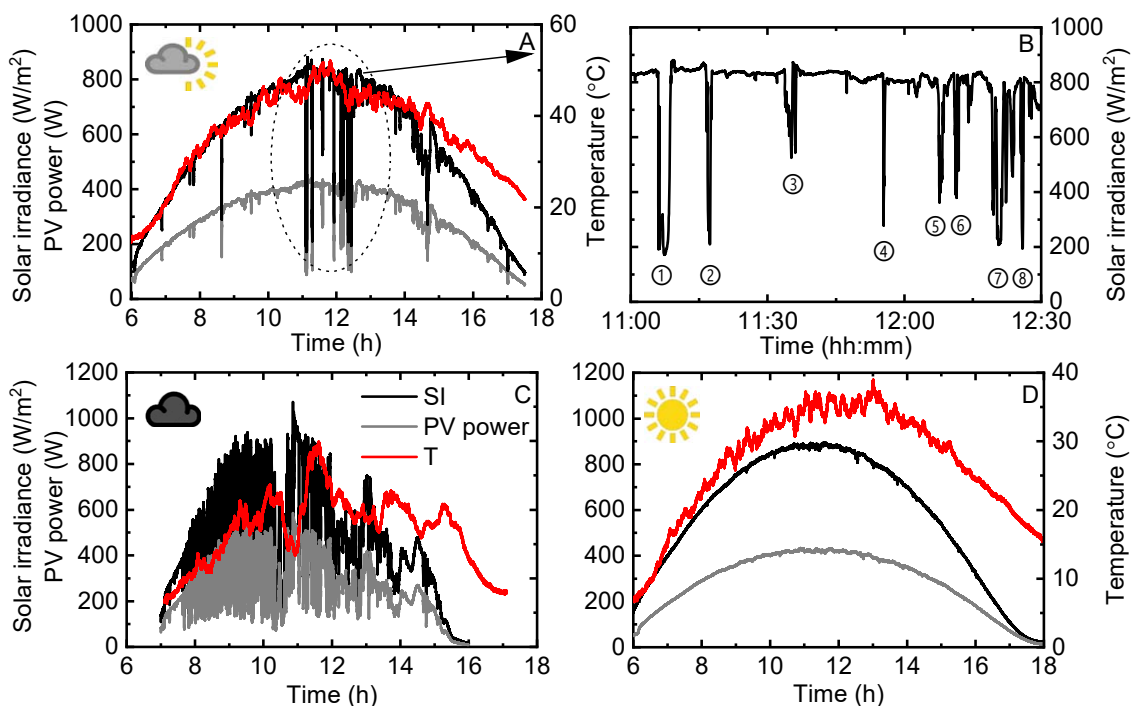


Figure 3-5: Graphs showing the variation of the amount of sunlight (black curves are plotted as solar irradiance), the real available PV power (grey curves), and temperature (red curves), as a function of time (A) on this partly cloudy day at the KIT Solar Park (26 May 2016); (B) eight large fluctuations from 11:00 to 12:30 during the middle of the day; (C) very cloudy day (5 May 2016); and (D) sunny day (13 Oct. 2016). The peaks of fluctuating SI are numbered from ① to ⑧. Adapted from [122], CC BY-NC-ND 4.0 License.

3.4. Energy storage units

3.4.1. Supercapacitor energy buffering

The motivation of using SCs as energy storage units for the PV-membrane system to buffer solar fluctuations and intermittency was elaborated in Section 2.3. In this research, 12 modular SCs (Maxwell Boostcap 15 V_{dc}, 58 F) were connected in series to achieve a maximum voltage of 180 V and capacitance of 4.8 F. This voltage limit was selected as it was approaching the V_{mp} of PV modules, which determines the maximum charging voltage and the sizing of the SCs according to the rated module voltage (15 V_{dc}). To bridge the short-term power gap on the order of a few minutes (Δt) over the voltage difference (ΔV), the capacitance of the SCs was given by Eq. 3-7:

$$C_{bank} = \frac{\Delta t \cdot I_{avg}}{\Delta V - I_{avg} \cdot R_{bank}}, \quad \text{Eq. 3-7}$$

where R_{bank} and I_{avg} represent the resistance and average discharging current of the SCs bank, respectively. The amount of energy (Wh) stored in the SCs was directly proportional to the voltage squares (V_{SC}) and capacitance (C), as provided by Eq. 3-8:

$$E = \frac{1}{2} \cdot CV_{SC}^2, \quad \text{Eq. 3-8}$$

The SOC is a useful indicator to evaluate the available energy as a percentage of the SC bank's maximum energy capacity, which is given by Eq. 3-9:

$$SOC = \frac{V_{SC}^2}{V_{SC_{max}}^2}, \quad \text{Eq. 3-9}$$

where V_{SC} is the voltage for the SCs bank; and $V_{SC_{max}}$ is the maximum voltage of the SCs bank (180 V_{dc}).

In general, there is no lower operating threshold for the SCs, which can be fully discharged. However, the limit of the charge controller constrained the minimum voltage to 30 V_{dc} that corresponded to 3% minimum SOC, and the maximum voltage to 177 V_{dc} that was equivalent to 97% maximum SOC to avoid overcharging.

For the experiments conducted in this research, SCs were applied as one energy storage option in the PV-membrane system to buffer short-term fluctuations and intermittency in SI. A charge controller based on pre-set voltage thresholds (V_{pump_off} , V_{pump_on} , $V_{charging_off}$, and $V_{charging_on}$) was designed to control the state of both the pump (on/off) and the SCs (charging/discharging). Full details about the charge controller and flow chart presenting all of the operational states are given in Section 3.5.

3.4.2. Lithium-ion battery energy storage

The total additional energy required over one solar day (denoted as E_{tot}) is calculate to estimate the capacity that needed for the batteries, which are required to provide the PV output power under a worst-case scenario (very cloudy day), and to raise it to the amount generated under a best-case scenario (sunny day), is given in Eq. 3-10:

$$E_{tot} = \int P_{sunny} dt - \int P_{very\ cloudy} dt , \quad \text{Eq. 3-10}$$

where P_{sunny} and $P_{very\ cloudy}$ represent the PV output power (W) on the sunny and the very cloudy day, respectively; and t is the operation time (h) over the entire day. The estimated E_{tot} required on one solar day is calculated to be approximately 1.5 kWh, as shown in Figure 3-6.

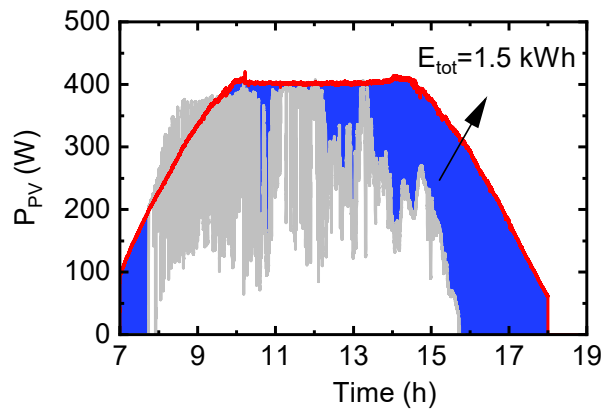


Figure 3-6: Total amount of energy required (E_{tot}) over the entire day, indicating the energy capacity needed from the batteries. Adapted from Li [278], CC BY-NC-ND 4.0 License.

To accurately select and size the battery pack for the stand-alone system, the following equation is commonly applied for this PV-membrane system [279]:

$$C_x = \frac{E_{tot}}{V_{dc}} \cdot \frac{T_{aut}}{DoD_{max}} , \quad \text{Eq. 3-11}$$

where C_x is the required battery capacity (Ah) at a specified discharge rate x ; E_{tot} is the total daily energy demand (Wh); V_{dc} is the nominal voltage of the DC bus (V); T_{aut} is the number of days of autonomy; and DoD_{max} is the maximum depth of discharge of the battery (%). Assuming battery voltage = $24 V_{dc}$, $T_{aut} = 1$, and $DoD_{max} = 80\%$, the total battery capacity is estimated to be approximately 84 Ah (energy capacity of 2.4 kWh).

Two lithium ion-phosphate (LiFePO_4) battery packs (Power Brick, PowerTech Systems, France, $24 V_{DC}$) were connected in parallel to supply a battery capacity of 100 Ah to the PV-membrane system. Here, the discharge rate x is calculated to be 0.2 C, assuming that the maximum required discharge current from the pump is 20 A (details found in the datasheet [280]). A charge controller (Victron MPPT 100/20,

Netherlands) is utilized to control the charging and discharging of the batteries at a maximum current of 20 A (claimed – actually up to 15 A in practice), while a DC/DC converter (MeanWell SD-500L-48, Taiwan) is used to step-up the battery voltage from 24 V_{dc} to 48 V_{dc} to drive the pump.

The typical way of expressing the storage capacity of batteries is SOC, while the alternative way is the depth of discharge (DoD). The SOC represents the available capacity in the battery as a fraction of the total nominal capacity; whereas, DoD is the usage of the capacity as a fraction of the initial capacity of the battery. In this work, the initial SOC was varied to simulate having a battery bank with different ranges of energy storage capacities. Before each of the experiments, the initial SOC was estimated on the basis of the V_{OC}-method that was used by Baccouche *et al.* [281]. Eight segments were divided on the SOC-V_{OC} characteristic of a Li-ion cell by approximating the piecewise linear curve, with each segment expressed in a linear relationship as follows:

$$SOC = f(V_{OC}) = a \cdot V_{OC} - b, \quad \text{Eq. 3-12}$$

where the varying coefficients a and b rely on the V_{OC} intervals [281, 282]. This formula is adapted with a factor of seven to obtain the output voltage of 24 V, assuming a single Li-ion cell with a V_{OC} of 3.6 V [283]. The method of SOC estimation has been programmed in a computer running LabVIEW. Subsequently, the Coulomb counting method is used to calculate the SOC during the experiments as expressed in Eq. 3-13:

$$SOC = SOC_0 + \frac{1}{Q_{rated}} \cdot \int_{t_0}^{t_0+\tau} I_b d\tau \cdot 100, \quad \text{Eq. 3-13}$$

where SOC_0 represents the initial SOC; Q_{rated} represents the rated capacity of the battery (unit, Ah); I_b is the battery current (A); t_0 is the time (h); and τ is the time duration of charging/discharging.

3.5. Charge controller and system resilience

A house-made charge controller was designed to control the state of the pump (on/off) and charging/discharging behaviour of the SCs. The control algorithms were established based on the pre-set voltage sensing thresholds to enhance system resilience, i.e., V_{pump_off} , V_{pump_on} , $V_{charging_off}$, and $V_{charging_on}$. In this control system, the charge controller can communicate with the laboratory computer via the RS232 interface. It has integrated current and voltage sensors that enabled the measurements via Profilab.

3.5.1. Flow chart

The operation of the charge controller was determined by the voltage thresholds control to trigger different events. The initial voltage set-points were established – pump off, pump on, charging off, and charging on voltage. The voltage settings can be modified through software (Termite) by converting bits to

voltage. Afterwards, the measurements, including voltage and current of PV, pump, and SCs, can be monitored by software (Profilab), while the data were sent via the RS232 communications port to the control computer.

The flow chart of different states between SCs and pump is given in Figure 3-7 to assist in fully understanding the working principles of the charge controller. The voltage control (see conditions in diamonds) has been implemented to trigger different events (see the rectangles). The SCs are switched on during system operation via an internal switch and timer within the charge controller at $SI > 800 \text{ W/m}^2$, which spans the time window from 9:00 – 13:00 over the three solar days. It ensures that higher power is generated from the PV panels to run the system and charge the SCs. Without the timer, the occurrence of repeated start-ups and shut-downs would be observed during the low available PV power periods – early in the morning and late in the afternoon – and thus room for optimisation in the controller remains (discussed in Section 5.4). An overview and full electrical schematic have been detailed in previous work [122].

Specifically, four pre-set voltage thresholds were established, namely, a lower voltage to switch off the pump ($V_{\text{pump_off}}$), a higher voltage to switch on the pump ($V_{\text{pump_on}}$), as well as two related thresholds to determine the charging and discharging behaviour of the SCs ($V_{\text{charging_off}}$ and $V_{\text{charging_on}}$). The voltage of the SCs (V_{sc}), pump (V_{pump}), and the PV panels (V_{pv}), is monitored to determine the status of the pump (on or off) and the states of the SCs (charging or discharging). The $V_{\text{charging_off}}$ and $V_{\text{charging_on}}$ of the SCs are chosen to control the depths of charging and discharging. This approach aims to shorten the discharge depth of the SCs for the first few fluctuations (the pump would extract less current), such that the pump can be operated continuously at the maximum possibility when several high fluctuations are encountered. The decision regarding which operating state to be in is mainly determined by $V_{\text{pump_off}}$ and $V_{\text{pump_on}}$. Increasing the $V_{\text{pump_on}}$ threshold value allows the pump to remain in the on-state for a longer period, as less current is needed to obtain the maximum power (built-in MPPT). Increasing the $V_{\text{pump_off}}$ value enables the SCs to be charged at a higher charging rate, although this would result in a rapid voltage drop of V_{pv} and undesired system shut-downs. The SOC is governed by the other two voltage thresholds – $V_{\text{charging_off}}$ and $V_{\text{charging_on}}$. The lower $V_{\text{charging_off}}$ setting leads to a smaller SOC that is directly proportional to the square voltage of V_{SCs} .

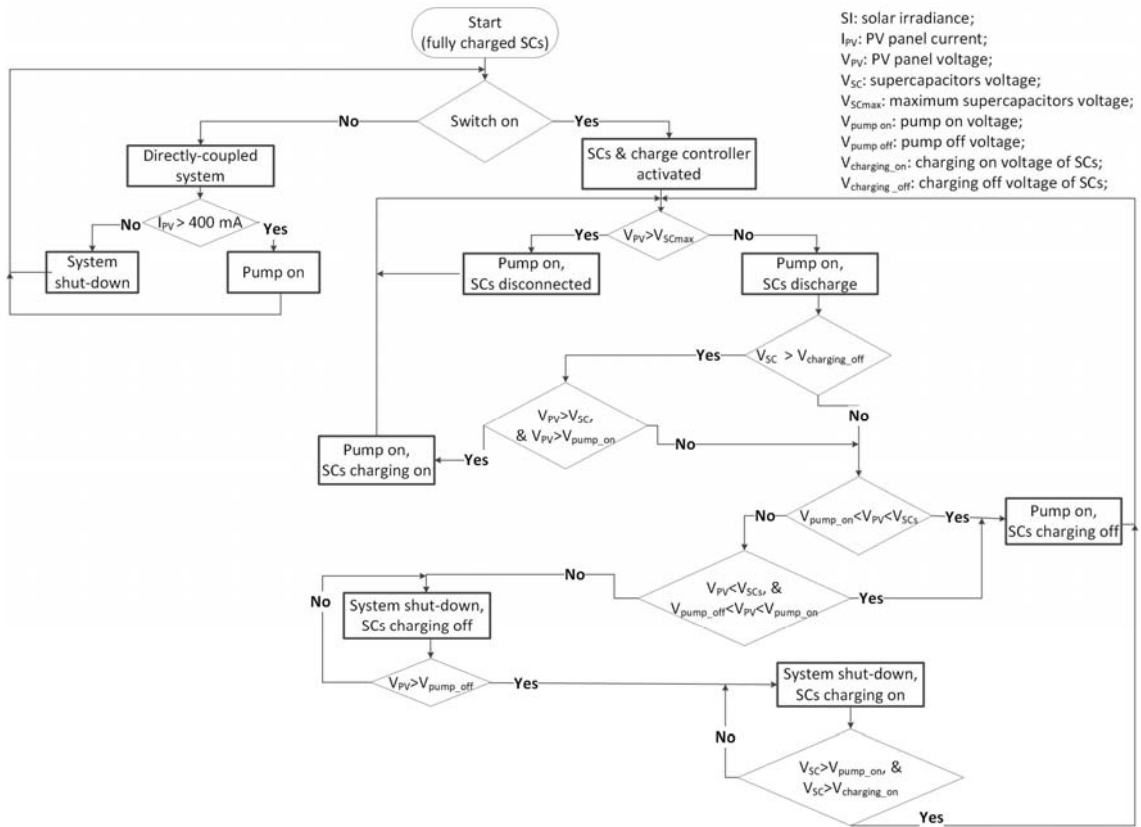


Figure 3-7: Flow chart of the charge controller within the PV-membrane system based on voltage control thresholds (V_{pump_off} , V_{pump_on} , $V_{charging_off}$, and $V_{charging_on}$), illustrating the different states between the pump and SCs. Adapted from [122], CC BY-NC-ND 4.0 License.

3.5.2. Settings for system control

Throughout this research, two settings are established to target different purposes. To investigate the impacts of ramp rates of PV voltage on the PV-membrane system (see Section 4), the two thresholds ($V_{charging_off}$ and $V_{charging_on}$) were deactivated to remove the constraints of the charging limits. Here, the charge controller voltage thresholds of V_{pump_on} and V_{pump_off} were varied in order to obtain the optimum system performance – defined as high permeate production and low SEC. Based on the set-point operation of the system at 10 bar and the maximum current that can be provided by the PV panels ($I_{mpp} = 1.8$ A), the four voltage thresholds for switching on the pump (V_{pump_on} : 120, 140, 160, and 180 V) were determined by characterizing the pump over a wide range of operating pressures. The five pump-off voltages (V_{pump_off} : 60, 70, 80, 90, and 100 V) were selected according to the minimum hydraulic pressure needed to overcome the osmotic pressure of the feed water (4 bar) to permit permeate production.

The modifications were made correspondingly to adapt to different solar days (see Section 5), incorporating real fluctuations and intermittency over the entire solar day at 1 s temporal resolution. A positive temperature coefficient lamp (1500 W, Osram R7s-p15) was connected in series with the pump to increase the inner resistance [278], such that conflicts with the pump built-in MPPT can be avoided; whereas, the

disadvantage would be the induced power loss on this lamp. To enable a broad pressure operating range, $V_{\text{pump_on}}$ was selected in terms of the set-point operation (detailed in Section 3.1.3) of the PV-membrane system at 10 bar, and the maximum photocurrent (2.7 A) that can be delivered at a rated PV capacity of 500 W. The $V_{\text{pump_off}}$ threshold was set based on the minimum required hydraulic pressure to overcome the osmotic pressure at a feed salinity of 5 g/L NaCl (approximately 4 bar). The charging on/off voltages were selected accordingly to have a large range of SOC. For these reasons, the four voltage set-points were as follows: $V_{\text{pump_off}} = 60$ V; $V_{\text{pump_on}} = 120$ V; $V_{\text{charging_off}} = 80$ V; and $V_{\text{charging_on}} = 140$ V. This corresponds to an SOC in the range of 20 – 100%. Note that for the current measurements, a positive current value expresses the system sourcing current either via photocurrent generation from the PV modules (I_{PV}) or the discharge of SCs (I_{sc}), while a negative value represents the current that withdraws from the pump (I_{pump}) or the charging current for the SCs (I_{sc}).

3.5.3. Parameters of system resilience

The charge controller with SCs energy buffering was applied to reduce system shut-down events and enhance system resilience (see Chapter 5). The methods in [284] were used to calculate the resilience factor (RF) throughout, while the performance parameters were adapted to determine the RF of flux (RF_{flux}) in the present work by using Eq. 3-14. The critical terms are clarified in Figure 3-8 for one fluctuation in SI.

$$RF = S_p \cdot \frac{F_d}{F_0} \cdot \frac{F_r}{F_0}, \quad \text{Eq. 3-14}$$

where S_p represents the speed recovery factor ($S_p = 1$); F_r represents the new stable performance after recovery; F_d is the performance immediately after disruption; F_0 is the original stable system performance; $\frac{F_d}{F_0}$ represents the absorptive capacity (C_{abs}), which indicates the ability to retain the proportion of original system performance immediately post-disruptions; and $\frac{F_r}{F_0}$ expresses the adaptive capacity (C_{ada}), which indicates the ability to retain the proportion of original system performance when a new stable level is achieved after recovery (see Figure 3-8). The speed recovery factor represents the elapsed duration for system performance to recover post-disruptions, as given in Eq. 3-15:

$$S_p = \frac{t_\delta}{t_r^*} \cdot \exp[-a(t_r - t_r^*)] \text{ for } t_r \geq t_r^*, \quad \text{Eq. 3-15}$$

where t_δ is the slack time (s) – defined as the maximum amount of time post-disruptions before recovery; t_r^* is the time to fully recover back to the initial performance again; t_r represents the time to a new equilibrium status; and a is the parameter controlling decay in resilience, as outlined in Figure 3-8. Here, $S_p = 1$, as $t_r = t_r^*$, and the ratio $\frac{t_\delta}{t_r^*}$ was close to unity during the calculations. It needs to be noted that the system performance is calculated in terms of short timescales (a few seconds or minutes), and a few minutes are required to obtain a new stable state. Thus, performance values associated with epochs that occur towards

the end of a disruption are selected, this is because they are more heavily weighted than those that occur earlier in the disruption [285].

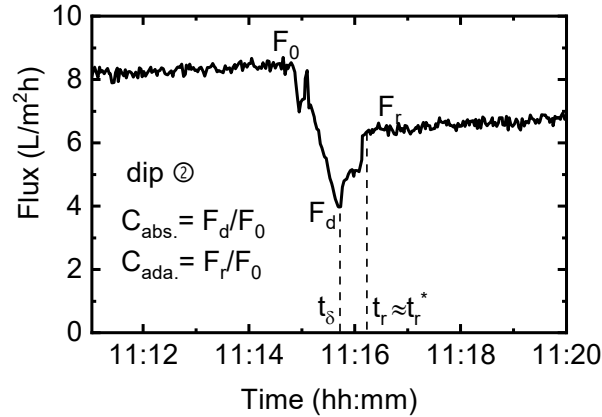


Figure 3-8: Graphical representation of the parameters that define the concept of resilience factor of flux. The data represents dip ② of the SI fluctuations in the partly cloudy day Figure 3-5B. All the parameters are defined in the main text. Adapted from [286], CC BY-NC-ND 4.0 License.

It is important to note that this RF analysis is applicable for the dips in SI on the partly cloudy day (labelled ① - ③ in Figure 3-5B) during the 90-min window, but is not able to be applied on a solar day characterised by constantly varying SI, such as the very cloudy day (Figure 3-5C). Here, a minimum time period of a few minutes is required to retain a relatively stable state. To evaluate the system resilience over the entire solar days, the parameters $\#_{SD}$ and t_{SD} along with system performance (namely motor power, TMP, flux, cumulative TDS, production and SEC) are investigated. While for the eight dips in the SI (Figure 3-5B), the RF_{flux} was determined as a function of feed water salinity and PV power capacity, and the average RF_{flux} was plotted in Sections 5.3 and 5.4. It should be aware of that the RF values approaching unity indicate increased resilience. A data screening was performed for the permeate flowrate less than 5 L/h as it reaches the limit of the flow sensor.

3.6. UF membrane backwashing control and water

3.6.1. Backwashing system overview

Two UF membrane backwashing configurations were implemented in this PV-membrane system, as shown in Figure 3-2. The switching sequence of the valves for achieving backwashing is discussed in the following section. The system was powered with a rated power capacity of 500 W, while the maximum power point voltage and current were $V_{mp} = 188$ V and $I_{mp} = 2.7$ A, respectively. Three solar days – sunny, partly cloudy, and very cloudy days – were selected to represent markedly different weather conditions and

levels of fluctuations in SI, as discussed in Section 3.3. This output power was used to assess the effectiveness of BW during all-day tests (discussed in detail below). It is worth noting that the SAS is employed only for powering the filtration pump, and each experiment starts with fully charged SCs (177 V) without further recharging when the voltage drops to the lower limit of the DC/DC converter (60 V). The output of the SCs passes through a DC/DC converter (Vicor, VI-N54EM) to step-down the high input voltage of the SCs to a constant voltage of $48V_{dc}$. The output of the DC/DC converter is connected to a second helical rotor pump (s242T-40, China), which is used as one BW configuration.

The alternative BW configuration is achieved via a bladder tank (Sanibel Comfort 6140017, Germany), which was motivated by the fact that the bladder tank is a passive element and can be charged by the main filtration pump. This approach eliminates the additional pump and associated power source, thus reducing component failures as a consequence of additional devices, and representing a technologically simpler and more robust approach [65].

3.6.2. Bladder tank

The bladder tank is utilized to store a certain amount of water when reaching the maximum capacity and release the water to flush the UF membrane when necessary. The bladder tank applied in the PV-membrane system possessed a useful volume of 6 L and a maximum pressure of 10 bar. In the backwashing experiments, the pre-charge pressure of the bladder tank was set to 1 bar in order to ensure low wear operation according to the manufacturer, and the backwashing pressure was set to 4 bar to not exceed the maximum TMP of the UF membrane.

Firstly, the pre-charged bladder tank was filled with UF permeate by the filtration pump by switching on valves ⑤ and ⑥, as well as switching off valve ③ with the charging phase finished until the water pressure in the bladder tank reached 4 bar (valves labelled in Figure 3-2). Subsequently, valves ③, ⑤, and ⑥ were reversed to continue the filtration phase after the BW cycle was completed. The BW phase is activated via turning off the filtration pump and valve ③, meanwhile switching on valves ④, ⑤, and ⑥. This BW function is automatically achieved with the opening and closing of the valves by switching the 8-channel relay card from the LabVIEW program. The BW volume was estimated at around 4 L through integrating the BW area, which is slightly less than the 6 L usable volume stated by the manufacturer.

3.6.3. Backwashing pump

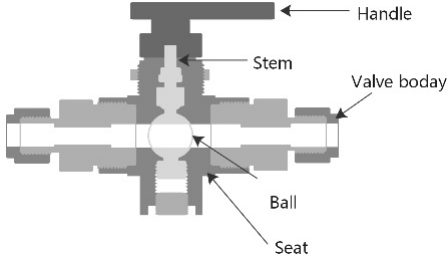
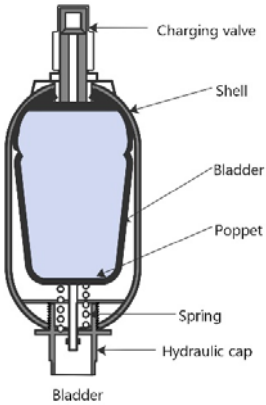
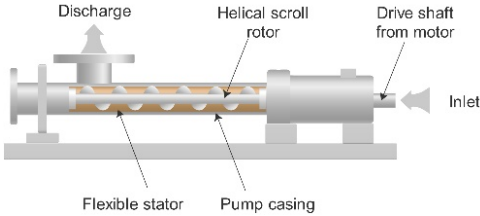
The other BW configuration is implemented via a second helical rotor pump placed in a SS BW tank (volume 100 L). The BW pump has a broad input voltage range ($24 - 48V_{dc}$), and exhibits a rated power of 284 W, maximum pressure of 4 bar, and flowrate up to 2000 L/h. However, the claimed stainless steel construction of the pump was dubious, as a consequence of the occurrence of rapid corrosion in the brackish feedwater.

The BW function via the pump was realized in a similar manner to the BW bladder tank discussed above. The BW volume was fixed at 4 L to match the volume of the bladder tank. Prior to each of the experiments, the prepared solution in the BW tank was a mixture of DI water and NaCl at a concentration of 5 g/L. 4 L of water from both the permeate and concentrate sides was manually taken back to the BW tank after each BW cycle to maintain the concentration of bentonite in the feed tank.

3.6.4. “Simulated fouling” setup

To simulate the effects of membrane fouling, a ball valve (see Figure 3-2, No. ⑨) was installed in the UF feed stream to achieve different pressure drops across the UF membrane. This method was motivated by the fact that the effort to induce fouling in a laboratory environment on a system – comprised of a 4" UF membrane (surface area of 6 m²) and 4" spiral wound RO membrane (surface area of 7.2 m²) – is significantly challenging. In particular, for engineers who are not involved in water chemistry, it presents as an interesting way to simulate the effects of fouling on system performance in order to determine the energy consumption of the BW process. In this research, the UF membrane module was operated in dead-end mode. The hypothesis is made based on choosing a similar pressure drop that occurs when using a real foulant, and the simple valve implementation can serve as a baseline to permit the analysis of energy consumption without the added complexity of inducing a foulant into the system. The valve was regulated from 100% open to 10% open (marked externally from position 1 to 10). Detailed information concerning the valve that regulates the pressure drop across the UF membrane to simulate fouling, bladder, and BW pump are summarized in Table 3-3 to achieve a clear understanding of the BW configurations. Even though this valve creates a pressure change in the simulated TMP for the BW process, the filtration process would not be affected.

Table 3-3: Detailed information of components used for the backwashing studies in this research. Adapted from [266], CC BY-NC-ND 4.0 License.

Component	Schematic	Purpose	BW settings	Filling time
Simulated valve		Create artificial pressure drop across the UF membrane	100% open to 10% open from position 1 to 10 (marked outside)	–
Bladder tank		BW of UF membrane as a passive device	BW volume: 4 L (determined by pre-charged air pressure and water release pressure)	~50 s at constant SI of 1000 W/m ²
BW pump (helical rotor pump)		BW of UF membrane as active device (powered by SCs)	BW volume: 4 L (Lab-VIEW controller)	–

3.6.5. Energy consumption calculations

The calculations of energy consumption (all based over one cycle) in terms of different configurations are summarized below to establish the foundation of systematically examining the effects of two BW operations on the total specific energy consumption (TSEC) in the PV-membrane system.

i) Energy consumption: BW pump + SCs (E_{BW_SC} , Wh)

The amount of electrical power that is consumed during the filtration and BW processes can be seen in Figure 3-9. E_{BW_SC} represents the energy consumption of the BW pump powered by SCs; t_{filt_on} represents

the time with RO permeate production; t_{filt_off} is the period when this filtration mode is ended; and t_{BW_off} is the time when the BW cycle is stopped. It is worth noting that the t_{BW_on} (BW cycle starts) is 1 s lagging behind t_{filt_off} , and thus t_{BW_on} is not displayed in Figure 3-9. In Eq. 3-16, where E_{BW_SC} is defined, t_{BW_on} and t_{filt_off} are assumed to have the same value:

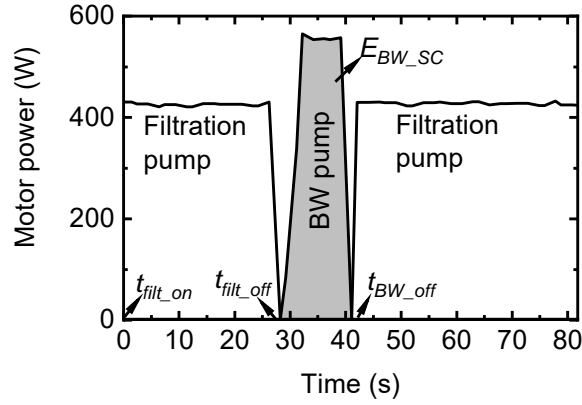


Figure 3-9: Graph demonstrating the electrical power consumed during the filtration and BW phases for the PV-membrane system using the BW when powered by the SCs. The integrated area (light grey) indicates the energy consumption of the BW pump during one cycle. Adapted from [266], CC BY-NC-ND 4.0 License.

$$E_{BW_SC} = \int_{t_{filt_off}}^{t_{BW_off}} V \cdot I \cdot \eta_{converter} dt, \quad \text{Eq. 3-16}$$

where V and I represent the measured voltage and current of SCs, respectively; η indicates the efficiency of the DC/DC converter (estimated to be 85%); and t is the total BW duration (see Figure 3-9).

It is important to note that V remains constant, while I decreases gradually along with the power consumption of the BW pump due to the fact that the power source (SCs) is not recharged during the BW process. It can be seen that the BW pump operates with a power consumption of 560 W, which is ascribed to the occurrence of corrosion when the wetted parts (questionable SS construction) were in contact with salts. In addition, the power consumption of the BW pump is anticipated to decline after a few BW cycles due to less energy stored in the SCs.

ii) Energy consumption: BW via bladder tank (E_{BW_BL} , Wh)

As shown in Figure 3-10A, the flowrate of BW bladder (BL) and RO permeate demonstrate the discharge of the bladder tank and the refilling phase via the filtration pump, respectively. Moreover, Figure 3-10B indicates electrical power consumption during filtration, bladder discharging, and refilling phases. The sole energy consumption of the BW bladder tank (denoted as E_{BW_BL} , Wh) is presented as the integrated area of the bladder tank refilling phase (grey area).

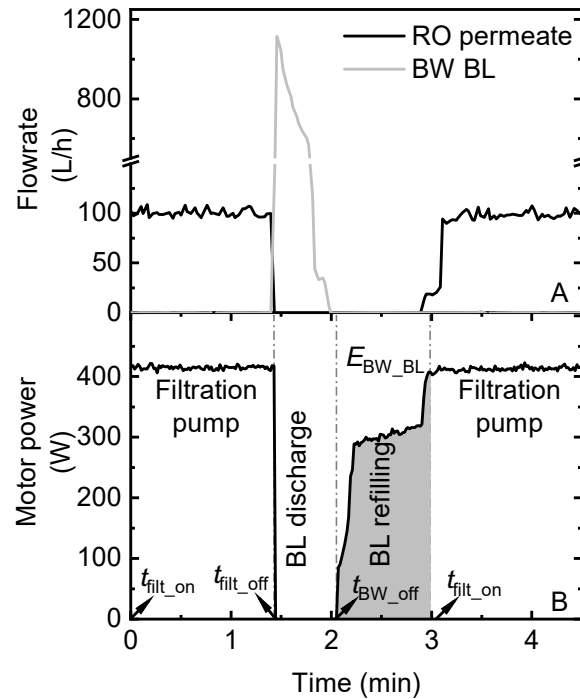


Figure 3-10: Electrical power consumed during filtration, bladder (BL) discharging, and refilling process. Note that the integrated area during bladder refilling (light grey) indicates the energy consumption of bladder BW. Adapted from [266], CC-BY-NC-ND 4.0 License.

$$E_{BW_BL} = \int_{t_{BW_off}}^{t_{filt_on}} P_{filt_pump} dt, \quad \text{Eq. 3-17}$$

where P_{filt_pump} represents the power consumption of the filtration pump; and $t_{total\ refill}$ is the total refilling duration of the bladder from t_{BW_off} to t_{filt_on} , as indicated in Figure 3-10.

iii) Energy consumption: filtration pump (E_{filt_pump} , Wh)

During the filtration phase, the energy consumption of the filtration pump is as follows:

$$E_{filt_pump} = \int_{t_{filt_on}}^{t_{filt_off}} P_{filt_pump} dt, \quad \text{Eq. 3-18}$$

where P_{filt_pump} is the power consumption of the filtration pump; and $t_{total\ filtration}$ is the total filtration time. Given the fact that the RO membrane provides resistance to the flow, the power consumption of the filtration pump remains the same at varied salt concentration.

iv) Total specific energy consumption of the system (TSEC: Wh/L)

The total specific energy consumption (TSEC, Wh/L) of the PV-membrane system during filtration and backwashing processes is then examined by using Eq. 3-19:

$$TSEC = \frac{E_{filt_pump} + E_{BW}}{V_{Production} - V_{BW}}, \quad \text{Eq. 3-19}$$

where E_{filt_pump} is the energy consumption of filtration pump (defined in Eq. 3-18); E_{BW} is the BW energy consumption (defined in Eq. 3-16 and Eq. 3-17 depending on operating mode); $V_{Production}$ is the cumulative produced RO permeate water; and V_{BW} is the BW volume (fixed at 4 L). The TSEC takes into account the total energy required by both the filtration and BW energy in the system, the total amount of produced permeate water with this energy, and the lost backwash water during the cleaning process.

3.6.6. Backwashing figures-of-merit

Aside from the evaluation of energy consumption (outlined above), the effects of operating conditions on membrane fouling are examined using the parameters below. While the first parameter expresses the cleaning efficiency of the BW, the other parameters represent the extent of UF membrane fouling.

TMP_{UF} reversibility: represents the percentage of fouling that can be restored over one BW cycle, defined as:

$$TMP_{UF} \text{ reversibility (\%)} = \frac{TMP_i^{final} - TMP_{i+1}^{initial}}{\Delta TMP_i}, \quad \text{Eq. 3-20}$$

where TMP_i^{final} is the final TMP of filtration cycle i ; $TMP_{i+1}^{initial}$ is the initial TMP of filtration cycle $i+1$; and ΔTMP_i is the TMP increase at the filtration cycle i .

Cake resistance (R_c): during membrane fouling, the foulants create a cake layer on the membrane surface and induce resistance to permeate transport, thus resulting in flux decline and TMP increase. The total resistance (R) is comprised of membrane resistance (R_m) and cake resistance (R_c) by using the resistance-in-series model as follows:

$$R = R_c + R_m = R_m + \alpha M_d, \quad \text{Eq. 3-21}$$

where the single cake resistance R_c represents the reversible and irreversible membrane resistance, which is taken as the mass of foulant forming the cake M_d , multiplied by the specific cake resistance α .

The membrane resistance by using DI water (10 bar) without fouling is calculated in Eq. 3-22:

$$R_m = \frac{TMP}{\mu J_0}, \quad \text{Eq. 3-22}$$

where TMP represents the applied filtration pressure; J_0 represents the permeate flux of the clean UF membrane; and μ is the viscosity of the solution (1 kg/ms at 20 °C) [287].

Particles remain in a dispersed phase and form a concentrated polarized layer [288, 289] during the filtration process. The flux is demonstrated as follows [289, 290]:

$$J = \frac{TMP - \pi_m}{\mu(R_m + \alpha M_d)}, \quad \text{Eq. 3-23}$$

where TMP is the transmembrane pressure; and π_m is the osmotic pressure.

The critical osmotic pressure ($\pi_{critical}$) can be achieved on the membrane and cause the formation of layers of irreversibly aggregated particles [288]. This leads to the following Eq. 3-24 for the permeate flux:

$$J = \frac{TMP - \pi_m}{\mu(R_m + \alpha M_d)} = \frac{TMP - \pi_{critical}}{\mu(R_m + \alpha M_d)}, \quad \text{Eq. 3-24}$$

It is worth noting that osmotic pressure for the bentonite (0.1 bar) was taken from the work of Besiere *et al.*, and is assumed to be constant when no irreversible fouling occurred [289]. On the other hand, critical osmotic pressure was taken as 0.06 bar when irreversible fouling occurred [289].

Calculated bentonite mass (m_C): The concentration of bentonite is calculated based on the mass balance using Eq. 3-25:

$$m_C(t) = C_B \cdot Q \cdot t, \quad \text{Eq. 3-25}$$

where Q represents the UF permeate flowrate (L/h); C_B is the concentration of the bentonite (mg/L); and t is the time (min). Data interpretation was carried out as shown in Eq. 3-26:

$$m_C(i) = m_C(i - 1) - C_B(i - 1) \cdot Q, i = 0, 1, 2, 3 \dots t - 1, \quad \text{Eq. 3-26}$$

Observed bentonite mass (m_B): the observed bentonite mass is calculated in terms of turbidity values. Three samples were taken from the same locations of the feed tank at the end of the filtration cycle and at the start of the next filtration cycle. The turbidity was measured for three filtration cycles, and the deposited mass on the membrane surface is calculated using Eq. 3-27:

$$m_B = (Turbidity_{filt_start} - Turbidity_{filt_end}) \cdot V_{feed} \cdot 3, \quad \text{Eq. 3-27}$$

where NTU_{filt_start} is the turbidity at the start of the filtration cycle; NTU_{filt_end} is the turbidity at the end of the filtration cycle; and V_{feed} is the feed water volume. Here, the average data over three filtration cycles were applied (measurements were given in the appendix). It is noted that this represents an approximate estimation considering the large volume of the feed tank (250 L), and the feed water and bentonite suspensions are assumed to be well mixed.

Cake thickness (\mathcal{E}): Cake thickness (denoted as \mathcal{E}) of the bentonite in terms of varied intervals was estimated based on the deposited mass, assuming uniform spheres of constant packing density ($\rho = 1 \text{ g/cm}^3$) with hexagonal packing arrangements on the membrane surface. The total area of the inner tube is calculated to be approximately 22 cm^2 , while the particle size to pore size ratio is 25, and the total packing area of the bentonite (A_{total}) is approximately 550 cm^2 . The cake thickness is calculated as follows:

$$\varepsilon = \frac{m_B}{A_{total} \cdot \rho}, \quad \text{Eq. 3-28}$$

where A_{total} is the total packing area of the bentonite, and ρ is the packing density (1 g/cm³).

Fouling rates (F_V, F_B): the simulated fouling rate achieved using the valve F_V is estimated as follows:

$$F_V = \frac{TMP_{BW_{initial}} - TMP_{BW_i}}{TMP_{UF}}, (i = 1, 2, 3, 4 \dots \dots 10) \quad \text{Eq. 3-29}$$

where $TMP_{BW_{initial}}$ is the initial TMP of backwashing when the valve is 100% open; TMP_{BW_i} represents TMP_{BW} at different valve positions; and TMP_{UF} is the TMP of the UF membrane.

Comparatively, the experimentally-observed fouling rate using bentonite, F_B , is defined as follows:

$$F_B = 1 - \frac{TMP_{BW} - TMP_{BW_{initial}}}{TMP_{UF_{final}}}, \quad \text{Eq. 3-30}$$

The values are taken as the average peak values over five cycles. It is worth noting that the F_V is calculated to correspond to the real fouling rate (F_B) that occurs when bentonite is introduced into the feed-water as a fouling agent. This was conducted to determine the energy consumption of these two methods and the feasibility of inducing fouling without adding a chemical agent.

3.7. Experimental design

Systematic experiments were performed to study the operation of the PV-membrane system under both steady-state and fluctuating conditions. The charge controller and SCs were incorporated to adapt to the ramp rates in PV voltage, improve system resilience, and reduce shut-down events to the periodical fluctuations on varied solar days. These experiments aimed to provide the baseline to understand how the system responds to different fluctuations and intermittency, and also evaluate system control on: i) utilizing the available power from the PV source and energy storage units; ii) reducing the system shut-downs; iii) enhancing system resilience; and iv) decreasing UF membrane fouling via backwashing control. Experimental designs are described in detail below. It is noted that throughout all of the experiments performed in this work, a previously published set-point operating strategy was implemented [215], as discussed in Section 3.1.3. The regulating valve on the concentrate stream was set to 10 bar at the SI of 1000 W/m² with a feed flowrate of 420 L/h.

3.7.1. Steady-state experiments

Constant SI experiments were used to characterize the performance of the PV-membrane system under stable conditions over a wide range from 200 to 1200 W/m². These experiments (Section 4.1) provide a baseline to allow a system comparison with results obtained under fluctuating conditions.

The SAS was used to provide power over the SI range from 200 to 1200 W/m², corresponding to the power output of PV modules (350 W_p) and the motor power. The SI was kept constant for 15 min to allow stabilization of the performance parameters. The average performance values were taken over 13 min, as 1 min was required to stabilize input power availability. This allowed the performance comparison and consistency between experiments.

3.7.2. Ramp rates in PV voltage

SI variations can cause fluctuations of PV power output as a consequence of passing clouds, wind speed, and ambient temperature [291]. The fluctuations and intermittency in the SI result in a lower permeate quality and the overall drinking water demand not being met. Ramp rate is employed as the most intuitive measure to quantify the severity of fluctuations in SI – defined as the variation of the magnitude or frequency of the SI over a given time interval [39, 292].

Therefore, a systematic study of the impacts of different ramp rates in PV voltage was conducted to elucidate the dynamic characteristics of the PV-membrane system. An extreme solar day was chosen to pose a challenge to the PV-membrane system. Figure 3-11 shows the SI data (1 s resolution) on the very cloudy day. The range of SI fluctuating amplitudes, ramp rates, and frequency in PV voltage and SI were analysed and interpreted to represent the real SI fluctuations, as indicated in Figure 3-12. As illustrated in Figure 3-11B, the maximum occurrence of ΔSI ramp rate (280 W/m²·s) was 0.01% of the time. Comparatively, the occurrence of maximum ramp rate voltage ΔV_{PV} (2 V/s) was 0.36% of the time (see inset graph of Figure 3-11C). Given the most commonly occurring conditions, the most frequently occurring ramp rate of ΔSI (97%) was in the range of 0-50 W/m²·s, while 83% of ΔV_{PV} occurred in the range of 0-0.1 V/s. As a consequence, it can be seen that the ΔV_{PV} at 2 V/s and 0.1 V/s indicate a worst-case (greatest change in real weather conditions) and best case (least change in real weather conditions), respectively.

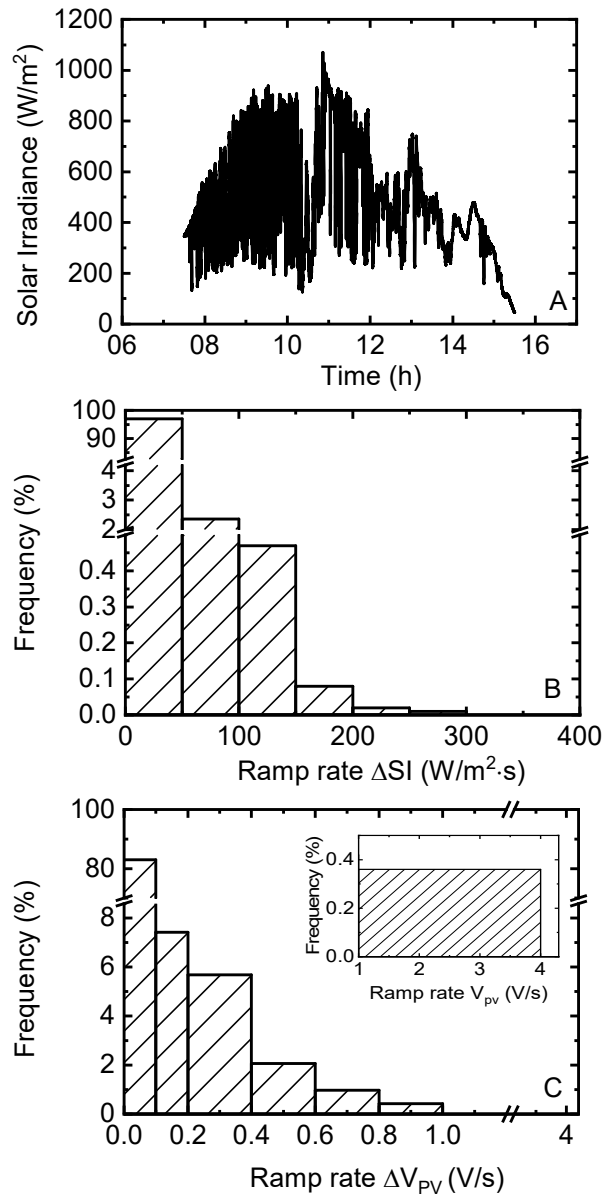


Figure 3-11: Solar irradiance measure on a very cloudy day (A) with 1 s of the resolution, and histogram of frequency analysis of weather data as a function of the ramp rates of solar irradiance ΔSI (B) and PV voltage ΔV_{PV} (C). The inset graph in (C) shows the frequency of ramp rate ΔV_{PV} in the range 1 – 4 V/s (data taken from the KIT Solar Park on 13th Oct. 2016). Adapted from [122], CC-BY-NC-ND 4.0 License.

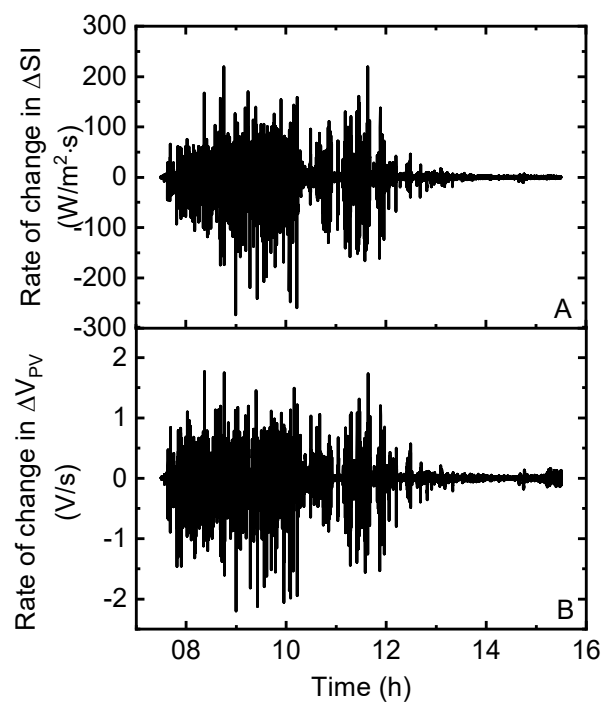


Figure 3-12: The magnitude of fluctuations in (A) ΔSI and (B) ΔV_{PV} voltage under a very cloudy day (data obtained from the KIT Solar Park on 13th Oct. 2016). Adapted from [122], CC-BY-NC-ND 4.0 License.

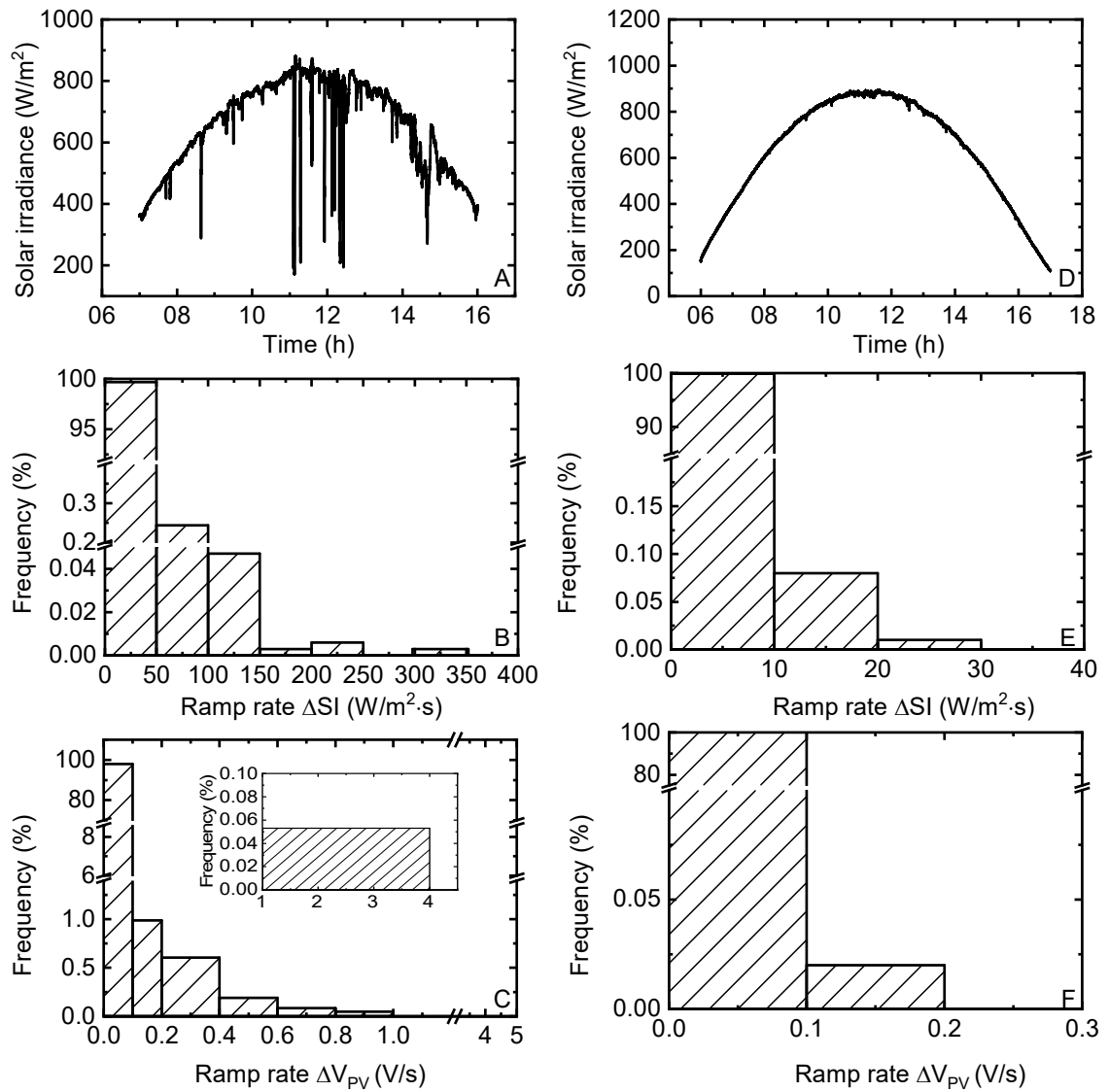


Figure 3-13: Solar irradiance on the partly cloudy day (left graphs) and sunny day (right graphs): (A, D) with 1 s resolution, and histogram of frequency analysis of weather data as a function of the ramp rates of solar irradiance ΔSI (B, E) and PV voltage ΔV_{PV} (C, F). The inset graph in (C) shows the frequency of ramp rate ΔV_{PV} in the range 1 – 4 V/s (data were taken from the KIT Solar Park on 26th May 2016 and 5th May 2016. Adapted from [122], CC-BY-NC-ND 4.0 License.

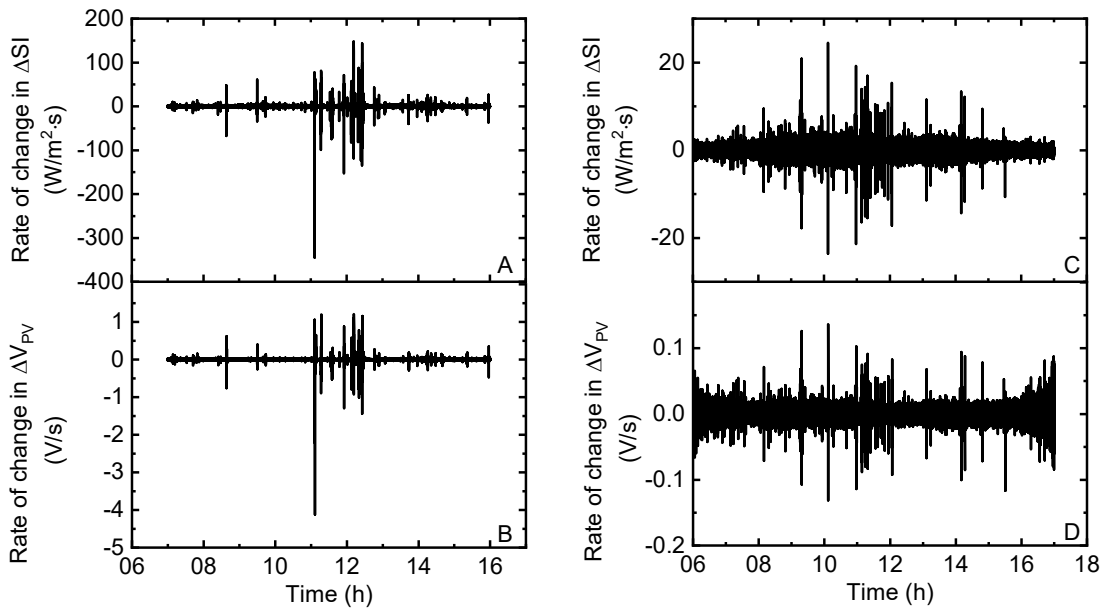


Figure 3-14: The magnitude of fluctuations in (A) ΔSI and (B) ΔV_{PV} voltage under the partly cloudy day (left graphs) and sunny day (right graphs) (data obtained from the KIT Solar Park on 26th May 2016 and 5th May 2016. Adapted from [122], CC-BY-NC-ND 4.0 License.

In addition, compared to the ramp rate in ΔSI and ΔV_{PV} on the sunny and partly cloudy day (see Figure 3-13 - Figure 3-14), the greatest ΔSI magnitude ($350 \text{ W/m}^2 \cdot \text{s}$) occurred only 0.05% of the time during the partly cloudy day, as shown in the inset graph of Figure 3-13C. Since this result is the observed maximum value from only three solar days in one particular geographic location, a slightly higher value ($\Delta SI = 400 \text{ W/m}^2 \cdot \text{s}$) was chosen in order to assure relevance to other challenging days and environments. It is important to note that very large variations in SI have been reported in Norway ($\Delta SI \sim 900 \text{ W/m}^2 \cdot \text{s}$) [25]; however, the number of annual events where $\Delta SI > 500 \text{ W/m}^2 \cdot \text{s}$ occurred was extremely infrequent (0.0006% of the time). In contrast, more than 250 occurrences of $\Delta SI \geq 400 \text{ W/m}^2 \cdot \text{s}$ [25] were observed, supporting the decision to use the ΔSI value of $400 \text{ W/m}^2 \cdot \text{s}$ in the present work. The experimental procedure was performed as follows.

i) Square waves of SI: magnitude variations of $SI = 200, 400, 600,$ and 800 W/m^2 were provided ranging from extreme to small to map out the effects of step response on the PV-membrane system (see Figure 3-15).

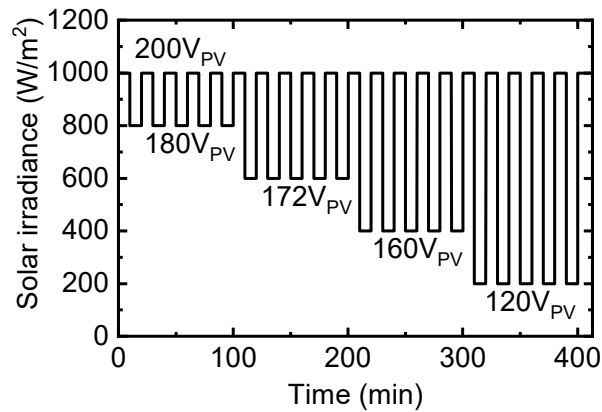


Figure 3-15: Example of SI fluctuations on the performance of the PV-membrane system. The SI values were used as an input to the SAS, while the PV voltages at each step were given via the measurements of the charge controller. Adapted from [122], CC-BY-NC-ND 4.0 License.

ii) Ramp rates of PV voltage: ramp rates in PV voltage experiments were used to study how the PV-membrane system behaves to rapid and slow variations (5, 2, 1, 0.5, 0.2, and 0.1 V/s). It is worth noting that 5 V/s, which was beyond the realistic condition, was chosen to deliberately challenge the system. As indicated in Figure 3-12B, the realistic worst-case scenario is 2 V/s, while 1, 0.5, 0.2, and 0.1 V/s all represent the more frequently occurring ramp rates. The experiments were carried out with five cycles by varying the SI amplitude from 1000 to 600 W/m² (variations of SI = 400 W/m²), which represent the most severe fluctuations in real weather conditions (see Figure 3-12A).

The experimental procedure designed above was also applied to evaluate system resilience to periodic fluctuations using energy buffering control (Sections 4.4 and 4.5). The ramp rates in PV voltage were used over the range from 5 – 0.1 V/s with the SCs and charge controller as follows:

i) Charge controller performance: the most rapid (but realistic) ramp rate of 2 V/s was carried out to determine the control behaviour of the overall PV-membrane system. This experimental setup of coupling the membrane system to the energy buffering control units (charge controller and SCs) allowed for both simultaneous charging/discharging of the SCs and operation of the system. The results can be seen in Section 4.4.

ii) Ramp rates in PV voltage with charge controller and SCs: ramp rates over a broad operating range were conducted to determine how the charge controller coped with varied fluctuations.

iii) Voltage threshold variations (Section 4.5): different voltage thresholds (pump off/on) were varied to obtain the optimum system performance by achieving maximum cumulative permeate production, minimum SEC, and drinkable water quality that complies with WHO guidelines. The voltage thresholds were selected based on the power requirements of the pump and the system operation set-point. Four voltage thresholds for switching on the pump ($V_{\text{pump_on}}$: 120, 140, 160, and 180 V) were determined. Five pump off

voltages ($V_{\text{pump_off}}$: 60, 70, 80, 90, and 100 V) were chosen according to the minimum hydraulic pressure required to overcome the osmotic pressure of the feed water to produce permeate (approximately 4 bar).

3.7.3. Real solar days

The experiments were performed using high-temporal-resolution (1 s) of real solar data with the BW30 membrane module, and conducted with the following configurations:

- i) Directly-coupled system under three solar days – serves as the baseline for the resilience of the PV-membrane system under varied solar days using 5 g/L NaCl at a rated PV capacity of 500 W;
- ii) System resilience with SCs and charge controller under three solar days – compares system performance once adding the SCs and charge controller (all at the same voltage thresholds) with the results above (5 g/L NaCl + 500 W PV);
- iii) System resilience with different feed salinities under highly variable SI fluctuations on the partly cloudy day – investigate the ability of the charge controller and SCs to influence system resilience under different feed salinities (1, 2.5, 7.5, and 10 g/L NaCl at a rated PV capacity of 500 W);
- iv) System resilience with varied PV power capacity under the partly cloudy day at a feed salinity of 5 g/L NaCl – examine the ability of PV capacity (300, 400, 600, 800, and 1000 W) to reduce system shut-downs ($\#_{SD}$ and t_{SD}) and improve resilience with SCs buffering and charge controller.

It is worth noting that all of the experiments performed with SCs and charge controller are configured with the same pre-set voltage thresholds for comparison, as discussed in Section 3.5.2.

3.7.4. Ultrafiltration membrane backwashing

All of the experiments were carried out with the same BW volume (4 L of UF permeate) at a feed salinity of 5 g/L to compare energy consumption based on different BW configurations. The tests were performed in the following orders, firstly with two BW configurations: i) at constant SI + simulated valve (no bentonite); and ii) over three different solar days (varied SI) + low bentonite concentration (100 mg/L). Subsequently, iii) with the BW bladder tank at a constant SI + high bentonite concentration (300 mg/L); and finally iv) with a simulated valve at a constant SI to correlate with the experiments in iii). The details are provided below:

- i) Energy consumption with “simulated fouling” using a valve with varied BW configurations

As can be seen from Figure 3-2, one ball valve (No. ⑨) was installed in the UF feed stream to allow different pressure drops to be created to simulate the impacts of membrane fouling. It serves as a baseline to permit studies of energy consumption without the addition of a fouling agent into the system.

In this setup, the SAS is programmed to operate with a constant SI that is equivalent to the performance of the PV panels under full sunshine ($SI = 1000 \text{ W/m}^2$) to power the filtration pump. The BW configurations are: i) passive (bladder tank); and ii) BW pump powered by SCs. The experiments were conducted with a BW interval of 10 min, with five cycles being performed to ensure that the results are

reproducible. The induced pressure drop across the ball valve was changed via adjusting the valve with different angles, i.e., completely open (90°), 45° , and 30° , which corresponds to a pressure drop of 0, 1.2, and 1.1 bar, respectively. It is then used to simulate the real fouling induced by the bentonite by correlating the fouling rate between F_v and F_B .

ii) System characteristics under real solar days at a low fouling rate with two BW configurations

The aim of this section is to better understand the system characteristics with two BW configurations under real solar days that are directly subjected to fluctuations with different weather conditions, i.e., sunny, partly cloudy, and very cloudy day. The experiments were 8 – 11 h in length throughout the day, depending on the season and weather conditions. It is anticipated that one reliable and energy-efficient BW configuration will be chosen from these operations under real solar days.

The bentonite was added at a concentration of 100 mg/L (NTU = 35) as a fouling agent to simulate natural turbid water [293]. The BW interval was maintained at 90 min, as it covered the whole solar day with BW operations, thus minimizing the risks of severe fouling as a result of long-term operations. Furthermore, this value was in the range of BW intervals that have been widely used in water treatment plants [294].

iii) Energy consumption with a high fouling rate with bladder tank BW at a constant SI

To assess the impact of BW intervals on the PV-membrane system, and allow the effects of membrane fouling to be evaluated within a shorter timeframe, a higher concentration of bentonite (300 mg/L, NTU = 100) was added to the feedwater. In particular, cake resistance, layer thickness, and system TSEC were studied in detail.

Different BW intervals (10, 20, 30, 45, 60, 90, and 120 min) were conducted with the bladder tank to represent the wide operating range used in the literature to examine the impacts on TSEC. The concentration of bentonite (60 g) in the feed tank (feedwater volume of 200 L) over time was estimated based on mass balance; whereas, the amount of bentonite deposited onto the UF membrane surface was calculated by NTU measurements. The detailed calculations can be found in Section 6.3. It is worth noting that the filtration pump was powered with the simulated output power at a constant SI of 1000 W/m^2 from SAS in order to guarantee consistent membrane performance before and after each of the experiments.

iv) Comparisons between “simulated fouling” and fouling with BW bladder tank at a constant SI

The pressure drop across the simulated valve for the BW bladder tank was varied over a broad range to overlap with the increased TMP_{UF} that occurred via bentonite fouling. These experiments were carried out to determine if the simulated fouling can represent the real bentonite fouling for the scientific work. The experiments were carried out with a range of different pressure drops across the valve (see Figure 3-2, No. ⑨) from completely open until 10% open. The pressure drops are represented by naming the valve positions from 1 to 10.

3.7.5. System performance with Li-ion batteries and SCs

Experiments were conducted on the PV-membrane system equipped with Li-ion battery storage and SCs over varied solar days to evaluate the impacts on system performance when incorporating fluctuations and intermittency, in particular with respect to water production and SEC. The experiments performed are specified below:

i) Operation on the partly cloudy day: as a reference, system performance using the BW30 membrane (5 g/L NaCl feed salinity) under the partly cloudy day was determined to examine the directly-coupled system performance. System performance – in particular, permeate production and SEC – are compared between the reference and fully-charged Li-ion batteries on this day;

ii) Operation under other solar days: the experiments are performed with and without fully charged batteries on the very cloudy and the sunny day to evaluate the impacts of batteries on the dynamic characteristics of the PV-membrane system when subjected to varied weather conditions;

iii) Operation with different battery capacities: the initial SOC was varied over a wide range (70, 50, 40, 30, and 20%) and tested on the partly cloudy day to determine how the PV-membrane system would respond when equipping with a smaller capacity battery pack, in particular regarding the SEC, permeate EC, and permeate production. The varied initial SOC from 70% to 20% corresponded to the energy storage capacities of 1.7, 1.2, 1, 0.7, and 0.5 kWh of the Li-ion batteries;

iv) Comparisons between Li-ion batteries and SCs: to study the impacts of different energy storage technologies on the PV-membrane system with the same PV power rating, system performance was compared when equipped with SCs, and fully-charged Li-ion batteries on the partly cloudy day.

3.8. Error analysis

In this research, calculations of the error bars for the experimental results are specified below. The main error of the measurable parameters – flowrate, pressure, current and voltage, temperature, EC – includes the analytical error (from the sensors, see Table 3-2) and systematic errors (from the filtration system). The analytical error was calculated in terms of the maximum deviation of relatively stable measurements using Eq. 3-31, while the main sources of systematic error result from pressure and temperature variations. The sum of these two parameters results in total systematic error.

$$\Delta y_{abs} = \frac{y_{max} - y_{min}}{2}, \quad \text{Eq. 3-31}$$

where Δy_{abs} is the absolute error of parameter y ; y_{max} is the maximum measured y ; and y_{min} is the minimum measured y .

For unmeasurable parameters, such as SEC, flux, resilience factors, cake thickness, cake resistance, and production, the “max-min error method” was used to estimate the errors. The difference of the maximum estimated result and minimum estimated result is used to calculate the absolute error by Eq. 3-32. The

systematic relative errors were estimated by taking into account pressure and temperature variations throughout (sum-up the relative error with the systematic relative error) as shown in Eq. 3-32.

$$\Delta J(\text{with system error}) = J \cdot \left(\frac{\Delta J_{abs}}{J} + \Delta Sf \right), \quad \text{Eq. 3-32}$$

where $\Delta J(\text{with system error})$ represents the absolute error with systematic error; ΔJ_{abs} is the absolute error of the flux J , which was calculated by Eq. 3-31; $\frac{\Delta J_{abs}}{J}$ is the relative error of flux; and ΔSf is the system error.

4. Effect of ramp rates in solar irradiance

The results in this chapter were published in Renewable Energy 149, 877-889, (2020) [122]. The co-author Achim Voigt helped with the design of the charge controller. The co-authors Andrea Schäfer and Bryce Richards were involved in the overall concept of the experimental design, the interpretation of the results and the review of the work.

The main aim in this chapter is to elucidate the dynamic characteristics of the PV-membrane system, and therefore determine optimal settings in the charge controller to achieve optimum system performance - defined as the maximum permeate production and low SEC. Specifically, the following three main research questions are answered:

- i) How does the response of variable ramp rates in PV output voltage (V_{PV}) affect the control algorithms of the charge controller?;
- ii) What extent of variations (V_{PV}) can the charge controller and SC energy storage elements be able to enhance PV-membrane system performance when subjected to the most rapid ramp rates that occur under realistic solar conditions?;
- iii) How do pre-set voltage thresholds of the charge controller affect attaining the best PV-membrane system performance?

4.1. Steady-state experiments

The operation of the PV-membrane system under steady-state SI served as a baseline for the experiments conducted under fluctuating conditions. Figure 4-1 summarizes overall system performance in the range of SI from 200 – 1200 W/m².

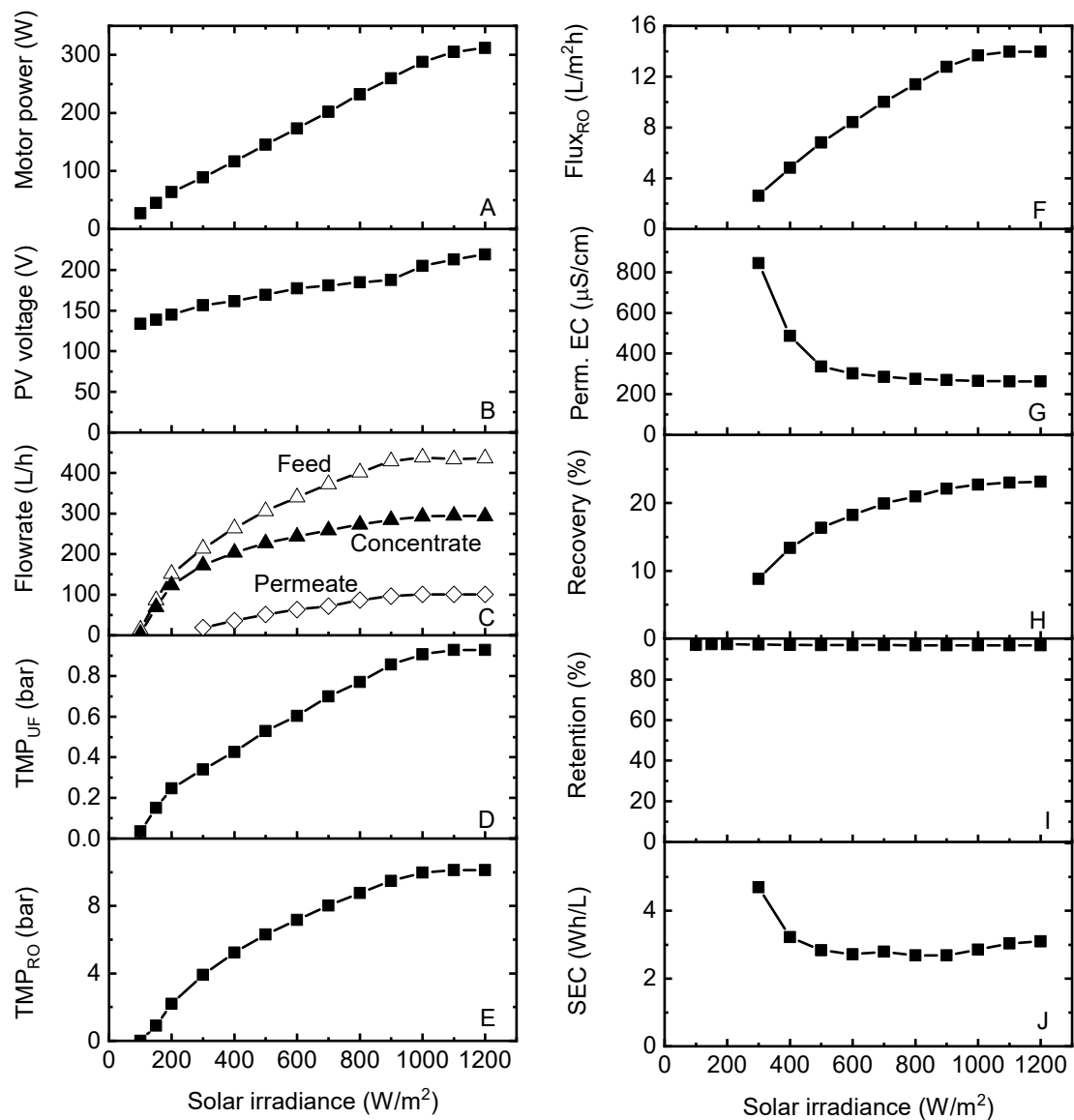


Figure 4-1: PV-membrane system performance plotted as a function of constant SI levels. (A) motor power, (B) PV voltage, (C) feed, permeate and concentrate flowrates, (D) TMP_{UF} , (E) TMP_{RO} , (F) $flux_{RO}$, (G) permeate EC, (H) recovery, (I) retention, and (J) SEC. Adapted from [122], CC-BY-NC-ND 4.0 License.

As shown in Figure 4-1A and Figure 4-1C, the SI needs to rise to a minimum SI of 300 W/m^2 (motor power = 88 W , $TMP_{RO} = 4 \text{ bar}$) before permeate production starts. The motor power consumption (Figure 4-1A) increases roughly linearly with increasing SI, while the PV voltage rises logarithmically (Figure 4-1B). A linear correlation is observed between TMP across both the UF and RO membrane (see Figure 4-1D – E) in the SI range of 400 to 1200 W/m^2 . The same trend occurs to the membrane flux (Figure 4-1F), which increases from 4.8 to $14 \text{ L/m}^2\text{h}$. At a low SI = 300 W/m^2 , a high NaCl concentration in the permeate stream causes a high EC, but at SI > 400 W/m^2 this leads to a permeate EC less than $500 \mu\text{S/cm}$ (Figure

4-1G). The recovery follows the same pattern as TMP_{RO} and remains in the range of 15% to 30% at SI values higher than 400 W/m^2 (Figure 4-1H), while the retention maintains $> 96\%$ in the same range of SI (Figure 4-1I). At a $SI > 400 \text{ W/m}^2$, the SEC is kept at a stable value of approximately 3 Wh/L; whereas, the SEC is higher as a consequence of limited flux at lower SI. It can be seen that the SEC values were consistent with the previously wind-powered membrane system equipped with a BW30 membrane (3.0 – 3.6 Wh/L) for treating synthetic brackish water (5.5 g/L NaCl) with motor power in the range of 120 W to 300 W [35]. It is worth mentioning that the salt concentration used in this work (5 g/L, NaCl) is slightly lower than the one used in previous work. Nevertheless, the SEC is in good agreement with previously published work on PV-powered membrane systems equipped with the same BW30 membrane and 5 g/L NaCl brackish feedwater [39]. The SEC of the present system is slightly higher than the previously reported value of 2.5 Wh/L, where SI values were $> 400 \text{ W/m}^2$. This is primarily caused by different system configurations, including: i) the UF membrane now being equipped after the pump with a maximum TMP_{UF} of 0.9 bar (previously, UF was submerged in the feed tank with a maximum suction TMP_{UF} of 0.6 bar); ii) a total pressure drop of $0.6 \sim 1$ bar occurred due to two reducing fittings for the flow sensor [295]; and iii) several valves were installed for system backwashing, with each valve exhibiting a pressure drop of 0.25 bar. Overall, a total pressure drop of approximately 2.4 bar occurs within the system, and thus approximately 30 W more power is required to drive the filtration process (at the set-point pressure of 10 bar). Eventually, given that a different pump – more powerful and exhibiting a wider operating range, but with a lower flowrate – was applied in the present system, and the SEC adds up to 10% ~15% (0.3 ~ 0.5 Wh/L) higher than previously. These results are also in close accordance with the results obtained earlier in field trials, in which treating natural brackish feedwater (5.3 g/L) with the same BW30 module led to an SEC of 2 ~ 2.4 Wh/L [199, 264]. In another reported PV-membrane system with the same BW30 membrane, the SEC was in the range of 3.3 ~ 4.7 Wh/L when treating 2 g/L NaCl feedwater [200]. The system in Bilton's work was able to produce 300 L of clean water on a sunny summer's day with overall SEC in the range of 2.5 ~ 4 Wh/L; unfortunately, the type of membrane used was not specified [58].

Steady-state measurements are utilized to provide a baseline for comparison with fluctuations in power. Overall, the system performs in a stable manner at $SI > 300 \text{ W/m}^2$. Regarding the SOW, the system is operated at a recovery $< 30\%$, and the permeate complies with the WHO guideline value through the full operating range with feed water of 5 g/L NaCl.

4.2. Square waves of solar irradiance

Measurements of square waves of SI (see Figure 4-2A) were conducted via the SAS to fully elucidate the dynamic characteristics of the PV-membrane system when it is directly undergoing rapid fluctuations. The results are plotted in Figure 4-2.

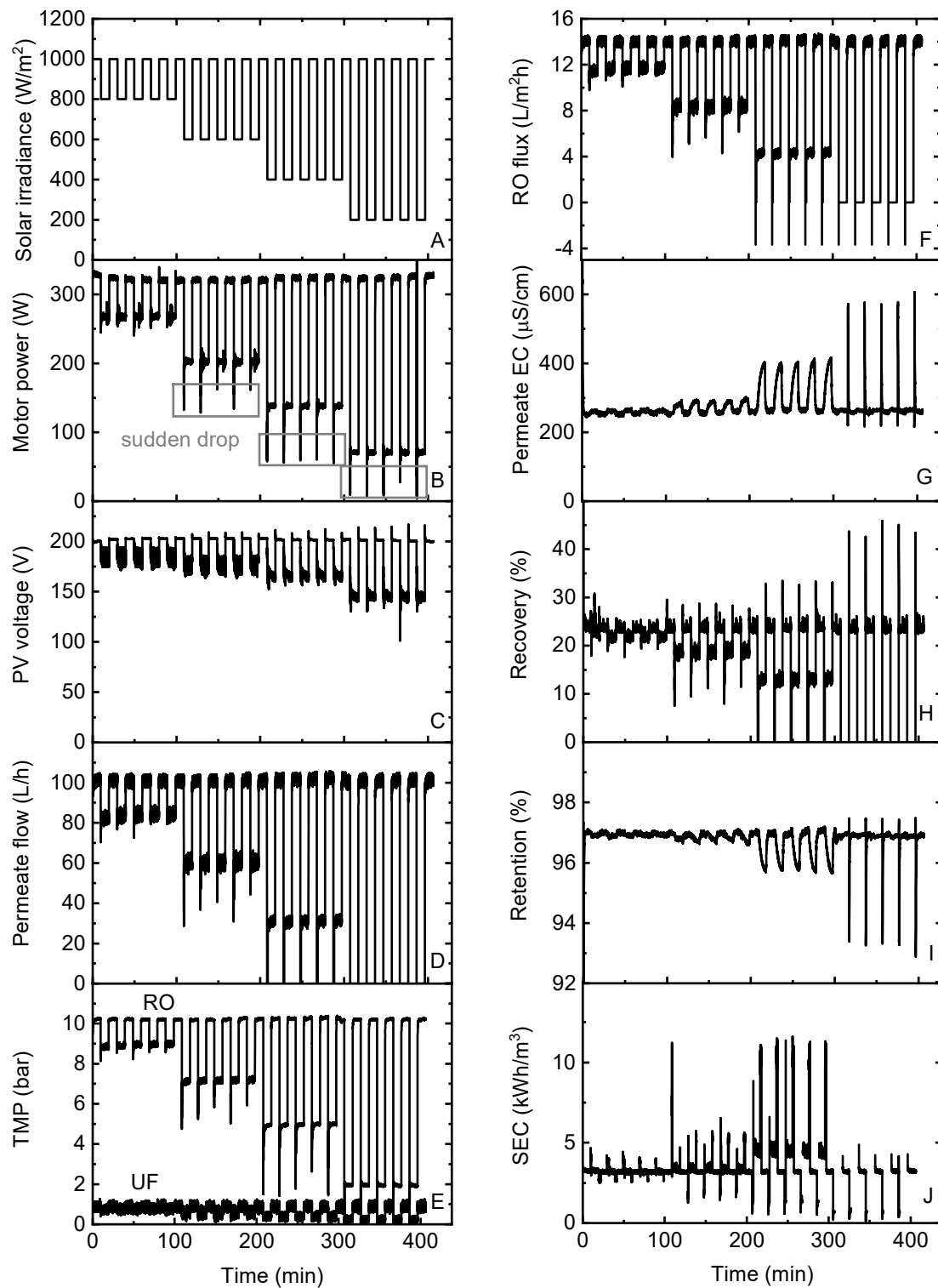


Figure 4-2: PV-membrane system performance under different solar irradiance fluctuations, including (A) solar irradiance, (B) motor power, (C) PV voltage, (D) permeate flow, (E) TMP, (F) $flux_{RO}$, (G) permeate EC, (H) recovery, (I) retention, and (J) SEC. Adapted from [122], CC-BY-NC-ND 4.0 License.

As indicated in Figure 4-2B, the motor power follows the step closely when the SI decreases from 1000 to 800 W/m². However, when the SI reduces from 1000 to 600 W/m², the downward step causes a sudden motor power drop from 320 W down to 150 W for a period of 8 s prior to jumping back to 200 W. The occurrence of this sudden drop of motor power is caused by the built-in MPPT of the pump, which cannot respond quickly enough to the rapidly changing SI. Similar sudden drops are also observed during the steps from SI = 1000 W/m² down to 200 – 400 W/m². It can be seen from Figure 4-1C that the system can only produce permeate at a SI > 300 W/m² during steady-state operation conditions; however, here the pump keeps working at SI = 200 W/m² (motor power of 60 W). Again, a sudden power drop is seen during the transitions from 1000 to 200 W/m², causing motor power momentarily reaching 0 W (pump shut-down). The corresponding PV voltage at each SI level is provided in Figure 4-2C – the significance of this will become clear later when discussing the operation of the charge controller. As shown in Figure 4-2D and Figure 4-2E, the permeate flowrate and TMP_{RO} follow the same pattern as the motor power during the rapid transitions, which is ascribed to the fact that they are both determined by the driving force of the pump. It is worth mentioning that the negative permeate flow and flux values (Figure 4-2D and Figure 4-2F, respectively) indicate the occurrence of naturally-induced backwash permeate in the system. This has also been reported in the literature, and commonly occurs when the TMP drops below the osmotic pressure [296]. The backwash flowrate was obtained manually by reading the display of the permeate flow sensor. 10 points of backwash flowrate over a 2 min period were taken to obtain a total backwash volume of 340 mL. During the rapid SI transitions, system performance deteriorates as indicated by periods of low flux or even no flux (Figure 4-2F) and recovery (Figure 4-2H), as well as a higher permeate EC (Figure 4-2G). The average retention is (maintained at 96.8%, Figure 4-2I) similar to the steady-state value of 96.9% (Figure 4-1I). Large spikes of SEC (Figure 4-2J) appear during the transition periods due to the extremely low permeate flux compared with reduced motor power, and thus the division of these two numbers leads to a high SEC. It should be noted that the SEC values at SI = 200 W/m² cannot be shown, as the system is not capable of producing any permeate as a result of insufficient pressure.

These results build fundamental understandings when varying the ramp rates of SI and PV output voltage in subsequent experiments, and indicate potential problems that might occur due to built-in MPPT. For the remaining experiments, the ramp rate of ΔSI was fixed at 400 W/m², as it represents the greatest variation under real weather conditions (see Figure 3-12A), and at this ΔSI value, the system encounters performance issues.

4.3. Ramp rates of PV voltage without energy buffering

As discussed in Section 4.2, the pump is unable to react spontaneously to the sudden drop in motor power arising from a square wave SI due to the built-in MPPT. However, it is unlikely that such a transition as sudden as a square wave can occur in natural environments – instead, the step will take place within a certain amount of time. As indicated in Figure 3-11, two typical ramp rates were chosen (2 and 0.1 V/s) to

represent the worst-case and most frequently occurring cases, respectively, in real weather conditions. The system characteristics in response to these two ramp rates are presented in Figure 4-3, while the experimental results performed with remaining ramp rates (5, 1, 0.5, and 0.2 V/s) in ΔV_{PV} are provided in Figure 4-4 and Figure 4-5.

These results demonstrate that the sudden drop in motor power from 320 W to 170 W (see Figure 4-3A and Figure 4-4A) occurred at $\Delta V_{PV} \geq 1$ V/s, while no sudden drop in motor power can be seen at $\Delta V_{PV} \leq 0.5$ V/s (Figure 4-5A and G). As discussed above, the flux, TMP, recovery, and SEC followed the same trend as the motor power. Despite the fact that the changes in TMP and flux caused by this sudden drop were not significant, the impact of this on overall system performance equipped with SCs in real weather conditions can be paramount. For instance, the sudden power drop due to rapid SI fluctuations could trigger additional shut-down events of the pump when the SCs are kicking in. The SEC graphs (Figure 4-3F and Figure 4-4F and L) indicate abrupt variations with ramp rates ≥ 1 V/s. However, the SEC at $\Delta V_{PV} \leq 0.5$ V/s (Figure 4-5F and L) changes more gradually, indicating that the system can respond better to slow variations.

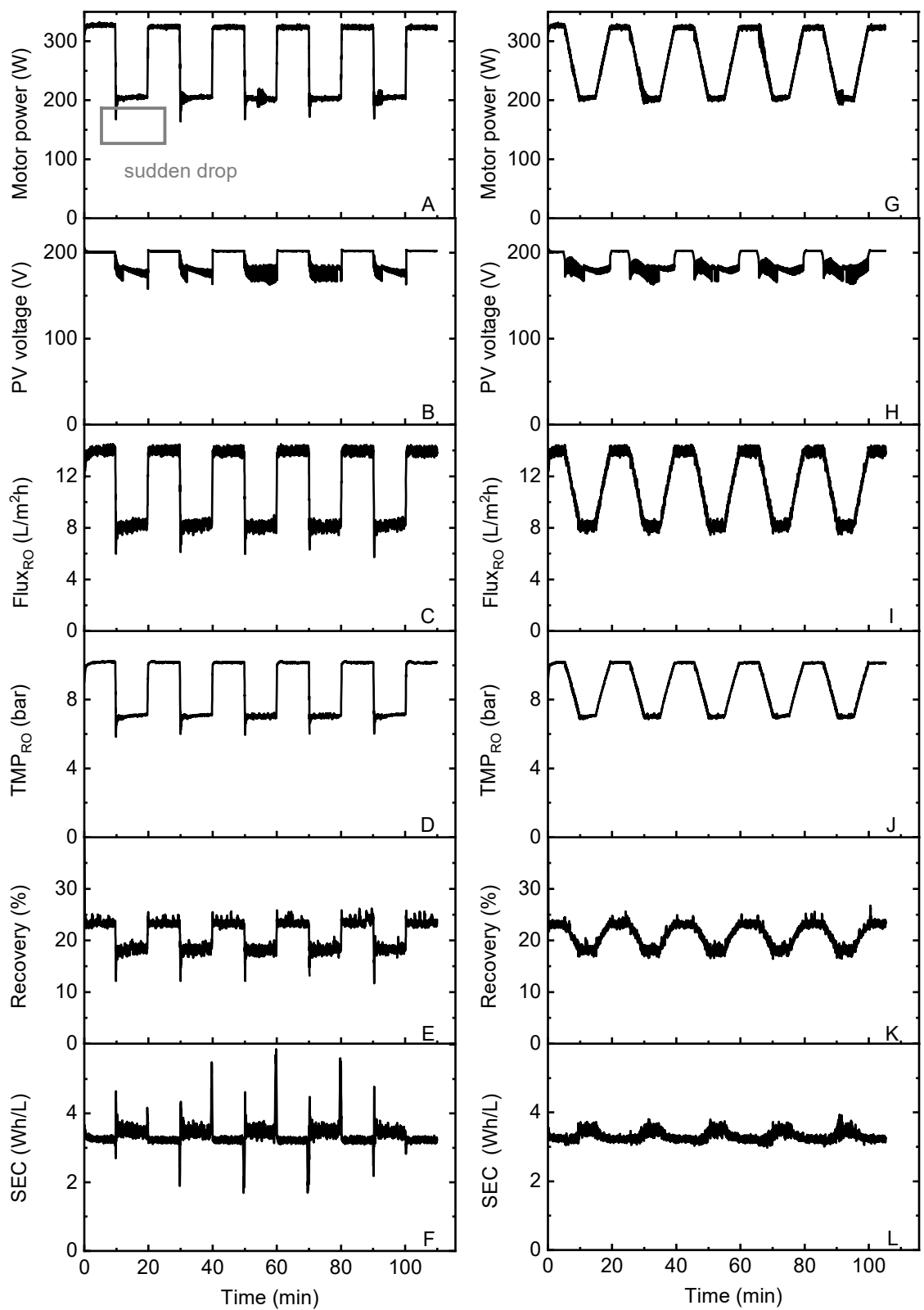


Figure 4-3: PV-membrane system performance under two different voltage ramp rates (left: 2 V/s; right: 0.1 V/s) with five cycles: (A, G) motor power, (B, H) PV voltage, (C, I) flux_{RO}, (D, J) TMP_{RO}, (E, K) recovery, and (F, L) SEC. Adapted from [122], CC-BY-NC-ND 4.0 License.

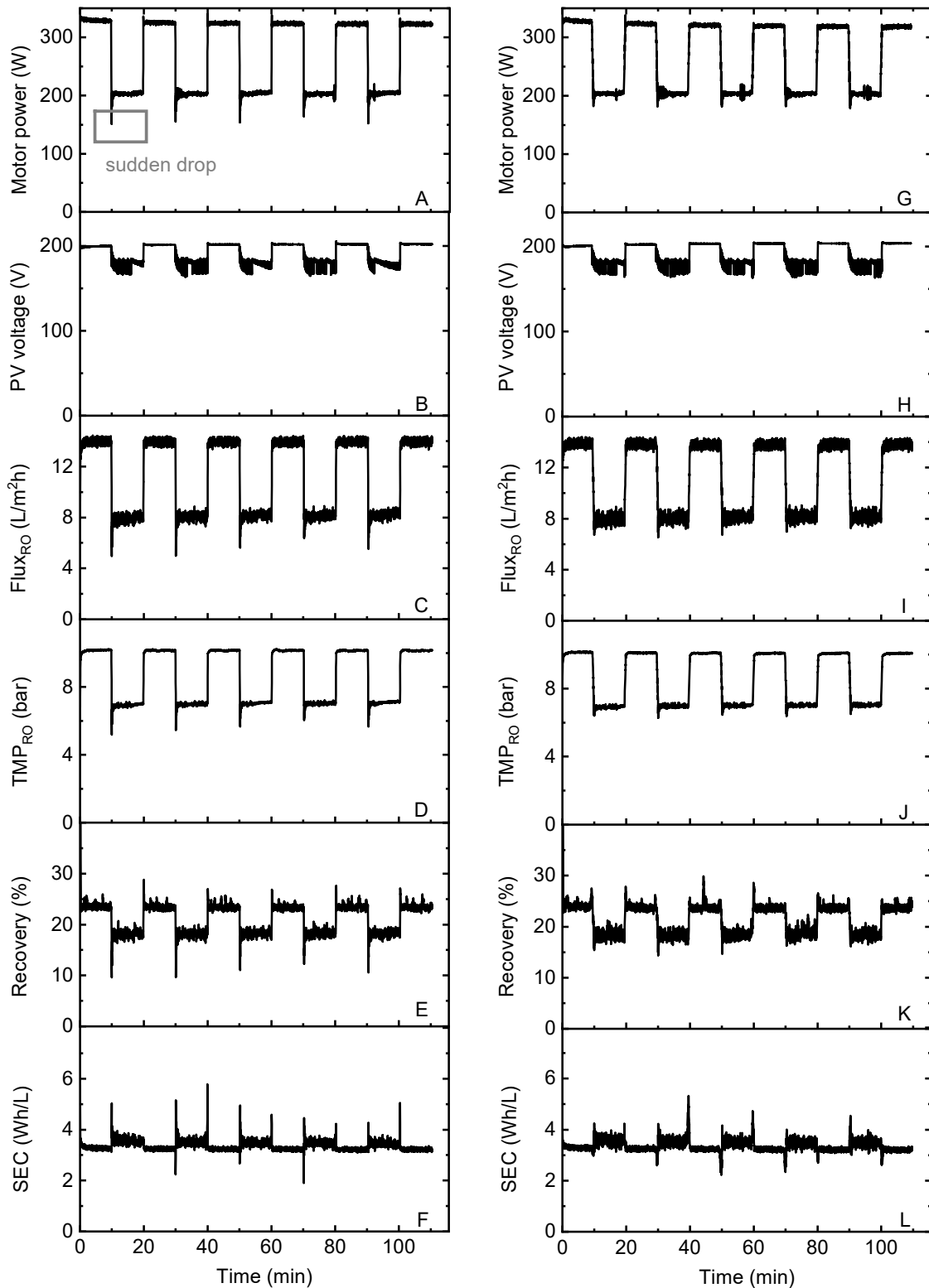


Figure 4-4: PV-membrane system performance under different voltage ramp rates with five cycles (left: 5 V/s, right: 1 V/s), demonstrating the parameters from top to bottom in an order of (A) motor power, (B) PV voltage, (C) $flux_{RO}$, (D) TMP_{RO} , (E) recovery, and (F) SEC. Adapted from [122], CC-BY-NC-ND 4.0 License.

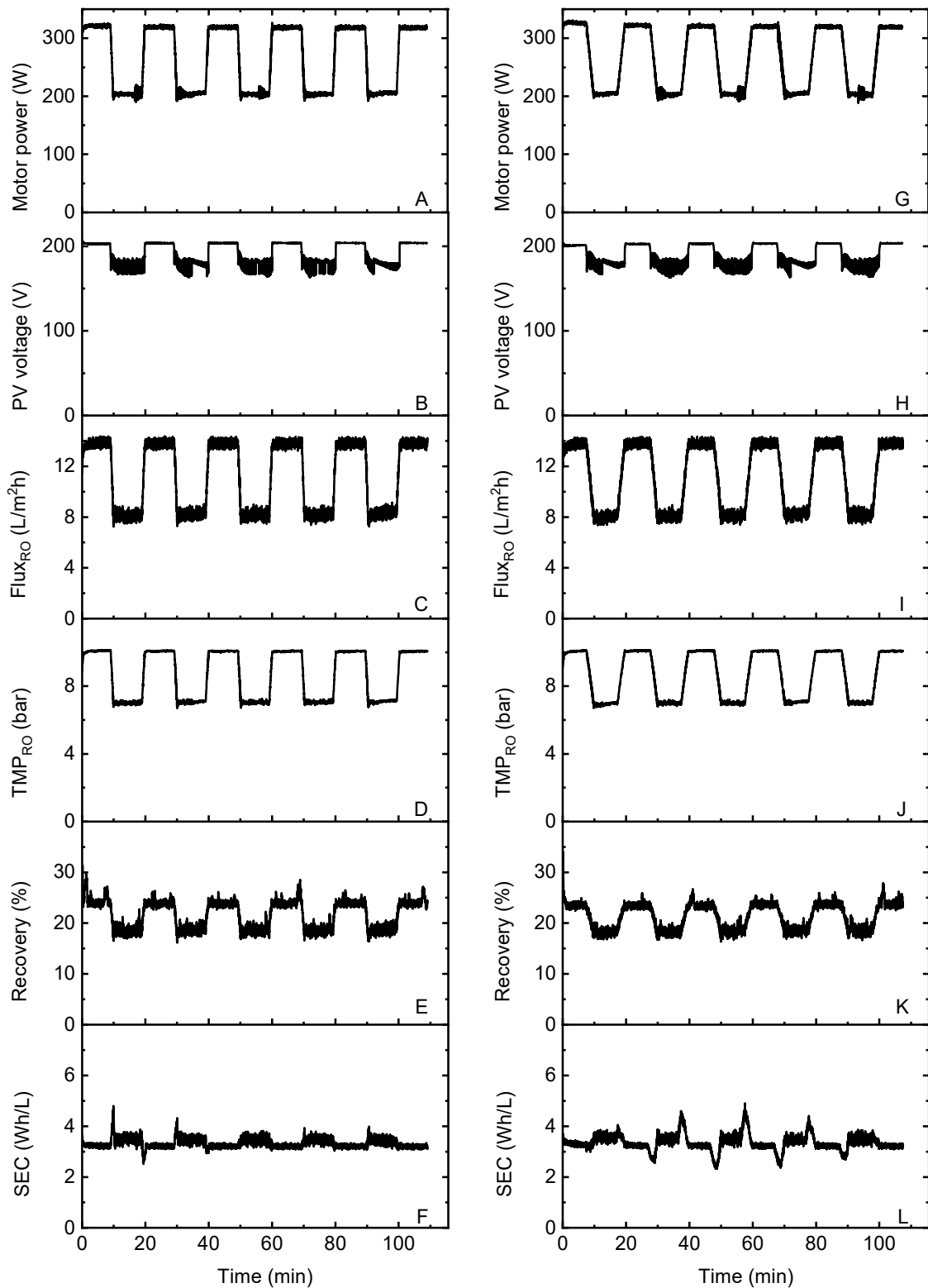


Figure 4-5: PV-membrane system performance under different voltage ramp rates with five cycles (left: 0.5 V/s, right: 0.2 V/s), demonstrating the parameters from top to bottom in an order of (A) motor power, (B) PV voltage, (C) flux_{RO} , (D) TMP_{RO} , (E) recovery, and (F) SEC. Adapted from [122], CC-BY-NC-ND 4.0 License.

4.4. Charge controller performance

To evaluate the performance of the charge controller, experiments were conducted with SCs at a ramp rate of 2 V/s to represent the most rapid variations observed under realistic conditions (see Figure 3-11C). One full SI fluctuation cycle result is provided (see Figure 4-6) to highlight the operational principle of the charge controller. Here, it should be mentioned that the addition of energy storage or control components to a system cannot make it more efficient, as the benefits of the new component have to compensate for the losses when included in the system [205]. However, the benefits of SCs employed in the RE system have been addressed, such that the ability to buffer short-term fluctuations and reduce the number of system shut-downs as a consequence of intermittency from the RE source [35, 205].

The overall behaviour of the PV-membrane system regarding electrical parameters (Figure 4-6B – E) and membrane parameters (Figure 4-6F – G) are demonstrated in Figure 4-6. The motor power remains at 320 W during the on-period as a result of the built-in MPPT (see Figure 4-6B) under this testing condition (Figure 4-6A). Afterwards, it increases up to 360 W at the beginning of the off-period as the discharging current of SCs achieves the maximum ($I_{SC} = 4.3$ A). Then, the power drops to zero at $t = 16$ min. The variations in motor power availability can be explained by examining the voltages and currents in the system (Figure 4-6C-D), as well as the SOC of the SCs (Figure 4-6E). When the system is operating at low SI (starting at $t = 10$ min in Figure 4-6C, see ①), the SCs start to discharge until V_{sc} reaches V_{pump_off} at 60V (at $t = 16$ min in Figure 4-6C). At the pump-off phase (see ②), the V_{pv} starts to rise (see ③) and subsequently charges the SCs (state ④). At $t = 20$ min, the SI goes back to 1000 W/m², and more currents are flowing to the system, and thus V_{PV} keeps rising until reaching the V_{pump_on} (160V at $t = 22$ min). As can be seen in Figure 4-6D, a positive current value represents the system sourcing current, either via photocurrent generation (I_{PV}) or discharge of the SCs (I_{SC}). Comparatively, a negative current occurs when charging the SCs or consuming the power of the pump (I_{pump}). When the low SI value of 600 W/m² is applied (starting at $t = 10$ min in Figure 4-6D, see ⑥), the I_{PV} drops slightly, after which the SCs starts to discharge (state ⑤) to the pump (see state ⑦) until reaching the lower limit of the SOC (11% as indicated in Figure 4-6E). It is worth noting that during the discharging process of the SCs, the pump draws current from both the PV panels (SAS in this case) and the SCs to maintain maximum power (due to the built-in MPPT). It needs to remind that the charging off/on thresholds within the controller were not activated, such that constraints of limiting the charging/discharging of SCs were removed. This causes the shut-down of the pump at state ② during the SCs charging period before reaching the V_{pump_on} . As a result, the V_{PV} is solely used for recharging the SCs (see ⑧), and the pump restarts at $t = 22$ min, at which point the SOC reaches 80 % (see Figure 4-6E).

The impacts of the fluctuation cycle on desalination performance can be seen in Figure 4-6F and G. The TMP_{RO} and permeate flowrate remain at 10 bar and 100 L/h, respectively, for an additional 6 min 20 s after the dropping of SI at $t = 10$ min. An additional 10 L of permeate is produced during this buffering

periods. The system restarts at $t = 21 \text{ min } 30 \text{ s}$, which is $\sim 1.5 \text{ min}$ later than the system would have restarted without SCs. The forfeited permeate production during this timeframe is calculated to be 2.5 L, whereas, an overall net benefit in permeate production of 7.5 L remains. The potential gains will be significant when this energy buffering period is extrapolated to cover the amount of the time over one full solar day, the challenge would be the spontaneously discharge of SCs at the beginning of the day. This issue will be addressed in Chapter 5.

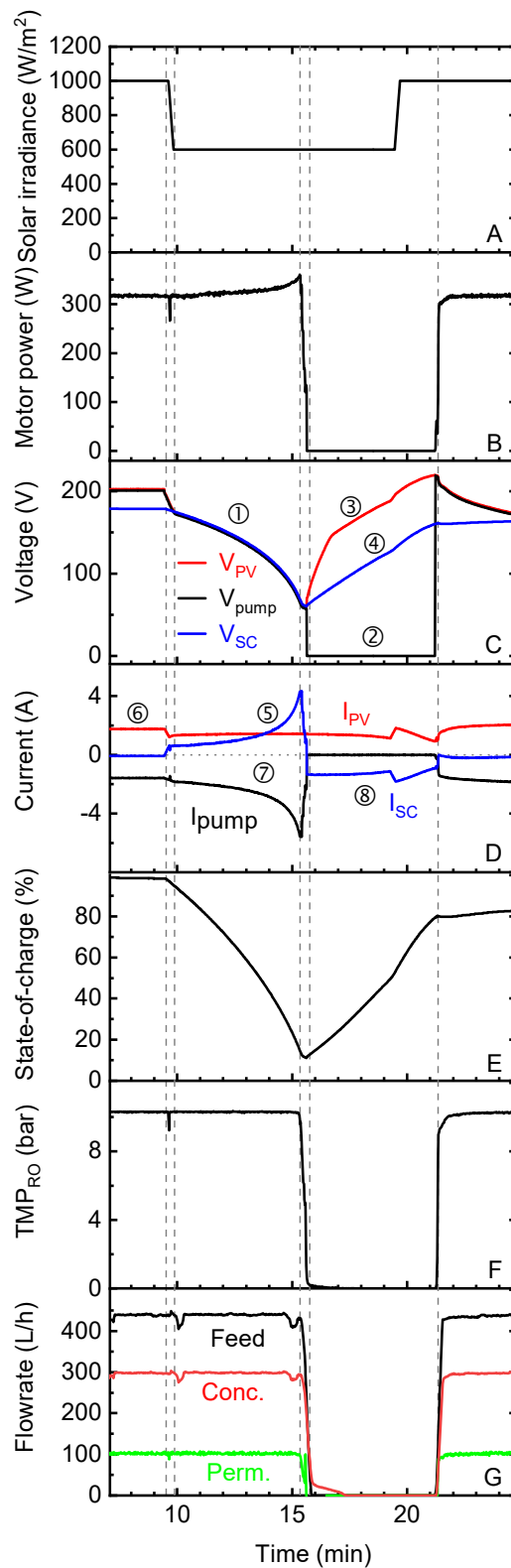


Figure 4-6: PV-membrane system performance with SCs and charge controller under one cycle of SI fluctuations, (A) solar irradiance, (B) motor power, (C) voltage, (D) current, (E) state-of-charge, (F) TMP_{RO} , and (G) flowrate. Adapted from [122], CC-BY-NC-ND 4.0 License.

4.5. Voltage threshold variations

In this section, the effects of selecting different voltage thresholds on the PV-membrane system operation was studied. As mentioned previously, the charge controller was designed based on pre-set voltage thresholds, which can be easily adapted via software by the operator. At this point, it is useful to recall all the different operating states of the charge controller within the PV-membrane system (see Figure 3-7). The decision about which operating state to be in is controlled by two key voltage thresholds, $V_{\text{pump_off}}$ and $V_{\text{pump_on}}$. The $V_{\text{pump_on}}$ threshold is anticipated to impose a greater impact on system performance than the $V_{\text{pump_off}}$ threshold. This is ascribed to the fact that with increasing $V_{\text{pump_on}}$ values, the system is running for a longer period of time in the pump-on state due to less current needed to maintain maximum power (built-in MPPT). At a certain point, it is anticipated that the $V_{\text{pump_on}}$ threshold value is too high, and the system spends little time at this stage. Moreover, an increase in the $V_{\text{pump_off}}$ threshold value allows the V_{PV} to charge the SCs at a higher charging rate that is directly proportional to the voltage. After understanding this, experiments were performed with different combinations of $V_{\text{pump_on}}$ and $V_{\text{pump_off}}$ thresholds to determine the optimal values, in which maximum accumulative water production and low SEC can be achieved. The following experiments were conducted at the same ramp rate (2 V/s) and SI (1000 – 600 W/m²) as used above (see Figure 4-6A), while the pre-set voltage thresholds were configured ($V_{\text{pump_off}} = 60, 70, 80, 90,$ and 100 V, $V_{\text{pump_on}} = 120, 140, 160,$ and 180 V) as detailed in Section 3.5.2.

The impacts of selecting different $V_{\text{pump_on}}$ and $V_{\text{pump_off}}$ thresholds on system performance are illustrated as contour plots in Figure 4-7. At $V_{\text{pump_on}} = 160$ V, the maximum average power consumption is observed compared to any of the other $V_{\text{pump_on}}$ (see Figure 4-7A). This is because the motor requires less current at high voltages to drive the pump and maintain maximum power (dictated by the built-in MPPT). Meanwhile, I_{PV} is sufficiently high to flow to both the pump and SCs, allowing continuous charging of SCs. Accordingly, the high average motor power availability at $V_{\text{pump_on}} = 160$ V can be seen with high flux and TMP_{RO} (see Figure 4-7B and C, respectively), as it determines the driving force from the pump. As shown in Figure 4-7C and D, the results follow the same trend, with TMP_{RO} and SOC rising as $V_{\text{pump_on}}$ increases. The effects of $V_{\text{pump_on}}$ thresholds become less on average on-period of SEC (3.1 to 3.3 Wh/L, see Figure 4-7E). This highlights the inherent characteristics of SCs, in that they constitute an excellent source of power, but a limited source of energy.

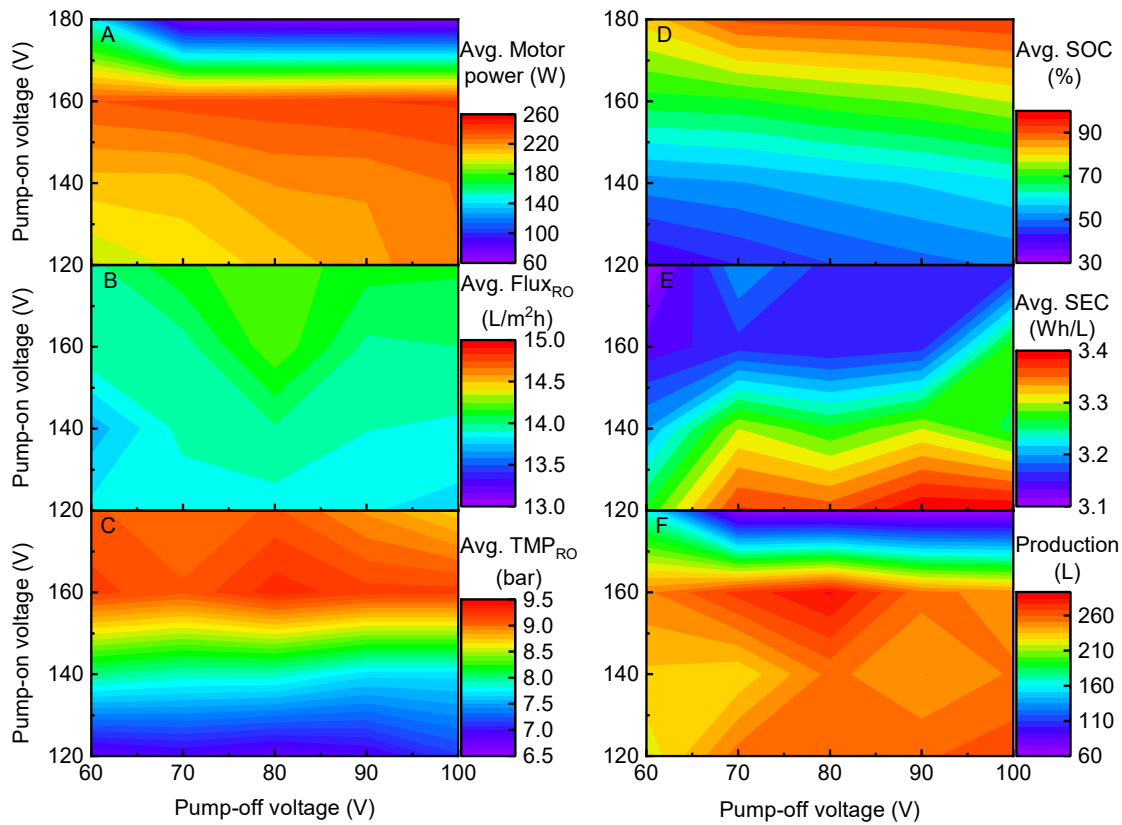


Figure 4-7: Contour plots of the pump-on and pump-off voltage thresholds with SCs and charge controller over five cycles (duration: 1h 50 m) showing (A) average motor power, (B) average flux_{RO}, (C) average TMP_{RO}, (D) average SOC, (E) average on-period SEC, and (F) cumulative permeate production. Adapted from [122], CC-BY-NC-ND 4.0 License.

From the above analysis, it can be seen that the system performs better at $V_{\text{pump_on}} = 160$ V, because the pump consumes less current to remain the desired pumping power during the discharging of SCs when comparing with low $V_{\text{pump_on}}$ (120 and 140 V). Therefore, the SC discharge time is extended, so that the on-period of the system is prolonged. However, the $V_{\text{pump_on}}$ threshold at 180 V results in the minimum average motor power (see Figure 4-7A) and the highest SOC, which indicates insufficient discharging behaviour (see Figure 4-7D). This high voltage threshold causes the pump to not be able to start, as the voltage is divided to charge the SCs. Consequently, the V_{PV} is too low to switch on the pump. Therefore, the PV output is used solely to charge the SCs and leads to less permeate production.

Compared to the pump-on voltage, the pump-off voltage has fewer effects on system performance. However, it is evident that a clear rising trend exists of permeate production with the increase of $V_{\text{pump_off}}$ (Figure 4-7F). This is because the charging rate is directly proportional to the voltage when the pump is off, and the higher $V_{\text{pump_off}}$ results in faster charging of SCs to reach the upper limit of SOC. As a result, the total off-period of the system is shortened, thus enabling more permeate to be produced. From the results, it can be concluded that the optimum system performance is achieved at $V_{\text{pump_on}} = 160$ V and

$V_{\text{pump_off}} = 90 \text{ V}$, in particular with respect to high cumulative permeate production (Figure 4-7F) and relatively low SEC (Figure 4-7E). Therefore, this indicates the optimal voltage threshold settings for the charge controller to achieve optimum performance at this BW30 membrane and feedwater salinity.

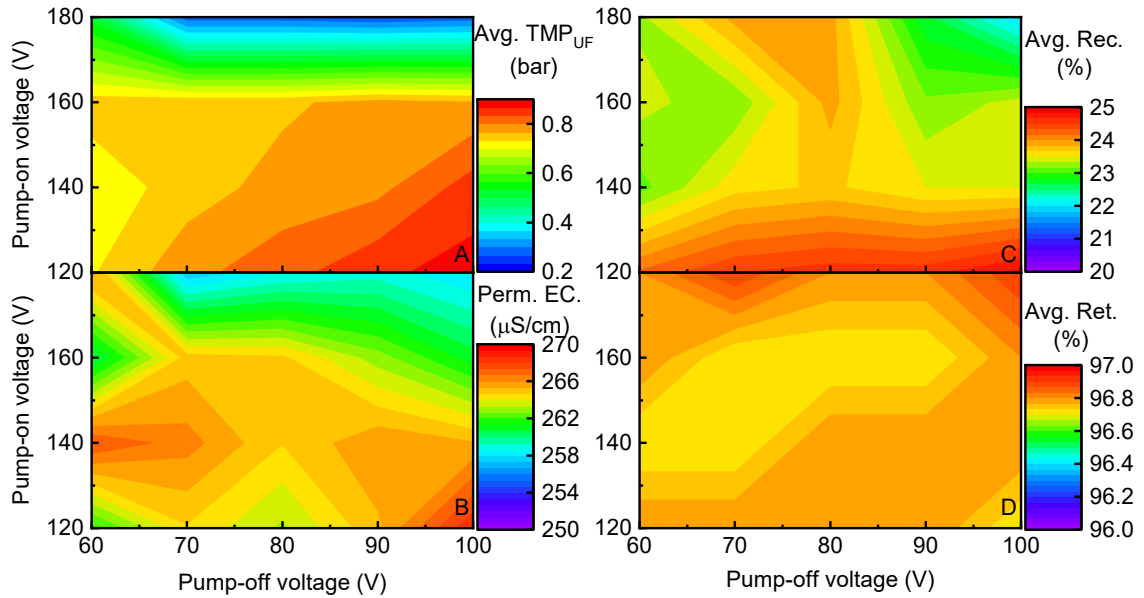


Figure 4-8: Contour plots of the pump-on and pump-off voltage thresholds with SCs and charge controller over five cycles (Duration: 1 h 50 min) showing (A) average TMP_{UF} , (B) average permeate EC, (C) average recovery, and (D) average retention. Adapted from [122], CC-BY-NC-ND 4.0 License.

Figure 4-8 presents the membrane performance parameters, including flux, permeate EC, recovery, and retention. The average TMP_{UF} (Figure 4-8A) follows the same trend as TMP_{RO} as discussed above. The permeate quality (Figure 4-8B) complies with the target WHO guideline, independent of the voltage threshold settings. Referring to Figure 4-8C, the average recovery is within the recommended limit of 30% to alleviate RO membrane fouling. These results further show that the constant set-point operating strategy at 10 bar based on this feedwater salinity and membrane enables the system to operate within the SOW [215]. Likewise, the average retention (Figure 4-8D) remains $> 96.5\%$ among all of these combinations of thresholds. This is supported by the fact that the additional electronics cannot make desalination more efficient, but the net benefits in the long-term would remain. For instance, system shut-down events due to intermittency of the RE source can be largely reduced. It is expected that the charge controller associated with energy storage units might also be advantageous for directly-coupled PV- or wind-powered systems, such as for water purification, water pumping, or ice-making systems [297, 298].

4.6. Summary

To fully understand the performance of the PV-membrane system when powered by solar energy, systematic ramp rates in SI and voltage tests were performed over a broad range of fluctuating conditions, which were extracted from real weather data under relatively extreme conditions. The system performed in a stable manner (flux > 2 L/m²h, retention > 90%, recovery > 10%) for a wide range of steady-state SI (300 – 1200 W/m²) by using 5 g/L NaCl and BW30 membrane, and it was capable of producing drinkable water that complied with the 1000 mg/L target. When applied with simulated ramp rates of voltage (5, 2, 1, 0.2, and 0.1 V/s), the system was operated with a 10 bar set-point at an average recovery (20-25%) lower than 30% to reduce fouling of the RO membrane. The system responds better to slow variations (ramp rates in PV voltage ≤ 0.5 V/s) compared with variations higher than 1 V/s, which are indicative of the most frequently occurring ramp rates under real weather conditions. It is demonstrated that good performance was achieved, with an average recovery of 21%, retention of 96.8%, flux of 11 L/m²h, and SEC of 3.3 Wh/L. Through the addition of SCs, an energy buffering charge controller was designed to control the on/off state of the pump and charging/discharging of the SCs. The charge controller can cope well with fairly extreme conditions, regardless of the variations of ramp rates. In addition, it improves resilience to periodic fluctuations, even in worst-case scenarios (ramp rate of 2 V/s). The SCs can bridge the power gap up to 6 min 20 s, thus providing additional energy to power the pump as necessary. Moreover, the pre-set voltage thresholds at $V_{\text{pump_on}} = 160 \text{ V}$ and $V_{\text{pump_off}} = 90 \text{ V}$ resulted in the PV-membrane system producing the greatest amount of clean drinking water at a low SEC.

The following chapter examines the impacts of real solar days with a variety of feedwater salinities and PV power capacities on PV-membrane system performance with and without SCs and charge controller, as well as the overall improvements in water quantity and quality and the decrease of system shut-down events. Testing the ability of the charge controller to deal with the fluctuations encountered over a range of different solar days is necessary to determine the effectiveness of energy buffering (charge controller with SCs) at reducing the system shut-downs and enhancing system resilience.

5. Effect of energy buffering control on reducing system shut-downs and enhancing resilience

The results of this chapter have been submitted to the journal Renewable Energy. The co-author Achim Voigt helped with solving the MPPT issues of the pump and design of the charge controller. The co-author Yang-Hui Cai helped with the system cleaning, the calculation of the error bars for the experimental results, review of the manuscript. The co-authors Andrea Schäfer and Bryce Richards were involved with the overall concept, design of the experiments, the interpretation of the experimental results and review of the manuscript.

In this chapter, to reduce the system shut-down events and enhance resilience, the PV-membrane system incorporated with SC energy buffering and charge controller was performed under real SI fluctuations and intermittency with high-temporal-resolution (1 s) on varied solar days (from sunny, partly cloudy, to very cloudy days). The goals of adding energy buffering control were to: i) reduce the number of system shut-down events ($\#_{SD}$) and duration (t_{SD}), which are known to be the most harmful to system performance; and ii) improve system resilience – represented by the cumulative TDS and SEC throughout the entire solar days, and quantified by resilience factor (RF) for dips in the SI (see Figure 3-5B). The following three main research questions were addressed:

- i) Can the SCs and charge controller enhance system resilience under varied full-length solar days, in particular with reducing $\#_{SD}$, t_{SD} , and SEC?;
- ii) What are the impacts of feed salinity on the ability of the SCs and charge controller to reduce $\#_{SD}$ and t_{SD} ?;
- iii) How does the amount of PV power available influence the ability of the SCs and charge controller to reduce $\#_{SD}$ and t_{SD} , and enhance system resilience?

5.1. Directly-coupled system resilience with different solar days

To evaluate the impacts of varied solar days (from sunny, partly cloudy, to very cloudy) on the resilience of the directly-coupled system, experiments with a feed salinity of 5 g/L at a rated PV capacity of 500 W were carried out, as shown in Figure 5-1. These results served as the baseline to enable the performance comparison when adding SCs and charge controller.

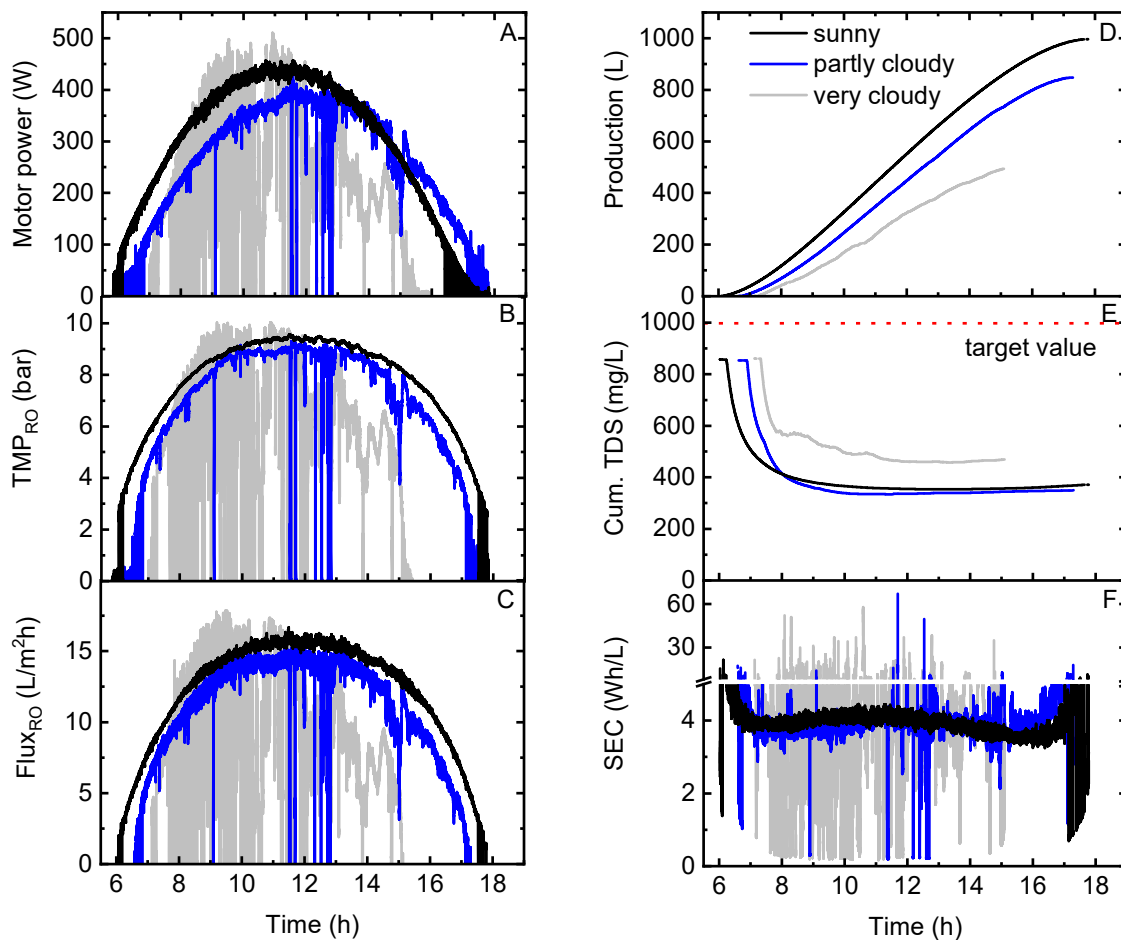


Figure 5-1: Experiments conducted using the PV-membrane system under three different solar days (BW30, 5 g/L NaCl at a rated PV capacity of 500 W): (A) motor power, (B) TMP_{RO} , (C) $flux_{RO}$, (D) cumulative permeate production, (E) cumulative TDS, and (F) SEC. Adapted from [286], CC-BY-NC-ND 4.0 License.. The target value – indicated by the dotted red line in (E) – of 1000 mg/L NaCl was taken from the WHO, where the drinking water becomes unpalatable at higher values [299].

As indicated in Figure 5-1A, system shut-downs were observed at $SI < 300 \text{ W/m}^2$, and pump motor power dropped to 0 W several times during both partly and very cloudy days. This sudden drop in power was also reflected in the TMP_{RO} and the flux (Figure 5-1B and C). Production on the sunny day (black curve in Figure 5-1D) exhibited the highest value of around 1000 L, which is approximately 150 L more than that on the partly cloudy day, and 50% higher than the production on the very cloudy day. These results emphasize the importance of having adequate average SI levels on system performance throughout the entire solar days (580, 545, and 430 W/m^2 on sunny, partly cloudy, and very cloudy days, respectively) to produce sufficient permeate to increase productivity. As can be seen in Figure 5-1E, cumulative TDS decreased from the initially high value produced when the system was switched on from 6:00 to 7:50 (on all days), subsequently decreased gradually until 14:00 once the SI rose above 500 W/m^2 at around 8:00, and

went up again by the end of the day due to the limited permeate volume with low quality produced at the decreasing SI. From 8:00 to 11:00 on the very cloudy day, the gradually decreasing TDS values (grey curves in Figure 5-1E) during rapid fluctuations indicated that system performance had not fully recovered to its original level after disruptions [300]. It can be further seen from the average SEC values on the very cloudy day (average SEC of 4.6, 3.8 and 4.0 Wh/L on very cloudy, partly cloudy and sunny day, respectively as shown in Table 5-2) that the SEC exhibited the most severe fluctuations, indicating the impacts of flux variations caused by fluctuations of power input. These observations are in accordance with previous study [39] that discussed for the cumulative water production on the solar days.

The $\#_{SD}$ and t_{SD} are summarized in Table 5-1 to quantify system resilience throughout the three varied solar days. Due to the fairly good weather conditions on the clear sunny day, no shut-down events were observed. On the partly cloudy day, eight shut-down events with a total down-time of 5.4 min occurred; whereas, on the very cloudy day, $\#_{SD}$ and t_{SD} increased markedly to 85 and 119 min, respectively.

Table 5-1: Directly-coupled PV-membrane system shut-down events under three entire solar days. Adapted from [286], CC BY-NC-ND 4.0 License.

Solar days	$\#_{SD}$ (-)	t_{SD} (min)
Sunny	0	0
Partly cloudy	8	5.4
Very cloudy	85	119

Overall, the directly-coupled system resilience throughout the three solar days is presented in the following manner: i) quantifications of both $\#_{SD}$ and t_{SD} with adequate adaptive capacity, indicating the potential for including short-term (in the order of a few minutes) energy buffering (e.g., SCs) to enhance system resilience; ii) recovery of flux fluctuations that affect permeate production; iii) qualified permeate TDS that complies with the targeted value as a result of the use of a tight RO membrane (BW30); and iv) appropriate average SEC values (3.8 – 4.6 Wh/L) that enable operations during fluctuations that exhibit varied SI levels from sunny to very cloudy days. In the next section, the system performance with SCs and charge controller, evaluation of shut-down events and resilience are compared with the directly-coupled PV-membrane system.

5.2. System resilience with SCs and charge controller

The potential of the SCs and charge controller to improve system resilience under three solar days was examined, in particular with reducing $\#_{SD}$, t_{SD} , and improving SEC. Experiments were carried out with SCs and charge controller (see detailed graphs in Figure 5-2 - Figure 5-4), and then compared with the

directly-coupled reference case described above. These results are summarized in Figure 5-5 for further comparison.

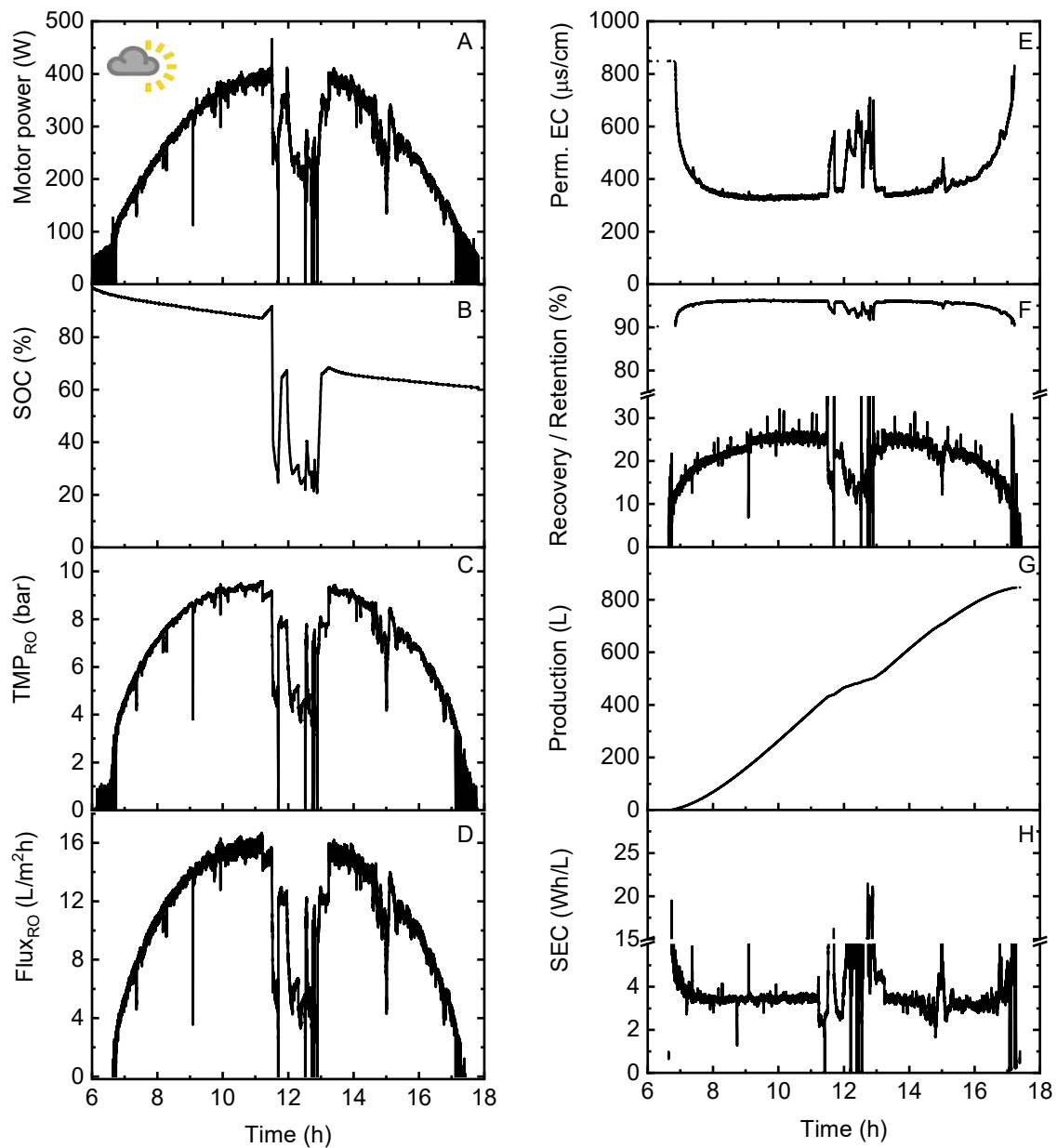


Figure 5-2: PV-membrane system performance with SCs and charge controller buffering under the partly cloudy day, illustrating (A) motor power, (B) SOC, (C) TMP_{RO} , (D) $flux_{RO}$, (E) permeate EC, (F) retention / recovery, (G) production, and (H) SEC. Adapted from [286], CC-BY-NC-ND 4.0 License.

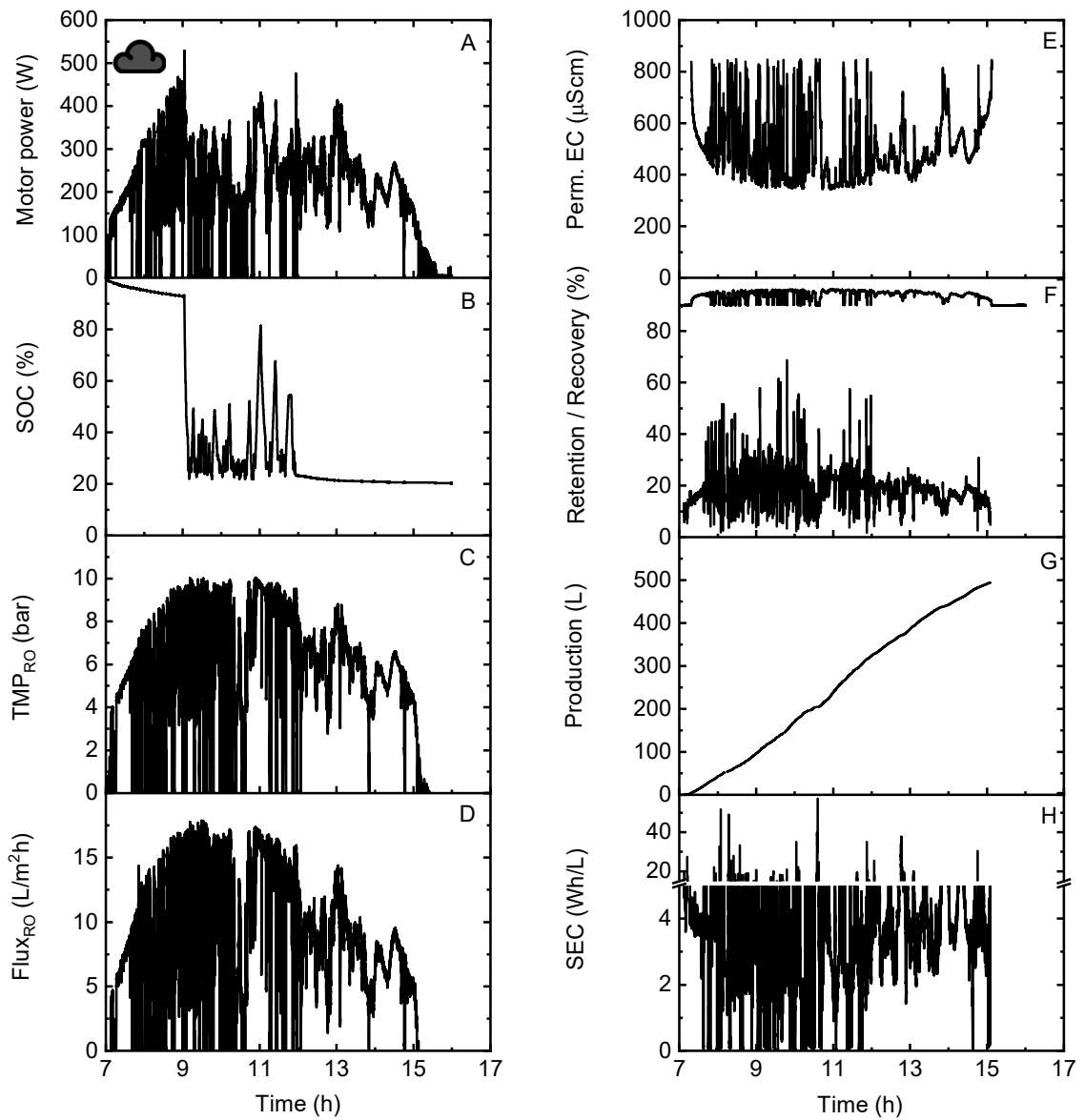


Figure 5-3: PV-membrane system performance with SCs and charge controller buffering under the very cloudy day, illustrating (A) motor power, (B) SOC, (C) TMP_{RO} , (D) $flux_{RO}$, (E) permeate EC, (F) retention / recovery, (G) production, and (H) SEC. Adapted from [286], CC-BY-NC-ND 4.0 License.

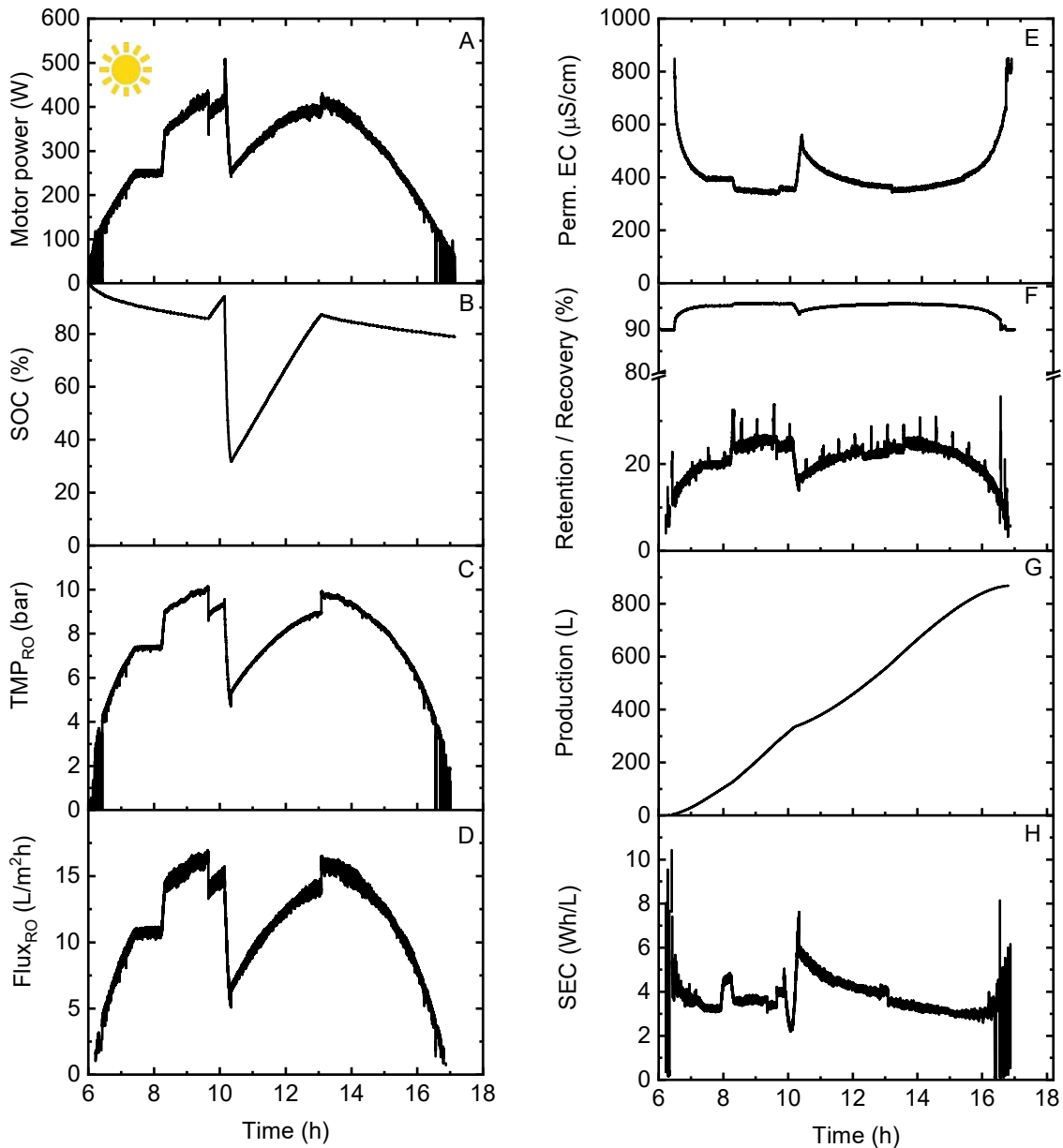


Figure 5-4: PV-membrane system performance system performance with SCs and charge controller buffering under the sunny day, illustrating (A) motor power, (B) SOC, (C) TMP_{RO} , (D) $flux_{RO}$, (E) permeate EC, (F) retention / recovery, (G) production, and (H) SEC. Adapted from [286], CC-BY-NC-ND 4.0 License.

As indicated in Figure 5-5A and B, with the addition of SCs and charge controller on the partly and very cloudy day, the $\#_{SD}$ was reduced by 2 – 13 events, while the t_{SD} was improved by 37% and 12%, respectively. The employment of SCs and charge controller exhibit little difference to the production on the three solar days (Figure 5-5C), which is likely attributed to: i) the small energy capacities of the SCs; and ii) that the incorporation of the energy storage component to the system did not make it more efficient, in particular a small decline in production was observed on the sunny day. Regarding the SEC, it was

improved by 22% and 8% on the very cloudy and sunny day, respectively, but showed a comparable value on the partly cloudy day (Figure 5-5D). This suggests that the overall reduction of motor power consumption (W) plays a major role in reducing the SEC, which outweighs the impacts of limited increase of permeate production (L). Note that the pressure (3%) and temperature variations (2.4%) contribute to the total relative system error of 3% by using Eq. 3-32, and this value is used throughout for the other error calculations. The calculated relative error for the flux is 0.5%, while current (2%) and voltage variations (1.3%) result in the power variations.

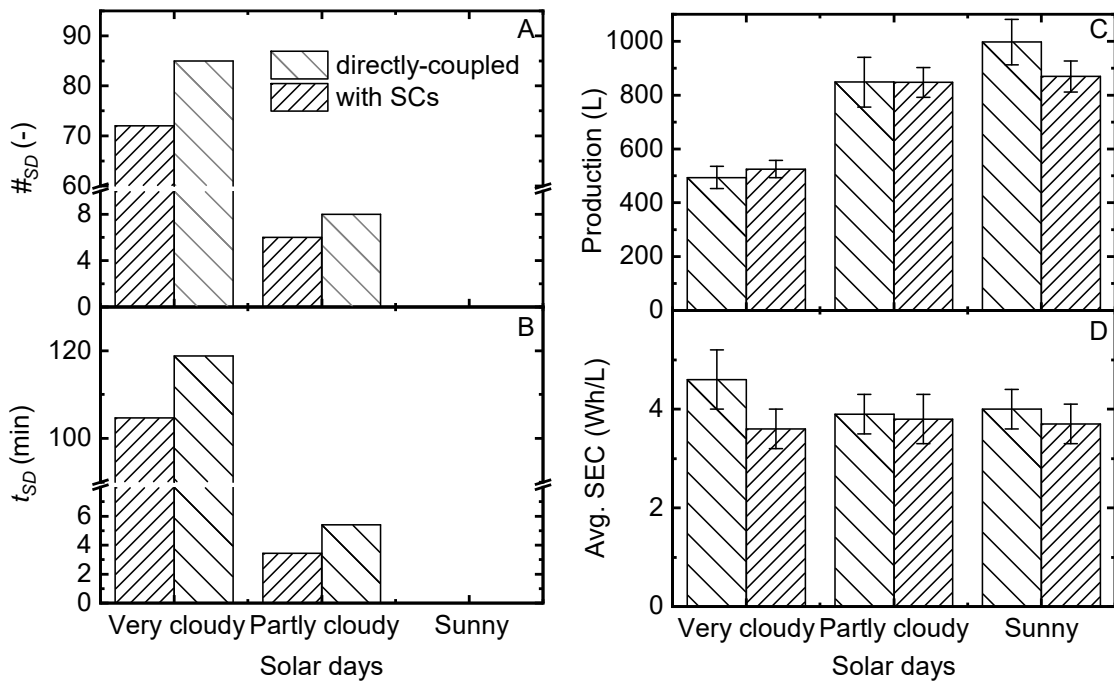


Figure 5-5: Bar plots of the PV-membrane system performance with/without SCs and charge controller over very cloudy, partly cloudy, and sunny days, illustrating (A) #_{SD}, (B) t_{SD}, (C) production, and (D) average SEC. Adapted from [286], CC BY-NC-ND 4.0 License. The error bars are calculated based on the error propagations in Section 3.8.

The cumulative and average performance of the PV-membrane system under the three solar days in terms of the two operation modes are summarized in Table 5-2. Overall, the variations of flux (determined the #_{SD} and t_{SD}) were caused by the changes of pump power consumption that is dominantly influenced during the cloudy hours. To examine system control with SCs buffering and charge controller in more depth, the electrical characteristics of system performance during highly variable fluctuations with a duration of approximately 90 min (see Figure 5-6A) were investigated, as indicated in Figure 5-6. At this point, recall that the experiment was started at around 11:00 when SI reaches 800 W/m² and with fully charged SCs (V_{SCs} = 177 V).

Table 5-2: Summary of the PV-membrane system performance with two operation modes under three solar days with a rated PV capacity of 500 W at a feed salinity of 5 g/L NaCl [286].

Solar days	Operation modes	# _{SD}	<i>t</i> _{SD}	Avg. SEC	Cum. production	Avg. motor power	Avg. SOC
		(-)	(min)	(Wh/L)	(L)	(W)	(%)
Sunny	with SCs	0	0	3.7	870	289	80
	directly-coupled	0	0	4.0	997	312	–
Partly cloudy	with SCs	6	3.4	3.8	847	253	73
	directly-coupled	8	5.4	3.8	848	255	–
Very cloudy	with SCs	72	105	3.6	525	195	43
	directly-coupled	85	119	4.6	494	227	–

As shown in Figure 5-6A, when the SI started to decrease at dip ① from 850 to 200 W/m², the pump consumes ~ 500 W (Figure 5-6B) due to the prompt discharge of SCs, then steadily decreased until reaching the $V_{\text{charging_off}}$. Subsequently, the SI was bounced back to the high level at around 870 W/m², the V_{PV} and V_{pump} (Figure 5-6C) rose to $V_{\text{pump_on}}$ (120 V) and remained stable at this stage until encountering the next periods of fluctuations (e.g. dip ②). This can be explained from the system voltages and currents (Figure 5-6C and D), as well as the SOC (Figure 5-6E). Referring to Figure 5-6D, the SCs discharged to the pump promptly (added I_{sc} to I_{pump} at small I_{PV} at low SI). The small I_{sc} values (flat blue curves in Figure 5-6D) occurred at the time that the I_{PV} was solely powered to the pump, after which the SI returned to high levels after fluctuations. It corresponds to around 10 W (error calculated to be ~ 3.3%) of power consumption at the V_{SC} value (blue curves in Figure 5-6C), which contributes to approximately 2% of power loss. Two shut-downs occurred (see Figure 5-6B) at dips ⑥ and ⑧ when reaching the lower limit of $V_{\text{charging_off}}$ (pre-set value at 80 V), which equals 20% of SOC. As a result, the I_{PV} is only sufficient to charge the SCs (blue curves rising in Figure 5-6D), and 20% of the energy (Figure 5-6E) is unused to prevent power oscillations of the pump as a consequence of the charging requirement of the SCs at this rated PV capacity of 500 W. It is estimated to exhibit a maximum power consumption up to approximately 170 W on the PTC lamp (assuming 330 W power consumption at the set-point of 10 bar without lamp included [278]).

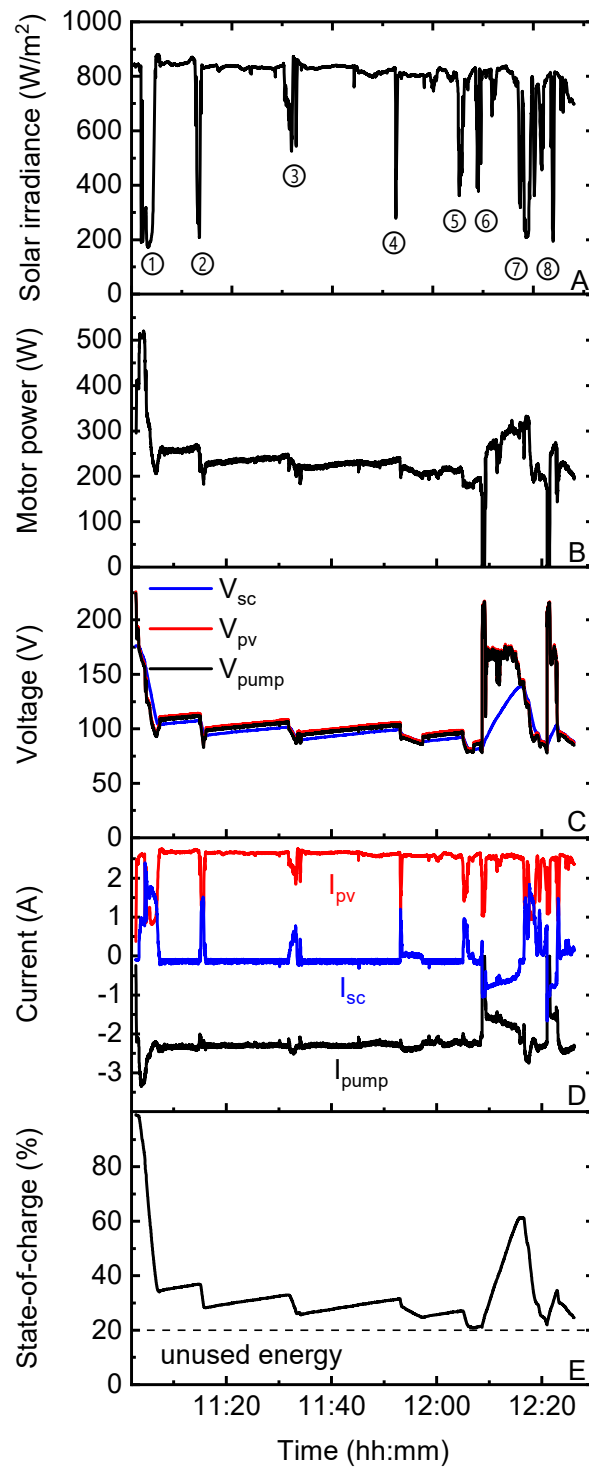


Figure 5-6: PV-membrane system electrical performance in the middle of the partly cloudy day (11:00 – 12:30) with SCs and charge controller at a rated PV capacity of 500 W (BW30+5 g/L NaCl). (A) solar irradiance, (B) motor power, (C) system voltages (V_{pump} , V_{SCs} and V_{PV}), (D) system currents (I_{pump} , I_{SCs} and I_{PV}), and (E) state-of-charge. Adapted from [286], CC BY-NC-ND 4.0 License..

The above discussions demonstrated the power distribution among the PV, pump and SCs with the charge controller during the 90 min periods, and the charge controller based on the pre-set voltage sensing thresholds enabled the SCs buffering in minutes' timescales during severe fluctuations in SI. In the next section, the system shut-down events and resilience factor of flux (RF_{flux}) at this time window as a function of feed salinity were examined.

5.3. Impact of feed salinity on system resilience with/without SCs buffering control

To elucidate the impacts of feed salinity on the ability of the SCs and charge controller to reduce $\#_{SD}$ and t_{SD} , and enhance system resilience, Figure 5-7 shows the experiments with varied salinities of 1, 2.5, 5, 7.5, and 10 g/L NaCl at the same rated PV capacity of 500 W.

For the directly-coupled system setup, as indicated in Figure 5-7A and B, the $\#_{SD}$ and t_{SD} (see grey triangles) showed a rising pattern when increasing the feed salinity from 2.5 to 7.5 g/L; whereas, the $\#_{SD}$ and t_{SD} values remained the same at the feed salinity of 1 and 2.5 g/L, 7.5 and 10 g/L, respectively. The average $RF_{flux} < 0.2$ (Figure 5-7C) at the feed salinity of 7.5 and 10 g/L reflect the low resilience of the PV-membrane system during this 90-min fluctuation. This occurs as the flux decreases to 0 L/m²h at high feed salinity due to high osmotic pressure (6.3 and 8.2 bar for 7.5 and 10 g/L NaCl, respectively). In summary, increasing feed salinity resulted in the increased system shut-down events and reduced resilience. This occurred as higher driving force is needed to overcome the increased osmotic pressure of the feed water at high salinity.

With the addition of the SCs and charge controller, the $\#_{SD}$ is reduced by 1- 4 events at the feed salinity ≥ 2.5 g/L. However, the $\#_{SD}$ at 1 g/L NaCl is increased by 1 event (black square in Figure 5-7A). This occurred because the SCs discharged excessively at dip ① (see Figure 3-5B), and thus the I_{PV} is needed to charge the SCs once $V_{PV} < V_{charging_on}$ (pre-set value of 140 V) when the pump is subjected to the other fluctuations (low V_{PV}), causing one more system shut-down at dip ⑤. The t_{SD} is restricted to a range between 1 – 4.5 min at the feed salinity ≤ 7.5 g/L; whereas, the duration is increased markedly at the feed salinity of 10 g/L (with $\#_{SD}$ reduced once at dip ①). This occurred due to the fact that the high salinity at 10 g/L resulted in low flux compared to lower feed salinities. While t_{SD} was prolonged due to the requirement for charging the SCs, and the pump can only be restarted when V_{PV} reaches 120 V (V_{pump_on}). Looking at Figure 5-7C, the RF_{flux} values close to 0.3 at the feed salinity ≤ 5 g/L reflect the enhancement of system resilience. It was noted that the RF values were still far from unity, which were caused by the limited energy storage capacity of SCs and PV power. Nevertheless, RF_{flux} decreased at feed salinity of 7.5 and 10 g/L NaCl, which suggested the flux was less resilient to power variations after energy buffering. Moreover, it also indicated the low adaptive capacity ($C_{ada.}$) needed to maintain the original system performance at a

new performance level after fluctuations. These findings primarily were caused by the low PV power capacity, pressure limitation of the pump, and low flux (average and cumulative values provided in Table 5-3).

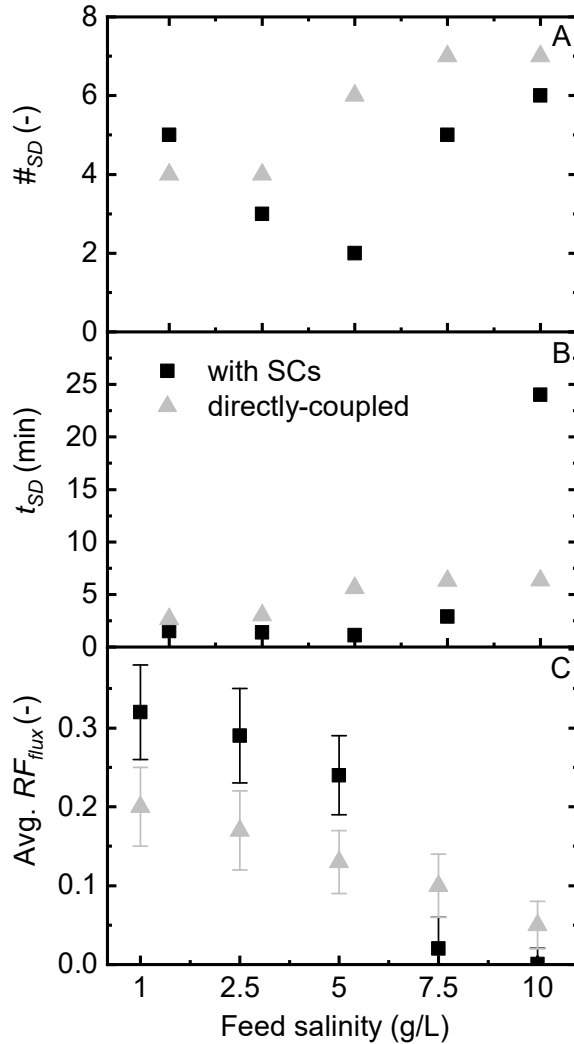


Figure 5-7: Impact of feed salinity on system resilience with/without SCs buffering control during the highly variable 90-min period with large SI fluctuations in the middle of the partly cloudy day (a rated PV capacity of 500 W): (A) $\#_{SD}$, (B) t_{SD} , (C) average RF_{flux} . Note that the averaged RF values in flux are taken from the values at each peak from ① - ⑧, as shown in Figure 3-5B. Adapted from [286], CC BY-NC-ND 4.0 License. The error bars were calculated by using error propagations (see Section 3.8).

Table 5-3: Average and cumulative performance of the PV-membrane system with/without SCs and charge controller under highly variable fluctuations with varied feed salinities on the partly cloudy day at a rated PV capacity of 500 W. Adapted from [286], CC BY-NC-ND 4.0 License.

Feed salinity (g/L)	Operation modes	Avg. motor power (W)	Avg. TMP_{RO} (bar)	Avg. SOC (%)	Cum. production (L)
1	with SCs	256	5.4	38	126
	directly-coupled	380	8.5	–	176
2.5	with SCs	263	5.9	40	105
	directly-coupled	380	8.4	–	155
5	with SCs	225	5.3	31	72
	directly-coupled	375	8.2	–	132
7.5	With SCs	256	5.5	39	41
	directly-coupled	386	8.1	–	95
10	with SCs	245	5.2	34	20
	directly-coupled	379	9.1	–	75

It is anticipated that the system should be able to adapt to the fluctuations when adding SCs and charge controller, however, this was not achievable at these high salinities due to i) the limited rated PV capacity to power the pump and provide the I_{PV} to the SCs (strong power source) simultaneously; and ii) small energy storage capacity in SCs, indicating the demand to increase the energy capacity of the storage units (e.g. more SCs in parallel or batteries). For this reason, in the next section, to investigate how it influences the ability of SCs and charge controller to reduce system shut-downs and improve system resilience, the PV capacity was varied in a wide range.

5.4. Impact of PV power capacity on system resilience with SCs buffering control

To examine how PV power capacity affects the ability of SCs and charge controller to reduce system shut-downs and improve system resilience to power variations, experiments were carried out by varying the PV power capacity over a wide range (300, 400, 600, 800, and 1000 W) at the feed salinity of 5 g/L under 90-min fluctuating conditions on the partly cloudy day (plotted in Figure 5-8).

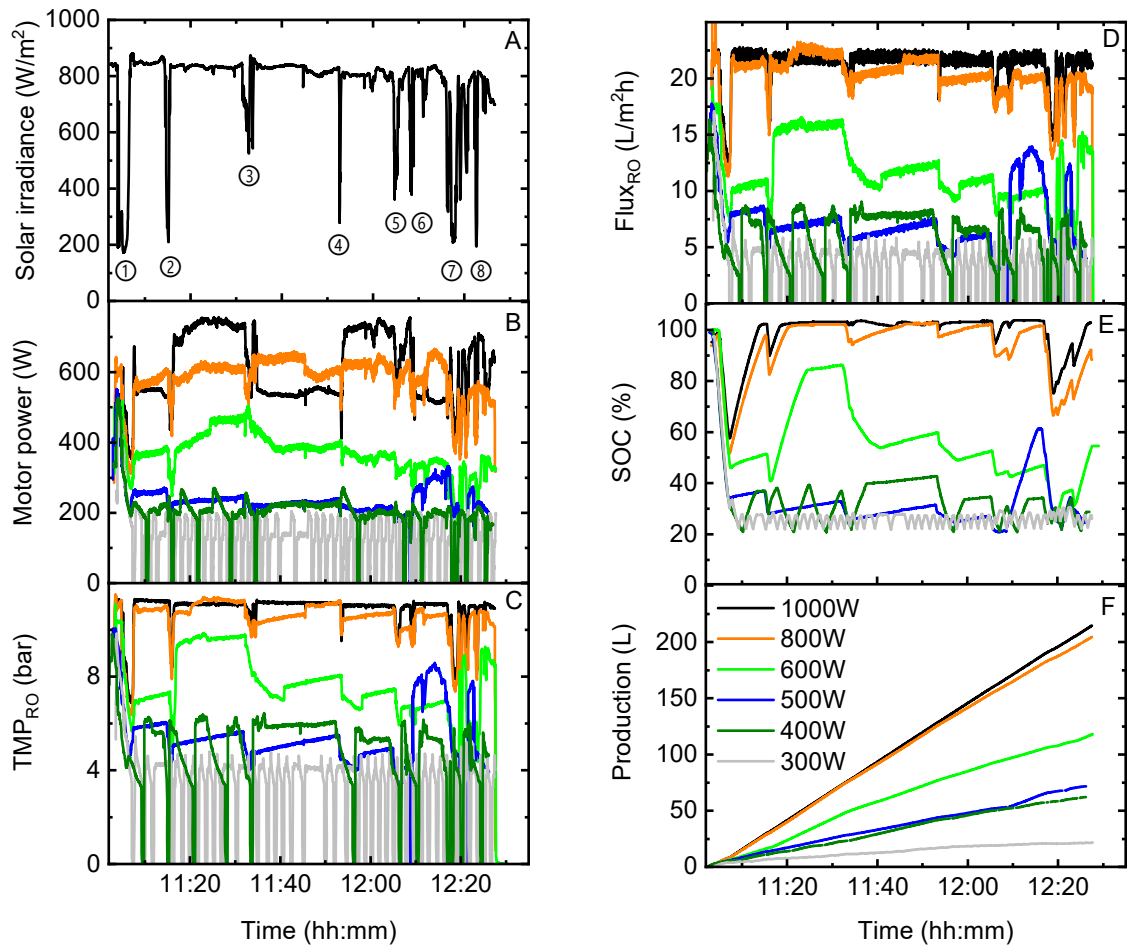


Figure 5-8: Performance of the PV-membrane system with SCs and charge controller under highly variable fluctuations on the partly cloudy day as a function of PV power capacity (BW30+5 g/L NaCl), illustrating (A) solar irradiance, (B) motor power, (C) TMP_{RO} , (D) $flux_{RO}$, (E) state-of-charge, and (F) production. Adapted from [286], CC BY-NC-ND 4.0 License.

For a PV capacity < 500 W, the motor power dropped to zero several times (see Figure 5-8A), and along with zero TMP_{RO} and flux (see Figure 5-8B and C), which implies the occurrence of shut-down events. This occurred as the small PV power was not able to charge the SCs and drive the pump simultaneously. While for a PV power capacity ≥ 600 W, the high motor power (see Figure 5-8A, average value > 300 W as shown in Table 5-4) allows a high TMP_{RO} to be obtained to overcome the osmotic pressure of the feed water (approximately 4 bar) and results in high flux (Figure 5-8B and C) and production (Figure 5-8D). No system shut-downs are observed when adding SCs and charge controller. This reduced system off-time (hence reduce loading on electronics) avoids wear on the pump motor due to constant restarting, as a result, pump duty point is continuously optimised based on the input power available. Whereas, several shut-down events are still observed on the directly-coupled system. The lower limit of SOC (see the lowest dips in Figure 5-8D for buffering) shows a declining trend from 55 – 20% when decreasing PV power capacity from 1000 to 300 W. It suggests that SCs are fully discharged when less power is available from

PV and maximum power withdrew from the pump. Subsequently, a detailed description of the charging/discharging mechanism in terms of the pre-set voltage sensing thresholds is discussed (current-voltage curves plotted in Figure 5-9).

At the reference case ($I_{mpp} = 2.7$ A, PV = 500 W), the V_{PV} returns back to high voltage ranging from 180 – 210 V (see Figure 5-9D) once the SCs are fully discharged at $V_{charging_off} = 80$ V (SOC reaching a lower limit of 20%) at dip ⑥ (shut-down in Figure 5-6). However, I_{PV} only reached ~1.1 A (depending on the SI levels), which is too small to provide current for the pump and charging SCs. It can be seen that the 400 W case ($I_{mpp} = 2.1$ A) exhibited higher TMP_{RO} and flux than those (dark green vs. dark blue curves in Figure 5-8B and C) in the 500 W case during the first five fluctuations (dips ① - ⑤) over the on-periods of the motor power. This occurred several times after the system shut-downs, and the TMP_{RO} momentarily returned back to the status of the directly-coupled configuration (SCs disconnected) for a short period of time until $V_{PV} > V_{charging_on}$. The same phenomenon occurred when the TMP_{RO} (and thus flux) at 500 W surpassed the values at 400 W once the system shut off at the dip ⑥. However, more frequent occurrence of system shut-downs at 400 W (zero current in Figure 5-9E) suggested a poorer ability of the charge controller and SCs for reducing the system shut-down events. This becomes more obvious for the 300 W case, with more frequent oscillations being observed in Figure 5-9F. In the 600 W case, the high I_{PV} was capable of charging the SCs continuously (with SOC > 40%, see light green curve in Figure 5-8E) without system shut-downs, i.e., 3 – 30% of I_{PV} was used to charge the SCs (calculated from Figure 5-9C). As a result, the SCs was discharged to the pump (SOC dropping from approximately 50% to 30%) when the V_{PV} dropped to 80 V at dip ③. Thus, this PV power capacity enables better system performance under SCs buffering control than that in the 500 W case. The benefits of powering with high PV capacity become more evident on the 800 and 1000 W cases, which can be shown by: i) zero occurrence of shut-down events; and ii) the SOC reaches up to 100% when SI increases to the 800 W/m² once again. At a PV capacity of 1000 W, the pump consumed up to 750 W for significant periods of time, and this high power consumption occurred while SOC reaches approximately 100% (see the black curves in Figure 5-8E). As a result, all of the I_{PV} is provided to the pump (see Figure 5-9A) that extracts as much current as it needs. The disadvantage would be the induced power loss across the lamp (estimated to be approximately 400 W) during this period where SOC reaches up to 100%. Whereas, shut-down events are significantly improved. Overall, increasing the PV power capacity plays a big role in reducing the system shut-down events and improve resilience.

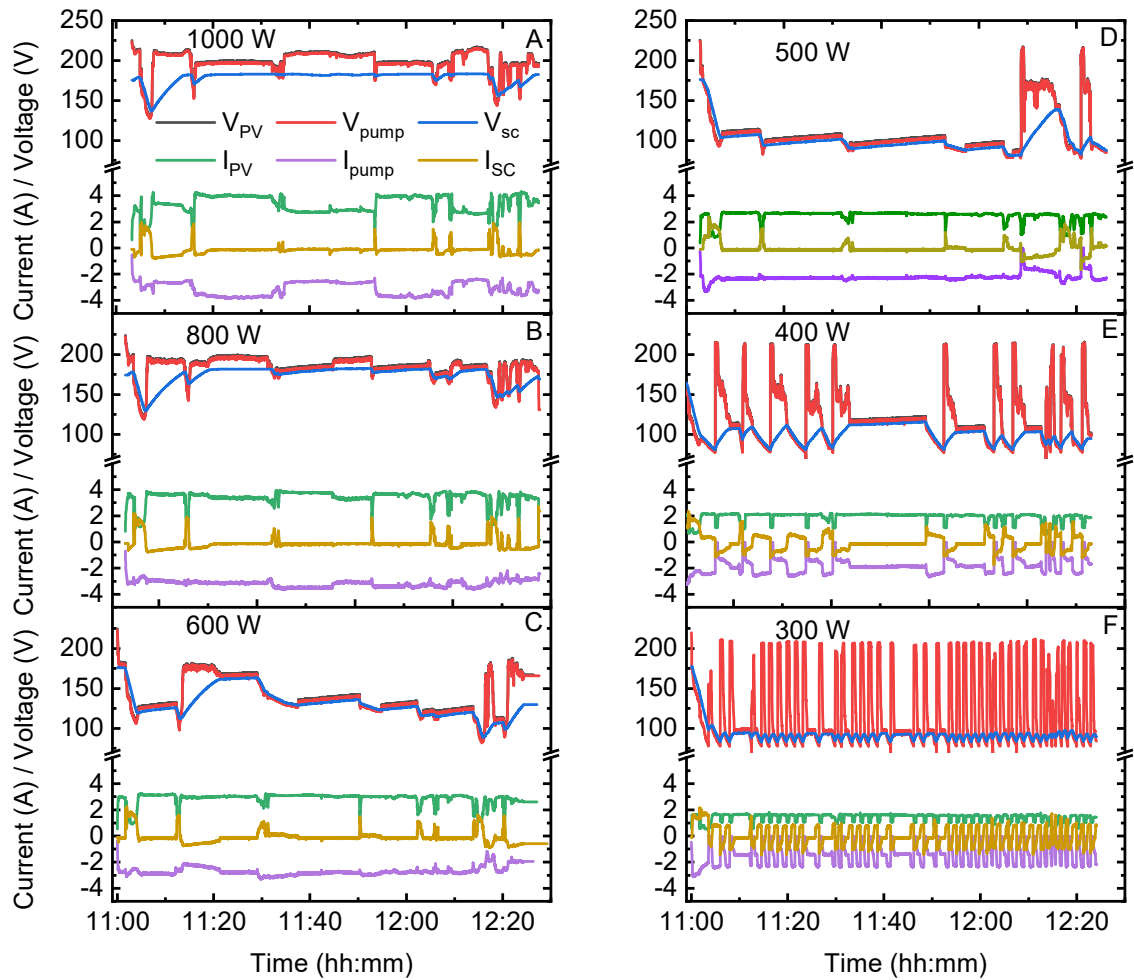


Figure 5-9: Current-voltage curves of the PV-membrane system under highly variable fluctuations on the partly cloudy day at varied PV power capacity with SCs and charge controller (5 g/L NaCl): (A – F) 1000 – 300 W. Adapted from [286], CC BY-NC-ND 4.0 License.

The cumulative and average system performance with/without SCs and charge controller in terms of varied PV power capacity under highly variable fluctuations on the partly cloudy day are summarized in Table 5-4. When compared with the directly-coupled system configuration, the $\#_{SD}$ and t_{SD} are largely improved at PV power capacity ≥ 500 W. The advantages of increasing the PV power capacity can be seen from the increase of permeate flux and production, while no large differences of SEC occur, even when doubling the PV power from 500 to 1000 W. The high SOC values ($> 50\%$) at PV power ≥ 600 W indicate the sufficient charging photocurrent from the PV resource that results in zero system shut-downs. On the other hand, the low values of approximately 34% suggest deep discharging behaviors of the SCs to supply additional energy to the system due to less energy from the PV resource.

Table 5-4: Cumulative and average system performance with SCs buffering and charge controller in terms of varied PV power capacity. Adapted from [286], CC BY-NC-ND 4.0 License.

PV power (W)	Operation modes	# _{SD} (-)	<i>t</i> _{SD} (min)	Avg. motor power (W)	Avg. <i>flux</i> _{RO} (L/m ² h)	Avg. TMP _{RO} (bar)	Avg. SOC (%)	Avg. SEC (Wh/L)	Production (L)	Avg. perm. EC (μS/cm)	Avg. <i>RF</i> _{flux} (-)
1000	with SCs	0	0	611	21.0	10.9	98.4	4.0	243	334	0.75
	directly-coupled	2	1.6	543	18.0	10.3	–	4.2	177	361	0.42
800	with SCs	0	0	583	18.8	10.7	96.9	4.3	189	325	0.73
	directly-coupled	4	2.1	569	18.2	10.6	–	4.7	180	343	0.27
600	with SCs	0	0	366	12.1	7.5	54.4	4.3	119	379	0.57
	directly-coupled	5	2.9	450	16.3	9.6	–	4.3	161	360	0.21
500	with SCs	2	1.1	235	7.2	5.4	33.2	4.8	72	440	0.24
	directly-coupled	5	5.9	377	14.0	8.2	–	4.0	146	365	0.13
400	with SCs	11	6.7	198	6.5	4.9	33.8	4.6	62	446	0
	directly-coupled	7	7.1	303	11.6	6.9	–	4.0	115	429	0.07
300	with SCs	42	23	124	4.6	3.0	34.2	4.2	41	766	0
	directly-coupled	7	8.9	227	8.5	5.5	–	4.0	83	512	0.05

In order to quantify the above observations in system shut-down events and resilience of flux, the #_{SD} and *t*_{SD}, average *RF*_{flux} have been examined as a function of PV power capacity. The averaged results at all fluctuations (dips ① - ⑧ in Figure 3-5B) with BW30 at the feed salinity of 5 g/L NaCl are plotted in Figure 5-10.

As shown in Figure 5-10A and B, #_{SD} and *t*_{SD} exhibited a decreasing trend with the increase of PV power capacity, irrespective of system configuration. When the SCs and charge controller were added, the #_{SD} were increased at low PV capacity < 500 W, and the reasons have been explained above. Over all of the fluctuations (dips from ① - ⑧ in Figure 3-5B), the averaged *RF*_{flux} (> 0.3, see Figure 5-10C) increased primarily at PV power ≥ 500 W; in particular, the values rose to 0.8 with the addition of the SCs and charge controller. The improvement is attributed to i) higher initial flux (*F*₀) caused by high driving force from the pump; ii) higher flux after recovery (high *F*_r); and iii) the improved flux after disruption (*F*_d) due to the energy buffering of SCs at low SI. Consequently, the PV-membrane system is more resilient with a high PV capacity as well as the SCs and charge controller. In summary, the #_{SD}, *t*_{SD} and average *RF*_{flux} during

the severe fluctuations confirmed that the system shut-downs and resilience were improved via increasing the PV power capacity, albeit at increased initial investment cost. With this SCs energy capacity (21 Wh), it is found that at PV power of 800 W leads to a better capacity for both operating system (no shut-down events) and buffering fluctuations (more resilient system). Nevertheless, the increased costs are difficult to quantify to derive an overall water cost depending, among other things, on the feed water quality in different locations and the average SI levels on site. Furthermore, higher energy capacity SCs can be used for buffering longer period of fluctuations for the future work in the PV-membrane systems.

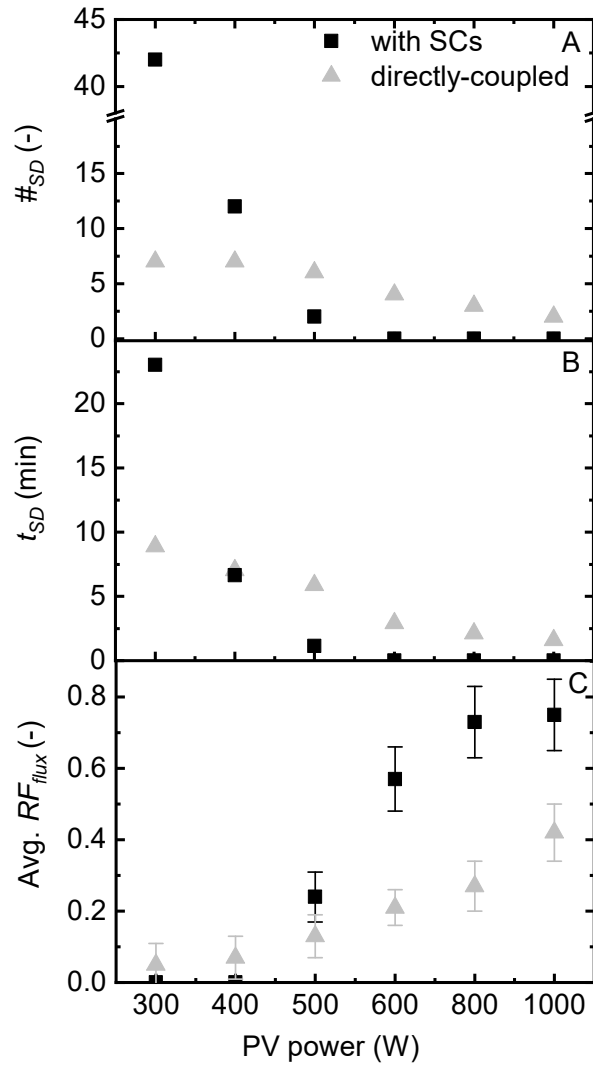


Figure 5-10: Resilience factor as a function of PV power capacity in the PV-membrane system with/without SCs buffering control during the highly variable 90-min period with large SI fluctuations in the middle of the partly cloudy day (A) $\#_{SD}$, (B) t_{SD} , and (C) average RF_{flux} . Adapted from [286], CC BY-NC-ND 4.0 License. The error bars were estimated by using error propagation method (see Section 3.8).

5.5. Summary

In this chapter, the potential of SCs energy buffering and charge controller to reduce system shut-down events and enhance system resilience was studied under varied full-length solar days (sunny, partly cloudy, and very cloudy days). The quantification of system resilience – $\#_{SD}$, t_{SD} , cumulative TDS, as well as average RF_{flux} under 90 min of SI fluctuations – were conducted with two operation modes (directly-coupled, with SCs and charge controller).

The directly-coupled PV-membrane system at a rated PV capacity of 500 W when treating 5 g/L NaCl, the system was demonstrated to be more resilient on the partly cloudy and sunny days than on the very cloudy day due to the small duration of fluctuations. Once the SCs and charge controller were added, t_{SD} was reduced by 37% and 12% on the partly cloudy and very cloudy day, respectively. While the $\#_{SD}$ was reduced by 2 – 13 events on the same two solar days. The average SEC was improved by 22% and 8% on the very cloudy and sunny day, respectively, with comparable SEC values on the partly cloudy day. During the high 90-min fluctuations on the partly cloudy day when incorporating the SCs and charge controller, RF_{flux} values increased to approximately 0.3 at the feed salinity ≤ 5 g/L; whereas, it exhibited the opposite trend at the feed salinity of 7.5 and 10 g/L. It is concluded that the PV-membrane system is more resilient to flux variations with energy buffering up to salinity of 5 g/L, but limited to the high feed salinity at 7.5 and 10 g/L NaCl based on the rated PV = 500 W. When varying the PV power capacity, no system shut-down events were observed at PV power capacity ≥ 600 W, and RF_{flux} values increased from 0.3 to 0.8, both of which indicate the system is more resilient to variations in SI when incorporating with high PV capacity. These findings demonstrate the ability of the charge controller and SCs buffering to reduce system shut-downs and enhance resilience when the system is subjected to fluctuations and intermittencies over a range of different solar days.

6. Energy consumption analysis of system backwashing

The results of this chapter have been published in Separation and Purification Technology, 287, 120388, (2022) [266]. The co-author Michele Milia helped with the backwashing setup and conducted the experiments for Section 6.1. The co-authors Andrea Schäfer and Bryce Richards were involved with the overall concept design, the interpretation of the experimental results and review of the manuscript.

This chapter aims to investigate the energy consumption of different BW implementations on the performance of the PV-membrane system. The two BW configurations were both implemented in between the UF and RO membrane modules: i) a bladder tank; and ii) a dedicated BW pump placed inside of a UF permeate tank powered by SCs.

The PV-membrane system was tested both at constant solar irradiance ($SI = 1000 \text{ W/m}^2$) and under real weather conditions with periodic backwashing. The following research questions were addressed:

- i) Which BW configuration is more energy-efficient for UF membrane backwashing when operating under varied weather conditions?;
- ii) What are the impacts of BW interval using the bladder tank on system TSEC with induced bentonite fouling?;
- iii) What is the E_{BW} when the pressure drop across the valve (using clean water) can simulate the TMP increase of UF membrane (ΔTMP_{UF}) induced by using a fouling agent (bentonite)?

6.1. Energy consumption with “simulated fouling”

In this section, the experiments were carried out with two different BW configurations via using the simulated valve to obtain a TMP_{UF} of approximately 1 bar. The results are provided in Figure 6-1.

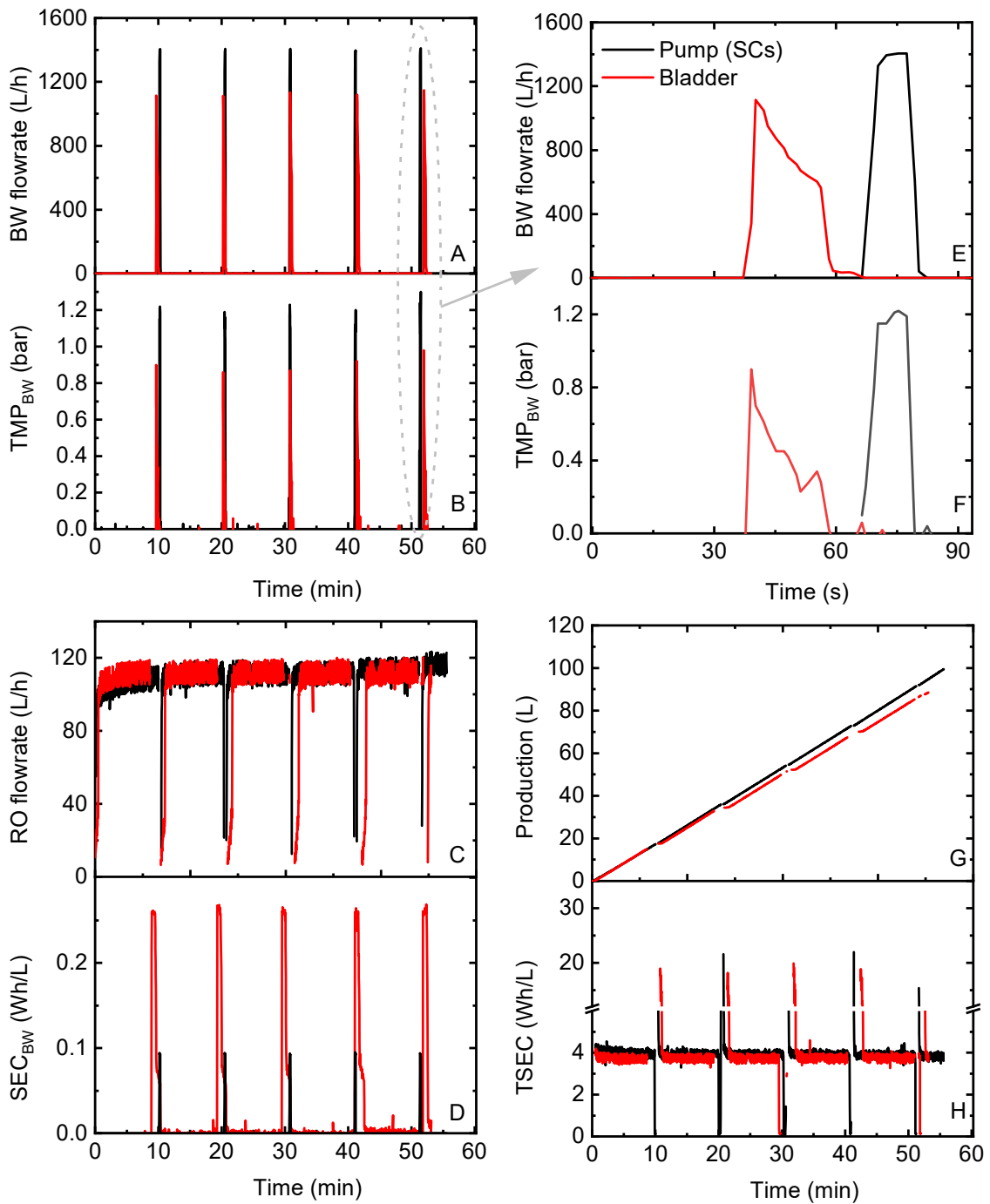


Figure 6-1: Comparisons of system BW performance with two different system configurations at the simulated valve of 45° (pressure drop of 1.2 bar), illustrating (A) BW flowrate, (B) TMP_{BW} , (C) RO flowrate, (D) SEC_{BW} , (E) zoomed-in graph of A, (F) zoomed-in graph of B, (G) production, and (H) TSEC. Adapted from [266], CC BY-NC-ND 4.0 License.

It can be seen from Figure 6-1A that the bladder tank exhibited a BW duration of 29 s at a peak flowrate of 1120 L/h (BW flux of 187 L/m²h), while the BW pump powered by SCs exhibited a BW duration of 14 s at a peak flowrate of 1400 L/h (BW flux of 233 L/m²h) to realize the same BW volume as the bladder tank (4 L). The BW flowrate and TMP_{BW} at one cycle is provided on the zoomed-in graph of Figure 6-1E and F. The “simulated fouling” via bladder tank indicates an average TMP_{BW} of 0.9 bar (see Figure 6-1B); whereas, when using the BW pump, an average TMP_{BW} of 1.2 bar is achieved. This 33% higher TMP_{BW} occurred as a result of the use of 17% higher BW peak flowrate, thus shortening the BW duration of the BW pump. The results are consistent with the reported BW values in UF systems for drinking water production (BW flux: 230 – 300 L/m²h, BW pressure: 1 – 1.5 bar) [301]. As shown in Figure 6-1F, the TMP_{BW} exhibited high values at the start, and low values near the end of the BW process. The critical pressure for the detachment and removal of the bentonite cake layer was reported to be 0.17 bar [302]. It is noted that the observed TMP_{BW} < 0.17 bar near the end lasts only 1 – 3 s (see Figure 6-1F), which contributes only a minor effect to BW efficiency. However, for the simulated cases, the use of an actuated valve can be implemented for further evaluation of BW efficiency. The time-lag that occurred in Figure 6-1D of the bladder tank results from the refilling time of the bladder tank. It exhibited a higher BW EC (Wh, see Figure 6-1C) as a consequence of the longer time (approximately 50 s) needed to refill the bladder, and this is reflected in the TSEC (Wh/L, see Figure 6-1F) of the process, as well. Over one cycle, the bladder tank exhibits a BW SEC of 0.3 Wh/L, while the BW pump indicates a BW SEC of 0.09 Wh/L (see Figure 6-1D). This result is well aligned with the reported value [303] for the classical BW process, while the BW SEC using a bladder tank was not found in the literature. The TSEC exhibited a mean value of approximately 4 Wh/L, which is consistent with the reported results in previous investigations [58, 122, 200]. A Sankey diagram was drawn to demonstrate the energy flows in the system in terms of the two BW configurations in Figure 6-2 (input values are summarized in Table 6-1). Details of the BW parameters are summarized in Table 6-2 for further comparison.

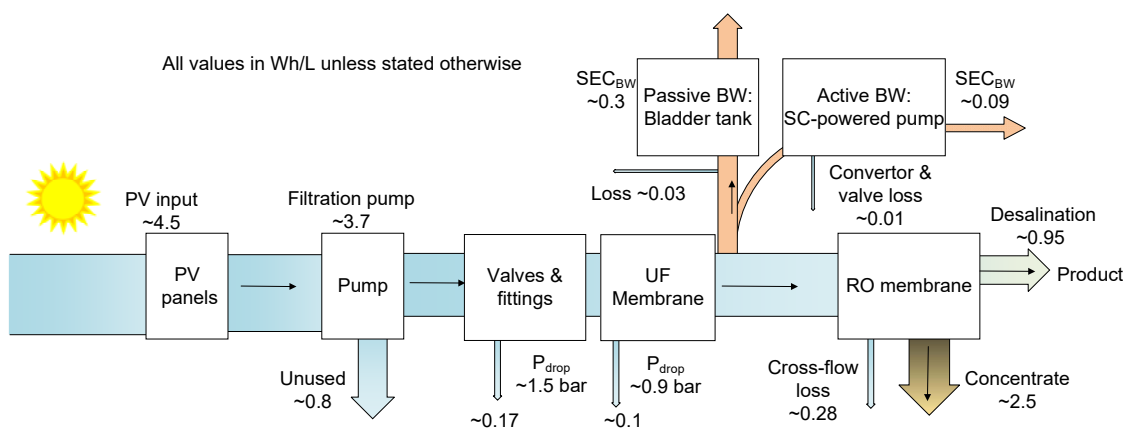


Figure 6-2: Sankey diagram demonstrating the specific energy flows in the PV-membrane system in terms of two backwashing configurations at the feed salinity of 5 g/L NaCl. The desalination (blue) and BW (orange) processes are highlighted with different colours. Adapted from [266], CC BY-NC-ND 4.0 License. Calculations are provided below.

The specific energy flows under the operating conditions of $SI = 1000 \text{ W/m}^2$, pressure drop of 1.2 bar on the Sankey diagram of Figure 6-2 are calculated step by step below [266]. The input values are summarized in Table 6-1 for a clear overview.

$$PV \text{ input } SEC = \frac{PV \text{ output power}}{RO \text{ permeate flowrate}} = \frac{500 \text{ W}}{110 \frac{L}{h}} = 4.5 \frac{Wh}{L};$$

$$Motor \text{ efficiency} = \frac{Motor \text{ power}}{PV \text{ input power}} \cdot 100\% = \frac{409 \text{ W}}{500 \text{ W}} \cdot 100\% = 81\%;$$

$$Unused \text{ SEC} = \frac{PV \text{ input power} - Motor \text{ power}}{Permeate \text{ flowrate}} = \frac{(500 - 409)W}{110 \frac{L}{h}} = 0.8 \frac{Wh}{L};$$

$$Filtration \text{ pump } SEC = \frac{Motor \text{ power}}{Permeate \text{ flowrate}} = \frac{409 \text{ W}}{110 \frac{L}{h}} = 3.7 \frac{Wh}{L};$$

Valves and fittings losses = feed flowrate \times pressure drop

$$= 450 \frac{L}{h} \cdot \frac{1}{3600 \text{ s}} \cdot \frac{m^3}{1000 \text{ L}} \cdot 1.5 \text{ bar} \cdot \frac{10^5 \text{ Pa}}{\text{bar}} = 0.17 \frac{Wh}{L};$$

UF membrane losses = feed flowrate \times pressure drop

$$= 450 \frac{L}{h} \cdot \frac{1}{3600 \text{ s}} \cdot \frac{m^3}{1000 \text{ L}} \cdot 0.9 \text{ bar} \cdot \frac{10^5 \text{ Pa}}{\text{bar}} = 0.1 \frac{Wh}{L};$$

$$RO \text{ desalination} = \text{filtration pump } SEC \cdot \frac{RO \text{ permeate flowrate}}{\text{Feed flowrate}} = 3.8 \frac{Wh}{L} \cdot \frac{110 \frac{L}{h}}{450 \frac{L}{h}} = 0.95 \frac{Wh}{L};$$

$$RO \text{ concentrate} = (\text{filtration } SEC - RO \text{ desalination}) \cdot \frac{TMP_{concentrate}}{TMP_{feed}}$$

$$= \frac{(3.8 - 0.95)Wh}{L} \cdot \frac{8.7 \text{ bar}}{10 \text{ bar}} = 2.5 \frac{Wh}{L};$$

$$\text{Cross - flow loss} = RO \text{ concentrate} \cdot \frac{\text{pressure loss}}{\text{feed pressure}} = 2.5 \cdot \frac{(10 - 8.7) \text{ bar}}{10 \text{ bar}} = 0.28 \frac{Wh}{L};$$

$$\text{Converter and valve loss} = SEC_{BW} \cdot (1 - \eta_{converter}) = 0.09 \cdot (1 - 85\%) = 0.01 \frac{Wh}{L};$$

Bladder valve loss = feed flowrate \times pressure drop

$$= 450 \frac{L}{h} \cdot \frac{1}{3600 \text{ s}} \cdot \frac{m^3}{1000 \text{ L}} \cdot 0.25 \text{ bar} \cdot \frac{10^5 \text{ Pa}}{\text{bar}} = 0.03 \frac{Wh}{L};$$

Table 6-1: Measured input values from the PV-membrane system used as inputs for the Sankey diagram in Figure 6-2 under operating conditions at $SI = 1000 \text{ W/m}^2$, pressure drop of 1.2 bar. Adapted from [266], CC BY-NC-ND 4.0 License.

Parameters	Values
PV input power (W)	500
Motor power (W)	418
Feed flowrate (L/h)	450
Permeate flowrate (L/h)	110
Valve pressure drop (bar)	0.25
Reducing fitting pressure drop (bar)	0.1
TMP_{UF} (bar)	0.9
$TMP_{con.}$ (bar)	8.7
TMP_{RO} (bar)	10
Converter efficiency	0.85

Regarding the two BW configurations, a Sankey diagram (see Figure 6-2) is drawn to illustrate the specific energy flows in the system. The line widths are the specific energy flows in response to the above calculations. Starting on the left, a total of 4.5 Wh/L is needed from the PV power source (sun). The unused specific energy is 0.8 Wh/L, indicating a motor efficiency of approximately 80%, which is as anticipated for a motor of this size. The filtration pump indicates an SEC of 3.7 Wh/L, which is in accordance with previous studies [122, 278]. The total energy loss of valves, fittings, and UF membrane reached around 0.27 Wh/L due to an overall pressure drop of 2.4 bar [122]. The cross-flow loss represents the pressure drop between the feed and concentrate streams, while the 2.5 Wh/L demonstrates the energy contained in the pressurized concentrate water. On the far right of the diagram, an SEC of 0.95 Wh/L is required to overcome the osmotic pressure at a water salinity of 5 g/L during the filtration process. On the top branch between the UF and RO membrane, the passive bladder tank shows an SEC of 0.3 Wh/L, with losses on the switching valves of 0.03 Wh/L. The branch right arrow indicates the SEC of the SC-powered BW pump at a value of 0.09 Wh/L, and the combined loss on the convertor and valve is approximately 0.01 Wh/L.

The Sankey diagram demonstrates that specific filtration energy dominates – with more than 80% energy from the PV panels being used for the desalination process – while the SEC_{BW} (either bladder tank or BW pump) remains small. However, this BW SEC can be significant, as observed from severe fouling that occurs in the real (with bentonite) case. At this point, it is recommended to apply a bladder tank with a higher useful volume (BW volume) for a future backwashing process; however, the comparisons of these passive and active BW configurations remain instructive and significant.

Table 6-2: Summary of the main BW parameters of the two different BW configurations. Note that the additional time and energy taken by recharging SCs is estimated to permit a fair comparison in the last row (details provided in the text). Adapted from [266], CC BY-NC-ND 4.0 License.

BW configuration	Peak BW flowrate* (L/h)	BW duration* (s)	TMP _{BW} (bar)	E _{BW} from 5 cycles (Wh)	Production (L)	TSEC (Wh/L)
Bladder tank	1120	29	0.9	21	89	5.8
BW pump + SCs (without recharging)	1400	14	1.2	7.4	99	5.0
BW pump + SCs (with recharging)	1400	14	1.2	7.4	97	5.1

* Taken as an average from five cycles.

It is clearly observed that the BW pump powered by SCs is able to implement five backwashing cycles without recharging the SCs. It might be necessary, however, to recharge the SCs after running out in the real case scenario. As a consequence, the energy calculations should be compensated by the time used for recharging the SCs back to 100%. To fully recharge the SCs, it is expected to take 1 min 48 s (calculated by the energy storage capacity of the SCs) assuming that the PV (500 W power rating) is solely used to recharge the SCs. Considering the remaining energy of the SCs after five cycles (70 s total BW periods), the lost permeate during these recharging periods (calculated to be approximately 2 L) needs to be subtracted from the calculations. These values contribute minor variations (2% of accumulated permeate) of the TSEC compared to those without recharging to the SCs. In the next section, further comparisons of energy consumption of the two BW configurations operating under a variety of weather conditions (real solar days) were carried out.

6.2. System performance under real solar days with bentonite

In this section, the system behaviour of the two BW configurations was investigated under real solar days induced by an inorganic fouling agent (100 mg/L bentonite), incorporating both fluctuations and intermittency. The preferred energy efficient configuration with real fouling is to be confirmed with that in “simulated fouling” conditions. The overall system behaviour with two BW configurations under the partly cloudy day is shown in Figure 6-3. This day was selected, as it exhibits fairly good weather conditions (high SI) to allow system operation, but also incorporates high levels of fluctuations to challenge the system.

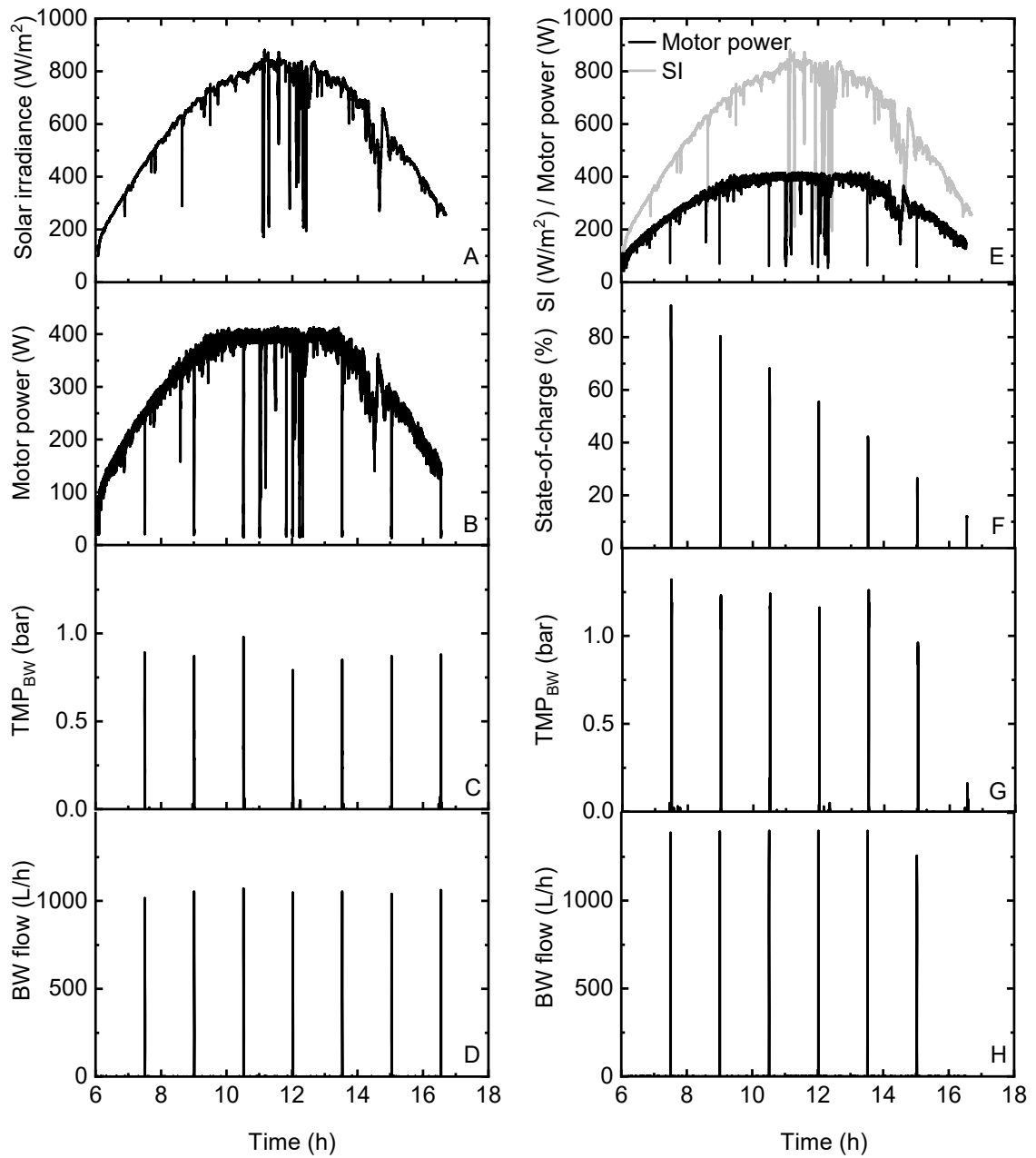


Figure 6-3: Comparisons of system backwashing characteristics using the bladder tank configuration (A – D) and the BW pump powered by SCs (E – H), illustrating (A) solar irradiance, (B) motor power consumption of the filtration pump, (C) TMP_{BW} , (D) BW flow, (E) solar irradiance (in grey) and motor power (W) consumption of the filtration pump (in black), (F) TMP_{BW} , (G) BW flow, and (H) state-of-charge. Adapted from [266], CC BY-NC-ND 4.0 License.

The filtration pump consumes the same power (see Figure 6-3B and black curves in Figure 6-3E), as it is directly driven by the PV power. Apart from deliberately shutting down the filtration pump during BW operations, the motor power drops below 100 W several times at $SI < 300 \text{ W/m}^2$ between the periods of

10:00 and 12:20, causing no RO permeate to be produced (not shown in the graph). While the naturally-induced backwash of the RO membrane due to the drop of the TMP_{RO} below the osmotic pressure was observed, this has also been elaborated in other studies [122, 296, 304]. As shown in the bladder tank configuration, the BW flowrate keeps at approximately 1050 L/h during each BW cycle (see Figure 6-3D) at the TMP_{BW} of 1 bar (Figure 6-3C). At the end of this solar day, seven BW cycles were achieved as a result of the regular filling of UF permeate by the filtration pump, which is directly driven by SI. It can be seen that the BW flowrate is slightly lower (6.7%) than that in the simulated valve as discussed above, because the TMP_{BW} with bentonite fouling is around 11% higher than that in the simulated valve. Comparatively, the BW pump shows similar BW characteristics to those in the simulated valve detailed above for the first five cycles (see Figure 6-3F and G). Subsequently, it drops slightly to 1300 L/h with an average TMP_{BW} of 0.96 bar, as the energy left in the SCs was not able to provide the desired energy to the BW pump (see Figure 6-3F). This is mirrored in the SOC in Figure 6-3H, indicating six BW cycles before reaching the lower limit of the SOC under this day (constrained by the working voltage of the electronics within the DC/DC converter).

Other system performance parameters with these two BW configurations under this partly cloudy day – including flux, TMP_{UF} , production, and SEC – are presented in Figure 6-4 and Figure 6-5. It can be seen that the system exhibits similar filtration behaviour, regardless of the BW configurations. This underlines that the choice of BW configurations needs to be determined from the aspects of minimizing the additional electronics and failure risks when deployed in remote areas. Furthermore, to assess how the BW process affects overall system performance when tested under different solar days, the experimental results under the very cloudy and sunny day with/without BW are provided in Figure 6-6 - Figure 6-9, and summarized in Table 6-3.

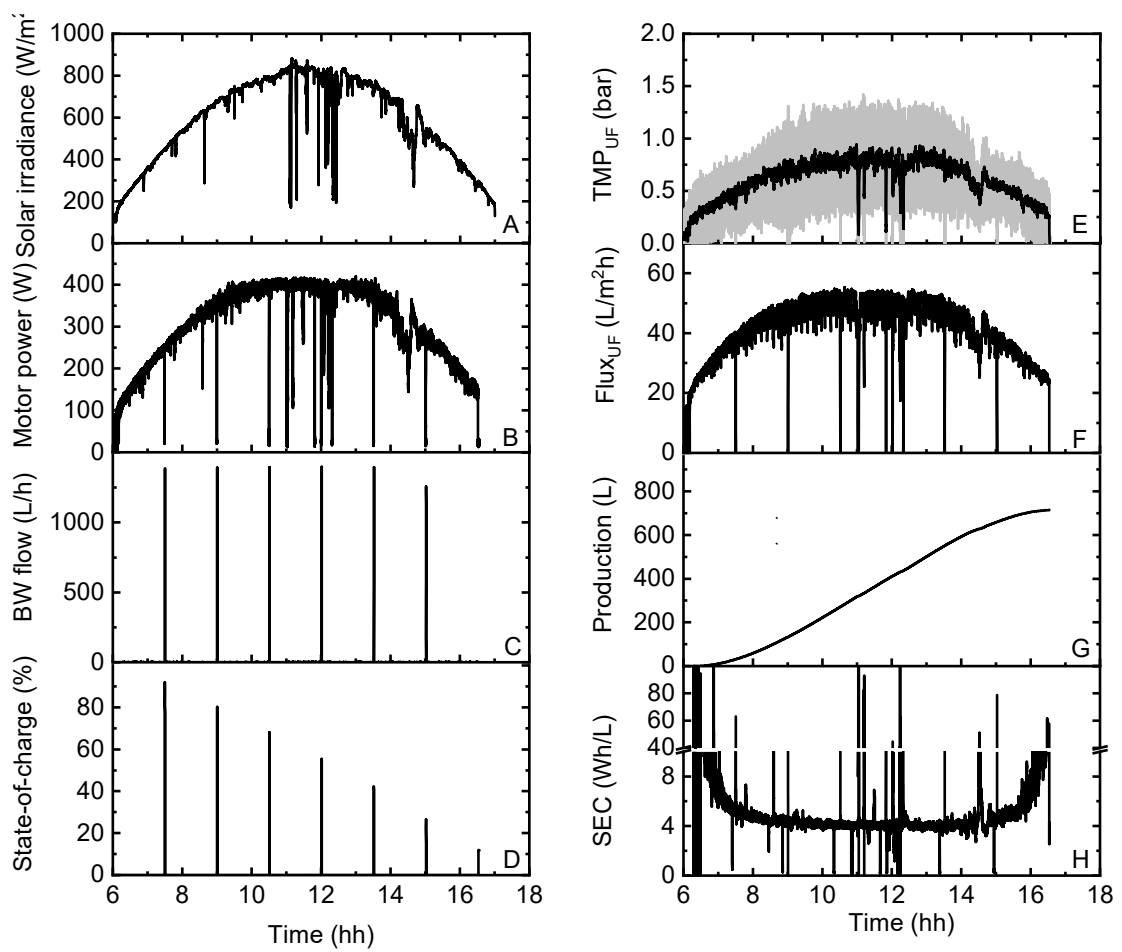


Figure 6-4: System backwashing characteristics with the BW pump powered by SCs under the partly cloudy day, illustrating (A) solar irradiance, (B) motor power, (C) BW flowrate, (D) state-of-charge, (E) TMP_{UF} , (F) $flux_{UF}$, (G) production, and (H) SEC. Adapted from [266], CC BY-NC-ND 4.0 License.

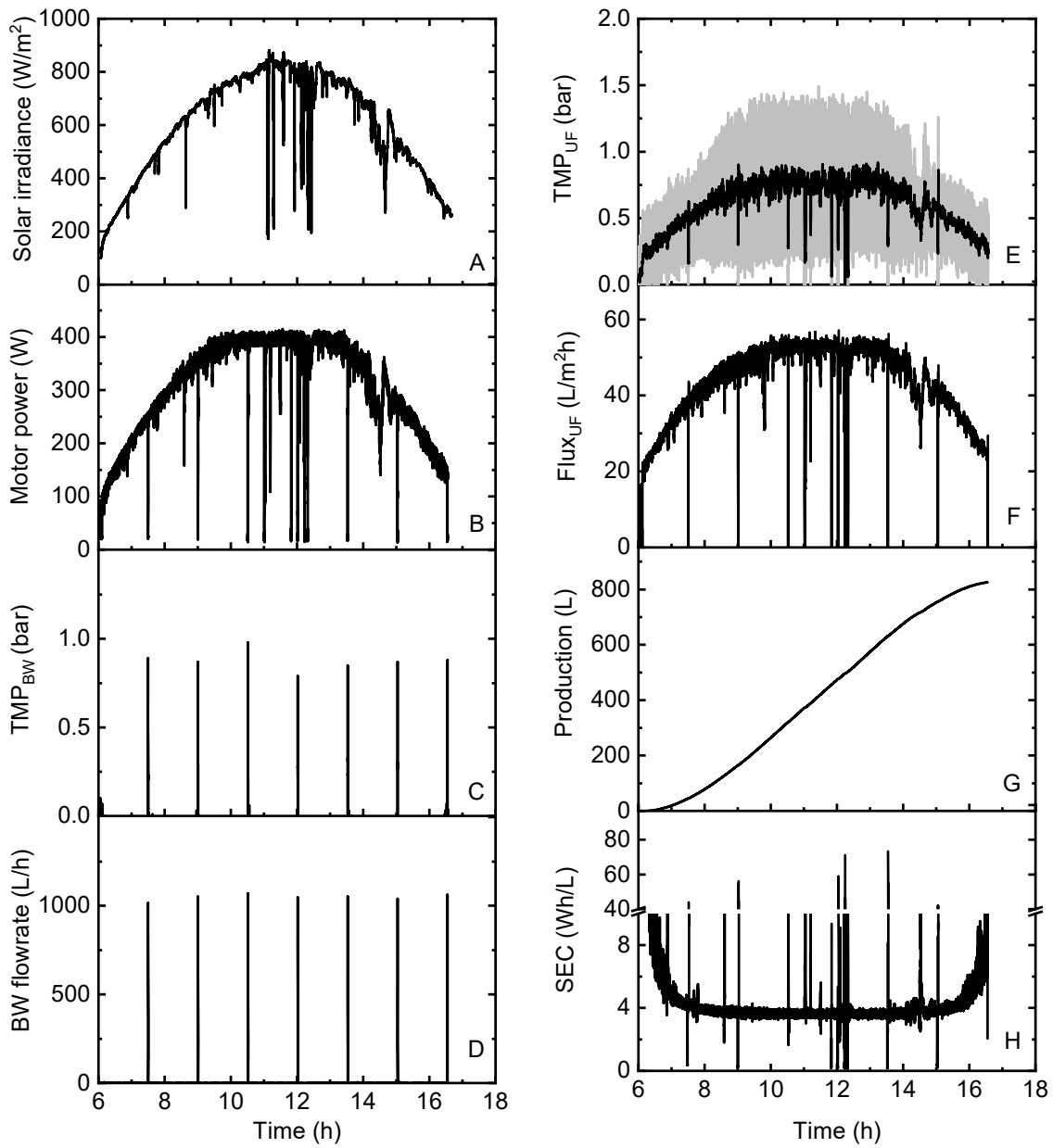


Figure 6-5: System backwashing characteristics with bladder tank under the partly cloudy day, illustrating (A) solar irradiance, (B) motor power, (C) BW flow, (D) TMP_{BW} , (E) TMP_{UF} , (F) $flux_{UF}$, (G) production, and (H) SEC. Adapted from [266], CC BY-NC-ND 4.0 License.

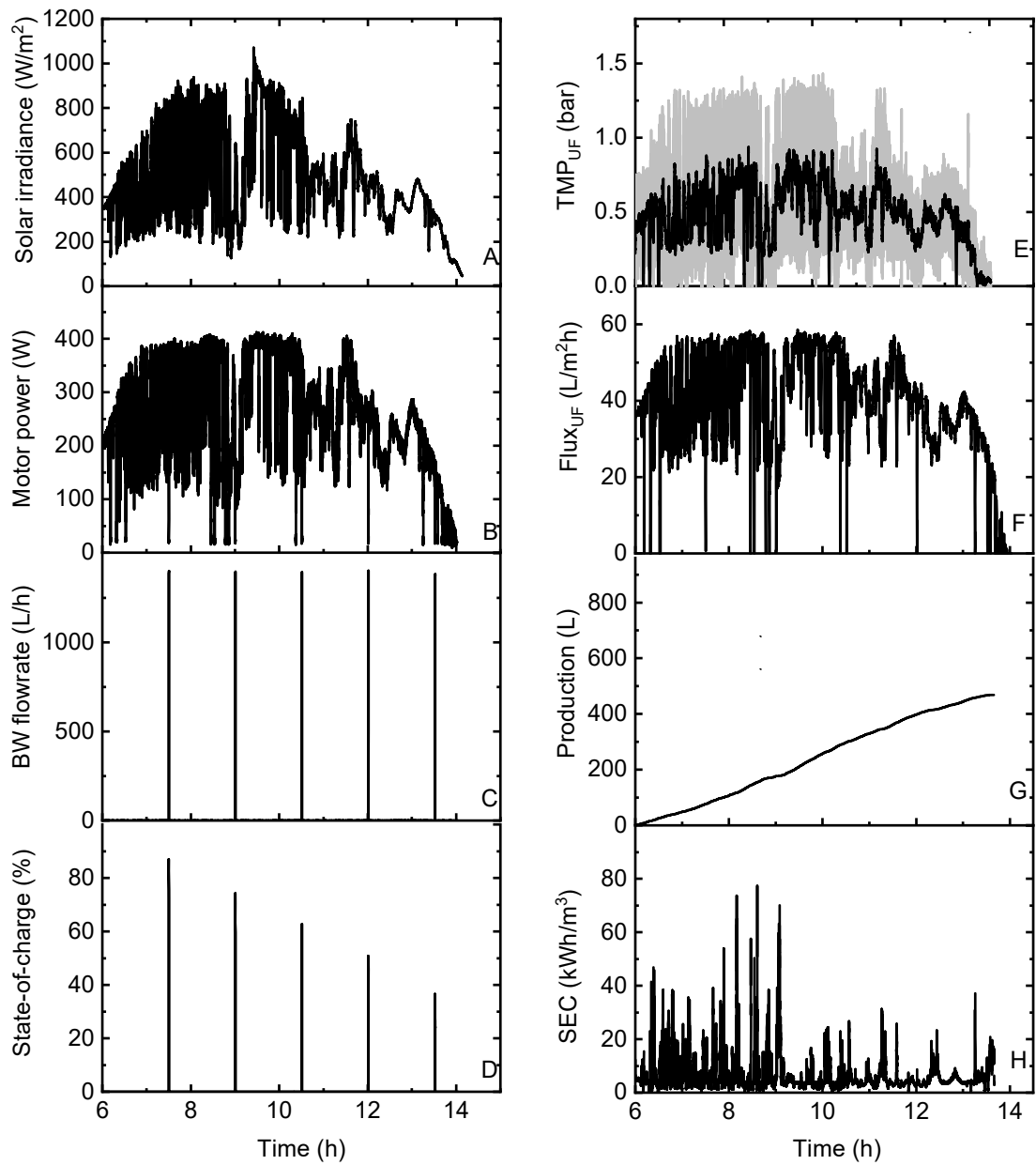


Figure 6-6: System backwashing characteristics with the BW pump powered by SCs under the very cloudy day, illustrating (A) solar irradiance, (B) motor power, (C) BW flow, (D) state-of-charge, (E) TMP_{UF} , (F) $flux_{UF}$, (G) production, and (H) SEC. Adapted from [266], CC BY-NC-ND 4.0 License.

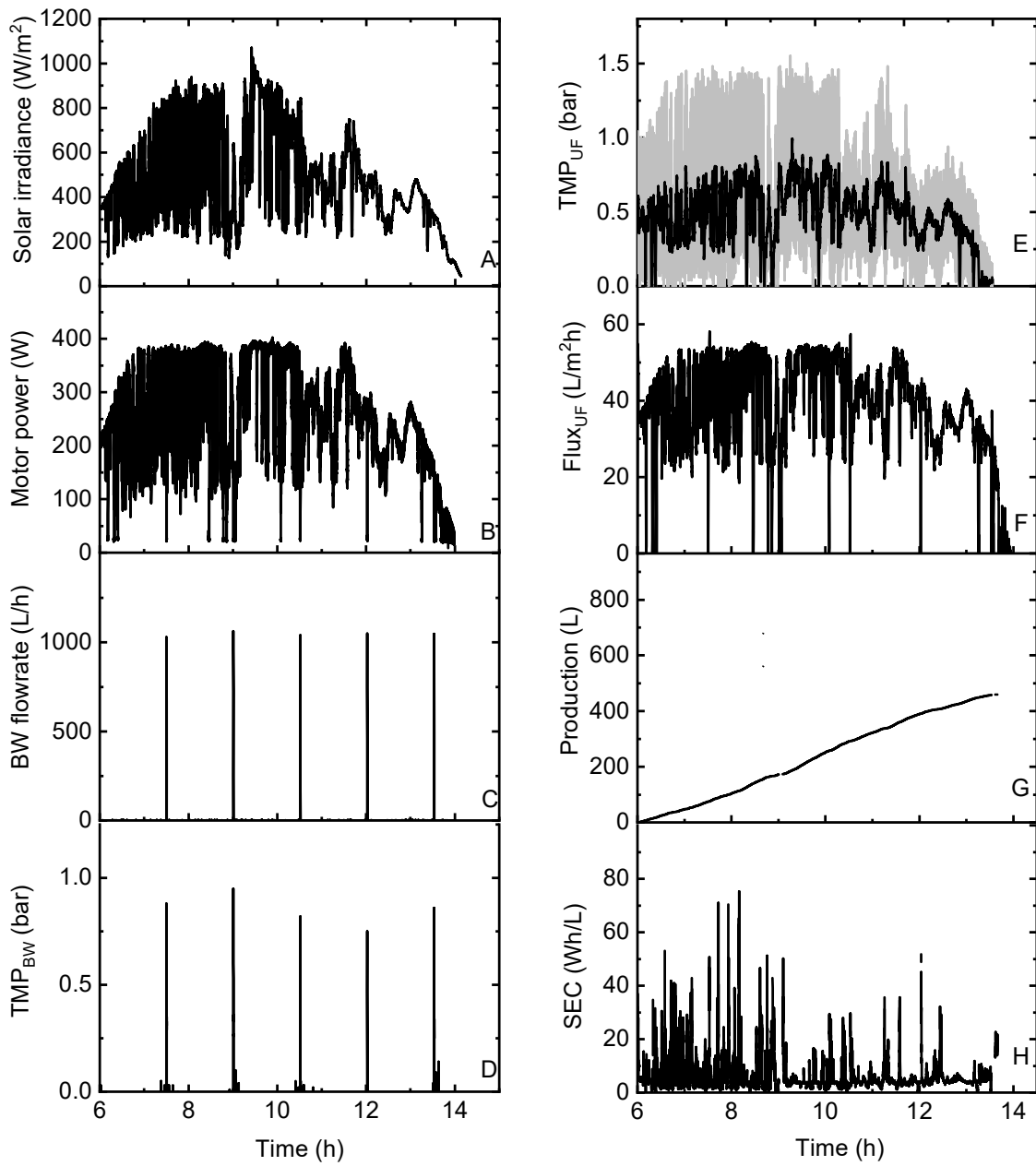


Figure 6-7: System backwashing characteristics with bladder tank under the very cloudy day, illustrating (A) solar irradiance, (B) motor power, (C) BW flow, (D) TMP_{BW} , (E) TMP_{UF} , (F) $flux_{UF}$, (G) production, and (H) SEC. Adapted from [266], CC BY-NC-ND 4.0 License.

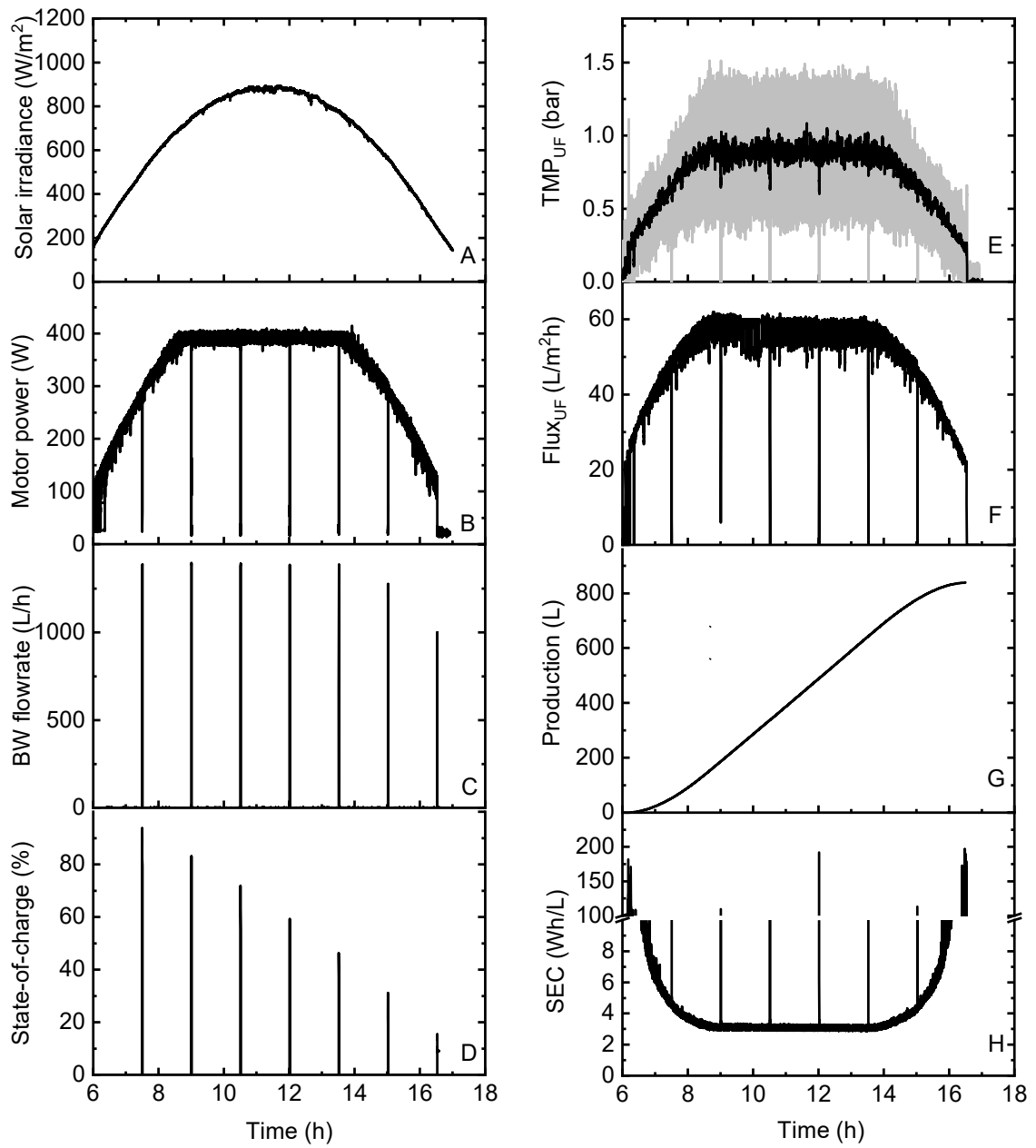


Figure 6-8: System backwashing characteristics with the BW pump powered by SCs under the sunny day, illustrating (A) solar irradiance, (B) motor power, (C) BW flow, (D) state-of-charge, (E) TMP_{UF} , (F) $flux_{UF}$, (G) production, and (H) SEC. Adapted from [266], CC BY-NC-ND 4.0 License.

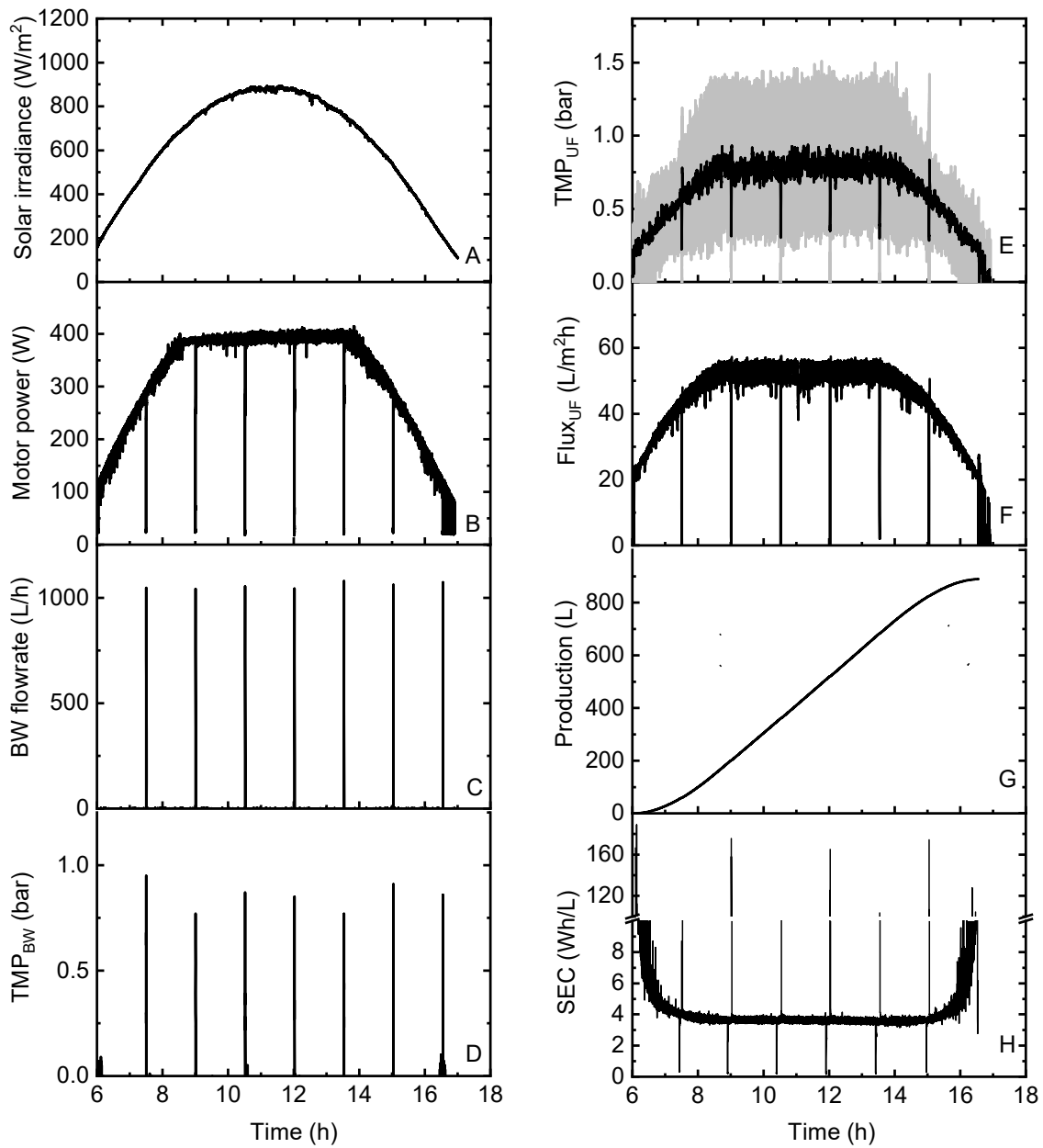


Figure 6-9: System backwashing characteristics with bladder tank under the sunny day, illustrating (A) solar irradiance, (B) motor power, (C) BW flow, (D) TMP_{BW} , (E) TMP_{UF} , (F) $flux_{UF}$, (G) production, and (H) SEC. Adapted from [266], CC BY-NC-ND 4.0 License.

Table 6-3: Summary of system performance with/without BW under different solar days. Adapted from [266], CC BY-NC-ND 4.0 License.

Solar day	BW configurations	Production (L)	Total E_{BW} (Wh)	TSEC (Wh/L)
Partly cloudy	BL	754	22.8	4.5
	BW pump	714	11	4.1
	Reference	771	0	4.2
Very cloudy	BL	459	18.9	4.5
	BW pump	469	9.2	4.5
	Reference	476	0	4.2
Sunny	BL	889	14	4
	BW pump	839	12.4	4.3
	Reference	904	0	3.9

The results of these experiments under three different solar days with respect to TSEC are plotted in Figure 6-10. The bladder tank and BW pump show similar TSEC values despite the different solar days. The TSEC remains at approximately 4 Wh/L, indicating that there is not a large energy cost for implementing one BW cycle every 90 min throughout the day for this PV-membrane system under this operating condition. In addition, the impacts of varied weather conditions on the TSEC of different BW configurations are trivial, which indicates that the PV-membrane system operates well when directly subjected to fluctuations even during the very cloudy day. Therefore, the BW choice is required to be taken into account from the aspect of reducing the additional electronics and failure risks when applied in remote areas. In terms of cost, the capital cost of SCs is € 1360/kWh [305], with a low O&M cost of € 0.85 /kW-y [306].

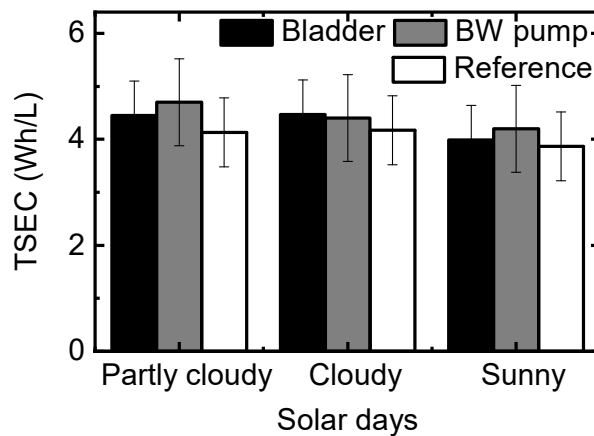


Figure 6-10: The TSEC of the PV-membrane system with different backwashing implementations under different solar days. The white bar represents the reference (without BW), while the black and grey bars represent the bladder tank and BW pump, respectively. The error bars were estimated by error propagation (see Section 3.8). Adapted from [266], CC BY-NC-ND 4.0 License.

In the next section, a higher fouling rate was achieved by inducing a high bentonite concentration (300 mg/L) to assess the influence of BW interval on the TSEC of system performance. At this stage, it should be mentioned that after these solar day experiments, the BW pump exhibited severe corrosion due to the use of brackish feedwater and non-stainless grade steel for the rotor of the pump. As a result, the BW pump was discarded to avoid possible damage to the RO membrane and corrosion of other components in the system. No proper replacement pump could be found that possessed: i) stainless steel construction; ii) suitable pressure; and iii) appropriate flowrate. Therefore, the experiments in the following sections were performed with the bladder tank only.

6.3. Bladder tank backwashing with high fouling rate

In this section, the bentonite concentration in the feedwater was increased by a factor of three to 300 mg/L (100 NTU) to induce a high fouling rate to the UF membrane, while keeping the operating condition at a constant SI of 1000 W/m². This enables the investigation of the impacts of BW intervals on the membrane fouling within a short time window. The BW efficiency via the bladder tank configuration was evaluated for a wide range of BW intervals (10 – 120 min), focusing on the TSEC and fouling rate. The TMP_{UF} at six different BW intervals is shown in Figure 6-11.

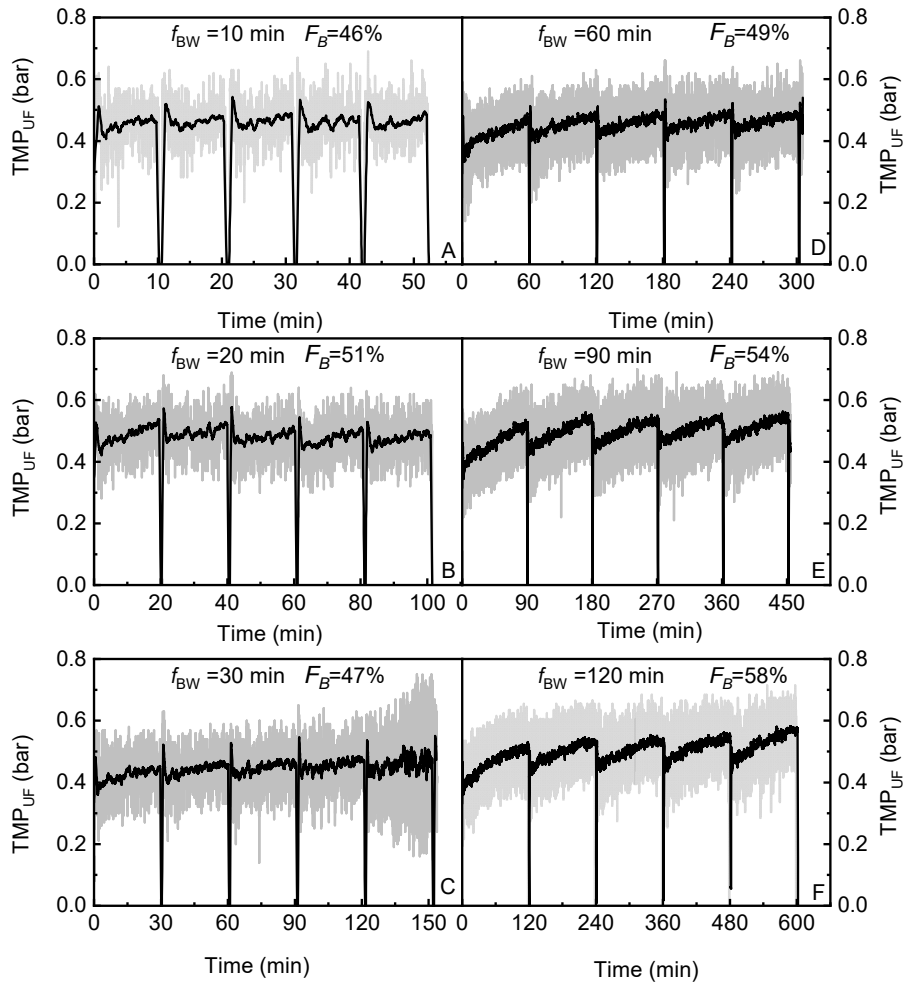


Figure 6-11: The TMP of the UF membrane with bladder tank with five cycles of backwashing at variable frequencies. f_{BW} is the BW interval, and F_B is the fouling rate. Adapted from [266], CC BY-NC-ND 4.0 License.

It can be seen from Figure 6-11 that a more significant increase of TMP_{UF} occurred at BW intervals ≥ 60 min. The change in TMP across the UF membrane (ΔTMP_{UF}) increased now by 0.1 – 0.2 bar, suggesting that a BW cycle was required. Meanwhile, the beginning of the TMP_{UF} value for each filtration cycle exhibits a clear rising trend over time at BW intervals > 30 min. This suggests the occurrence of irreversible fouling, which confirms the existence of the critical filtered volume (CFV) [289, 307]. For the UF permeate flux of around $45 \text{ L/m}^2\text{h}$, the CFV is estimated to be around 45 L/m^2 (an error of $\pm 0.5\%$). It is comparable with the reported value [289], which indicated a CFV of 85 L/m^2 for the UF flux of $50 \text{ L/m}^2\text{h}$ with the clay suspensions (mean diameter centred on 700 nm) at a concentration of 20 mg/L. Using the TMP_{UF} value, the bentonite fouling rate was estimated to be ranging from 46 – 60%, depending on BW interval. The F_B (displayed in Figure 6-11) values indicate a clear rising trend at $f_B > 30$ min, which suggest the occurrence of membrane fouling at longer BW intervals. Nevertheless, an outlier

at the BW interval of 20 min is observed, which is probably attributable to experimental error and potential residue from the previous experiment.

To estimate the cake resistance of bentonite on the membrane surface (assuming even distributions), the concentration of bentonite (60 g) in the feed tank (feedwater volume of 200 L) over time and observed bentonite depositions are plotted in Figure 6-12. The measured average turbidity values over three cycles (at the end of each filtration cycle as discussed in Section 3.7.5) at BW interval from 10 to 120 min were 85, 76, 36, 15, 10 and 3 NTU, respectively.

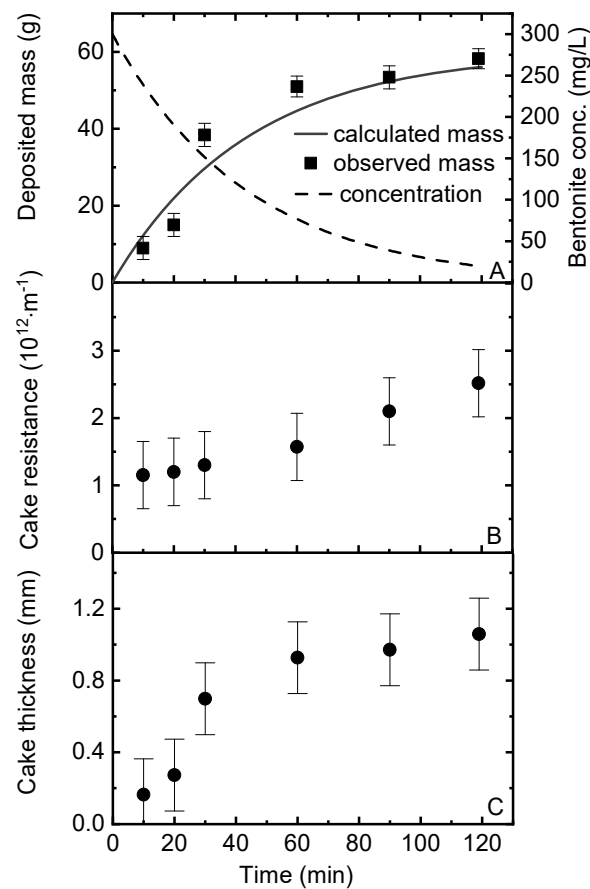


Figure 6-12: (A) Calculated bentonite concentration in the feedwater tank with no BW cycles running, calculated and observed mass deposition on the membrane surface, (B) cake resistance and (C) thickness of the bentonite layer as a function of filtration time. The NTU data were obtained with an average value of three cycles. The error bars were estimated by error propagation in Section 3.8. Adapted from [266], CC BY-NC-ND 4.0 License.

As indicated in Figure 6-12A, the concentration of bentonite decreased exponentially over filtration time. It can also be seen from Figure 6-12B that the mass deposited onto the membrane surface. Practically all of the bentonite was pumped into the UF membrane at a BW interval of 120 min, suggesting that the

total bentonite in the feedwater is inside of the UF membrane. As shown in Figure 6-12B, the cake resistance remains relatively constant at an R_c of approximately $1.2 \cdot 10^{12} \text{ m}^{-1}$ for BW intervals ≤ 30 min, and then it increases significantly at BW intervals longer than 60 min as the cake formed over time whereas irreversible fouling appeared [308]. Moreover, after 120 min, the cake resistance has increased by 50%. In addition, the thickness of the bentonite layer increases linearly with the deposited mass (see Figure 6-12C), the deposit build-up is slow at BW intervals lower than 60 min (thickness 0.1 – 0.7 mm), and the thickness increases by a further 60% to 1.1 mm. This analysis verified the occurrence of real fouling at the UF membrane surface by including bentonite. Further investigations of the effects of BW intervals on BW efficiency and TSEC are carried out.

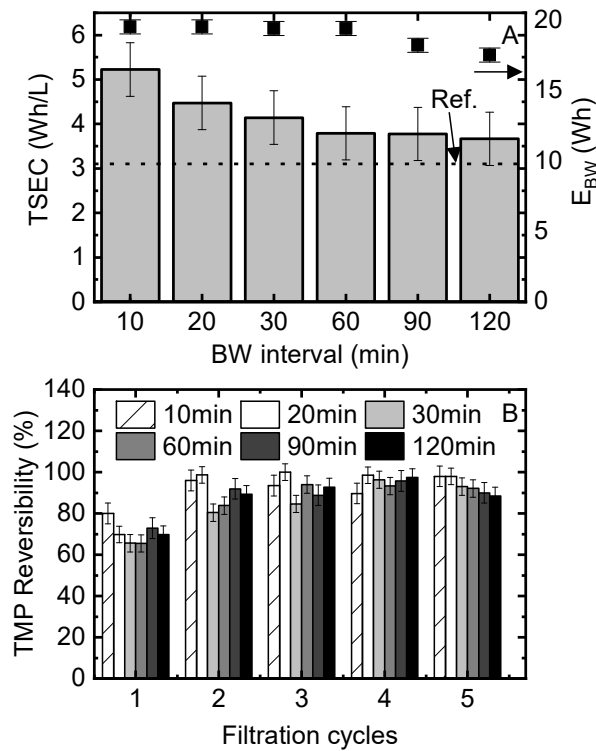


Figure 6-13: Summary of (A) TSEC as a function of BW frequency and (B) TMP reversibility over five filtration cycles using the BW bladder tank. The error bars were estimated by error propagation in Section 3.8. Adapted from [266], CC BY-NC-ND 4.0 License.

The TSEC and TMP reversibility are summarized in Figure 6-13 for further comparisons. Referring to Figure 6-13A, the TSEC decreases with less frequent cleaning and plateaued at around 3.7 Wh/L when f_{BW} is ≥ 60 min. It is worth noting that the reference (dotted line in Figure 6-13A) represents the TSEC (= the filtration SEC) when neither bentonite nor BW was applied. The optimal TSEC is anticipated to be a trade-off between the additional energy required for cleaning the membrane, and a reduction in the energy consumption of the filtration pump as a result of the aforementioned cleaning. At a BW interval < 60 min,

the increased energy consumption due to frequent backwashing is not compensated by the consequent reduction in filtration energy utilization. For BW intervals from 60 to 120 min, the additional energy required by the BW is justified by the reduction in filtration utilization, causing a lower TSEC. In practice, the total mass of bentonite that can be deposited on the membrane surface is limited to 60 g.

At BW interval > 60 min, more than 88% bentonite is deposited on the membrane surface (calculated from Figure 6-12A), and this leads to the same EC. As a result, the TSEC approaches the normal filtration SEC (without bentonite and BW implementations). With a higher bentonite concentration, the TSEC is anticipated to increase again at even longer BW intervals (a few hours or days), as bentonite fouling would cause a higher TMP_{UF} (and thus energy consumption). The results are well aligned with the reported values in another PV-membrane system, which exhibited an SEC ranging from 3.3 – 4.7 Wh/L with the same membrane at a feed salinity of 2 g/L [200]. Nevertheless, the TSEC exhibits higher values than those aforementioned [309, 310] as a result of the application of the RO membrane in this study. The E_{BW} of the bladder tank indicates a decreasing trend with the BW interval, as energy consumption is primarily dominated during the filling phase by the filtration pump. Furthermore, the filling time of the bladder tank is shorter at higher BW intervals due to the increase of fouling on the membrane surface. It is critical to mention that the filtration pump can drive harder to reach the maximum power at the set-point pressure (approximately 420 W at 10 bar) due to the size of the rated PV capacity (500 W). This can be evidenced by calculating the filtration pump power during the filling phase over one cycle at varied BW intervals (see Figure 6-14). The E_{BW} at the BW interval of 10 min per cycle (4 Wh, Figure 6-14A) is approximately 7.1% higher than that at the BW interval of 120 min per cycle (3.7 Wh, Figure 6-14B).

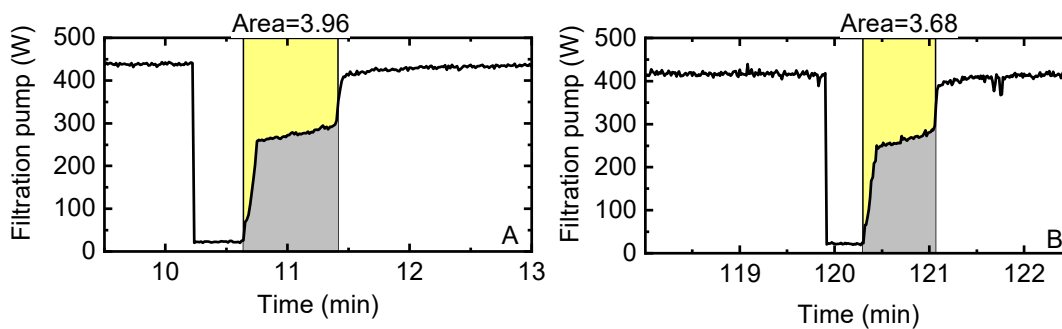


Figure 6-14: Filtration pump power over one filtration cycle at BW intervals of (A) 10 min; and (B) 120 min. Adapted from [266], CC BY-NC-ND 4.0 License.

In contrast, the lower BW interval leads to higher TMP reversibility, indicating that TMP_{UF} can be restored with more frequent cleaning (see Figure 6-13B). It is seen that the reversibility does not always reach 100% at BW interval < 60 min, which can be ascribed to several aspects: i) insufficient mixing leads to the settlement of bentonite at the bottom of the feed tank (250 L); ii) agglomeration of bentonite in the feed tank that cannot be detected; iii) bentonite residuals in the feed pipeline (dead volume: $0.2 \cdot 10^{-3} \text{ m}^3$) that cannot be backwashed; iv) surface interactions between bentonite and NaCl, as illustrated in the study

of Bacchin *et al.* [290]; and v) measurement errors due to the limits of sensors, as well as induced vibration and noise at the switching valves [311]. These factors constitute limitations of the system design that need to be improved for the future work.

6.4. Comparisons between “simulated fouling” and real fouling

In this section, with an attempt to coincide with the fouling rates encountered using the bentonite fouling agent, experiments of varying pressure drops across the valve used in Section 6.1 were conducted over a broad range. The goal was to determine the feasibility of simulating the real fouling via creating pressure drops across the valve by comparing energy consumption between “simulated fouling” (valve) and “real fouling” (bentonite solution).

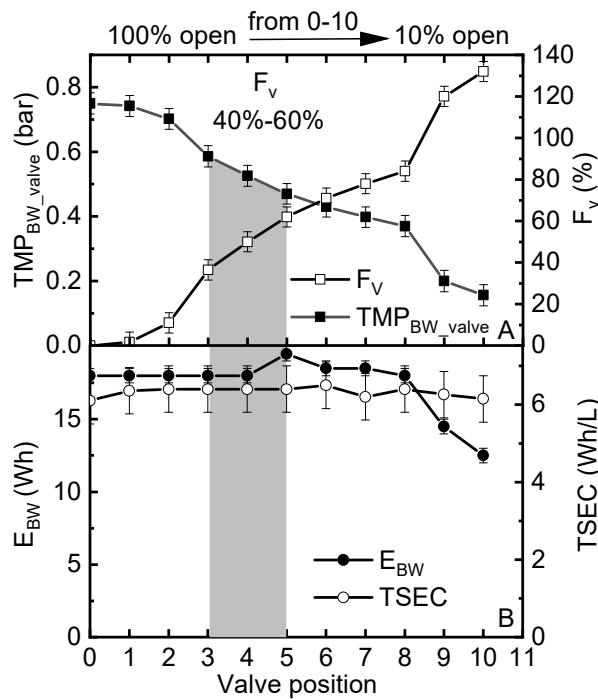


Figure 6-15: Graphs showing (A) TMP_{BW} , F_v (fouling rate), and (B) total specific energy consumption (TSEC), and E_{BW} at varied positions. The valve was varied from completely open (position 0) to 10% open (position 10). The averaged values of TMP_{BW} were taken over five cycles. Error bars were estimated by using error propagation method in Section 3.8. Adapted from [266], CC BY-NC-ND 4.0 License.

As indicated in Figure 6-15A, valve position 3 ($TMP_{BW_valve} = 0.59$ bar) to position 5 ($TMP_{BW_valve} = 0.47$ bar) exhibit a simulated fouling rate in the range of 40 – 60 %. These results were calculated by using the change in TMP across the UF membrane (ΔTMP_{UF}). This range is consistent with the fouling rate that appeared with bentonite (300 mg/L, from 40% to 58% as calculated in Section 6.3). The E_{BW} of the simulated valve (see Figure 6-15B) shows similar values with the bentonite fouling when compared with the

BW EC (E_{BW}) from Figure 6-15B and Figure 6-13A, suggesting that the resistance created via the simulated valve was capable of representing the cake resistance of bentonite fouling. The bladder tank demonstrates a specific BW EC of 0.17 to 0.3 Wh/L to produce the net permeate volume relying on the fouling rates, as discussed in Section 6.1. These values are slightly higher compared with other BW methods [303]. This is likely a consequence of the energy consumed to fill the tank with filtrate UF water by the filtration pump, and the BW EC is anticipated to be minimized by optimizing the operation parameters. The resistance created by the simulated valve is maintained constant during the BW operation phase, while the induced cake resistance decreases. It can be concluded from Figure 6-13 that the TMP_{UF} at the beginning of each filtration cycle is recovered back to the initial pressure, and thus the cake layer can be lifted off of the membrane surface as a result of the hydraulic force. As a result, accumulation of the depositions entering into the next filtration cycle can be avoided, indicating the reversible fouling that occurred in this work. Nevertheless, the variations of TSEC between the simulated valve and the bentonite fouling are primarily dominated by the filtration EC. This is because: i) the permeate loss is relatively low compared with RO permeate production; and ii) the ratio of total EC and net permeate volume is highly affected due to the small BW interval used in these experiments (10 min for the simulated valve).

In summary, the addition of the simulated valve can assist to create resistance that correlates well with the cake resistance created by real fouling. These findings are anticipated to assist other researchers who are interested in studying aspects of UF membrane fouling, without the risk of inducing irreversible fouling. Naturally, the limitation is that the resistance remains the same during the BW process due to this simple ball valve. This appears to demonstrate that it will not react dynamically during a BW cycle like a real UF membrane when a cake layer lifts off during bentonite fouling, indicating that the real cleaning efficiency cannot be obtained. If desired, a more advanced version could be implemented in which an actuated valve is added to simulate these more dynamic characteristics. More importantly, the occurrence of irreversible fouling for real systems must be taken into account during BW operations.

6.5. Summary

In this chapter, two different UF membrane backwashing configurations were implemented into the PV-membrane system, namely, a passive bladder tank and a dedicated BW pump powered with SCs. The energy consumption was compared by using a fixed BW volume of 4L. The bladder tank exhibited a higher SEC_{BW} (0.3 Wh/L) than that with the BW pump (0.09 Wh/L), which is largely attributable to the longer time (approximately 50 s) required to refill the bladder. However, the bladder tank is recommended for backwashing when the system is deployed in remote areas, as the elimination of additional electronics makes the bladder tank more robust and lowers the risk of failure.

Under real solar days with the bentonite fouling agent, the fully charged SCs enabled 5 to 7 BW cycles at BW intervals of 90 min. The bladder tank exhibited slightly higher TSEC, at approximately 4 Wh/L, than the BW pump based on the fact that the TSEC was primarily driven by the RO membrane. The use of

bentonite allowed surface fouling of the UF membrane module, and an increase of TMP_{UF} is observed around 0.2 bar at the maximum $f_{BW} = 120$ min. More bentonite started to deposit on the membrane surface at filtration time > 30 min, and practically all of the bentonite was pumped into the membrane at $f_{BW} = 120$ min. The analysis of cake resistance and thickness of the layer over the filtration time revealed that the deposit was directly linked to the BW interval per cycle, and thus membrane fouling can be mitigated with frequent cleaning (BW). Comparatively, the TSEC decreased with less frequent cleaning, and reached a stable value of 3.7 Wh/L when $f_{BW} \geq 60$ min, as the cake layer remained the same, indicating that fewer BW cycles saved energy, and consequently the TSEC approached the normal SEC of filtration. In this case, a BW interval of every 60 min is recommended as a good balance between energy consumption and mitigation of UF membrane fouling.

Finally, the use of a ball valve to simulate fouling assists with UF membrane fouling studies without the need to induce irreversible fouling to the membrane and handle complex feed solutions. Indeed, it is proven to be a reasonable substitute to create cake resistance at the UF membrane surface in the PV-membrane system.

7. Use of lithium-ion batteries for energy storage

The results in this chapter have been published in Applied Science 11 (2), 856, (2021) [278]. The co-author Ana Carvalho helped with the battery configuration and performed the experiments with the batteries. The co-authors Andrea Schäfer and Bryce Richards contributed to the overall design of the experiments, the interpretation of the experimental results and review of the manuscript.

It has been demonstrated that the usage of SCs and LA batteries in off-grid PV-membrane systems can improve water quality and quantity. Nevertheless, due to the high energy intensity and large charging/discharging cycles, the application of Li-ion batteries in off-grid PV systems – in particular, with the impacts on SEC, water quality, and quantity – needs further investigation. In addition, experiments that compare the performance of different energy storage options – SCs vs. Li-ion batteries vs. directly-coupled system without storage – need to be carried out. In this chapter, the following research questions are addressed:

- i) How does the addition of up to 1-d worth of energy storage of Li-ion batteries affect the SEC and permeate production of a PV-membrane system operated under varied solar days?;
- ii) What are the impacts of using different amounts of battery storage capacity (realized by limiting the initial SOC of the batteries) on the PV-membrane system?;
- iii) How do the different energy storage options influence the PV-membrane system when compared with SCs and Li-ion batteries?

7.1. Operation performed on the partly cloudy day (with and without fully-charged batteries)

The aim is to evaluate the impacts of adding 1-d worth of energy storage on water production and SEC to the PV-membrane system. The system performance on the partly cloudy day was compared, as shown in Figure 7-1.

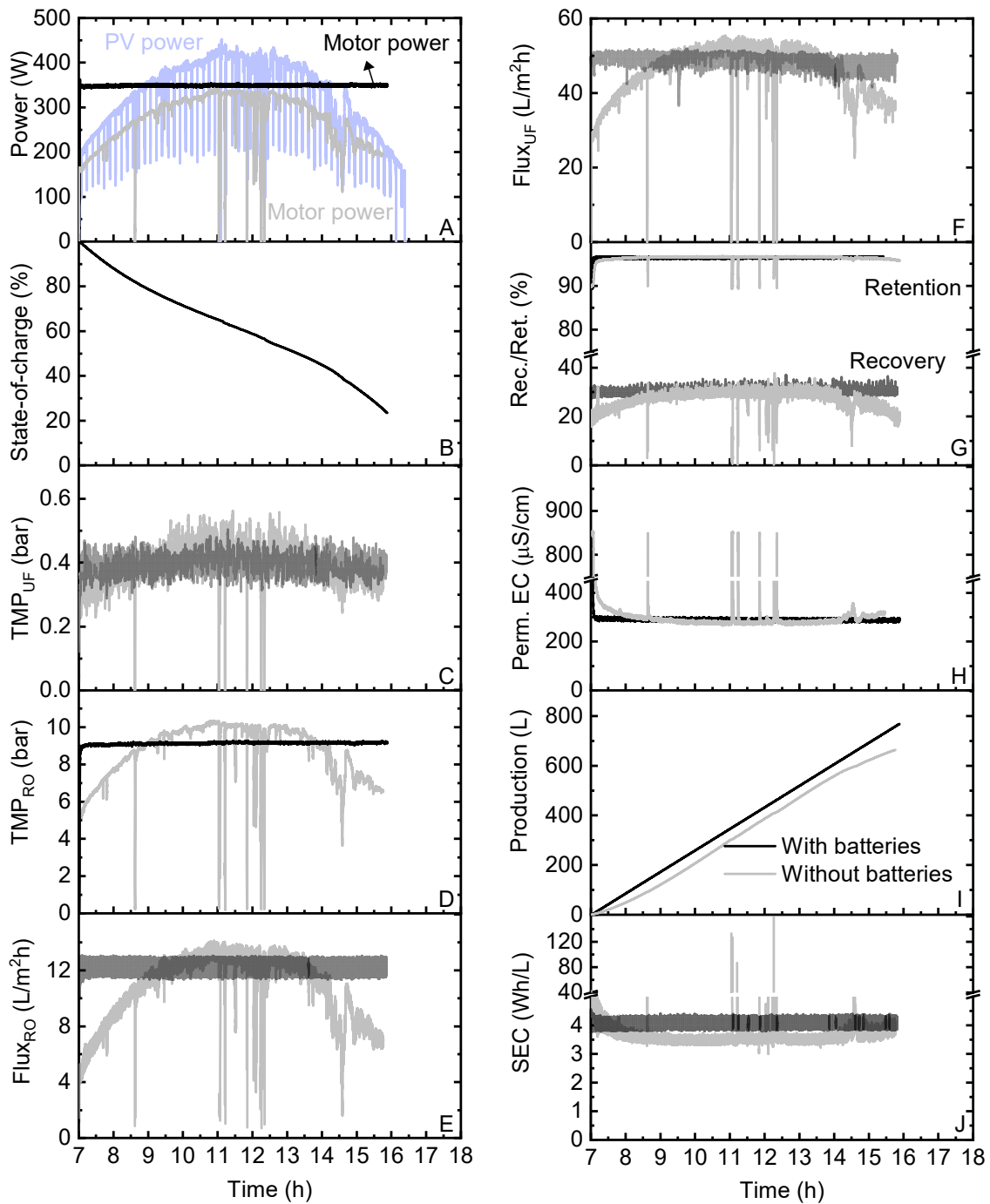


Figure 7-1: Performance of the PV-membrane system without/with fully-charged battery storage (100% SOC) under the partly cloudy day, illustrating (A) motor power, (B) state-of-charge, (C) TMP_{UF}, (D) TMP_{RO} (E) flux_{RO}, (F) flux_{UF}, (G) retention/recovery, (H) permeate EC, (I) production, and (J) SEC. Adapted [278], CC BY-NC-ND 4.0 License.

The motor power consumption was constant at around 350 W throughout the entire period when adding batteries (Figure 7-1A, black curve). This is approximately 20 W higher than the motor power without batteries in the system during the middle of the day (Figure 7-1A, grey curve). This occurred since the pump was always seeking to extract the desired current from both PV and batteries. As a consequence, the discharging current of the batteries was added to the PV current to provide the desired current of the pump. Therefore, the batteries were discharged continuously throughout the entire day, causing the drop of SOC from 100% to 20% (Figure 7-1B). When comparing the maximum PV output power (light blue in Figure 7-1A) and the pump power, an approximately 50 W power loss can be anticipated on the additional electronics. This is likely due to the fact that the additional electronics do not make the system more efficient. The typical efficiency of the batteries, DC/DC converter, and charge controller is 96% [280], 88% [312], and 98% [313], respectively, which results in a total efficiency of 83%. Another reason for this power loss was that the motor was operated at a constant voltage of 48 V_{dc} when connected to the batteries. This low voltage reduced the ability of the pump motor to start, as well as drew a higher current [314], which conversely further decreased motor efficiency and produced more resistive losses.

The low system efficiency resulted in the low TMP_{RO}, and thus the RO flux (black curve in Figure 7-1C and Figure 7-1D). Comparatively, when no batteries were incorporated, the TMP_{RO} and RO flux (grey curve in Figure 7-1C and Figure 7-1D) followed the same trend as the changes of SI. This occurred since the driving force changed with the variations of SI for the desalination process by supplying the required hydraulic pressure to overcome the osmotic pressure of the feed water. This affects the recovery and retention that were determined by mass transfer at low pressure (grey curve in Figure 7-1E), and ultimately results in fluctuations in the permeate EC (grey curve in Figure 7-1F) and SEC (grey curve in Figure 7-1H).

Furthermore, the motor power (grey curve in Figure 7-1A) directly followed the variations in SI when no batteries were deployed. Due to the lack of energy from solar panels, it dropped to 0 W several times during periods of fluctuations and intermittency, thus causing system shut-downs. It can also be seen that the TMP and flux (black curve in Figure 7-1C and D) remained constant when batteries were added, as the power was drawn from the batteries continuously throughout the entire day. Overall, the recovery of approximately 30% (Figure 3G) led to the average permeate EC of 294 μS/cm (Figure 7-1H, WHO guideline value of 1700 μS/cm) [315] and SEC of approximately 4 Wh/L (see Figure 7-1J). It is worth noting that the relatively low recovery ensures a low salinity concentrate stream, and the possibilities for suing the disinfected waster stream for washing and livestock watering purposes. The requirements to maintain conditions of sheep and beef cattle are 21800 and 8800 μS/cm, while the tolerance of healthy growth is 6700 μS/cm and 10000 μS/cm, respectively [265]. As a consequence, it is necessary that the usage of the concentrate stream remains at a level below these limits. Overall, the fully-charged batteries enabled the increase of production from 664 L/d to 767 L/d (~ 16% improvement), with water quality also improving from 304 to 294 μS/cm (~ 3%). The average parameters are summarized in Table 7-1 in Section 7.3.

7.2. Operation under other solar days (with and without fully-charged batteries)

This section aims to study the effects of different levels of SI conditions on system performance, again both in the directly-coupled and with fully-charged batteries. Figure 7-2 shows the cumulative permeate water production, permeate EC, and SEC of the PV-membrane system under the very cloudy and sunny day. From the top two graphs of Figure 7-2, when incorporating the batteries, the motor power remained constant at 350 W throughout the day despite two different weather conditions (Figure 7-2A and Figure 7-2F). This was approximately 20 W higher than the motor power in the directly-coupled system during the middle of the day. The reasons for this have been discussed in Section 7.1 (Figure 7-1A). It was found that the saturation in Figure 7-2A and F was more pronounced when compared with the value where the motor power saturated under the partly cloudy day. The saturation occurred at $SI > 800 \text{ W/m}^2$, and the SI above 800 W/m^2 exhibited the shortest duration on the partly cloudy day. On the other hand, the high temperature (above $40 \text{ }^\circ\text{C}$, see Figure 3-5B) also caused the low PV voltage (approximately 10 V lower when reaching saturation), thus decreasing power input to the pump. On the very cloudy day, the performance with batteries improved in the following manner: production increased by 81% from 395 to 714 L/d; average permeate EC improved by 27% from 347 to 274 $\mu\text{S/cm}$; and average SEC decreased by 17% from 4.8 to 4.1 Wh/L. The average parameters are summarized in Table 7-1 in Section 7.3.

On the sunny day, as shown in Figure 7-2H, it was found that permeate production without batteries was lower in the morning due to the low levels of SI, and then it approached the battery case at 16:00. This occurred during the periods (9:30 to 15:15) when the TMP_{RO} of the directly-coupled configuration exceeded the TMP_{RO} with batteries (see Figure 7-2G). As discussed above, this is because the direct-coupled PV-membrane system exhibited higher efficiency, thus producing markedly more permeate for most of the day (from 9:30 to 15:15) at $SI > 800 \text{ W/m}^2$. Amongst these three solar days, the SEC with batteries on the sunny day achieved the highest value. This occurred because a high average SI was able to supply higher current to the pump from the PV and a small portion of current from the batteries. As a result, the discharging rate of batteries was decreased (i.e., a fraction of approximately 20% current supplement to the pump at the maximum SI during the middle of the day). Therefore, the batteries played a minor role in producing sufficient permeate throughout the day, but losses were still encountered, which caused the increase of the SEC. This indicated the likelihood of system redundancy when incorporating additional devices. Performance on the sunny day was summarized as follows: the water production increased from 770 to 892 L/d (15.8% improvement); the permeate EC improved from 353 to 290 $\mu\text{S/cm}$ (17.8% improvement); and the average SEC increased from 4.0 to 4.3 Wh/L (see Table 7-1 in Section 7.3).

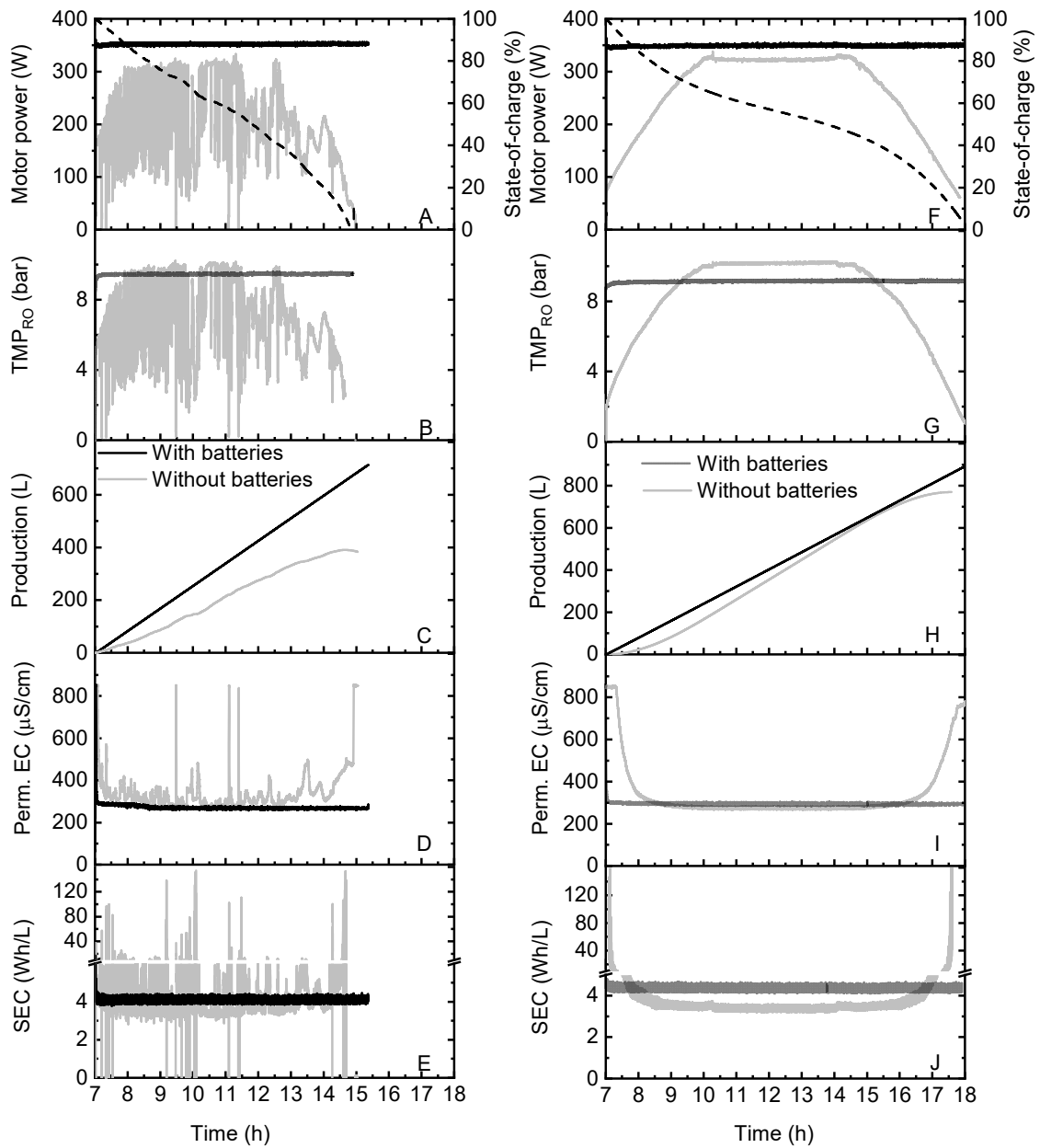


Figure 7-2: Cumulative performance of the PV-membrane system with/without (grey curves) fully-charged battery storage (100% initial SOC, black curves) on the very cloudy day (left graph) and sunny day (right graph) in terms of (A, F) motor power and state-of-charge, (B, G) TMP_{RO} , (C, H) production, (D, I) permeate EC, and (E, J) SEC. Adapted from [278], CC BY-NC-ND 4.0 License.

From the results presented above, it can be found that the batteries played a significant role in smoothing fluctuations and intermittency, reducing shut-down events, and improving water quantity and quality. These results were not surprising given the fact that the Li-ion batteries showed high efficiency and energy intensity. The main disadvantage would be the increased cost of the system, which ultimately affects the

cost of water (as discussed in Section 7.4). This is expected to decrease over time, however, as the technology matures.

7.3. Operation with different energy storage capacities

The aim of this section is to assess the impacts of different energy capacities (realized by varying the initial SOC) on PV-membrane system performance when operated on the partly cloudy day, with a particular focus on SEC and production. Figure 7-3 illustrates the behaviour of the PV-membrane system under the partly cloudy day starting with the batteries at an initial SOC of 50%.

The pump was operated at the full power regime of 7 h 20 min (see Figure 7-3A) with the addition of batteries prior to reaching the limits of their capacity. Consequently, the pump was directly subjected to fluctuations, as well as repeated attempts at charging and discharging of the batteries after 14:00. This was compared to the pump that ran at full power for 9 h 20 min with fully charged batteries (see Figure 7-1A). As shown in Figure 7-3B, from 7:00 to approximately 14:00, the batteries provided power to the system continuously at a maximum discharging current up to 20 A (see Figure 7-3B). This can be seen from the decline of the SOC to 0% at 14:15 (Figure 7-3D). The occurrence of oscillations indicated that the batteries reached the lower limit of the DC/DC converter (20 V). Subsequently, the PV started charging the batteries, and thus caused the shut-down of the pump. It is important to note that these repeatable attempts of charging and discharging of the batteries resulted in oscillations of the pump, which produced power fluctuations of the pump. These power fluctuations were encountered since the charge controller was not capable of powering the pump and charging the batteries simultaneously, indicating a system shortcoming that requires improvement in future research. The flux and TMP of the RO membrane followed the same trend as the pump discussed above (see Figure 7-3E and F). The moving average values in the graphs indicated a pattern of the SI on the PV-membrane system as a consequence of the attempt of turning on the pump. Overall, the system produced 669 L permeate, which was comparable with the production (663 L) of the directly-coupled system. In addition, the SEC was increased by 15.9% from 3.7 to 4.0 Wh/L. As a consequence, batteries with an initial SOC > 50% (energy capacities > 1.2 kWh) are recommended to be applied for further improvement of water quality and quantity. The remaining performance graphs of the PV-membrane system in terms of varied initial SOC (70, 40, 30, and 20%) are provided in Figure 7-4 – Figure 7-7 for further comparisons.

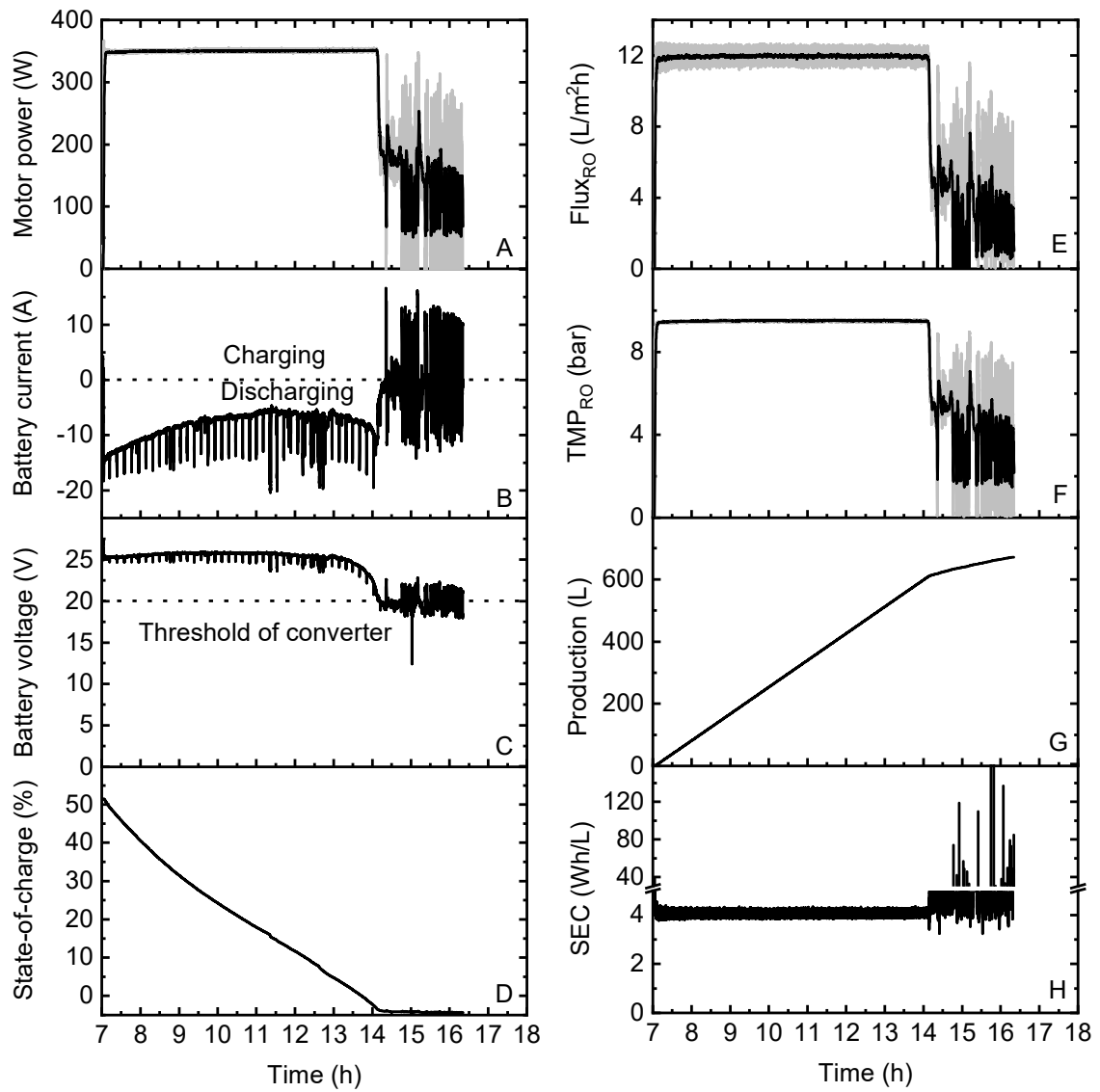


Figure 7-3: The performance of the PV-membrane system equipped with batteries at 50% SOC under the partly cloudy day, illustrating (A) pump power, (B) battery current, (C) battery voltage, (D) state-of-charge, (E) $flux_{RO}$, (F) TMP_{RO} , (G) production, and (H) SEC. Note that the black curves on graph (A), (E), and (F) are the moving average values of 10 points. Adapted from [278], CC BY-NC-ND 4.0 License.

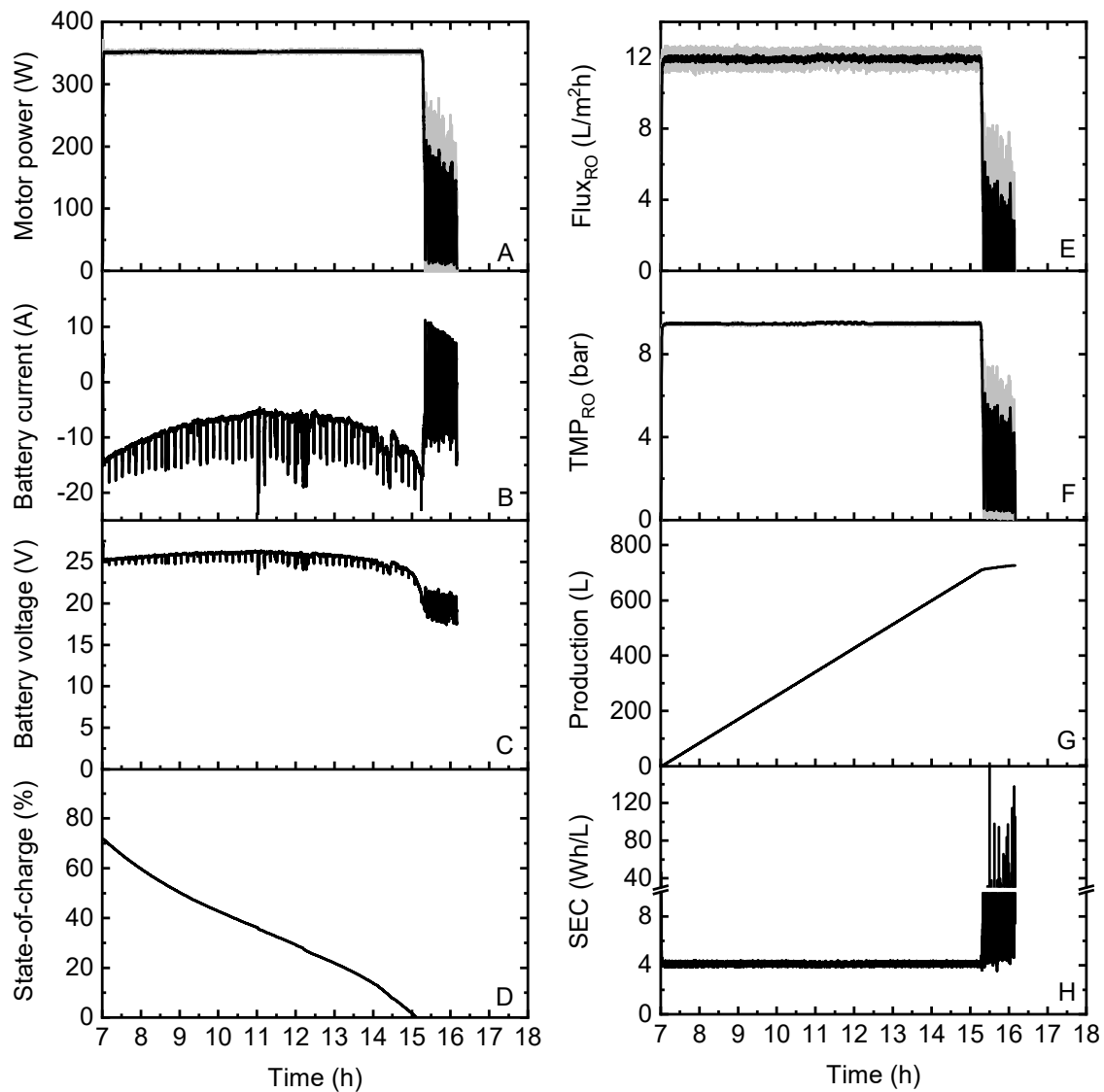


Figure 7-4: The performance of the PV-membrane system equipped with batteries at 70% SOC under the partly cloudy day, illustrating (A) motor power, (B) battery current, (C) battery voltage, (D) state-of-charge, (E) flux_{RO} , (F) TMP_{RO} , (G) production, and (H) SEC. Note that the black curves on graph (A), (E), and (F) are the moving average values of 10 points. Adapted from [278], CC BY-NC-ND 4.0 License.

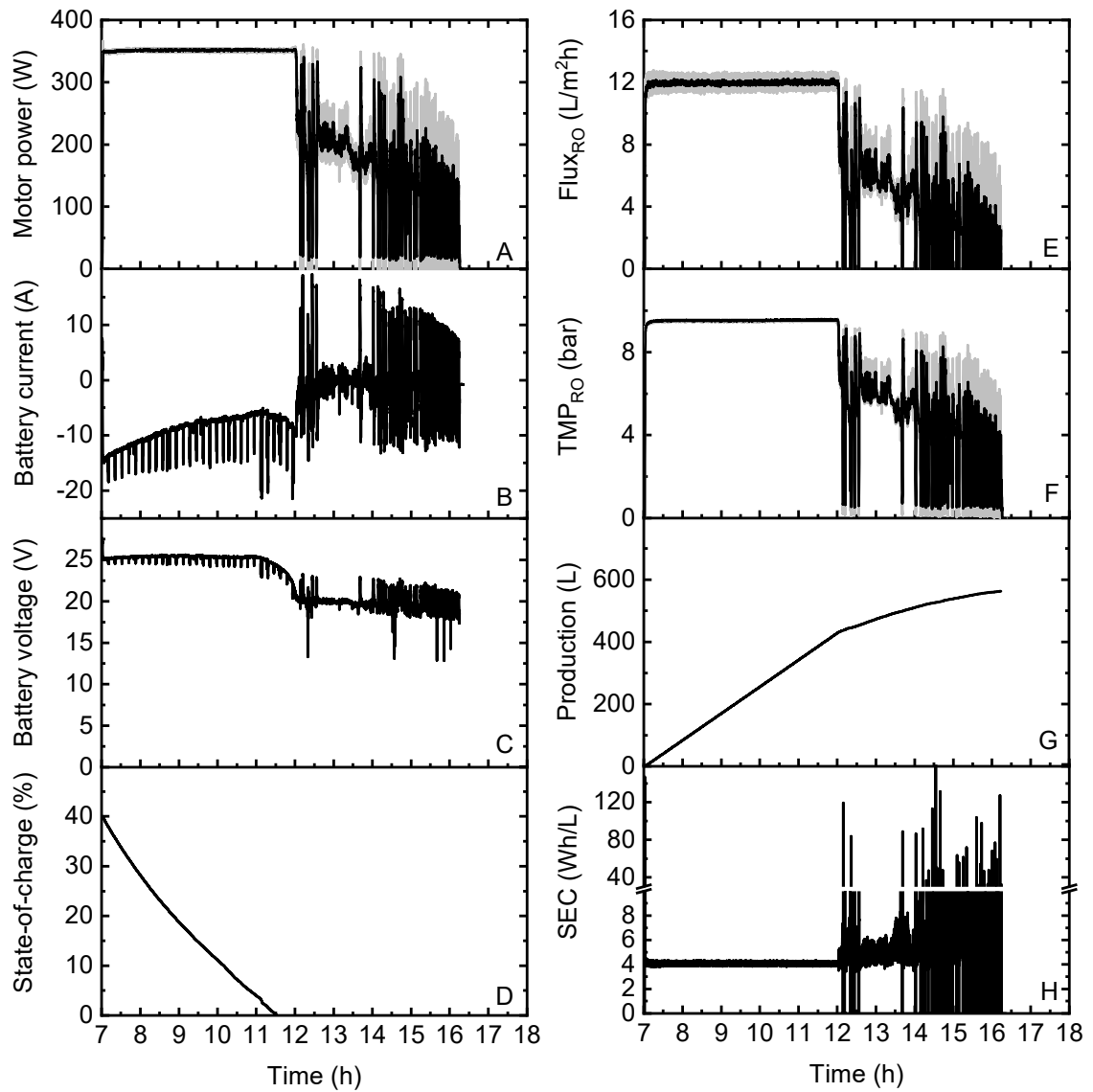


Figure 7-5: The performance of the PV-membrane system equipped with batteries at 40% SOC under the partly cloudy day, illustrating (A) motor power, (B) battery current, (C) battery voltage, (D) state-of-charge, (E) $flux_{RO}$, (F) TMP_{RO} , (G) production, and (H) SEC. Note that the black curves on graph (A), (E), and (F) are the moving average values of 10 points. Adapted from [278], CC BY-NC-ND 4.0 License.

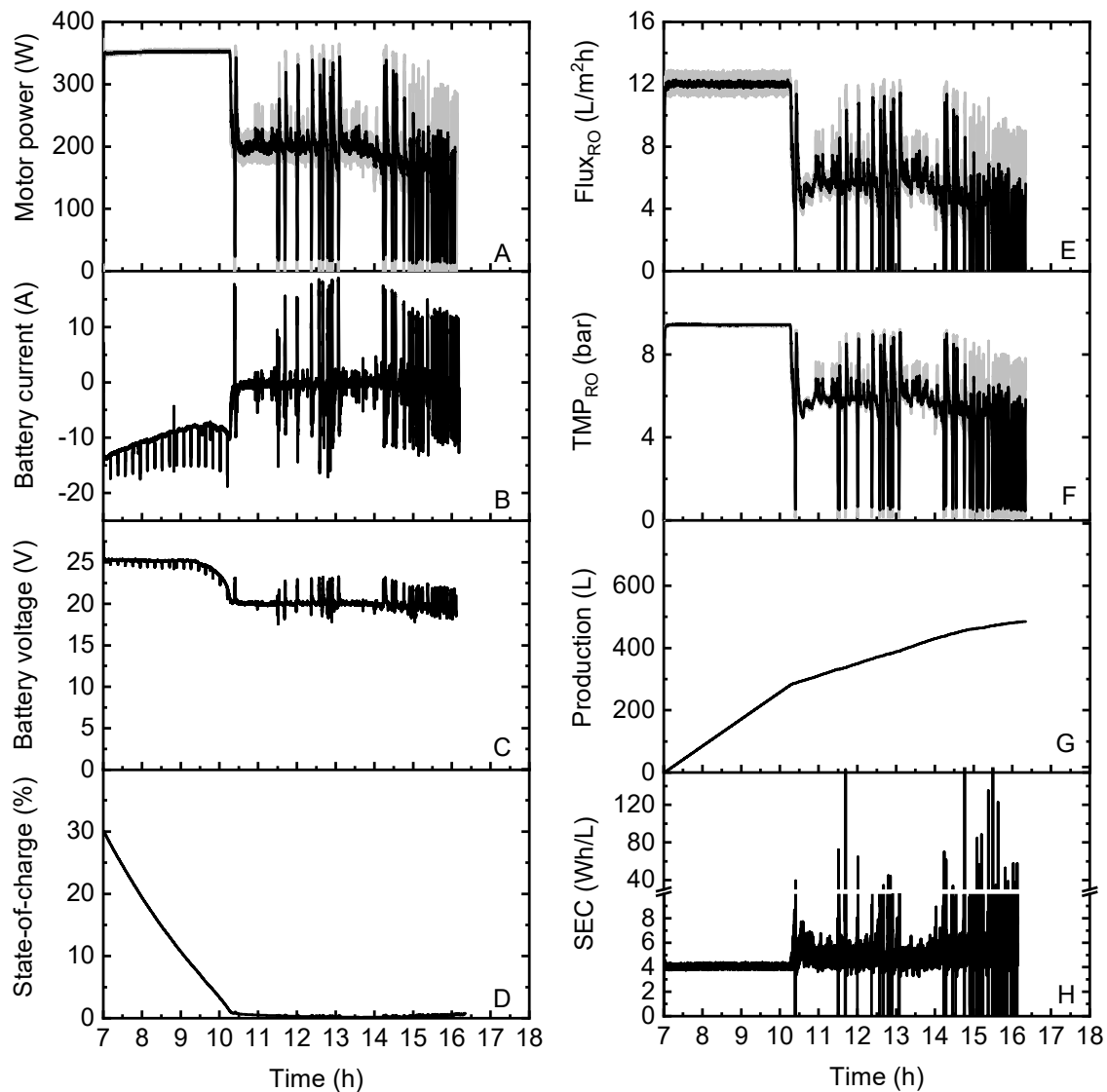


Figure 7-6: The performance of the PV-membrane system equipped with batteries at 30% SOC under the partly cloudy day, illustrating (A) motor power, (B) battery current, (C) battery voltage, (D) state-of-charge, (E) flux_{RO} , (F) TMP_{RO} , (G) production, and (H) SEC. Note that the black curves on graph (A), (E), and (F) are the moving average values of 10 points. Adapted from [278], CC BY-NC-ND 4.0 License.

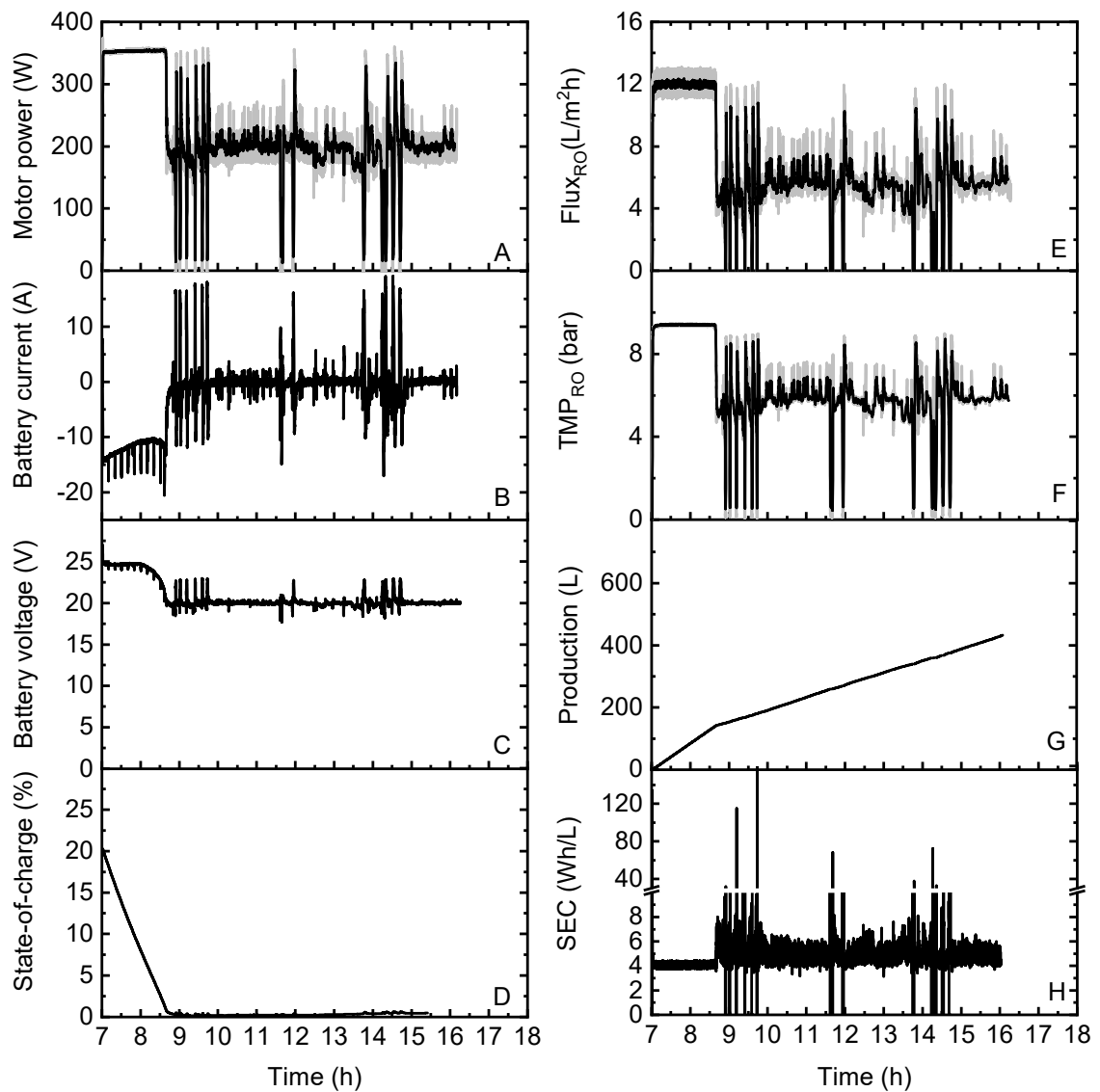


Figure 7-7: The performance of the PV-membrane system equipped with batteries at 20% SOC under the partly cloudy day, illustrating (A) motor power, (B) battery current, (C) battery voltage, (D) state-of-charge, (E) $flux_{RO}$, (F) TMP_{RO} , (G) production, and (H) SEC. Note that the black curves on graph (A), (E), and (F) are the moving average values of 10 points. Adapted from [278], CC BY-NC-ND 4.0 License.

As indicated in Figure 7-8, the effect of different energy storage capacities (varied SOC) on the PV-membrane system with average SEC, water quality, and quantity were evaluated. Water production decreased along with the drop of the initial battery SOC (see Figure 7-8A). The improvement of water production occurred at an initial SOC > 50%. The average permeate EC was less influenced by SOC (see Figure 7-8B) due to the dense membrane with high retention (BW30) that was employed in these experiments. As shown in Figure 7-8C, the SEC increased with the decrease of the SOC, showing that the lower SOC reduced the flux and increased the SEC. It is perhaps intuitive that the SEC is bound to return to the

reference case when the batteries are fully discharged. However, this is anticipated to occur when the batteries are disconnected from the pump so that they do not have the same voltage potential, and thus the repeatable attempt of charging and discharging behaviour can be avoided.

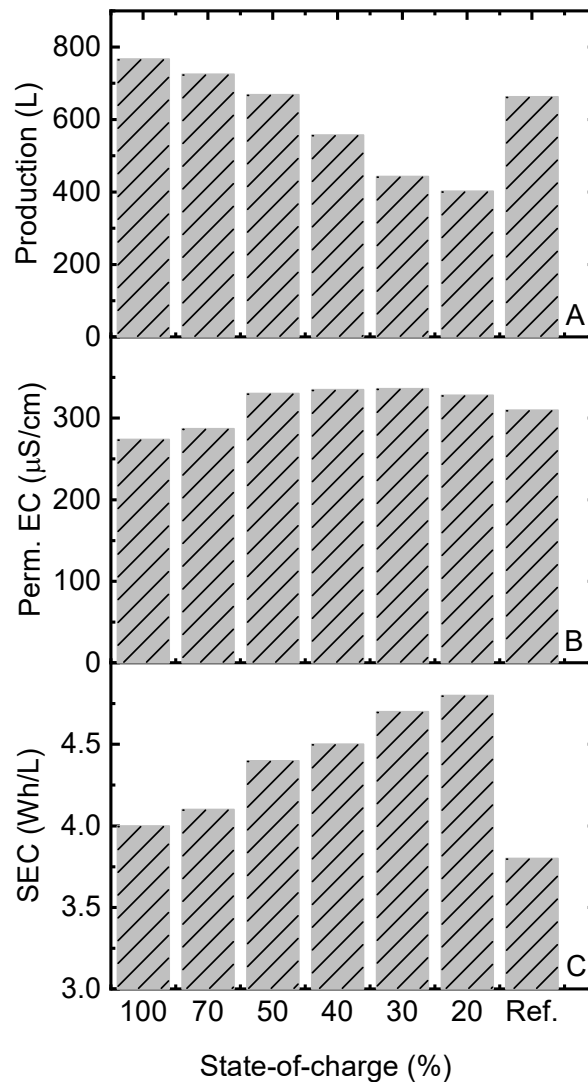


Figure 7-8: Key performance indicators of the PV-membrane system performance as a function of the initial energy storage capacity of the batteries (different SOC) on the partly cloudy day, illustrating (A) water production, (B) permeate EC, and (C) SEC. Note that Ref. represents the directly-coupled system performance (without batteries), as discussed in Section 7.1. Adapted from [278], CC BY-NC-ND 4.0 License.

The overall average performance values are given in Table 7-1 to provide a clear overview of system performance with batteries present based on varied energy storage capacities over the three solar days. The improvement of water production and quality has been discussed above. The SEC of the reference on the very cloudy day exhibited the highest value, which is likely due to: i) the flux decreased instantaneously with the significant reduction of power input as a result of large fluctuations of the SI (not shown in the

graphs); ii) the reduction of flux to 0 L/m²h due to insufficient effective pressure to produce permeate; and iii) the occurrence of shut-down events due to inadequate power to achieve system pressure that resulted from large variations of SI, thus causing slow recovery (resilience) of the system to produce sufficient permeate as a result of input power intermittency [38]. Furthermore, the average retention and permeate EC showed no large differences, which was attributable to the tight membrane with high retention that was more resilient to variations in permeate quality [38].

With the addition of batteries, the impacts of varied energy capacity (varied initial SOC from 100% full down to 20% full) on the partly cloudy day became more apparent. Permeate production gradually increased from 402 to 767 L as the pump extracted power from both the batteries and PV source, enabling the pump to be operated with full power over this period (see the full-power duration in Table 7-1). In contrast, the average SEC decreased from 4.8 Wh/L to 4.0 Wh/L, as the system spent more time in the regime of full-power operation. The average RO flux exhibited the same patterns as permeate production. When comparing the SEC with fully-charged batteries and the reference case, it was observed that the reference SEC on the sunny and the partly cloudy day was lower than that with batteries. However, it was significantly higher on the very cloudy day. This highlights the role of incorporating Li-ion batteries to obtain more permeate as a result of providing constant power versus additional pump power consumption in terms of the fluctuations in SI. Indeed, this emphasizes the design of systems with a focus on energy consumption and enhancement of water quality and quantity, which can be achieved at the expense of system efficiency, as well as the possibility of underutilizing the energy storage devices.

Table 7-1: Overall average performance of the PV-membrane system with/without batteries over the three solar days. Adapted from [278], CC BY-NC-ND 4.0 License.

Solar days	Initial SOC (%)	Avg. flux _{RO} (L/m ² h)	Avg. TMP _{RO} (bar)	Avg. perm. EC (μS/cm)	Avg. retention (%)	Perm. production (L)	Avg. SEC (Wh/L)	Full-power duration (hh:mm)
Partly cloudy	20	7.3	6.6	328	96.2	402	4.8	1:55
	30	7.4	6.7	336	96.0	443	4.7	3:02
	40	9.0	7.2	335	95.9	557	4.5	5:09
	50	9.9	8.2	330	95.9	669	4.4	7:22
	70	11.9	8.9	287	96.3	725	4.1	8:16
	100	11.3	9.4	274	96.4	767	4	9:20
	Ref.	10.7	8.4	310	96.3	663	3.7	–
Very cloudy	100	11.8	9.4	274	96.3	646	4.1	8:00
	Ref.	7.3	6.5	347	95.9	396	4.6	–
Sunny	100	11.3	9.1	290	96.4	892	4.3	11:00
	Ref.	10.2	8.2	353	95.8	770.	4.0	–

From the experiments performed above, it can be seen that the charge controller was not able to charge the batteries and run the pump simultaneously when reaching the limit voltage of the batteries after the batteries are fully discharged. The charge controller for PV systems normally regulates the voltage to avoid overcharging/discharging. Further improvement of the charge controller needs to be achieved, for instance, the use of a buck-boost converter to control bidirectional power from the PV and batteries to enhance system performance. Another way to improve system performance can be realized by connecting the batteries in series to increase voltage output ($48 V_{dc}$); thus, eliminating the DC/DC converter as the pump can be operated in a wide voltage range ($30 \sim 300 V_{dc}$). As a result, the voltage of the batteries was not limited to be at 20 V, which avoids repeatable charging and discharging behaviour. Furthermore, power loss is reduced as a consequence of fewer electronics deployed in the system. The two minor disadvantages are: i) this battery configuration increases the failure rate if one battery does not function properly, causing the voltage to collapse and the battery pack to turn off [126]; and ii) careful cell matching is needed for connections in series, in particular when drawing heavy loads [126]. Therefore, an equitable trade-off between robust long-term system operation and performance needs to be made.

7.4. System performance comparisons of batteries and SCs

The final important result can be seen when the results from this work are compared to system performance with SCs. It is noted that these two system setups are configured with the same PV power rating (500 W), but varied PV voltage settings due to the voltage constraints between the SCs and batteries (discussed in Section 3.3). Figure 7-9 demonstrates the experimental results of the PV-membrane system when equipped with SCs and batteries.

As in the previous experiments discussed above, the motor pump with batteries consumed constant power at approximately 350 W (black curve in Figure 7-9A). Figure 7-9B indicates that the motor pump with batteries worked at a constant voltage of $48 V_{dc}$, and the PV supplied the photocurrent (see Figure 7-9D) to the pump as required. Meanwhile, the batteries were able to provide continuous current to the pump throughout the day (see Figure 7-9E) as a result of their high energy storage capacity (2.4 kWh). However, the motor power with SCs largely followed variations in the SI (plotted in Section 7.3). This relied on the fact that the pump with SCs was controlled with respect to PV voltage (controlled by pre-set voltage thresholds as discussed in Section 3.5, see grey curves in Figure 7-9C) and mainly drew current from the PV, thus leading to higher power consumption of the pump. In addition, a PTC lamp was connected in series with the pump to increase inner resistance, and this variable resistance was used to buffer the sudden drops caused by the built-in MPPT between the SCs and SAS. This was at the expense, however, of an average power loss of approximately 50 W on this solar day. As illustrated in Figure 7-9E, prompt discharging behaviour of the SCs occurred at the beginning of the day. During the period of 11:00 to 12:30 when large fluctuations appeared, the SCs started discharging to the pump for energy buffering due to the

lack of PV power. It is worth noting that the SOC only decreased to approximately 85% during the discharging periods, which was controlled by the pre-set voltage threshold setting ($V_{\text{charging_off}}$) to prevent deep discharging of the SCs, thus avoiding the large voltage drop of the pump. This was implemented on the charge controller settings, as the pump always seek to draw the maximum power from the power sources (both PV and SCs), and as a result, the SCs cannot provide energy buffering when encountering the next large fluctuation if they are fully discharged at the first large fluctuation. As a consequence, no shut-down events were observed, although several large fluctuations occurred. The advantages of eliminating the shut-down events are decreasing potential damage to the pump and RO membrane [96], and enhancement of permeate water quality and quantity [275].

The desalination performance of the PV-membrane system is determined by the SOC of the energy storage components, which depends on the PV power availability. The TMP_{RO} (Figure 7-9C) determined the RO flux (Figure 7-9E) and permeate EC (Figure 7-9F). Furthermore, the permeate production with SCs approached the value with batteries (see Figure 7-9G), indicating that the system with SCs produced much higher permeate for most of the day. This occurred when the TMP_{RO} exceeded the values with batteries (see Figure 7-9C). The SEC with batteries was much lower than the value with SCs, suggesting that less energy was needed to produce a unit of clean water. When compared to the reference case, the use of SCs for energy buffering resulted in a 9% increase in water production and a 13% improvement in SEC. As discussed in Section 7.1, the improvement of system performance with batteries is ascribed to the improved power quality provided to the membrane system, as a result of supplying energy and constant power throughout the day. Moreover, water quantity improved by 16% with Li-ion batteries. It is expected that an overlap exists with SCs if the batteries have small capacities (e.g., approximately 1 Ah providing 5 min of power to the system). Therefore, Li-ion batteries are preferred as energy storage units in this PV-membrane system, as a consequence of their high energy intensity, charge/discharge cycles, and reduced cost per kW.

Intuitively, increasing the size of the energy storage units would provide power for longer periods of fluctuations. Nevertheless, this would constitute a trade-off between the benefits of increasing storage time and the added cost of energy storage capacity. It has been reported that the capital cost of SCs was estimated to be relatively stable at US\$1600/kWh [306], while the cost of Li-ion batteries reached US\$135/kWh in 2020, with a further reduction below US\$100/kWh anticipated in 2024 due to technological advancements and economies of scale [305]. In addition, the O&M cost of SCs was approximately US\$1/kW-y [306]; whereas, the O&M cost of Li-ion batteries was in the range of US\$6-14/kW-y in 2017 [316], with a further decrease in cost expected to US\$8/kW-y by 2025 [306].

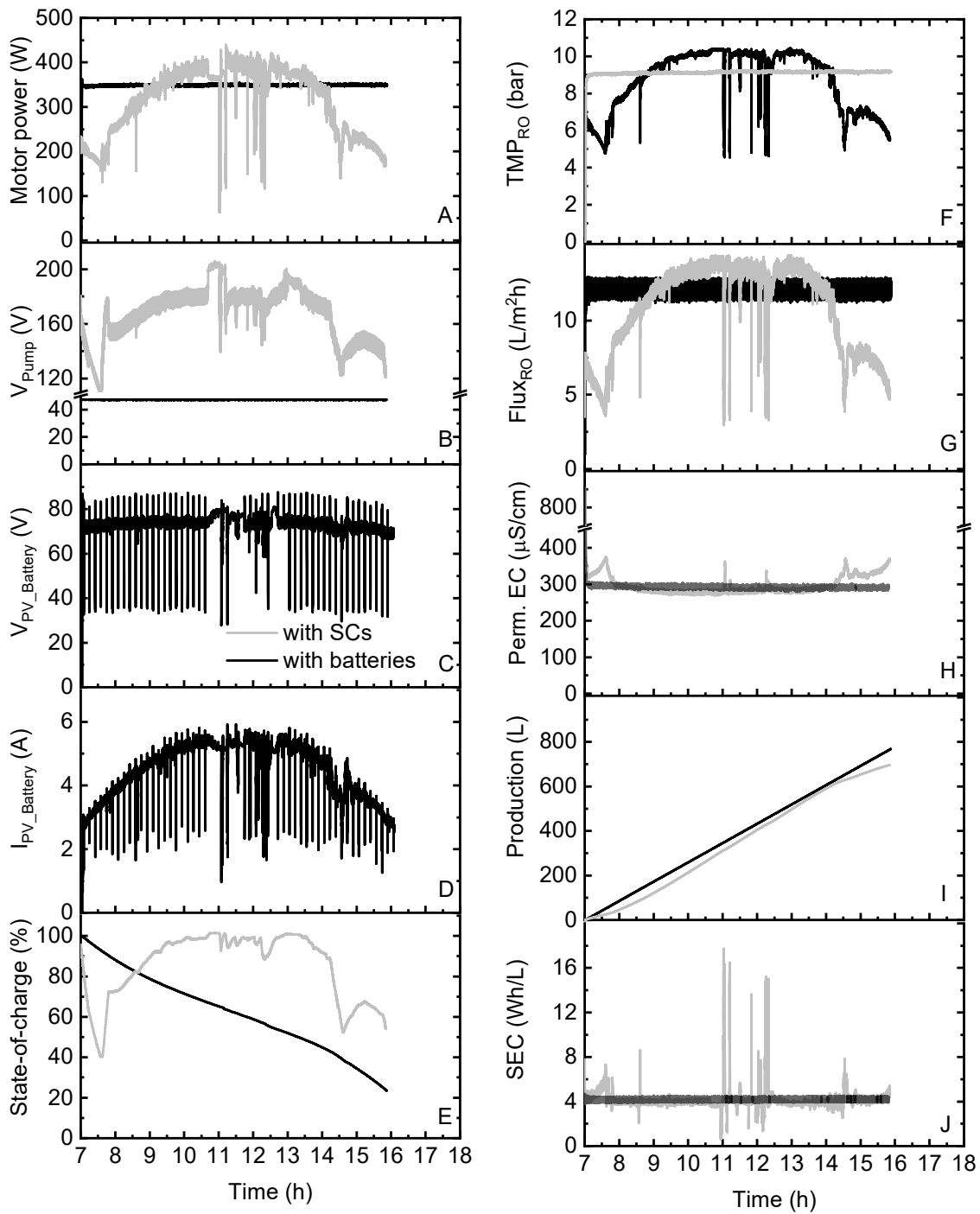


Figure 7-9: Performance of the PV-membrane system with fully-charged Li-ion batteries (black curve) compared to the system with SCs and charge controller (grey curve) on the partly cloudy day, illustrating (A) motor power, (B) V_{Pump} , (C) $V_{PV_Battery}$, (D) $I_{PV_Battery}$, (E) state-of-charge, (F) TMP_{RO} , (G) $flux_{RO}$, (H) permeate EC, (I) production, and (J) SEC. Adapted from [278], CC BY-NC-ND 4.0 License.

Further work is needed to: i) select a charge controller for batteries with high voltage output, such as 48 V_{dc}; ii) apply the pulse-width modulation method to the pump to eliminate power losses on the PTC lamp, as well as reduce the average power delivered by the PV and SCs; and iii) examine the effect of integrating Li-ion batteries and SCs on PV-membrane system performance and overall improvements in water quality and quantity.

7.5. Summary

In this chapter, two different electrical energy storage options – Li-ion batteries and SCs – to improve the water quantity of a PV-membrane system were studied and compared to the directly-coupled system performance. The Li-ion batteries with energy storage of 2.4 kWh enabled full-power operation of the pump for 8 – 11 h over the three different solar days. As a result, the fully charged batteries (energy storage capacity of 2.4 kWh) allowed a 15 – 80% increase in water production and a 3 – 27% increase in water quality. It was also observed that the average permeate quality with/without Li-ion batteries all fulfilled the WHO guidelines, which indicates good system design and a proper choice of membrane and PV array sizing. In particular, on the partly cloudy day, the impacts of varying the energy storage capacities on the PV-membrane system were investigated. It was found that the increase of water production occurred at an initial SOC $\geq 50\%$ (energy capacity of 1.2 kWh); whereas, system shut-downs appeared after the batteries were fully discharged as a result of repeated attempts of charging and discharging behaviours at initial SOC $< 50\%$. Finally, system performance on the partly cloudy day between the addition of Li-ion batteries and SCs were compared. The addition of SCs for short-term energy buffering resulted in a 9% increase in water production and a 13% decrease in SEC. When compared with Li-ion batteries on the same solar day, SCs led to a 16% increase in water production and an 8% increase in SEC.

To sum it up, Li-ion batteries appeared to be an appropriate energy storage option for PV-membrane systems, due to their high energy intensity, large number of charging/discharging cycles, and steadily decreasing cost. When considering the PV-membrane system for a targeted lifetime of 20 y in off-grid and remote areas, the option of oversizing the PV power capacity and allowing for a directly-coupled system potentially offers a more reliable and robust solution. Further investigations are required to: i) study the sizing approach with the associated life-cycle cost analysis over the 20-y life expectancy; and ii) design a suitable energy management system to enable short-term delivery of large amounts of power for SCs buffering and longer-term energy storage for Li-ion batteries.

8. Conclusions and outlook

8.1. Conclusions

The main goal of this Ph.D. research was to examine the reliability, system control, and energy storage technologies of the direct-coupled PV-membrane system. To address this knowledge gap of design experience and experimental data on PV-membrane systems, this study aims to enhance applications of these two combined technologies (PV and membrane technologies) in decentralized and remote areas. A summary of the significant findings are presented below.

Design of the reliable and robust PV-membrane system

An essential part of the initial design process was to deliver clean water at the lowest cost over the lifetime of the system. A review of all components within a PV-membrane system for brackish water desalination was performed in terms of: i) efficiency; ii) operating range; and iii) reliability to achieve reliable and robust system design. Failure and degradation modes, and lifetime and robustness issues associated with field operation, are also discussed. The outcome suggests that a small-scale (power rating < 1.5 kW) PV-membrane system – based on a helical rotor pump driven by a direct-current brushless motor and powered by silicon photovoltaic modules – may achieve a life expectancy of 20 y while operating at an SEC of 1.5 – 3 Wh/L. The analysis is essentially used to identify the optimal combination of components, system construction, and possible reliability improvements, while the investigation into component and system failures allows the weakest links to be avoided and optimization of the current system used for this research.

Energy buffering control for ramp rates in solar irradiance

The impacts of variations (ramp rates) in both SI and output voltage of the solar panels on the performance of a PV-membrane system equipped with SCs for buffering fluctuations were investigated. A charge controller based on high-temporal-resolution (1 s) pre-set voltage sensing thresholds were designed in order to ensure the best use of energy between PV and SCs, allowing for resilient operation of the system under variable ramp rates conditions. With no SCs present and under periodic fluctuations in SI from 1000 to 600 W/m², the system responded well to voltage ramp rates of 0.5 V/s. At a rapid ramp rate of $\Delta V_{PV} = 2$ V/s, the charge controller enabled the SCs to bridge the power gap for up to 6 min 20 s. The SOC varied from 11 to 86%, irrespective of ramp rate magnitude. The combination of voltage thresholds of $V_{\text{pump_on}} = 160$ V and $V_{\text{pump_off}} = 90$ V resulted in optimum system performance, and realized a high permeate production at a low SEC. These findings, determined under a challenging solar day, serve as a solid foundation for the application of PV-membrane systems operating under realistic weather conditions.

System control for reducing system shut-downs and enhancing resilience under real solar days

Fluctuations and intermittencies of solar energy cause shut-downs of the directly-coupled PV-membrane system. To reduce system shut-down events and enhance resilience, a charge controller based on preset sensing voltage thresholds for SCs-based energy buffering is implemented under varied solar days. The key parameters – number of shut-down events ($\#_{\text{shut-down}}$), shut-down duration ($t_{\text{shut-down}}$), and the resilience factor in flux (RF_{flux}) – were evaluated, in particular on the partly cloudy day that exhibited a 90-min period with a high level of fluctuations. Under partly and very cloudy days, the SCs and charge controller enabled reduction of $t_{\text{shut-down}}$ by 37% and 12% and $\#_{\text{shut-down}}$ by 2 – 13 events, respectively. In addition, the average SEC was improved by 22% and 8% on the very cloudy day and the sunny day, respectively. During the 90-min fluctuations, $t_{\text{shut-down}}$ was constrained to 1 – 4.5 min, and $\#_{\text{shut-down}}$ was reduced by 1 – 4 events, for feedwater salinities of ≤ 7.5 g/L. When increasing the PV capacity to 600 – 1000 W, zero system shut-down events occurred, RF_{flux} increased from 0.3 to 0.8, and RF_{SEC} dropped to less than 2, indicating enhanced system resilience with the SCs and charge controller.

UF membrane backwashing control with two configurations

Two different UF membrane backwashing configurations were implemented to a PV-membrane system, namely, a passive bladder tank and a BW pump powered with SCs. Energy consumption was compared utilizing the fixed BW volume of 4 L. The bladder tank exhibited higher BW SEC (0.3 Wh/L) in comparison with the BW pump (0.09 Wh/L), which is primarily due to the longer time (approximately 50 s) required to refill the bladder. Nevertheless, given the passive device that reduces additional electronics and minimises the failure risks, the bladder tank configuration is recommended for backwashing in the PV-membrane system when deployed in remote areas. Under real solar days with bentonite foulant, the SCs are capable of providing 5 to 7 BW cycles at a BW interval of 90 min. The bladder tank indicated a slightly higher TSEC, at ~ 4 Wh/L, than the BW pump. A rise of TMP_{UF} to approximately 0.2 bar at the maximum BW interval of 120 min was observed, and more bentonite depositions occurred on the membrane surface at filtration times longer than 30 min. Indeed, practically all of the bentonite was deposited on the membrane surface at $f_{\text{BW}} = 120$ min when compared with the total mass that was added into the feedwater. However, the TSEC decreased less with frequent backwash and reached a stable value of 3.7 Wh/L at $f_{\text{BW}} \geq 60$ min. This indicated that fewer BW cycles saved energy, and as a result, the TSEC approached the normal filtration SEC. A trade-off between mitigating membrane fouling and reducing energy consumption exists. Finally, utilization of a valve to simulate fouling supports UF membrane fouling studies without inducing irreversible fouling to the membrane and handling complex feed solutions. It can serve as a reasonable substitute to form cake fouling on the membrane surface in the PV-membrane system. Further applications on real water are required to elucidate the BW efficiency and energy consumption of the UF membrane in the PV-membrane system.

PV-membrane system performance with two electrical energy storage options

The potential for Li-ion batteries and SCs to overcome long-term (1 d) and short-term (a few minutes) SI fluctuations on the PV-membrane system was studied. Experiments were carried out by using 5 g/L NaCl with varied battery capacities (100, 70, 50, 40, 30, and 20 Ah) to determine the impacts of decreasing

the energy storage capacities. On the partly cloudy day, clean drinking water was produced at an average SEC of 4 Wh/L with fully charged batteries. Furthermore, when comparing to the directly-coupled system, daily water production increased from 663 L to 767 L (16%), and the average EC reduced from 310 $\mu\text{S}/\text{cm}$ to 274 $\mu\text{S}/\text{cm}$ (12% improvement). For the SCs, a 9% increase in water production and a 13% improvement in average SEC was observed. When varying the battery capacities, water production improved at an initial battery capacity higher than 50 Ah (initial SOC > 50%). On the sunny day and the very cloudy day, the fully charged batteries enabled an increase of water production by 15% and 80%, and water quality improved by 18% and 21%, respectively.

The above conclusions regarding the PV-membrane system – i) design of a reliable and robust PV-membrane system; ii) energy buffering control for ramp rates in solar irradiance; iii) system control for reducing system shut-downs and enhancing resilience under real solar days; iv) UF membrane backwashing control with two configurations; and v) PV-membrane system performance with two electrical energy storage options – have addressed many of the technical barriers faced by directly-coupled RE-membrane systems. Overall, the employment of energy storage devices can largely improve system performance, allow autonomous operation. The disadvantages would be the reduced system efficiency and robustness while working in the remote areas. Alternatively, the option of employing more PV power modules and allowing for a directly-coupled PV-membrane system potentially provides a more reliable and robust solution with a target lifetime of 20 years in remote area. It is expected that this knowledge will assist to improve the reliability, resilience, feasibility, and reach of applications of such RE-membrane systems by establishing foundations for further research on system control, energy storage options, backwashing protocols, and long-term field testing in remote areas.

8.2. Outlook and suggestions for further research

Several interesting research topics that are beyond the scope of this Ph.D. dissertation, but are highly beneficial for further studies, are outlined below.

The effects of transient operation on long-term performance remain unknown. A pilot setup that takes into account the components' lifetime and efficiency with a real brackish water source and detailed measurements can be undertaken to evaluate performance over years. Further investigations that use a pilot plant with a wide variety of real brackish water are needed to form a more comprehensive overview.

The control algorithm of the charge controller based on simple pre-set voltage thresholds was designed to manage energy distributions between PV and SCs. The charge control with SCs buffering can assist to reduce the number of system shut-downs (and duration thereof) and enhance system resilience. The improved control system to reduce the power loss across the lamp is required for the future work, such as implementing the pulse width modulation to reduce the power consumption and eliminate the use of the lamp. Moreover, it would be beneficial to quantify the impacts of reducing the shut-down events on alleviating the wear and tear of the pump and membrane module for future studies.

Cleaning of the UF membrane was achieved by backwashing via the bladder tank or SCs-powered BW pump in the PV-membrane system. The addition of bentonite resulted in UF membrane fouling, and BW intervals were implemented to minimize the energy consumption of the system. However, to minimize membrane fouling and energy consumption, the backwashing criteria need to be mapped out when operating the PV-membrane system with real brackish water in long-term operation, e.g., backwashing can be activated when the increase of TMP exceeds a certain threshold. Remote control and sensing technology would be required to enhance applications of the PV-membrane system in decentralized, off-grid, and remote areas.

The last chapter examined the impacts of Li-ion batteries on the PV-membrane system under varied solar days. The benefits of using Li-ion batteries as long-term energy storage are clearly reflected in water quality and quantity. It would be interesting to combine the SCs and Li-ion batteries together, so that the SCs provide energy buffering during short periods of fluctuations (seconds to minutes), while the batteries supply energy storage during long-term fluctuations (several hours). In addition, although the bladder tank used in this research was primarily used for UF membrane backwashing, it can also be used as an energy storage unit. The three energy storage options – SCs, Li-ion batteries, and bladder tank – can be implemented and compared for a further understanding of the advantages and disadvantages of adding more components into the PV-membrane system. Finally, a cost estimation for water produced is required to determine the penetration of Li-ion batteries to RE-membrane systems.

Bibliography

- [1] World Health Organization (WHO): Progress on household drinking water, sanitation and hygiene 2000-2020: Five years in SDGs. <https://data.unicef.org> (accessed 3 October 2021).
- [2] IEA (2020), SDG7: Data and projections, IEA, Paris <https://www.iea.org/reports/sdg7-data-and-projections> (accessed 3 October 2021).
- [3] Richards BS, Shen J, Schäfer AI. Water-energy nexus perspectives in the context of photovoltaic-powered decentralized water treatment systems: A Tanzanian case study. *Energy Technology*. 2017;5:1-13.
- [4] Fritzmann C, Löwenberg J, Wintgens T, Melin T. State-of-the-art of reverse osmosis desalination. *Desalination*. 2007;216:1-76.
- [5] Ali A, Tufa RA, Macedonio F, Curcio E, Drioli E. Membrane technology in renewable-energy-driven desalination. *Renewable and Sustainable Energy Reviews*. 2018;81:1-21.
- [6] Fraunhofer ISE: Photovoltaics report, updated: 24 February 2022. <https://www.ise.fraunhofer.de/content/dam/ise/de/documents/publications/studies/Photovoltaics-Report.pdf> (accessed 20 March 2022).
- [7] European Technology & Innovation Platform PV: Fact sheets about photovoltaics (update September 2020) <https://etip-pv.eu/publications/fact-sheets/> (accessed 17 April 2022).
- [8] Schäfer AI, Hughes G, Richards BS. Renewable energy powered membrane technology: A leapfrog approach to rural water treatment in developing countries? *Renewable and Sustainable Energy Reviews*. 2014;40:542-56.
- [9] Richards BS, Schäfer AI. Photovoltaic-powered desalination system for remote Australian communities. *Renewable Energy*. 2003;28:2013-22.
- [10] EnergyTrend: Price trend: Polysilicon and wafer prices expected to rise continuously as high cost and production restrictions inhibit mid and downstream operating rate relentlessly. <https://www.energytrend.com/solar-price.html> (accessed 26 January 2022).
- [11] Reverse osmosis membrane market by material type, filter module, and application: Global opportunity analysis and industry forecast, 2020 - 2030. <https://www.researchandmarkets.com/reports/5314548/reverse-osmosis-membrane-market-by-material-type> (accessed 04 October 2021)2021.
- [12] Peters T. Membrane technology for water treatment. *Chemical Engineering & Technology*. 2010;33:1233-40.
- [13] Fane AG. Membranes for water production and wastewater reuse. *Desalination*. 1996;106:1-9.
- [14] Wintgens T, Melin T, Schäfer A, Khan S, Muston M, Bixio D, et al. The role of membrane processes in municipal wastewater reclamation and reuse. *Desalination*. 2005;178:1-11.
- [15] Soltanieh M, Gill WN. Review of reverse osmosis membranes and transport models. *Chemical Engineering Communications*. 1981;12:279-363.
- [16] Wijmans JG, Baker RW. The solution-diffusion model: a review. *Journal of Membrane Science*. 1995;107:1-21.
- [17] Koros WJ, Ma YH, Shimidzu T. Terminology for membranes and membrane process. *Pure & Appl Chemistry*. 1996;68:1479-89.
- [18] Oatley-Radcliffe DL, Walters M, Ainscough TJ, Williams PM, Mohammad AW, Hilal N. Nanofiltration membranes and processes: A review of research trends over the past decade. *Journal of Water Process Engineering*. 2017;19:164-71.
- [19] Baker RW. *Membrane technology and applications California*: John Wiley & Sons,Ltd; 2004.
- [20] Shenvi SS, Isloor AM, Ismail AF. A review on RO membrane technology: Developments and challenges. *Desalination*. 2015;368:10-26.
- [21] Nicolaisen B. Developments in membrane technology for water treatment. *Desalination*. 2003;153:355-60.
- [22] Jiang S, Li Y, Ladewig BP. A review of reverse osmosis membrane fouling and control strategies. *The Science of the total environment*. 2017;595:567-83.
- [23] Tian J-Y, Xu Y-P, Chen Z-L, Nan J, Li G-B. Air bubbling for alleviating membrane fouling of immersed hollow-fiber membrane for ultrafiltration of river water. *Desalination*. 2010;260:225-30.

- [24] Yan Z, Liu B, Qu F, Ding A, Liang H, Zhao Y, et al. Control of ultrafiltration membrane fouling caused by algal extracellular organic matter (EOM) using enhanced Al coagulation with permanganate. *Separation and Purification Technology*. 2017;172:51-8.
- [25] Chang H, Liang H, Qu F, Liu B, Yu H, Du X, et al. Hydraulic backwashing for low-pressure membranes in drinking water treatment: A review. *Journal of Membrane Science*. 2017;540:362-80.
- [26] Schäfer AI, Fane AG. *Nanofiltration: Principles, Applications and New materials*: Wiley-VCH; 2021.
- [27] Panagopoulos A, Haralambous KJ, Loizidou M. Desalination brine disposal methods and treatment technologies - A review. *The Science of the total environment*. 2019;693:133545.
- [28] Mansour S, Arafat HA, Hasan SW. Brine management in desalination plants. In: Arafat H, editor. *Desalination Sustainability: A technical, socioeconomic, and environmental approach*. 1st ed 2017. p. 207-36.
- [29] Ziolkowska JR, Reyes R. Prospects for desalination in the United States—Experiences From California, Florida, and Texas. *Competition for Water Resources* 2017. p. 298-316.
- [30] Graditi G, Colonnese D, Femia N. Efficiency and reliability comparison of DC DC converters for single phase grid connected photovoltaic inverters. *Speedam 2010, International Symposium on Power Electronics, Electrical Drives, Automation and Motion*. 2010.
- [31] Sharma V, Chandel S. Performance and degradation analysis for long term reliability of solar photovoltaic systems: A review. *Renewable and Sustainable Energy Reviews*. 2013;27:753-67.
- [32] Ranaweera I, Midtgård O-M, Yordanov GH. Short - term intermittency of solar irradiance in southern Norway. *29th European Photovoltaic Solar Energy Conference and Exhibition* 2014. p. 2635 - 8.
- [33] Manwell JF, McGowan JG. *Wind energy explained: Theory, design and application*. 2nd ed: John Wiley & Sons Ltd.; 2009.
- [34] Vindel JM, Polo J. Intermittency and variability of daily solar irradiation. *Atmospheric Research*. 2014;143:313-27.
- [35] Park GL, Schäfer AI, Richards BS. Renewable energy-powered membrane technology: Supercapacitors for buffering resource fluctuations in a wind-powered membrane system for brackish water desalination. *Renewable Energy*. 2013;50:126-35.
- [36] Freire-Gormaly M, Bilton AM. Experimental quantification of the effect of intermittent operation on membrane performance of solar powered reverse osmosis desalination systems. *Desalination*. 2018;435:188-97.
- [37] Ruiz-García A, Nuez I. Long-term intermittent operation of a full-scale BWRO desalination plant. *Desalination*. 2020;489:114526.
- [38] Boussouga Y-A, Richards BS, Schäfer AI. Renewable energy powered membrane technology: System resilience under solar irradiance fluctuations during the treatment of fluoride-rich natural waters by different nanofiltration/reverse osmosis membranes. *Journal of Membrane Science* 2021;617:118452.
- [39] Richards BS, Capão DPS, Früh WG, Schäfer AI. Renewable energy powered membrane technology: Impact of solar irradiance fluctuations on performance of a brackish water reverse osmosis system. *Sep Purif Technol*. 2015;156:379-90.
- [40] Shen J, Jeahanipour A, Richards BS, Schäfer AI. Renewable energy powered membrane technology: Experimental investigation of system performance with variable module size and fluctuating energy. *Separation and Purification Technology*. 2019;221:64-73.
- [41] Thomson M, Infield D. Laboratory demonstration of a photovoltaic-powered seawater reverse-osmosis system without batteries. *Desalination*. 2005;183:105-11.
- [42] Miranda MS, Infield D. A wind-powered seawater reverse-osmosis system without batteries. *Desalination*. 2002;153:9-16.
- [43] Lai W, Ma Q, Lu H, Weng S, Fan J, Fang H. Effects of wind intermittence and fluctuation on reverse osmosis desalination process and solution strategies. *Desalination*. 2016;395:17-27.
- [44] Ma H-P, Wang H-L, Qi Y-H, Chao Z-L, Tian L, Yuan W, et al. Reducing fouling of an industrial multi-stage nanofiltration membrane based on process control: A novel shutdown system. *Journal of Membrane Science*. 2022;644:120141.
- [45] DuPont water solution: FilmTec reverse osmosis membranes technical manual. <https://www.dupont.com/content/dam/dupont/amer/us/en/water-solutions/public/documents/en/45-D01504-en.pdf> (accessed 12 March 2022).
- [46] Kyriakarakos G, Dounis AI, Arvanitis KG, Papadakis G. Design of a fuzzy cognitive maps variable-load energy management system for autonomous PV-reverse osmosis desalination systems: A simulation survey. *Applied Energy*. 2017;187:575-84.

-
- [47] Zhou K, Ferreira JA, de Haan SWH. Optimal energy management strategy and system sizing method for stand-alone photovoltaic-hydrogen systems. *International Journal of Hydrogen Energy*. 2008;33:477 - 89.
- [48] Pianta R, Bolle M, Janex M-L, Chappaz A, Birou B, Ponce R, et al. Micro- and ultrafiltration of karstic spring water. *Desalination* 1998;117:61-71.
- [49] Kyriakarakos G, Dounis AI, Arvanitis KG, Papadakis G. A fuzzy logic energy management system for polygeneration microgrids. *Renewable Energy*. 2012;41:315-27.
- [50] Karavas C-S, Arvanitis KG, Kyriakarakos G, Piromalis DD, Papadakis G. A novel autonomous PV powered desalination system based on a DC microgrid concept incorporating short-term energy storage. *Solar Energy*. 2018;159:947-61.
- [51] Liu CCK, Park JW, Migita R, Qin G. Experiments of a prototype wind-driven reverse osmosis desalination system with feedback control. *Desalination*. 2002;150:277-87.
- [52] de Carvalho PCM, Riffel DB, de Oliveira RGV. Photovoltaic powered reverse osmosis plant without batteries control method and use of energy surplus. *Proc of VII INDUSCON2006*.
- [53] Salazar J, Tadeo F, Prada C. Renewable energy for desalination using reverse osmosis. *International Conference on Renewable Energies and Power Quality*. Granada (Spain)2010.
- [54] Palacin LG, Tadeo F, de Prada C, Salazar J. Operation of desalination plants using renewable energies and hybrid control. *Desalination and Water Treatment*. 2012;25:119-26.
- [55] Khiari W, Turki M, Belhadj J. Power control strategy for PV/Wind reverse osmosis desalination without battery. *Control Engineering Practice*. 2019;89:169-79.
- [56] Khiari W, Turki M, Belhadj J. Robust DC-Bus voltage control for batteryless brackish water reverse osmosis desalination prototype operating with variable wind and solar irradiance. *International Journal of Renewable Energy Research*. 2018;8:1544-52.
- [57] Kim JS, Chen J, Garcia HE. Modeling, control, and dynamic performance analysis of a reverse osmosis desalination plant integrated within hybrid energy systems. *Energy*. 2016;112:52-66.
- [58] Bilton AM, Kelley LC, Dubowsky S. Photovoltaic reverse osmosis — Feasibility and a pathway to develop technology. *Desalination and Water Treatment*. 2012;31:24-34.
- [59] Freire-Gormaly M, Bilton AM. Design of photovoltaic powered reverse osmosis desalination systems considering membrane fouling caused by intermittent operation. *Renewable Energy*. 2019;135:108-21.
- [60] Soric A, Cesaro R, Perez P, Guiol E, Moulin P. Eausmose project desalination by reverse osmosis and batteryless solar energy: Design for a 1 m³ per day delivery. *Desalination*. 2012;301:67-74.
- [61] Kamel AA, Rezk H, Abdelkareem MA. Enhancing the operation of fuel cell-photovoltaic-battery-supercapacitor renewable system through a hybrid energy management strategy. *International Journal of Hydrogen Energy*. 2021;46:6061-75.
- [62] Glavin ME, Chan PKW, Armstrong S, Hurley WG. A stand-alone photovoltaic supercapacitor battery hybrid energy storage system. 2008 13th International Power Electronics and Motion Control Conference (EPE-PEMC 2008). 2008:1688-95.
- [63] Bludszweit H, Fandos JM, Domínguez JA, Llombart A, Sanz J. Simulation of a hybrid system wind turbine-battery-ultracapacitor. *Renewable Energy and Power Quality Journal*. 2005;1:254-9.
- [64] Mehr TH, Masoum MAS, Jabalameli N. Grid-Connected Lithium-Ion battery energy storage system for load levelling and peak shaving. *Australasian Universities Power Engineering Conference, AUPEC 2013*. Hobart, TAS, Australia2013.
- [65] Li S, Cai Y-H, Schäfer AI, Richards BS. Renewable energy powered membrane technology: A review of the reliability of photovoltaic-powered membrane system components for brackish water desalination. *Applied Energy*. 2019;253:113524.
- [66] Hoa E, Lesjean B. International market survey on membrane-based products for decentralised water supply (POU and SSS Units). D2.5.3, *TECHNEAU 2008*.
<https://www.scribd.com/document/62796204/D2-5-3> (accessed 01 May 2022).
- [67] Kumar R, Rosen MA. A critical review of photovoltaic-thermal solar collectors for air heating. *Applied Energy*. 2011;88:3603-14.
- [68] Demain C, Journée M, Bertrand C. Evaluation of different models to estimate the global solar radiation on inclined surfaces. *Renewable Energy*. 2013;50:710-21.
- [69] Kaldellis JK, Kapsali M. Simulating the dust effect on the energy performance of photovoltaic generators based on experimental measurements. *Energy*. 2011;36:5154-61.
- [70] Mekhilef S, Saidur R, Kamalisarvestani M. Effect of dust, humidity and air velocity on efficiency of photovoltaic cells. *Renewable and Sustainable Energy Reviews*. 2012;16:2920-5.

- [71] Gwandu BAL, Creasey D. Humidity: A factor in the appropriate positioning of a photovoltaic power station. *Renewable Energy*. 1995;6:313-6.
- [72] Tan CM, Chen BKE, Toh KP. Humidity study of a-Si PV cell. *Microelectronics Reliability*. 2010;50:1871-4.
- [73] Hegedus S. Review of photovoltaic module energy yield (kWh/kW): comparison of crystalline Si and thin film technologies. *Wiley Interdisciplinary Reviews: Energy and Environment*. 2013;2:218-33.
- [74] Eikelboom JA, Jansen M. Characterisation of PV modules of new generations: Results of tests and simulations. https://scholar.google.com/scholar?q=Characterisation+of+PV+modules+of+new+generations:+Results+of+tests+and+simulations.&hl=zh-CN&as_sdt=0&as_vis=1&oi=scholar (accessed 12 March 2022)2000.
- [75] International Standard. IEC61215-1:2016: Terrestrial Photovoltaic (PV) Modules - Design Qualification and Type Approval - Part 1: Test Requirements. Geneva: International Electrotechnical Commission; 2005.
- [76] Cluintana MA, King DL. Commonly observed degradation in field aged photovoltaic modules. *Proceedings of the 29th IEEE photovoltaic solar energy conference and exhibition USA*. 2002.
- [77] Jordan DC, Kurtz S. Photovoltaic Degradation Rates — An Analytical Review. *Progress in Photovoltaics: Research and Applications*. 2012.
- [78] Sinapis K, Papageorgiou G, Durose K, van den Donker M, Folkerts W. Outdoor degradation of CdTe modules at open circuit and at maximum power point. *Proc 42th IEEE PVSC2015*.
- [79] Mansouri A. Defect detection in photovoltaic modules using electroluminescence imaging. *27th EU PVSEC*.
- [80] Barlow R, McNelis B, Derrick A. Solar pumping: An introduction and update on the technology, performance, costs, and economics. London, U.K.: Intermediate Technology Publications, Ltd.; 1993.
- [81] Wens M, Steyaert M. Basic DC-DC converter theory. Design and implementation of fully-integrated inductive DC-DC converters in standard CMOS. New York, USA: Springer Netherlands; 2011. p. 27-63.
- [82] Sizikov G, Kolodny A, Fridman EG, Zelikson M. Efficiency optimization of integrated DC to DC buck converters. *ICECS 2010*. 2010:1215-8.
- [83] Hafez AAA. Multi-level cascaded DC/DC converters for PV applications. *Alexandria Engineering Journal*. 2015;54:1135-46.
- [84] Abbas A. Simulation and analysis of an industrial water desalination plant. *Chemical Engineering and Processing: Process Intensification*. 2005;44:999-1004.
- [85] Prawoto Y, Ibrahim K, Wan Nik WB. Effect of ph and chloride concentration on the corrosion of duplex stainless steel. *The Arabian Journal for Science and Engineering*. 2009;34:115-27.
- [86] Yao B, Chen H, He XQ, Xiao QZ. Reliability and failure analysis of DC/DC converter and case studies. *International Conference on Quality, Reliability, Risk, Maintenance, and Safety Engineering2013*. p. 1133-5.
- [87] Liu Y, Huang ChY, Shan NN, Lu ChZh, Gao G. Failure analysis of VDMOS in DC/DC converter. In *Proceedings of The 16th IEEE International Symposium on Physical and Failure Analysis Intergrated Circuits2009*. p. 388-92.
- [88] Freeman D. Introduction to photovoltaic systems maximum power point tracking. Application Report. <https://www.ti.com.cn/cn/lit/an/slva446/slva446.pdf> (accessed 10 March 2022)2010.
- [89] Chianese D, Burà E, Realini A. MPPT3000 multifunction testing device for PV module. *23rd EU PVSEC Valencia2008*.
- [90] Faranda R, Leva S. Energy comparison of MPPT techniques for PV systems. *Wseas Transactions on Power Systems*. 2008;3:446-55.
- [91] Argaw N, Colorado D. Renewable energy water pumping systems handbook. NREL/SR-500-30481. <https://www.nrel.gov/docs/fy04osti/30481.pdf> (accessed 1 May 2022)2004.
- [92] Mepos Electronics: MPPT solar charger with constant current driver. <https://mepospower.com/images/datasheets/KMPA200JU.files/KMPA200JU.pdf> (accessed 01 February 2022).
- [93] Argaw N, Foster R, Ellis A. Renewable energy for water pumping applications in rural villages2003.
- [94] Goetz J, Hu WP, Milliken J. Sensorless digital motor controller for high reliability applications. Dallas, TX: IEEE; 2006. p. 1645-50.
- [95] Defrance L, Jaffrin MY. Comparison between filtrations at fixed transmembrane pressure and fixed permeate flux application to a membrane bioreactor used for wastewater treatment. *Journal of Membrane Science*. 1999;152:203-10.

-
- [96] McBride R, Morris R, Hanbury W. Wind power a reliable source for desalination. *Desalination*. 1987;67:559-64.
- [97] Heijman SGJ, Rabinovitch E, Bos F, Olthof N, van Dijk JC. Sustainable seawater desalination: Stand-alone small scale windmill and reverse osmosis system. *Desalination*. 2009;248:114-7.
- [98] Park GL, Schäfer AI, Richards BS. Renewable energy powered membrane technology: The effect of wind speed fluctuations on the performance of a wind-powered membrane system for brackish water desalination. *Journal of Membrane Science*. 2011;370:34-44.
- [99] Infield D. Performance analysis of a small wind powered reverse osmosis plant. *Solar Energy*. 1997;61:415-21.
- [100] Lising ER, Alward R. Unsteady state operation of a reverse-osmosis desalination unit. *Desalination*. 1972;11:261-8.
- [101] Amrouche SO, Rekioua D, Rekioua T, Bacha S. Overview of energy storage in renewable energy systems. *International Journal of Hydrogen Energy*. 2016;41:20914-27.
- [102] Perrin M, Saint-Drenan YM, Mattera F, Malbranche P. Lead–acid batteries in stationary applications: competitors and new markets for large penetration of renewable energies. *Journal of Power Sources*. 2005;144:402-10.
- [103] Li Y, Lu J. Metal–Air batteries: Will they be the future electrochemical energy storage device of choice? *ACS Energy Letters*. 2017;2:1370–7.
- [104] Sherman SB, Cano ZP, Fowler M, Chen Z. Range-extending Zinc-air battery for electric vehicle. *AIMS Energy*. 2018;6:121–45.
- [105] Palizban O, Kauhaniemi K. Energy storage systems in modern grids—Matrix of technologies and applications. *Journal of Energy Storage*. 2016;6:248-59.
- [106] Hadjipaschalis I, Poullikkas A, Efthimiou V. Overview of current and future energy storage technologies for electric power applications. *Renewable and Sustainable Energy Reviews*. 2009;13:1513-22.
- [107] Zakeri B, Syri S. Electrical energy storage systems: A comparative life cycle cost analysis. *Renewable and Sustainable Energy Reviews*. 2015;42:569-96.
- [108] Zhou Z, Benbouzid M, Frédéric Charpentier J, Scuiller F, Tang T. A review of energy storage technologies for marine current energy systems. *Renewable and Sustainable Energy Reviews*. 2013;18:390-400.
- [109] Perrin M, Malbranche P, Lemaire-Potteau E, Willer B, Soria ML, Jossen A, et al. Temperature behaviour: Comparison for nine storage technologies. *Journal of Power Sources*. 2006;154:545-9.
- [110] Dunlop J, Farhi B. Recommendations for maximizing battery life in photovoltaic systems: a review of lessons learned. *Proceedings of Forum 2001 Solar Energy: The Power to Choose*. Washington DC2001.
- [111] Hund T. Capacity loss in PV batteries and recovery procedures. *Photovoltaic System Applications Department, Sandia National Laboratories*.
- [112] Thomson M, Miranda MS, Infield D. A small-scale seawater reverse osmosis system with excellent energy efficiency over a wide operating range. *Desalination* 2002;153:229-36.
- [113] Garg MC, Joshi H. A review on PV-RO process: Solution to drinking water scarcity due to high salinity in non-electrified rural areas. *Separation Science and Technology*. 2014;50:1270-83.
- [114] VARTA: VARTA pulse / pulse neo. https://www.varta-storage.com/fileadmin/varta_storage/downloads/products/energy/varta-pulse/Datasheet_VARTA_pulse_en_17.pdf (accessed 01 May 2022).
- [115] Díaz-González F, Sumper A, Gomis-Bellmunt O, Villafáfila-Robles R. A review of energy storage technologies for wind power applications. *Renewable and Sustainable Energy Reviews*. 2012;16:2154-71.
- [116] Zubi G, Dufo-López R, Carvalho M, Pasaoglu G. The lithium-ion battery: State of the art and future perspectives. *Renewable and Sustainable Energy Reviews* 2018;89:292–308.
- [117] Maxwell Technologies: Maxwell BOOSTCAP ultracapacitors - small module technical papers. <http://www.maxwell.com/products/ultracapacitors/> (accessed 01 February 2022).
- [118] Barton JP, Infield DG. Energy storage and its use with intermittent renewable energy. *IEEE Transactions On Energy Conversion*2004. p. 441-8.
- [119] Beaudin M, Zareipour H, Schellenberglobe A, Rosehart W. Energy storage for mitigating the variability of renewable electricity sources: An updated review. *Energy for Sustainable Development*. 2010;14:302-14.
- [120] Zhong Y, Zhang JC, Li GY, Liu AG. Research on energy efficiency of supercapacitor energy storage system. 2006 International Conference on Power System Technology. 2006.

- [121] Burke A. R&D considerations for the performance and application of electrochemical capacitors. *Electrochimica Acta* 53. 2007:1083–91.
- [122] Li S, Voigt A, Schäfer AI, Richards BS. Renewable energy powered membrane technology: Energy buffering control system for improved resilience to periodic fluctuations of solar irradiance. *Renewable Energy*. 2020;149:877-89.
- [123] Gür TM. Review of electrical energy storage technologies materials and systems: challenges and prospects for large-scale grid storage. *Energy Environmental Science*. 2018;11:2696-767.
- [124] Ayadi M, Briat O, Lallemand R, Eddahech A, German R, Coquery G, et al. Description of supercapacitor performance degradation rate during thermal cycling under constant voltage ageing test. *Microelectronics Reliability*. 2014;54:1944-8.
- [125] Kusko A, DeDad J. Short-term, long-term, energy storage methods for standby electric power systems. *EEE Industry Applications Magazine*. 2007:66-72.
- [126] Huang J, Guo ZX. *Handbook of practical motor*: Shanghai Scientific & Technical Publishers; 2010.
- [127] Chennai R, Zarour L, Bouzid A, Kerbache T. Comparative study of photovoltaic pumping systems using a permanent magnet synchronous motor (PMSM) and an asynchronous motor (ASM). *Review Energy Renewable*. 2006;9:17 - 28.
- [128] Adira. *Adira handbook: A guide to autonomous desalination system concepts*. 2007.
- [129] Adu-Res. Co-ordination action for autonomous desalination units based on renewable energy systems. WP-4: Cost reduction strategies, report on techno-economic performance and cost reduction potential (2006). <https://cordis.europa.eu/project/rcn/75642/reporting/en> (accessed 01 April 2022).
- [130] AZUD WaterTech DWE Mobile Drinking Water Plant. <https://www.environmental-expert.com/products/azud-watertech-model-dwe-fw-mobile-fresh-water-treatment-plant-577631> (accessed 01 March 2022).
- [131] MMW Bluebox 1200 RO Solar. <http://www.muchmorewater.com/bluebox-1200-reverse-osmosis-solar.html> (accessed 01 March 2022).
- [132] TRUNZ Brackish System 300. <https://www.environmental-expert.com/products/trunz-model-tbs-300-brackish-water-treatment-system-407660> (accessed 01 April 2022).
- [133] Nesbitt B. *Handbook of pumps and pumping*. First edition 2006 ed: Elsevier in association with Roles & Associates Ltd; 2006.
- [134] Protogeropoulos C, Pearce S. Laboratory evaluation and system sizing charts for a second generation direct PV-powered, low cost submersible solar pump. *Solar Energy*. 2000;68:453-74.
- [135] Vick BD, Clark RN. Determining the optimum solar water pumping system for domestic use, livestock watering or irrigation. <http://hdlhandle.net/10113/46008>. Buffalo, New York 2009
- [136] Robinson R, Ho GE, Mathew K. Development of a reliable low cost RO desalination unit for remote communities. *Desalination*. 1992;86:9-26.
- [137] Liu CCK. The development of a renewable-energy-driven reverse osmosis system for water desalination and aquaculture production. *Journal of Integrative Agriculture*. 2013;12:1357-62.
- [138] Vick BD, Clark RN. Experimental investigation of solar powered diaphragm and helical pumps. *Solar Energy*. 2011;85:945-54.
- [139] Vick BD, Clark RN. Solar-PV water pumping with fixed and passive tracking panels. *American Solar Energy Society*, Reno, Nevada. 2002:6.
- [140] Sandvik Materials Technology: Sandvik SAF 2205 for wirelines. <https://www.materials.sandvik/en/materials-center/material-datasheets/tube-and-pipe-seamless/saf-2205/> (accessed 01 April 2022).
- [141] Yasukawa K, Uchida Y, Tenma N, Taguchi Y, Muraoka H, Ishii T, et al. Groundwater temperature survey for geothermal heat pump application in tropical asia. *Bulletin of the Geological Survey of Japan*. 2009;60:459-67.
- [142] Schäfer AI, Rossiter HMA, Owusu PA, Richards BS, Awuah E. Physico-chemical water quality in Ghana: Prospects for water supply technology implementation. *Desalination*. 2009;248:193-203.
- [143] Mulder M. *Module and process design, basic principles of membrane technology*. Netherlands: 2nd ed. Kluwer Academic Publishers; 1996.
- [144] Singh S, Henderson RK, Baker A, Stuetz RM, Khan SJ. Characterization of reverse osmosis permeates from municipal recycled water systems using fluorescence spectroscopy: Implications for integrity monitoring. *Journal of Membrane Science*. 2012;421–422:180-9.
- [145] Guo W, Ngo H-h, Li J. A mini-review on membrane fouling. *Bioresource Technology*. 2012;122:27-34.

-
- [146] Goh PS, Lau WJ, Othman MHD, Ismail AF. Membrane fouling in desalination and its mitigation strategies *Desalination*. 2018;425:130-55.
- [147] Li Q, Elimelech M. Organic fouling and chemical cleaning of nanofiltration membranes: measurements and mechanisms. *Environ Sci Technol*. 2004;38:4683-93.
- [148] Hilal N, Ogunbiyi OO, Miles NJ, Nigmatullin R, Hilal N, Ogunbiyi OO, et al. Methods employed for control of fouling in MF and UF membranes : A comprehensive review. *Separation Science and Technology*. 2005;40: 1957-2005.
- [149] Hoek EMV, Elimelech M. Cake-enhanced concentration polarization: A new fouling mechanism for salt-rejecting membranes. *Environmental Science and Technology*. 2003;37:5581-8.
- [150] Herzberg M, Elimelech M. Biofouling of reverse osmosis membranes: Role of biofilm-enhanced osmotic pressure. *Journal of Membrane Science*. 2007;295:11-20.
- [151] Elimelech M, Li Q, Elimelech M. Organic fouling and chemical cleaning of nanofiltration membranes: Measurements and mechanisms. *Environmental Science and Technology*. 2004;38:4683-93.
- [152] Al-Amoudi A, Lovitt RW. Fouling strategies and the cleaning system of NF membranes and factors affecting cleaning efficiency. *Journal of Membrane Science*. 2007;303:4-28.
- [153] Gao W, Liang H, Ma J, Han M, Chen ZI, Han Zs, et al. Membrane fouling control in ultrafiltration technology for drinking water production: A review. *Desalination*. 2011;272:1-8.
- [154] Ang WS, Tiraferri A, Chen KL, Elimelech M. Fouling and cleaning of RO membranes fouled by mixtures of organic foulants simulating wastewater effluent. *Journal of Membrane Science*. 2011;376:196-206.
- [155] Kim SL, Chen JP, Ting YP. Study on feed pretreatment for membrane filtration of secondary effluent. *Separation and Purification Technology*. 2002;29:171-9.
- [156] Sim LN, Chong TH, Taheri AH, Sim STV, Lai L, Krantz WB, et al. A review of fouling indices and monitoring techniques for reverse osmosis. *Desalination*. 2018;434:169-88.
- [157] Vrouwenvelder JS, van der Kooij D. Diagnosis, prediction and prevention of biofouling of NF and RO membranes. *Desalination*. 2001;139:65-71.
- [158] Wolf PH, Siverns S, Monti S. UF membranes for RO desalination pretreatment. *Desalination*. 2005;182:293-300.
- [159] Kabsch-Korbutowicz M. Impact of pre-coagulation on ultrafiltration process performance. *Desalination*. 2006;194:232-8.
- [160] Plappally AK, Lienhard JH. Costs for water supply, treatment, end-use and reclamation. *Desalination and Water Treatment*. 2012;51:200-32.
- [161] Jamaly S, Darwish NN, Ahmed I, Hasan SW. A short review on reverse osmosis pretreatment technologies. *Desalination*. 2014;354:30-8.
- [162] Drioli E, Macedonio F. Integrated membrane systems for desalination. In: Peinemann KV, Nunes SP, editors. *Membranes for water treatment*. Weinheim: Wiley-VCH Verlag GmbH & Co. KGaA; 2010. p. 93-146.
- [163] Brehant A, Bonnelyeb V, Perez M. Comparison of MF/UF pretreatment with conventional filtration prior to RO membranes of surface seawater desalination. *Desalination*. 2002;144:353-60.
- [164] Glueckstern P, Priel M. Comparative cost of UF vs. conventional pretreatment for SWRO systems. 5th IDS Annual Conference. Haifa2002.
- [165] Schäfer AI, Fane AG, Waite TD. Cost factors and chemical pretreatment effects in the membrane filtration of waters containing natural organic matter. *Water Research*. 2001;35:1509-17.
- [166] Li NN, Fane AG, Ho WSW, Matsuura T. *Advanced membrane technology and applications* Wiley; 2008.
- [167] Antony A, Low JH, Gray S, Childress AE, Le-Clech P, Leslie G. Scale formation and control in high pressure membrane water treatment systems: A review. *Journal of Membrane Science*. 2011;383:1-16.
- [168] Shen J, Schäfer AI. Factors affecting fluoride and natural organic matter (NOM) removal from natural waters in Tanzania by nanofiltration/reverse osmosis. *Science of the Total Environment*. 2015;527-528:520-9.
- [169] Katie G, Korak J. Evaluation of solar-powered systems for desalination of brackish groundwater. https://webcache.googleusercontent.com/search?q=cache:xFz2Y4750roJ:https://www.usbr.gov/research/projects/download_product.cfm%3Fid%3D1529+&cd=2&hl=zh-CN&ct=clnk (accessed 1 January 2022)2015.
- [170] Imbrogno A, Schäfer AI. Comparative study of nanofiltration membrane characterization devices of different dimension and configuration (cross flow and dead end). *Journal of Membrane Science*. 2019;585:67-80.

- [171] Ang WL, Nordin D, Mohammad AW, Benamor A, Hilal N. Effect of membrane performance including fouling on cost optimization in brackish water desalination process. *Chemical Engineering Research and Design*. 2017;117:401-13.
- [172] Crozes GF, Jacangelo JG, Anselme C, Laîné JM. Impact of ultrafiltration operating conditions on membrane irreversible fouling. *Journal of Membrane Science*. 1997;124:63-76.
- [173] Field RW, Wu D, Howell JA, Gupta BB. Critical flux concept for microfiltration fouling. *Journal of Membrane Science*. 1995;100:259-72.
- [174] Zhang W, Luo J, Ding L, Jaffrin MY. A review on flux decline control strategies in pressure-driven membrane processes. *Industrial & Engineering Chemistry Research*. 2015;54:2843-61.
- [175] Wilf M, Bartels C. Optimization of seawater RO systems design. *Desalination*. 2001;138:299-306.
- [176] Song L, Schuetze B, Rainwater K. Demonstration of a high recovery and energy efficient RO system for small-scale brackish water desalination.
https://www.twdb.texas.gov/innovativewater/desal/projects/texastech/doc/texas_tech_final_rpt.pdf
(accessed 01 February 2022)2012
- [177] Chen V, Fane AG, Madaeni S, Wenten IG. Particle deposition during membrane filtration of colloids: Transition between concentration polarization and cake formation. *Journal of Membrane Science*. 1997;125:109–22.
- [178] Shen J, Mkongo G, Abbt-Braun G, Ceppi SL, Richards BS, Schäfer AI. Renewable energy powered membrane technology: Fluoride removal in a rural community in northern Tanzania. *Separation and Purification Technology*. 2015;149:349-61.
- [179] Holt JK, Park HG, Wang Y, Stadermann M, Artyukhin AB, Grigoropoulos CP, et al. Fast mass transport through sub-2-nanometer Carbon Nanotubes. *Science*. 2006;312:1034–7.
- [180] Elimelech M, Phillip WA. The future of seawater desalination: energy, technology, and the environment. *Science*. 2011;333:712-7.
- [181] Park HB, Kameev J, Robeson LM, Elimelech M, Freeman BD. Maximizing the right stuff: The trade-off between membrane permeability and selectivity. *Science*. 2017;356.
- [182] Werber JR, Deshmukh A, Elimelech M. The critical need for increased selectivity, not increased water permeability, for desalination membranes. *Environmental Science & Technology Letters*. 2016;3:112-20.
- [183] DuPont water solution: Cleaning procedures for FILMTEC FT30 elements.
<https://www.dupont.com/content/dam/dupont/amer/us/en/water-solutions/public/documents/en/45-D01696-en.pdf> (accessed 12 April 2022)2021.
- [184] Irvine E, Welch D, Smith A, Rachwal T. Nanofiltration for colour removal – 8 years’ operational experience in Scotland. *Water Science and Technology: Water Supply*. 2001;1:55-63.
- [185] Qin J-J, Liberman B, Kekre KA. Direct osmosis for reverse osmosis fouling control: Principles, applications and recent developments. *The Open Chemical Engineering Journal*. 2009;3:8-16.
- [186] Nagel R, Rau E. Verfahren und vorrichtung zum aufbereiten von wasser durch umkehrosiose oder nanofiltration. Dpu markenam (Ed) Germany1997.
- [187] Nagel R, Rau E. Verfahren zum aufbereiten von wasser durch umkehrosiose oder nanofiltration. Dpu markenam (Ed). Germany1997.
- [188] Richards LA, Richards BS, Schäfer AI. Renewable energy powered membrane technology: Salt and inorganic contaminant removal by nanofiltration/reverse osmosis. *Journal of Membrane Science*. 2011;369:188-95.
- [189] Chen JP, Kim SL, Ting YP. Optimization of membrane physical and chemical cleaning by a statistically designed approach. *Journal of Membrane Science*. 2003;219:27-45.
- [190] Ebrahim S. Cleaning and regeneration of membranes in desalination and wastewater applications: State-of-the-art. *Desalination*. 1994;96:225-38.
- [191] Garcia-Fayos B, Arnal JM, Gimenez A, Alvarez-Blanco S, Sancho M. Static cleaning tests as the first step to optimize RO membranes cleaning procedure. *Desalination and Water Treatment*. 2015;55:3380-90.
- [192] Ari PH, Ozgun H, Ersahin ME, Koyuncu I. Cost analysis of large scale membrane treatment systems for potable water treatment. *Desalination and Water Treatment*. 2012;26:172-7.
- [193] Madaeni SS, Mohamamdi T, Moghadam MK. Chemical cleaning of reverse osmosis membranes. *Desalination*. 2001;134:77-82.
- [194] Guo H, Wyart Y, Perot J, Nauleau F, Moulin P. Low-pressure membrane integrity tests for drinking water treatment: A review. *Water Research*. 2010;44:41-57.

-
- [195] ASTM Committee. Standard practice for integrity testing of water filtration membrane systems. <https://www.astm.org/Standards/D6908.htm> (accessed 12 April 2022)2017.
- [196] Adham S, Gagliardo P, Smith D, Ross D, Gramith K, Trussell R. Monitoring the integrity of reverse osmosis membranes. *Desalination*. 1998;119:143-50.
- [197] Kumar M, Adham S, DeCarolis J. Reverse osmosis integrity monitoring. *Desalination*. 2007;214:138-49.
- [198] Lee H, Tan TP. Singapore's experience with reclaimed water: NEWater. *International Journal of Water Resources Development*. 2016;32:611-21.
- [199] Schäfer AI, Broeckmann A, Richards BS. Renewable Energy Powered Membrane Technology.1. Development and Characterization of a Photovoltaic Hybrid Membrane System. *Environmental Science & Technology*. 2007;41:998-1003.
- [200] Alghoul MA, Poovanaesvaran P, Mohammed MH, Fadhil AM, Muftah AF, Alkilani MM, et al. Design and experimental performance of brackish water reverse osmosis desalination unit powered by 2 kW photovoltaic system. *Renewable Energy*. 2016;93:101-14.
- [201] Peña García N, Del Vigo F, Chesters S, Armstrong M, Wilson R, Fazel M. A study of the physical and chemical damage on reverse osmosis membranes detected by autopsies. *The International Desalination Association World Congress on Desalination and Water Reuse Tianjin, China2013*. p. 20-5.
- [202] Hydranautics nitto group company: Technical application bulletin: RO/NF polyamide membrane feedwater requirements. <https://www.lenntech.com/Data-sheets/Hydranautics-TAB116-L.pdf> (accessed 01 February 2022)2013
- [203] American Water Chemicals: Membrane autopsy: damage from permeate backpressure <https://www.membranechemicals.com/en/membrane-autopsy-damage-permeate-backpressure/> (accessed 01 February 2022)2013
- [204] Rahal Z, Infield DG. Wind powered stand alone desalination. *European Wind Energy Conference, Dublin Castle, Ireland*. 1997.
- [205] Richards BS, Park GL, Pietzsch T, Schäfer AI. Renewable energy powered membrane technology: Brackish water desalination system operated using real wind fluctuations and energy buffering. *Journal of Membrane Science*. 2014;468:224-32.
- [206] Kang GD, Gao CJ, Chen WD, Jie XM, Cao YM, Yuan Q. Study on hypochlorite degradation of aromatic polyamide reverse osmosis membrane. *Journal of Membrane Science*. 2007;300:165-71.
- [207] Iborra MI, Lora J, Alcaina MI, Arnal JM. Effect of oxidation agents on reverse osmosis membrane performance to brackish water desalination. *Desalination*. 1996;108:83-9.
- [208] Tin MMM, Anioke G, Nakagoe O, Tanabe S, Kodamatani H, Nghiem LD, et al. Membrane fouling, chemical cleaning and separation performance assessment of a chlorine-resistant nanofiltration membrane for water recycling applications. *Separation and Purification Technology*. 2017;189:170-5.
- [209] Alspach B, Delphos P, Pressman J, Beaty J, Cooke T, Voutchkov N, et al. Committee report: Metrics & methods for MF/UF system optimization. *American Water Works Association, Denver2013*. p. 65-76.
- [210] Greenlee LF, Lawler DF, Freeman BD, Marrot B, Moulin P. Reverse osmosis desalination: Water sources, technology, and today's challenges. *Water Research*. 2009;43:2317-48.
- [211] Richards LA, Richards BS, Schäfer AI. Renewable energy powered membrane systems: Inorganic contaminant removal from australian groundwaters. *Membrane Water Treatment*. 2011;2:239.
- [212] Park GL, Schäfer AI, Richards BS. Effect of intermittent operation on a wind-powered membrane system for brackish water desalination. *Water Science and Technology*. 2012;65:867-74.
- [213] García Latorre FJ, Pérez Báez SO, Gómez Gotor A. Energy performance of a reverse osmosis desalination plant operating with variable pressure and flow. *Desalination*. 2015;366:146-53.
- [214] Feron P. The use of windpower in autonomous reverse osmosis seawater. *Desalination, Wind Engineering*. 1985;9:180-99.
- [215] Richards BS, Park GL, Pietzsch T, Schäfer AI. Renewable energy powered membrane technology: Safe operating window of a brackish water desalination system. *Journal of Membrane Science*. 2014;468:400-9.
- [216] Moreno F, Pinilla A. Preliminary experimental study of a small reverse osmosiswind-powered desalination plant. *Desalination*. 2005;171:257-65.
- [217] Pohl R, Kaltschmitt M, Holländer R. Investigation of different operational strategies for the variable operation of a simple reverse osmosis unit. *Desalination*. 2009;249:1280-7.
- [218] Irvine E, Grose ABF, Welch D, Donn A. Nanofiltration for colour removal - 7 years operational experience in Scotland. 2000:41-8.

- [219] Ødegaard H, Østerhus S, Melin E, Eikebrokk B. NOM removal technologies – Norwegian experiences. *Drinking Water Engineering and Science*. 2010;3:1-9.
- [220] Thorsen T, Fløgstad H. Nanofiltration in drinking water treatment literature review. *Techneau*, D5.3.4B. <https://silo.tips/download/nanofiltration-in-drinking-water-treatment> (accessed 01 December 2021)2006
- [221] Hem LJ. Nanofiltration for removal of humic substances: Survey on operational strategies. *Techneau*, D5.3.5B. <http://citeseerx.ist.psu.edu/viewdoc/download?doi=10.1.1.431.2267&rep=rep1&type=pdf> (accessed 01 December 2021)2008
- [222] Kelley L, Elasaad H, Dubowsky S. Autonomous operation and maintenance of small-scale PVRO systems for remote communities. *Desalination and Water Treatment*. 2014;55:2843-55.
- [223] Thomson M, Infield D. A photovoltaic-powered seawater reverse-osmosis system without batteries. *Desalination*. 2002;153:1-8.
- [224] Liu CCK. Wind-powered reverse osmosis water desalination for pacific islands and remote coastal communities. *Desalination and Water Purification Research and Development Program Report No 128*. <https://www.usbr.gov/research/dwpr/reportpdfs/report128.pdf> (accessed 10 March 2022)2009.
- [225] Pearce GK. The case for UF/MF pretreatment to RO in seawater applications. *Desalination*. 2007;203:286-95.
- [226] Richards BS, Capão DPS, Schäfer AI. Renewable energy powered membrane technology. 2. The effect of energy fluctuations on performance of a photovoltaic hybrid membrane system. *Environ Sci Technol*. 2008; 42: 4563-9.
- [227] Masson L, Richards BS, Schäfer AI. System design and performance testing of a hybrid membrane — photovoltaic desalination system. *Desalination*. 2005;179:51-9.
- [228] Omega: low flow turbine meters - FTB 9500 series. <https://br.omega.com/omegaFiles/green/pdf/FTB9500.pdf> (accessed 01 December 2021).
- [229] Penn Stainless Products, Inc: 440C stainless steel. <https://www.pennstainless.com/resources/product-information/stainless-grades/400-series/440c-stainless-steel/> (accessed 01 December 2021).
- [230] AST Bearings LLC: Bearing materials-technical information sheet ENB-04-0553. http://www.astbearings.com/assets/files/Bearing-Materials-Technical-Information-Sheet_ENB-04-0553.pdf (accessed 01 December 2021).
- [231] Prettyman JB, Johnson MC, Barfuss SL. Comparison of selected differential-producing, ultrasonic, and magnetic flow meters. *Journal - American Water Works Association*. 2016;108:E39-E49.
- [232] Lipták BG. *Instrument engineers' handbook- process software and digital networks*: CRC Press; 2002.
- [233] Lukat R. Understanding pressure sensor failure and reliability. <https://blog.wika.us/products/pressure-products/understanding-pressure-sensor-failure-reliability/> (accessed 22 April 2022)2015.
- [234] Santora M. What is a pressure gauge? <https://www.fluidpowerworld.com/what-are-gauges/> (accessed 27 April 2022)2015.
- [235] OMEGA. Pressure gauges and switches. <http://www.omega.com/prodinfo/pressuregauges.html> (accessed 01 December 2021).
- [236] WIKA Instrument, LP. Common reasons for gauge failure. <https://blog.wika.us/knowhow/8-common-reasons-for-pressure-gauge-failure/> (accessed 01 December 2021).
- [237] Cadwallader LC. Reliability estimates for selected sensors in fusion applications. INEL-96/0295. Idaho National Engineering Laboratory; 1996.
- [238] Hamachi M, Mietton-Peuchot M. Experimental investigations of cake characteristics in crossflow microfiltration. *Chemical Engineering Science* 1999;54:4023-30.
- [239] Trowbridge B. Accumulators increase efficiency and provide smooth operation in hydraulic systems <https://www.hydraulicspneumatics.com/technologies/accumulators/article/21882955/accumulators-increase-efficiency-and-provide-smooth-operation-in-hydraulic-systems> (accessed 27 April 2022)2011.
- [240] Campanella L, Ferri T, Pia Sammartino M, Sangiorgio P, Visco G. Development of a new sensor for total organic carbon (TOC) determination. *Sensor Review*. 2002;22:57-61.
- [241] Cohen N, Stange T. How smart is your on-line TOC analyzer? <http://particle-science.com.au/PDF/SmartTOC.pdf> (accessed 20 April 2022).
- [242] Covington AK. *Ion-Selective electrode methodology*. England: CRC Press; 2018.
- [243] Omar AF, Matjafri MZ. Turbidimeter design and analysis: A review on optical fiber sensors for the measurement of water turbidity. *Sensors*. 2009;9:8311-35.

-
- [244] De Souza NP, Basu OD. Comparative analysis of physical cleaning operations for fouling control of hollow fiber membranes in drinking water treatment. *Journal of Membrane Science*. 2013;436:28-35.
- [245] Goosen MFA, Sablani SS, Al-Maskari SS, Al-Belushi RH, Wilf M. Effect of feed temperature on permeate flux and mass transfer coefficient in spiral-wound reverse osmosis systems. *Desalination*. 2002;144:367-72.
- [246] Hashemian HM. Advanced methods for management of aging of nuclear plant instrumentation. *Proceedings of the International Meeting on Nuclear Power Plant and Facility Maintenance*. Salt Lake City, Utah 1991. p. 473-89.
- [247] Ghermandi A, Messalem R. Solar-driven desalination with reverse osmosis: the state of the art. *Desalination and Water Treatment*. 2012;7:285-96.
- [248] Maslin A, David Annandale and Marc Saupin. Decentralised water solutions island infrastructure project. *Proceedings of Renewable Energy Sources for Islands, Tourism and Water Desalination Conference Crete, Greece, EREC2003*. p. 287-94.
- [249] James WL. Design, construction and operation of a 1.2 kW photovoltaic reverse osmosis desalination plant. *SERIWA, Perth, Australia*. 1983:16-20.
- [250] Joyce A, Loureiro D, Rodrigues C, Castro S. Small reverse osmosis units using PV systems for water purification in rural places. *Desalination*. 2001;137:39-44.
- [251] Elasaad H, Bilton A, Kelley L, Duayhe O, Dubowsky S. Field evaluation of a community scale solar powered water purification technology: A case study of a remote Mexican community application. *Desalination*. 2015;375:71-80.
- [252] Abdallah S, Abu-Hilal M, Mohsen MS. Performance of a photovoltaic powered reverse osmosis system under local climatic conditions. *Desalination*. 2005;183:95-104.
- [253] Bouguecha S, Hamrouni B, Dhahbi M. Small scale desalination pilots powered by renewable energy sources: case studies. *Desalination*. 2005;183:151-65.
- [254] Qiblawey H, Banat F, Al-Nasser Q. Performance of reverse osmosis pilot plant powered by Photovoltaic in Jordan. *Renewable Energy*. 2011;36:3452-60.
- [255] de Carvalho PCM, Riffel DB, Freire C, Montenegro FFD. The Brazilian experience with a photovoltaic powered reverse osmosis plant. *Progress in Photovoltaics: Research and Applications*. 2004;12:373-85.
- [256] Ahmad GE, Schmid J. Feasibility study of brackish water desalination in the Egyptian deserts and rural regions using PV systems. *Energy Conversion and Management*. 2002;43:2641-9.
- [257] Almalawi SJ, AlRaddadi AM, AlZughabi MH, AlHazmi MM, Masoudi MH. Experimental study of mobile solar reverse osmosis for remote areas. *Journal of Solar Energy Engineering*. 2017;139:064502.
- [258] Bouhadjar SI, Kopp H, Britsch P, Deowan SA, Hoinkis J, Bundschuh J. Solar powered nanofiltration for drinking water production from fluoride-containing groundwater - A pilot study towards developing a sustainable and low-cost treatment plant. *Journal of Environmental Management*. 2019;231:1263-9.
- [259] Hrayshat ES. Brackish water desalination by a stand alone reverse osmosis desalination unit powered by photovoltaic solar energy. *Renewable Energy*. 2008;33:1784-90.
- [260] Shen J, Richards BS, Schäfer AI. Renewable energy powered membrane technology: Case study of St. Dorcas borehole in Tanzania demonstrating fluoride removal via nanofiltration/reverse osmosis. *Separation and Purification Technology*. 2016;170:445-52.
- [261] Kaunmuang P, Kirtikara K, Songprakorb R, Thepa S, Suwannakum T. Assessment of photovoltaic pumping systems in Thailand. *Solar Energy Materials & Solar Cells*. 2001;67:529-34.
- [262] DuPont water solutions: Inge dizzer P - Ultrafiltration modules. <https://www.lenntech.com/Data-sheets/Inge-Dizzer-P-L.pdf> (accessed 07 December 2021).
- [263] World Health Organisation: First consultation on post-2015 monitoring of drinking-water and sanitation, WHO/UNICEF joint monitoring programme for water supply and sanitation. 2011.
- [264] Richards BS, Capão DPS, Schäfer AI. Renewable energy powered membrane technology. 2. The effect of energy fluctuations on performance of a photovoltaic hybrid membrane system. *Environmental Science & Technology*. 2008;42:4563-9.
- [265] Schäfer AI, Broeckmann A, Richards BS. Renewable energy powered membrane technology. 1. Development and characterization of a photovoltaic hybrid membrane system. *Environmental Science & Technology*. 2007;41:998-1003.
- [266] Li S, Milia M, Schäfer AI, Richards B. Renewable energy powered membrane technology: Energy consumption analysis of ultrafiltration backwash configurations *Separation and Purification Technology*. 2022;287:120388.

- [267] Bürkert: Inline flow sensor for continuous flow measurement. <https://www.burkert.com/en/type/8011> (accessed 22 April 2022).
- [268] IFM: SM6000 magnitive inductive flow sensor. <https://www.ifm.com/de/en/product/sm6000> (accessed 22 April 2022).
- [269] Bürkert: Type 8316 - Pressure measuring device <https://www.burkert.com/en/type/8316> (accessed 22 April 2022).
- [270] Georg Fischer: Signet 2818-2823 conductivity/resistivity electrodes. <https://www.instrumart.com/assets/GFSignet-2818-2823-manual.pdf> (accessed 01 February 2022).
- [271] Bürkert: Conductivity meter. <https://www.burkert.com/en/type/8222> (accessed 22 August 2021).
- [272] Omega: DC and AC current input signal conditioners. http://www.omega.co.uk/ppt/pptsc.asp?ref=DRF-IDC_IAC&flag=1 (accessed 01 February 2022).
- [273] Omega: DC and AC voltage input signal conditioners. http://www.omega.co.uk/ppt/pptsc.asp?ref=DRF-VDC_VAC&flag=1 (accessed 01 February 2022).
- [274] Grundfos. Grundfos data booklet SQFlex. <http://www.grundfos.com/products/find-product/sq.html#brochures> (accessed 01 February 2022).
- [275] Park GL, Schäfer AI, Richards BS. The effect of intermittent operation on a wind-powered membrane system for brackish water desalination. *Water Science and Technology*. 2012;65:867-74.
- [276] Chroma: Programmable DC power supply (62000 H series) operating & programmable manual. http://www.mhzelectronics.com/ebay/manuals/chroma_62000h-series_power_supply_manual.pdf (accessed 7 December 2021).
- [277] Sunmodule SW 100 poly RGP. https://www.boutiquesolaire.fr/Docs/Solarworld/SW_poly_100-24.pdf (accessed 07 December 2021).
- [278] Li S, Carvalho APSGd, Schäfer AI, Richards BS. Renewable energy powered membrane technology: Electrical energy storage options for a photovoltaic-powered brackish water desalination system. *Applied Sciences*. 2021;11:856.
- [279] Australian standard: AS 4509.2-2002 Stand-alone power systems - System design guidelines. https://www.planetarypower.com.au/info/ausstd4509_2.pdf (accessed 17 April 2022): Council of Standards Australia; 2002.
- [280] Power Brick 24V Lithium-Ion battery pack. https://www.powertechsystems.eu/wp-content/uploads/specs/PowerBrick_PRO+_24V_50Ah_Lithium-Ion_battery.pdf (accessed 24 April 2022).
- [281] Baccouche I, Jemmali S, Mlayah A, Manai B, Amara NEB. Implementation of an improved coulomb-counting algorithm based on a piecewise SOC-OCV relationship for SOC estimation of Li-Ion battery. *International Journal of Renewable Energy Research*. 2018;8:178-87.
- [282] Baccouche I, Jemmalil S, Manai B, Chaibi R, Amaral NEB. Hardware implementation of an algorithm based on kalman filter for monitoring low capacity Li-Ion batteries. 7th International Renewable Energy Congress (IREC)2016. p. 1–6.
- [283] Battery university: Confusion with voltages. https://batteryuniversity.com/learn/article/confusion_with_voltages (accessed 26 March 2022).
- [284] Juan-Garcia P, Butler D, Comas J, Darch G, Sweetapple C, Thornton A, et al. Resilience theory incorporated into urban wastewater systems management. State of the art. *Water research*. 2017;115:149-61.
- [285] Tran HT, Balchanos M, Domercant JC, Mavris DN. A framework for the quantitative assessment of performance-based system resilience. *Reliability Engineering & System Safety*. 2017;158:73-84.
- [286] Li S, Voigt A, Cai Y-H, Schäfer AI, Richards BS. Renewable energy powered membrane technology: Energy buffering control to reduce the shut-down events and enhance system resilience under different solar days (submitted). *Renewable Energy*. 2022.
- [287] Shirazi S, Lin C-J, Chen D. Inorganic fouling of pressure-driven membrane processes – A critical review. *Desalination*. 2010;250:236-48.
- [288] Bacchin P, Espinasse B, Bessiere Y, Fletcher D, Aimar P. Numerical simulation of colloidal dispersion filtration: Description of critical flux and comparison with experimental results. *Desalination*. 2006;192:74-81.
- [289] Bessiere Y, Abidine N, Bacchin P. Low fouling conditions in dead-end filtration: Evidence for a critical filtered volume and interpretation using critical osmotic pressure. *Journal of Membrane Science*. 2005;264:37-47.
- [290] Bacchin P, Aimar P, Sanchez V. Influence of surface interaction on transfer during colloid ultrafiltration. *Journal of Membrane Science*. 1996;115:49-63.

-
- [291] Duffie JA, Beckman WA. Solar engineering of thermal processes, 3rd ed.: Wiley; 2006.
- [292] Tarroja B, Mueller F, Samuelsen S. Solar power variability and spatial diversification: implications from an electric grid load balancing perspective. *International Journal of Energy Research*. 2013;37:1002-16.
- [293] Remize PJ, Guigui C, Cabassud C. Evaluation of backwash efficiency, definition of remaining fouling and characterisation of its contribution in irreversible fouling: Case of drinking water production by air-assisted ultra-filtration. *Journal of Membrane Science*. 2010;355:104-11.
- [294] Lipp P. State of the art in drinking water treatment by MF/UF in Germany – a survey among MF/UF plants. *Water Science and Technology: Water Supply*. 2008;8:377-81.
- [295] Bürkert: Product overview-sensors, transmitters and controllers. <https://www.processindustryinformer.com/wp-content/uploads/2017/01/burkert-product-overview-sensors.pdf> (accessed 21 April 2022).
- [296] Sagiv A, Avraham N, Dosoretz CG, Semiat R. Osmotic backwash mechanism of reverse osmosis membranes. *Journal of Membrane Science*. 2008;322:225-33.
- [297] Axaopoulos PJ, Theodoridis MP. Design and experimental performance of a PV Ice-maker without battery. *Solar Energy*. 2009;83:1360-9.
- [298] Driemeier C, Zilles R. An ice machine adapted into an autonomous photovoltaic system without batteries using a variable-speed drive. *Progress in Photovoltaics: Research and Applications*. 2010;18:299-305.
- [299] World Healthy Organisation: Guidelines for drinking water quality, 4th edition, incorporating the 1st addendum. <https://www.who.int/publications/i/item/9789241549950> (accessed 8 December 2021)2017.
- [300] Gasser P, Lustenberger P, Cinelli M, Kim W, Spada M, Burgherr P, et al. A review on resilience assessment of energy systems. *Sustainable and Resilient Infrastructure*. 2019:1-27.
- [301] F. Coelho, J. Leclerc, D. Bourdiol, A.-C. Valentin, Sauvade P. 30 years of evolution in ultrafiltration systems and processes for drinking water production. 9th International Water Association (IWA) Membrane Technology Conference & Exhibition for Water and Wastewater Treatment and Reuse, International Water Association. Toulouse, France June 23-27, 2019.
- [302] Vroman T, Beaume F, Armanges V, Gout E, Remigy J-C. Critical backwash flux for high backwash efficiency: Case of ultrafiltration of bentonite suspensions. *Journal of Membrane Science*. 2021;620:118836.
- [303] Bessiere Y, Cui G, Remize PJ, Cabassud C. Coupling air-assisted backwash and rinsing steps: a new way to improve ultrafiltration process operation for inside-out hollow fibre modules. *Desalination* 2009;240:71-7.
- [304] Cai Y-H, Schäfer AI. Renewable energy powered membrane technology: Impact of solar irradiance fluctuation on direct osmotic backwash. *Journal of Membrane Science*. 2020;598:117666.
- [305] Statista Research Department: Lithium-ion battery pack costs worldwide between 2011 and 2020. <https://www.statista.com/statistics/883118/global-lithium-ion-battery-pack-costs/> (accessed 24 April 2022)2020.
- [306] Mongird K, Fotedar V, Viswanathan V, Koritarov V, Balducci P, Hadjerioua B, et al. Energy storage technology and cost characterization report. https://www.energy.gov/sites/prod/files/2019/07/f65/Storage%20Cost%20and%20Performance%20Characterization%20Report_Final.pdf (accessed 24 November 2021)July 2019.
- [307] Bacchin P, Aimar P, Field R. Critical and sustainable fluxes: Theory, experiments and applications. *Journal of Membrane Science*. 2006;281:42-69.
- [308] Tiller FM, Cleveland T, Lu R. Pumping slurries forming highly compactible cakes. *Ind Eng Chem Res* 1999;38:590-5.
- [309] Yamamura H, Okimoto K, Kimura K, Watanabe Y. Hydrophilic fraction of natural organic matter causing irreversible fouling of microfiltration and ultrafiltration membranes. *Water research*. 2014;54:123-36.
- [310] Massé A, Thi HN, Legentilhomme P, Jaouen P. Dead-end and tangential ultrafiltration of natural salted water: Influence of operating parameters on specific energy consumption. *Journal of Membrane Science*. 2011;380:192-8.
- [311] Zeng L-f, Liu G-w, Mao J-r, Wang S-s, Yuan Q, Yuan H, et al. Flow-induced vibration and noise in control valve. *Proceedings of the Institution of Mechanical Engineers, Part C: Journal of Mechanical Engineering Science*. 2015;229:3368-77.
- [312] Mean Well: 500 W single output DC-DC converter.

<https://www.meanwell-web.com/content/files/pdfs/productPdfs/MW/SD-500/SD-500-spec.pdf> (accessed 24 March 2022).

[313] SmartSolar: Charge controllers with load output.

https://www.victronenergy.com/upload/documents/Datasheet-SmartSolar-charge-controller-MPPT-75-10,-75-15,-100-15,-100-20,-100-20_48V-EN.pdf (accessed 24 March 2022).

[314] Cowern E. The highs and lows of motor voltage.

<https://www.ecmweb.com/design/article/20901278/the-highs-and-lows-of-motor-voltage> (accessed 29 March 2022)2000.

[315] World Health Organization: Guidelines for drinking-water quality, 4th edition.

<https://www.who.int/publications/i/item/9789241549950> (accessed 29 March 2022)2017.

[316] Aquino T, Roling M, Baker C, Rowland L. Battery energy storage technology assessment. November 29, 2017. Prepared for the Platte River Power authority by HDR/Omaha, Nebraska.

<https://www.prpa.org/wp-content/uploads/2017/10/HDR-Battery-Energy-Storage-Assessment.pdf> (accessed 24 November 2021)2017.
